Karlsruher Institut für Technologie

Granular Aluminum as a Nonlinear Medium for Superconducting Parametric Amplifiers

Zur Erlangung des akademischen Grades eines

Doktors der Naturwissenschaften (Dr. rer. nat.)

von der KIT-Fakultät für Physik des
Karlsruher Instituts für Technologie (KIT)

angenommene

Dissertation

von

M. Sc. Nicolas Zapata González

Tag der mündlichen Prüfung:
13 Februar 2026

Referent: Prof. Dr. Ioan Pop
Korreferent: Prof. Dr. Anja Metelmann

Para mi madre

Abstract

Quantum-limited parametric amplifiers based on superconducting circuits have become essential components for the readout of microwave quantum systems. They are typically realized by engineering a nonlinear medium that enables energy exchange between different microwave tones. In conventional implementations, a microwave circuit exploits the nonlinearity of Josephson junctions (JJs), which can be modulated through the application of strong pump tones. However, despite the remarkable progress achieved over the past decade, JJ-based amplifiers still suffer from two major limitations that hinder their applicability in the next-generation of quantum technologies: sensitivity to magnetic fields beyond the millitesla range and non-negligible higher-order nonlinearities. In recent years, amplifiers based on disordered superconductors have emerged as a promising alternative to overcome these constraints. Among them, granular aluminum (grAl) stands out as one of the richest and most versatile sources of nonlinearity.

In this thesis, we investigate the potential of grAl to replace JJs as the nonlinear element in parametric amplifiers. We leverage grAl's nonlinear properties to fabricate a practical standing-wave parametric amplifier, nicknamed the grAlPA, with a design resembling a superconducting Bose–Hubbard dimer. We engineer the grAlPA to provide signal gains above 20 dB, saturation powers around −110 dBm, signal–pump detuning of $\sim$ 100 MHz, and gain–bandwidth product close to 40 MHz. In the first part of the thesis, we demonstrate the applicability of the grAlPA as a magnetic-field-resilient amplifier. Remarkably, our device remains within less than one photon of added noise above the quantum limit for in-plane magnetic fields up to 1 T, highlighting its potential for the readout of hybrid quantum systems. In the second part, we exploit the interplay between grAl's diluted higher-order nonlinearities and low self-capacitance to realize a near quantum-limited amplifier with an unconventional gain–bandwidth product at gain levels up to 25 dB, a performance not previously reported in any JJ-based implementations. By applying two parametric pumps to the grAlPA, we simultaneously activate phase-preserving gain and frequency-conversion processes, enabling a tenfold enhancement of the amplifier bandwidth at 20 dB gain. The results of this thesis position granular aluminum as a promising alternative for the next generation of parametric devices, capable of overcoming the limitations that remain unresolved in JJ-based parametric amplifiers.

Acknowledgements

Where would we be without all the ups and downs in life? Looking back at all these years as a PhD student, I can say it was not easy. There were very difficult times when I wasn't sure I would reach the finish line. But those "eureka" moments during measurements, those final cleaning steps during fabrication, and, above all, the support from colleagues, friends, and family made it possible. After all, it was always my dream to work in science, and, as in any aspect of life, the rainbow comes after the storm. During the last few years, I feel I have grown immensely, both as a person and as a scientist, and I would like to thank everyone who, in one way or another, helped me along this path.

First of all, I would like to thank my doctoral advisor, Ioan. I will always admire your passion for science and especially the way you approach academia. You have an amazing touch with people and a remarkable way of motivating everyone around you. When I was finishing my Master's, I visited KIT for the first time for a short lab tour. Back then, I wasn't really sure which topic to choose for my PhD, but after that visit, the decision became very easy. I was impressed by how you run the group and how much you genuinely care about creating a positive and relaxed working atmosphere. I have to say, even during times when I wasn't doing well personally, it was this atmosphere that kept me going. So thank you very much for that. I also want to thank you for giving me the chance to pursue my own ideas and for trusting me to lead the amplifier team. You never said no to the (sometimes crazy) things I proposed, and even when some of them weren't exactly aligned with your main interests, you still let me explore them and try to get the best out of my experiments. I'm sorry I couldn't finish all the projects I started, some had to be dropped because of time, but I hope I still managed to contribute to the amplifier efforts of the group. And of course, I would also like to thank you for the opportunity to visit so many places, Delft, Vienna, Copenhagen, Barcelona, whether to install DJJAAs or to just give a talk. Those were incredible experiences that helped me build many valuable connections for my professional life. For all of that, and for plenty of other things that I won't detail here, otherwise this paragraph would never end, I sincerely thank you Ioan.

I would also like to thank Anja Metelmann for the fruitful collaboration and for agreeing to be my second reviewer. I remember reading your Bogo amp paper during my first year of the PhD, and back then I hoped that one day I would have the chance to try these ideas with my own amplifiers. In the field of parametric amplifiers, perhaps even more than in qubits, building an experiment closely connected to fundamental science has become quite rare nowadays. Being able to realize a (grAl) Bogo amp is something I will always be proud of, and a large part of this achievement was possible thanks to your interest in my experiments.

Thank you, Najmeh, also for providing all the theoretical support for the Bogo amp paper. It was definitely not an easy task, as both the theory and the experiments were really challenging. I'm really glad you kept working to understand the system until we finally managed to fit the data. I also really appreciate you letting me use your report and calculations for the theory sections of my thesis.

Of course, I couldn't let this section pass without thanking the person who worked with me for a large part of the PhD: Mitchell. I started out as your "supervisor," but you very quickly caught up and I would even say surpassed me in many ways. I am very happy to see how much you have developed over these years. Thank you for your patience and for all the ways you helped me in the lab, whether it was coming up with possible explanations for the weird things we saw in experiments, listening to all my complaints about everything, helping supervise students, proofreading this thesis, etc, etc, etc... You are truly a brilliant (lucky) person and scientist. And when the time comes, aim high, because (in fact) there is no group or company that wouldn't be super happy to have you in their team. Good luck in the rest of PhD man and I hope we'll have the chance to share a project again in the future.

I wouldn't have been able to work on so many projects without the help of all the students I supervised (or helped supervise) during my PhD: Reet, Immanuel, Adria, Lucas, Taym, and Xavier. I know it's not normal to supervise so many students as a PhD, but I'm really happy I had this opportunity because I learned a lot from all of you and discovered a skill I didn't know I had. I hope you all had a great time during your stay in Karlsruhe and that your careers are going really well.

I would like to thank all past and present members of the Black Forest Quantum group. Ivan, thanks for training me and introducing me to the field of parametric amplifiers. Thomas, thank you so much for all the support with CN-related things and for the help with the laser cutter. Dennis, Simon(1), Patrick, and Martin, thanks for all the great discussions and ideas you shared for my projects. Mayha and Ritika, thanks for the wonderful memories from the workshop in Trieste. Thanks to all the PhDs of my generation (the original members of the "young PhD paper group"): Ameya, Simon(2), Sören, Nico G, and Denis. Thanks for all the fun times and crazy drinking sessions. I'm happy we are all close to finish now and that we managed to get some really cool results. You are all brilliant, and I'm very glad to have shared this time with you. I look forward to seeing what the future holds and hope we'll meet again at some point. Of course, I have to mention one particularly crazy person, Mathieu. Thanks for all the tips and tricks for my experiments and for your endless discussions about all kind of topics, from deep scientific ideas to debates about why Avengers movies aren't great. Paul, Phillip, and (again) Mitchell, thanks for the fun times in the 3rd-floor office, talking about science and everything else. Paul, thanks for inviting us to your garden, I hope this becomes a tradition in the future! Danilo, Priya, and Sumeru, even though we didn't overlap much, it was a pleasure meeting you, and I wish you all the best for the next years at KIT.

I also want to acknowledge all the support from the technicians and administrative staff at CFN and IQMT. Lucas Radtke, Silvia Diewald, and Aina Quintilla, thank you for all

your help with cleanroom-related problems. Dorothea Trautmann and Carmen Dörflinger, thanks for helping me navigate the bureaucratic nightmare of KIT administration.

I also want to take this opportunity to thank all the external collaborators I had the pleasure of working with. In particular, I would like to mention Gary Steele and Georgios Katsaros. Thank you so much for letting me visit your labs and install one of our DJJAAs. I hope they were useful for your research.

Of course, I would like to thank the friends I met during my PhD and the old friends who stayed in touch over the years. Thomas and Paul, we really had a great time in the old WG. I still miss the perfect balance we managed to have there. I never experienced anything like it again in Karlsruhe. Luca and Marti, although it wasn't quite like the epic nights in Cologne, it was still great to go a little crazy once in a while across different places in Europe. Chris, it's amazing how we've managed to stay in contact after so many years, and how you're still supporting FC Köln even after losing so many matches. Oliver, hope to see you soon, hermano. Wilson Y, Joaks, Pableinz, and Wilson N, crazy times in the US! Five days of conference, three of them drunk, and the other two either at the casino or at Disneyland. Typical Ecuadorian lifestyle. Raquel and Loic, thanks a lot for all the parades in Lauterbourg and the Ecuadorian nights at your place. Sarita, Jose, Jonathan, Dario and Joel, thanks for all your help and support over these years. Crazy trips to Paris, Zadar, and Strasbourg. Even though we haven't had proper time to meet and catch up again, as Sarita once said, there's a time each year when just having the amount of chaos we can create in a week is enough to carry us through the rest of the year. Thank you all so much for your advice and for always being there when I needed you.

And last but not least, I'll switch to my native language to thank the two main pillars of my life: my girlfriend Miriam and my family.

Miry, gracias por todo el apoyo que me has dado todo este tiempo. No sabes cuanto significaba para mi verte, asi sea una vez al año, pero esos momentos me daban la energía que necesitaba para seguir adelante. No se que pasará con nosotros en el futuro pero toda la vida voy a estar agradecido, por que sin tí, no hubiera podido superar tantos obstáculos que tuve durante el PhD. Gracias de corazón. Ahora que se acaba esta etapa de mi vida espero que por fin tengamos la vida que soñamos.

Familia, no se ni como empezar a agradecerles todo lo que me han ayudado. El apoyo que fueron en los momentos más duros del doctorado, y que a pesar de mis equivocaciones, nunca deje de sentirlos a mi lado. Uno de los más grandes pesares de mi vida será siempre el haberme perdido tantos momentos con ustedes. Pero siempre iré con la cabeza en alto sabiendo que cumplí mis sueños. Quiero agradecerles especialmente a mi padre y a mi madre. Gracias pa, por darme esa tranquilidad que muchas veces necesitaba y ayudarme tanto todo este tiempo. Siempre me voy a acordar de ese viaje a Nueva York. Fue algo que en su momento necesitaba y me ayudo mucho a salir adelante. Y por su puesto, gracias ma. Por todo. Por tu cariño incondicional. Por tu paciencia para escucharme todos mis problemas. Por ser la mujer que eres, aguerrida y luchadora. Fue esa parte que herede de ti mamá. Siempre voy a estar orgulloso de haber podido crear ese lazo que tenemos ahora.
NZ

Contents

List of Publications

1. **N. Zapata**, N. E. Abari, M. Field, P. Winkel, S. Geisert, S. Ihssen, A. Metelmann, and I. M. Pop, "Double-Pumped Kerr Parametric Amplifier Beyond the Gain-Bandwidth Limit", arXiv (2025).
2. A. Kreiner, N. Hussain, R. Dhundhwal, H. Duan, **N. Zapata**, G. C. Marques, T. Cubaynes, T. Scherer, W. Wernsdorfer, M. Hirtz, I. M. Pop, J. Aghassi-Hagmann, and T. Reisinger, "Liquid metal printing for superconducting circuits", arXiv (2025).
3. A. Nambisan, S. Günzler, D. Rieger, N. Gosling, S. Geisert, V. Carpentier, **N. Zapata**, M. Field, M. V. Milošević, C. A. D. Lopez, C. Padurariu, B. Kubala, J. Ankerhold, W. Wernsdorfer, M. Spiecker, and I. M. Pop, "Quantum Coherence in Superconducting Vortex States", arXiv (2025).
4. M. Khorramshahi, M. Spiecker, P. Paluch, S. Geisert, N. Gosling, **N. Zapata**, L. Brauch, C. Kübel, S. Dehm, R. Krupke, W. Wernsdorfer, I. M. Pop, and T. Reisinger, "High-impedance granular-aluminum ring resonators", Phys. Rev. Appl. **24**, 024066 (2025).
5. R. Hanna, S. Ihssen, S. Geisert, U. Kocak, M. Arfini, A. Hertel, T. J. Smart, M. Schleenvoigt, T. Schmitt, J. Domnick, K. Underwood, A. R. Jalil, J. H. Bae, B. Bennemann, M. Féchant, M. Field, M. Spiecker, **N. Zapata**, C. Dickel, E. Berenschot, N. Tas, G. A. Steele, D. Grützmacher, I. M. Pop, and P. Schüffelgen, "On-chip stencil lithography for superconducting qubits", arXiv (2025).
6. D. Bénâtre, M. Féchant, **N. Zapata**, N. Gosling, P. Paluch, T. Reisinger, and I. M. Pop, "Simultaneous sweet-spot locking of gradiometric fluxonium qubits", Phys. Rev. Appl. **24**, 054031 (2025).
7. S. Ihssen, S. Geisert, G. Jauma, P. Winkel, M. Spiecker, **N. Zapata**, N. Gosling, P. Paluch, M. Pino, T. Reisinger, W. Wernsdorfer, J. J. Garcia-Ripoll, and I. M. Pop, "Low crosstalk modular flip-chip architecture for coupled superconducting qubits", Appl. Phys. Lett. **126** (2025).
8. S. Günzler, J. Beck, D. Rieger, N. Gosling, **N. Zapata**, M. Field, S. Geisert, A. Bacher, J. K. Hohmann, M. Spiecker, W. Wernsdorfer, and I. M. Pop, "Spin environment of a superconducting qubit in high magnetic fields", Nat. Commun. **16**, 9564 (2025).
9. **N. Zapata**, I. Takmakov, S. Günzler, S. Geisert, S. Ihssen, M. Field, A. Nambisan, D. Rieger, T. Reisinger, W. Wernsdorfer, and I. M. Pop, "Granular Aluminum Parametric Amplifier for Low-Noise Measurements in Tesla Fields", Phys. Rev. Lett. **133**, 260604 (2024).

10. S. Geisert, S. Ihssen, P. Winkel, M. Spiecker, M. Fechant, P. Paluch, N. Gosling, **N. Zapata**, S. Günzler, D. Rieger, D. Bénâtre, T. Reisinger, W. Wernsdorfer, and I. M. Pop, "Pure kinetic inductance coupling for cQED with flux qubits", Appl. Phys. Lett. **125**, 064002 (2024).

List of Figures

List of Tables

1 Introduction

Throughout history, science and technology have advanced in a synergistic manner. Driven by an intrinsic curiosity to understand the mechanisms that govern the universe, humanity has continually developed technologies of increasing sophistication. From the steam engine and early electrical machines to the advent of the laser and the transistor, each technological breakthrough has also enabled scientists to shed light on some of the most profound questions in physics. Quantum mechanics, one of the fundamental theories currently providing answers to many of these questions, has propelled the development of a new generation of technologies over the past years. In contrast to early inventions enabled by quantum theory, which rely on the behavior of macroscopic objects, modern quantum technologies are based on the control and readout of individual quantum systems such as superconducting qubits [1], trapped ions [2], photons [3], nanomechanical oscillators [4], and spins in semiconductors [5]. By harnessing the principles of entanglement and superposition, these platforms hold great promise for future applications in quantum sensing, quantum communication, and quantum computing.

Among the various physical implementations currently under exploration, superconducting quantum circuits shine as one of the most prominent platforms for the development of novel quantum technologies [1, 6]. Owing to the absence of resistive dissipation and thermal noise, they can be engineered to exhibit quantum mechanical properties at macroscopic scales [7]. Compared to other quantum platforms, they offer two key advantages. First, because their operational frequencies typically lie in the microwave frequency range, the community can leverage the vast knowledge developed for microwave telecommunications, to design fast and efficient control of quantum devices. Second, they can be reproducibly fabricated using standard nanofabrication techniques, originally developed for the semiconductor industry.

In a typical experimental setup, the superconducting quantum circuit is installed inside a cryostat operated at milikelvin temperatures and measured using microwave-frequency lines. However, the signals that carry the information encoded in the circuit's degrees of freedom are extremely fragile, and any perturbation or unwanted coupling to an uncontrolled environment can irreversibly destroy this information before it is detected or processed. Addressing this challenge necessitates not only optimizing the fabrication and operation of the quantum system itself, eliminating potential loss channels through which information can leak, but also carefully designing the readout setup to ensure efficient energy transfer through the microwave lines connected inside and outside the cryostat.

In general, one must build a measurement setup capable of amplifying the response of a quantum circuit without destroying the encoded information and while adding minimal

noise. In classical systems, semiconductor-based amplifiers can be used for this purpose. However, their noise levels are typically orders of magnitude larger than the signals produced by quantum devices [8, 9]. For this reason, the past two decades have witnessed the rise of microwave superconducting parametric amplifiers [10–13]. They can amplify the response of a quantum system while adding only the noise produced by vacuum fluctuations of the electromagnetic field [14]. Amplifiers that operate at this limit are now known as quantum-limited parametric amplifiers.

In their most common implementations, quantum-limited amplifiers are built by exploiting the nonlinearity of Josephson junctions (JJs). While it has long been known that JJs provide the nonlinearity required for parametric amplification, as evidenced by publications dating back to even 1967 [15], it was not until the 21st century, with the rise of quantum technologies, that research in this field reached its current level of sophistication. Nowadays, an extensive variety of amplifiers, with different designs and topologies, can be found in the literature [16–27]. They have been instrumental in the field of superconducting quantum circuits to achieve multiple milestones and to make high-fidelity readout a standard requirement [12, 13, 28].

Despite their successful applications in superconducting circuits, JJ-based amplifiers still suffer from two fundamental limitations. First, the inherent susceptibility of JJs to magnetic fields [29–32] prevents their use in platforms such as semiconductor qubits [33–37], electromechanical systems [38], molecular magnets [39], and dark-matter detectors [40–42]. These systems require magnetic fields that exceed the typical operational range of JJ amplifiers, and, to date, no definite alternative has been found to match the readout fidelities achieved in pure superconducting circuits. Second, although JJs provide the nonlinear medium required for amplification, their tendency to enter a chaotic regime at high driving powers[1] [43–45] poses a limitation for the scalability of quantum processors, where multiple quantum systems may need to be measured using a single amplifier [35, 46–48].

Parametric amplifiers exploiting the nonlinearity of disordered superconductors have emerged as a promising alternative. Several groups have employed NbN [49, 50], TiN [51] and NbTiN [52–60] to implement (near) quantum-limited amplifiers operating at magnetic fields as high as 6 T [50]. Moreover, these devices demonstrated saturation powers, a measure of the amplifier's power handling capabilities, up to three orders of magnitude higher than typical JJ-based implementations [50, 54–56]. These results sparked a quest for the most optimal alternative to JJ amplifiers, leading the community to explore various disordered superconductors.

In this project, we focus on an alternative disordered superconductor: granular aluminum (grAl). Initially seen as a testbed for many-body phenomena in superconductors [61–64], grAl has recently attracted a lot of attention due to its amenable fabrication and tunable nonlinearity. It has been used to realize various types of microwave resonators [65–70], superinductors [71–78], coherent quantum vortices [79] and weak links for superconducting

[1] In simple words, Josephson junctions might be too nonlinear for parametric amplifiers.

circuits [80, 81]. While its nonlinearity has proven versatile, it is a-piori not clear whether grAl could be used to fabricate a parametric amplifier[2]. A key distinction compared to other devices is the operating power: while resonators and qubits operate at powers around -130 dBm, an amplifier requires roughly -60 dBm, seven orders of magnitude higher power.

In this thesis, we present an implementation of a granular aluminum parametric amplifier, called grAlPA, and investigate its performance metrics. As we will show, grAl's unique nonlinear properties can be leveraged to realize a viable alternative to JJ-based devices.

This manuscript is organized as follows. In the remainder of this introductory chapter, we provide the theoretical background and fundamental concepts of superconducting parametric amplifiers. In Chapter 2, we give an overview of grAl superconducting properties and explain why it provides an optimal source of nonlinearity for building a parametric amplifier. We then move to Chapter 3, where we demonstrate that the grAlPA can successfully operate at magnetic fields up to 1 T, and we discuss the main considerations in its design and fabrication. Finally, Chapter 4 presents another way the grAlPA can outperform JJ-based amplifiers: in-situ control of its amplification bandwidth through the use of multiple parametric pumps.

1.1 Basics of parametric amplification

We begin this introductory section with a general explanation of the basic concepts of microwave parametric amplifiers. We provide a broad overview on their operation principles and what are the main metrics needed to consider when designing amplifiers. The discussions of this chapter will be useful across the thesis and also when introducing the main focus of this work: superconducting parametric amplifiers.

1.1.1 Microwave circuits

The origin of microwave circuits as a field in physics and engineering can be traced back to James Clerk Maxwell's 19th-century prediction that his equations support the propagation of electromagnetic waves [83]. Due to the mathematical complexity of Maxwell's original equations, the prediction was initially regarded merely as a curious theoretical result with no practical use in a laboratory. It was not until 1887, when Heinrich Hertz successfully verified the existence of electromagnetic waves propagating at a frequency of 50 MHz, that microwave radiation was recognized as an effective resource

[2] The potential of grAl for constructing a parametric amplifier was first recognized by Ioan and his former PhD student, Ivan Takmakov, during experiments driving a fluxonium qubit with a grAl superinductor. This accidental discovery is detailed in Ref. [82].

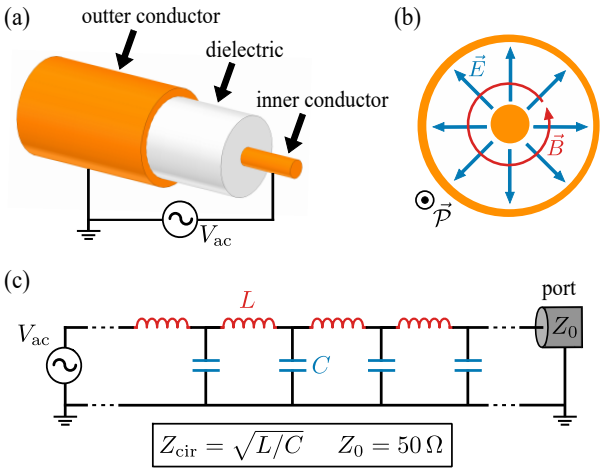

Figure 1.1: Equivalent circuit model of a microwave medium. **(a)** Schematics of a coaxial cable consisting of a cylindrical inner conductor surrounded by a dielectric layer and an outer hollow-cylindrical conductor. By applying an AC voltage V_{AC} between the conductors, the cable transmits energy through a TEM mode. **(b)** Field distribution of the TEM mode. The electric field $\vec{E}$ fills the region between the conductors, while the magnetic field $\vec{B}$ circulates around the inner conductor. Energy propagates in the direction of the Poiynting vector $\vec{\mathcal{P}}$. **(c)** Equivalent circuit model of the cable, where distributed capacitors C and inductors L, store the energy of the electric and magnetic field. The model is valid when the wavelength is much larger than the cable dimensions.

to transmit information over distant locations[3]. The advent of radar technology during World War II and, later, satellite communications in the 20th century, further advanced research in microwave theory and electronics, shaping the field as we know it today. Over the past two decades, superconducting quantum circuits have built upon this foundation, with the additional advantage that they can be analyzed within the theoretical framework of quantum mechanics.

The task of designing a microwave setup essentially boils down to engineering the spatial and temporal distribution of electromagnetic fields within a given medium. To achieve this, one must solve Maxwell's equations and adjust the geometry of the medium until the desired field distributions are obtained. For simple geometries, where analytical solutions can be derived, this process is relatively straightforward. This is the case, for example, of a coaxial cable, where one can show that a possible propagation mode is the so-called transverse electromagnetic (TEM) mode, in which the Poynting vector and the electric and magnetic fields are mutually perpendicular (see Fig. 1.1(a)-(b)). However, for more complex geometries, such as those typically used in superconducting circuits, finding analytical solutions to Maxwell's equations becomes extremely challenging, and one must instead rely on dedicated numerical solvers to simulate the electromagnetic response of the system.

To simplify the analysis of a microwave setup, its dynamics can be mapped to an effective lumped-element circuit model, as illustrated in Fig. 1.1(c). If the wavelength of the microwave signal is much larger than any characteristic dimension of the system, the evolution of the electric and magnetic fields can be represented as generated from an equivalent network of point-like capacitors and inductors [83]. Similarly, energy dissipation in

[3] At the time, Hertz was skeptical about the applicability of his discovery. When asked by his students about its potential use, he replied: "Nothing, I guess" [84]. Ironically, little could he have known that more than a century later, scientists would use his discovery to engineer complex quantum phenomena in the very same place where his original experiments were performed.

the system can be modeled using a combination of series resistors and parallel conductances, which account for resistive and dielectric losses, respectively. The arrangement of these elements determines the response of the system now in terms of the distribution of electrical currents and voltages across the circuit. They can then be solved using, for example, Kirchhoff's circuit laws instead of the full 3-dimensional Maxwell equations. As we will see later, this approach also provides a natural framework for quantizing the dynamics of a microwave circuit through canonical quantization.

The response of a circuit to a microwave signal depends on both its physical parameters and the imposed boundary conditions. For a lossless circuit, this response is largely determined by the ratio between its characteristic impedance, defined as $Z_{\text{cir}} = \sqrt{L/C}$, and the impedance of the surrounding microwave environment, which is commonly fixed[4] at $Z_0 = 50\ \Omega$. When $Z_{\text{cir}} = Z_0$, the energy of an incoming wave can be transferred through the circuit without any insertion loss, realizing an efficient transmission line. Conversely when $Z_{\text{cir}} \neq Z_0$, part of the energy is reflected at each end of the circuit. A microwave signal inside the circuit then bounces back and forth between the ends, forming a standing wave. In this regime, the circuit behaves as an electrical resonator.

1.1.2 How can we engineer a parametric amplifier?

The principles of parametric amplification have long been established across nonlinear optical [86], mechanical [87], and electrical [12] systems. Parametric amplification arises when a parameter characterizing a system or material, such as the refractive index in photonic crystals, the spring constant in mechanical oscillators, or the impedance in microwave circuits, is modulated at specific frequencies. A common example is that of a child on a swing[5], but here we choose to illustrate the origin of parametric amplification using the more extravagant example presented in the book of Baker and Blackburn [87].

Inside the cathedral of Santiago de Compostela, in northern Spain, hangs a 53 kg and 1.5 m tall incense burner known as the *Botafumeiro*. The burner is suspended approximately half a meter above the church floor by a rope of about 44 m in length, forming an effective pendulum (see Fig. 1.2). At roughly half its total length, the rope is connected to a support structure anchored to the top of the nave. During the liturgy, a team of priests, called *tiraboleiros*, set the burner into motion by pulling and pushing one side of the rope. As with any pendulum, the *Botafumeiro* oscillates at a natural frequency $\omega = \sqrt{g/l}$, determined by the gravitational acceleration g and the rope length l between the support point and the burner. By synchronizing their pulls so that the effective length l is momentarily reduced when the burner reaches its maximum height, the *tiraboleiros* inject energy into the system,

[4] The reason why the microwave community converged to a standard impedance of 50 Ω is not entirely clear. However, it may have come simply from practical convenience: for early air-dielectric coaxial cables, at 50 Ω there is a compromise between transmission losses and power handling [85].

[5] By modulating his center of mass (and thus his moment of inertia) at twice the swing's natural frequency, the child can transfer mechanical work into the kinetic energy of the swing and increase its oscillation amplitude [12, 88].

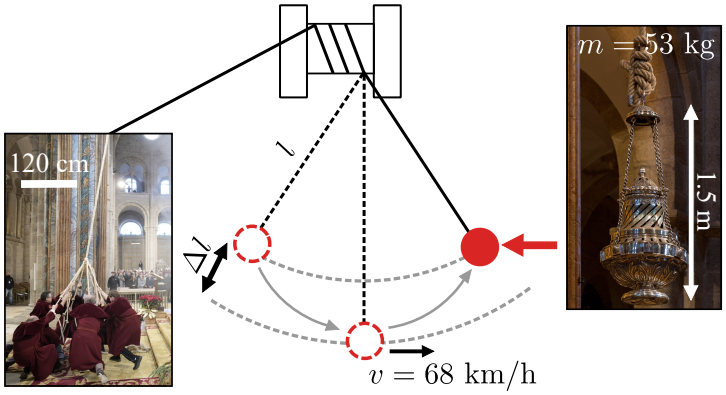

Figure 1.2: Parametric pumping of the *Botafumeiro*. By periodically modulating the length l of the rope connected to the *Botafumeiro* (right), the *tiraboleiros* (left) are able to do work on the system, amplifying the burner's oscillation amplitude. With this mechanism, the *Botafumeiro* can reach speeds of up to $v = 68$ km/h. Pictures retrieved from Ref. [89].

increasing the amplitude of the oscillations. This effect is maximized when the pulling is periodic and occurs at a frequency 2ω. In this sense, the action of the *tiraboleiros* act as a parametric pump: by modulating a defining parameter of the pendulum, which is in this case its length, they can increase the oscillations amplitude. Interestingly, through this mechanism the *Botafumeiro* can reach a swing amplitude of up to 82° arc and a maximum velocity of 68 km/h at the lowest point of its trajectory.

In a microwave circuit, the kind of manual modulation used in the *Botafumeiro* is not possible. Instead, parametric processes arise from the intrinsic nonlinearity of the circuit elements: capacitors and inductors. The values of L and C introduced in Fig. 1.1(c), were treated as linear parameters, defined to describe the interaction between the electric and magnetic fields in the system. However, more generally, these quantities can also depend on the amplitude of the electromagnetic field itself, taking the form

$$C(V) = C_0 \left(1 + \chi_2 V + \chi_3 V^2 + \cdots\right) = C_0 \left(1 + \sum_{i\in\mathbb{N}} \chi_{i+1} V^i\right), \tag{1.1}$$

and

$$L(I) = L_0 \left(1 + \zeta_2 I + \zeta_3 I^2 + \cdots\right) = L_0 \left(1 + \sum_{i\in\mathbb{N}} \zeta_{i+1} I^i\right). \tag{1.2}$$

where C_0 and L_0 denote the capacitance and inductance at zero fields, I denotes the current flowing through the inductance and V the voltage stored in the capacitor, respectively. The quantities ζ_{i+1} and χ_{i+1} (with $i \in \mathbb{N}$) parametrize the $i+1$-th order of nonlinearity in the inductance and capacitance, respectively[6]. The goal is therefore to engineer a microwave circuit whose elements realize the nonlinear relations in Eqs. (1.1) and (1.2). A nonlinear capacitance of the form of Eq. (1.1) can be implemented using varactor diodes [88] or by employing perovskite crystals as dielectric materials [90]. Conversely, a nonlinear inductance consistent with Eq. (1.2), which will be the primary focus of this thesis, can be realized using Josephson junctions [11–13], disordered superconductors [49–51, 55, 56, 65, 91–94], or proximitized semiconductors [95–99].

[6] The motivation for this notation is that nonlinearities are conventionally defined with respect to the equations of motion. For example, the coefficient ζ_{i+1} gives rise to a term of the form $\zeta_{i+1} \cdot I^{i+1}$ in the circuit's equations of motion (i.e. Kirchhoff's equations).

To develop an intuition on how a capacitor or inductor described by Eqs. (1.1) and (1.2) can generate parametric amplification, we analyze a simple LC resonator (cf. Fig. 1.4(a)) whose inductance is weakly nonlinear. Specifically, we assume an inductance of the form in Eq. (1.2) with a single nonzero coefficient $\zeta_2 = \zeta$ and $\zeta_i = 0$ for $i > 2$. The voltage and current in the circuit satisfy

$$V = -L(I)\frac{dI}{dt}, \quad I = C_0\frac{dV}{dt}. \tag{1.3}$$

By replacing Eq. (1.2) into Eq. (1.3), one can show that the current I follows the nonlinear equation

$$\frac{d^2I}{dt^2} = -\frac{1}{\omega_\mathrm{r}^2}I - \frac{\zeta}{\omega_\mathrm{r}^2}\left(\frac{dI}{dt}\right)^2 - \frac{\zeta}{\omega_\mathrm{r}^2}I\frac{dI}{dt}, \tag{1.4}$$

where $\omega_\mathrm{r} = 1/\sqrt{L_0C_0}$ is the resonance frequency of the circuit. Then, analogous to the *Botafumeiro* example, we assume that the system is driven by a strong microwave pump at frequency $\omega_\mathrm{p} = 2\omega_\mathrm{r}$. Simultaneously, the circuit is driven by a weak signal tone at $\omega_\mathrm{s} = \omega_\mathrm{r}$. We then solve Eq. (1.4) using the ansatz $I = I_\mathrm{p}\exp(2i\omega_\mathrm{r}t + i\phi_\mathrm{p}) + I_\mathrm{s}\exp(i\omega_\mathrm{r}t + i\phi_\mathrm{s}) + \mathrm{c.c.}$, where $I_{\mathrm{p/s}}$ and $\phi_{\mathrm{s/p}}$ are amplitudes and phases of the pump and signal tones. Then assuming a stiff pump approximation i.e. taking $I_\mathrm{s} \ll I_\mathrm{p}$, one finds that the gain of the signal tone at frequency ω_r can be written as

$$G = \left(\frac{\Delta I_\mathrm{s}}{I_\mathrm{s}}\right)^2 = \zeta^2\left|I_\mathrm{p}\right|^2\left(1 + \cos(2\phi_\mathrm{p} - 4\phi_\mathrm{s})\right). \tag{1.5}$$

Equation (1.5) reveals two key features of a parametrically pumped circuit. First, the amplitude of the signal current I_s is amplified, and the amplification strength increases with the nonlinear coefficient ζ. Second, the output signal depends on the relative phase between the pump and the signal, which realizes what is called a phase-sensitive amplifier. This phase dependence can be removed by applying the signal with a detuning Δ from the resonator frequency, i.e., by choosing $\omega_\mathrm{s} = \omega_\mathrm{r} + \Delta$. If the circuit is pumped at $2\omega_\mathrm{r}$, it can still provide amplification at the frequency ω_s. However, this process inevitably generates an additional tone at $\omega_\mathrm{i} = \omega_\mathrm{r} - \Delta$, called the idler, necessary to satisfy the energy conservation relation $\omega_\mathrm{p} = \omega_\mathrm{s} + \omega_\mathrm{i}$.

1.1.3 Amplifier classification

Although nonlinearity is the essential ingredient for engineering a parametric amplifier, such devices can be realized using a variety of geometries and operational modes. In this section, we provide a brief overview of the general classification of parametric amplifiers. They can be categorized according to four main criteria: the circuit geometry, the combination of frequencies involved in the parametric process, the number of interacting modes, and the dependence on the phases of the driving tones.

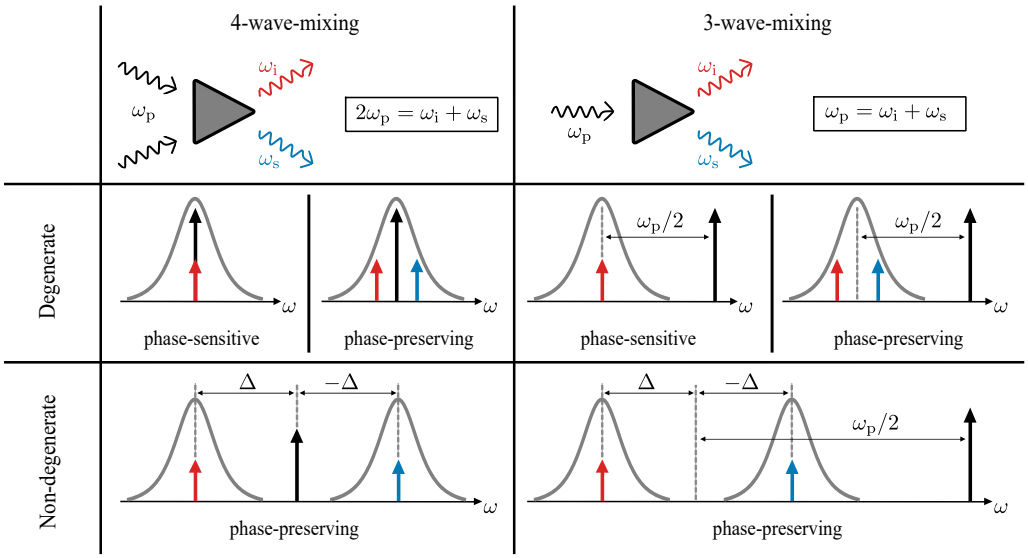

Figure 1.3: Parametric amplifiers classification. The dynamics of the mixing processes in the few-photons regime are shown in the upper column, where ω_p, ω_s and ω_i denote the pump, signal, and idler frequencies, respectively. The grey curves illustrate the typical Lorentzian gain profiles expected for standing-wave amplifiers. However, this classification also applies to TWPAs.

Standing-wave vs. traveling wave

A parametric amplifier can be classified according to the nature of the tones living inside the device. As discussed in Section 1.1.1, when the circuit impedance Z_{cir} differs from the impedance of its microwave environment Z_0, the system behaves as a resonator and supports standing waves. They can interact and produce gain by modulating the system's nonlinearity with a pump tone. These devices are known as Standing-Wave Parametric Amplifiers [11, 12]. In contrast, by engineering $Z_{\text{cir}} = Z_0$, the system effectively behaves as a transmission line, allowing waves to propagate without reflection. In this case, parametric interactions occur between waves traveling along the transmission line. This geometry is referred to as a Traveling Wave Parametric Amplifier (TWPA) [13].

3-wave-mixing vs. 4-wave-mixing

Parametric amplifiers can also be classified according to the order of nonlinearity in their components. Although, in principle, all orders of nonlinearity can produce parametric gain [100], nonlinearities above the third order are typically neglected because they are several orders of magnitude weaker than lower-order terms and require significantly higher pump powers for their activation.

A circuit with a third-order nonlinearity produces parametric amplification through 4-wave mixing processes. To understand the gain mechanism, we analyze the circuit dynamics in the few-photons regime. As depicted in Fig. 1.3, in 4-wave mixing, the energy of two pump photons at frequency ω_p is transferred into a signal and an idler photon at frequencies

ω_s and ω_i, satisfying the energy conservation condition $2\omega_p = \omega_s + \omega_i$. In contrast, a circuit operating with a second-order nonlinearity requires a pump tone at frequency $\omega_p = \omega_s + \omega_i$. In this case, a single pump photon splits into a signal and an idler photon, realizing a 3-wave-mixing amplifier.

Phase-sensitive vs. phase-preserving

As shown in Eq. (1.5), the gain of an amplifier can be phase-sensitive. This effect occurs whenever there is a degeneracy between the signal and idler frequencies (i.e. $\omega_s = \omega_i$), which creates phase-modulated interference in the correlations of the output fields. When only vacuum noise enters at the signal and idler frequencies, a phase-sensitive amplifier can generate single-mode vacuum-squeezed light [11, 86]. This non-classical state of light can be employed for enhanced quantum readout [101] and dynamically improved qubit coupling [102]. In contrast, when $\omega_s \neq \omega_i$ the amplifier operates in a phase-preserving mode. This is the conventional mode used for the readout of quantum devices [28, 103], and was first implemented by Ref. [28]. In this regime, at the vacuum level, the amplifier generates two-mode vacuum squeezing [11, 86], which is a key resource for quantum teleportation [104] and has the possibility to generate entangled qubits in a quantum processor [105].

Degenerate vs. non-degenerate

We define an amplifier as degenerate or non-degenerate depending on whether the signal and idler tones occupy the same or different physical modes of the device. Fig. 1.3 shows a schematic illustrating the difference between these two types of amplifiers. This classification is particularly important for standing-wave amplifiers, where the modes have finite bandwidths and well-defined frequency separation. We note that this definition differs from that in Ref. [12], where degeneracy was defined based on the frequency separation between the signal and idler. We choose not to follow that convention, as it can create confusion with the concepts of phase-sensitive and phase-preserving amplifiers.

1.2 Superconducting quantum circuits

In this section we provide an overview on some of the key aspects of superconducting quantum circuits. The discussion will be mainly focused on how these aspects allow us to fulfill the main requirements needed to implement parametric amplifiers. However, we refer the interested reader to Refs. [1, 6, 106] for a more complete review about superconducting quantum circuits.

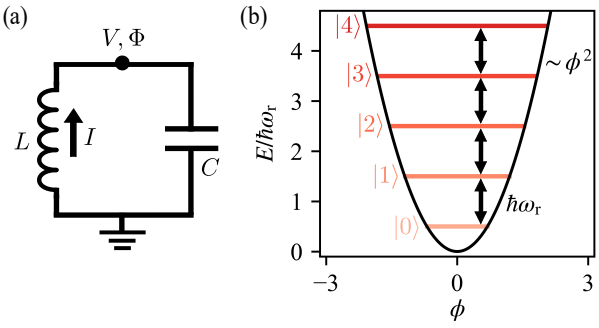

Figure 1.4: Circuit quantization of an LC resonator. **(a)** Effective circuit diagram. The node flux is defined as in Eq. (1.7). **(b)** Energy spectrum of the LC resonator, showing energy levels that resemble those of a harmonic oscillator. The levels are equally spaced, with a spacing determined by the resonator frequency ω_r. The black line represents the quadratic potential arising from the inductive energy of the circuit, which scales as ϕ^2, where $\phi = \Phi/\Phi_0$.

1.2.1 Circuit quantization and the quantum harmonic oscillator

During the writing of this thesis, John Clarke, Michel M. Devoret and John M. Martinis were awarded the Nobel Prize in Physics [107] for their work in macroscopic quantum mechanical tunneling and energy quantization in an electric circuit [7]. Their work addressed a question that had puzzled the scientific community for many years: Can a macroscopic object exhibit the properties of a quantum mechanical system? By the time they carried out their experiments, several phenomena that could not be explained using classical physics, like superfluidity and superconductivity, were already known [29, 108]. However, it remained unclear whether the discrete nature of energy levels in a macroscopic system could be directly probed in a laboratory. In 1980, Anthony Leggett predicted that, under sufficiently low dissipation and thermal noise, an electrical circuit could exhibit signatures of macroscopic quantum tunneling [109]. Both conditions are naturally satisfied in superconducting quantum circuits: resistive losses are effectively eliminated through the use of superconductors, and thermal noise is strongly suppressed at the typical temperatures (< 30 mK) and frequencies (4–12 GHz) required for their operation.

In the case of parametric amplifiers, such energy-level discretization is not directly accessible because, as we will see in the next sections, the effective dissipation in these devices exceeds the average spacing between their energy levels. Nevertheless, understanding the proper quantization procedure for a microwave circuit is essential for analyzing the noise added by the amplifier [10, 11] and for characterizing their ability to generate non-classical states of light [110–115].

As explained in the work of Vool and Devoret [116], the quantization procedure follows the formalism of canonical quantization i.e. quantizing the degrees of freedom that parametrize the system in its classical counterpart. To understand the formalism, we take the example of the simplest realizable microwave circuit: a lossless LC resonator (see Fig. 1.4(a)). At the classical level, this circuit can be modeled by the Hamiltonian

$$H = \frac{Q}{2C} + \frac{\Phi}{2L}, \tag{1.6}$$

where Q is the charge of the capacitor and Φ is called the node flux and is defined by

$$\frac{d\Phi}{dt} = V = -L\frac{dI}{dt}, \tag{1.7}$$

The Hamiltonian in Eq. (1.6) is the circuit analogue of the textbook mechanic harmonic oscillator, where the capacitance and inductance play the roles of the mass and spring constant, respectively. Moreover, using Eq. (1.7), we can verify that the charge and node flux are conjugate variables, analogous to the position and momentum of the mechanical counterpart. Consequently, Q and Φ can be transformed to quantum mechanical operators that satisfy the commutation relations $[\hat{\Phi}, \hat{Q}] = i\hbar$. Then, one can rewrite the Hamiltonian of the LC resonator in terms of the bosonic operator $\hat{a}$, such that[7]

$$\hat{H}/\hbar = \omega_{\mathrm{r}} \left(\hat{a}^{\dagger} \hat{a} + \frac{1}{2} \right) = \omega_{\mathrm{r}} \left(\hat{n} + \frac{1}{2} \right), \tag{1.8}$$

where $\omega_{\mathrm{r}} = 1/\sqrt{LC}$ is the resonator frequency and Q and Φ can now be defined as function of $\hat{a}$ as

$$\hat{\Phi} = \Phi_{\mathrm{ZPF}} \left(\hat{a} + \hat{a}^{\dagger} \right), \quad \hat{Q} = -iQ_{\mathrm{ZPF}} \left(\hat{a} - \hat{a}^{\dagger} \right). \tag{1.9}$$

The quantities Φ_{ZPF} and Q_{ZPF} are called the flux and charge zero point fluctuations, which are defined in terms of the resonator impedance $Z_{\mathrm{r}} = \sqrt{L/C}$, as

$$\Phi_{\mathrm{ZPF}} = \sqrt{\frac{\hbar Z_{\mathrm{r}}}{2}}, \quad Q_{\mathrm{ZPF}} = \sqrt{\frac{\hbar}{2Z_{\mathrm{r}}}}. \tag{1.10}$$

Similar to the case of a mechanic harmonic oscillator, the quantization of the LC resonator yields a spectrum with an equal spacing between the energy levels (see Fig. 1.4(b)).

1.2.2 The Josephson Junction

Although the LC resonator helps us understand how to quantize the dynamics of a superconducting circuit, it cannot be used directly to realize a parametric amplifier because it lacks a key ingredient: nonlinearity. Fortunately, there exists an element that can provide the necessary nonlinearity to a superconducting circuit: the Josephson junction (JJ) (illustrated in Fig. 1.5(a)). Originally predicted in 1962 by Brian D. Josephson [29], the Josephson effect is a manifestation of macroscopic quantum coherence in a superconductor. It appears when two superconducting electrodes with wave functions $\Psi_1 = \sqrt{n_1 e^{i\theta_1}}$ and $\Psi_2 = \sqrt{n_2 e^{i\theta_2}}$ (where $n_{1/2}$ and $\theta_{1/2}$ denote their Cooper pair densities and condensate phases, respectively), are connected by an insulating barrier[8]. In this case, the coherent transport of charges between the superconducting leads can take place due to the tunneling of Cooper pairs. This produces the appearance of a non-dissipative current with a current phase relation following Eq. (1.11), which is known as the DC Josephson effect.

$$I = I_{\mathrm{c}} \sin(\phi), \tag{1.11}$$

[7] An alternative quantization procedure based on the microscopic theory of superconductivity is presented in Ref. [117]. A more simplified, yet intuitive, derivation can also be found in the Appendix of Ref. [72].

[8] Although in general Josephson junction refers to any pair of superconducting electrodes connected by a weak link, here we focus only on the case when the weak link is an insulator.

where ϕ=$\theta_1 - \theta_2$ and I_c is the critical current of the junction. If the electrodes are biased by a DC current I, this current flows without dissipation as long as $I < I_c$. However, if $I > I_c$, a current coming from quasiparticles creates a potential drop V between the electrodes. This voltage can tune the time dependence of the relative superconducting phase ϕ according to Eq. (1.12), which known as the AC Josephson effect.

$$V = \frac{\Phi_0}{2\pi}\frac{d\phi}{dt}, \tag{1.12}$$

where $\Phi_0 = h/2e$ is the magnetic flux quantum.

Equations (1.11) and (1.12) show that a JJ can be viewed as a nonlinear inductance. To make this analogy more explicit, we can substitute Eq. (1.11) into Eq. (1.12) and compare the $I - V$ relation with Eq. (1.7). We can then identify an inductive term given by

$$L = \frac{L_J}{\sqrt{1 - \left(\frac{I}{I_c}\right)^2}} = L_J\left(1 + \frac{I^2}{I_*^2} + \cdots\right), \tag{1.13}$$

which effectively implements a current-dependent inductance similar to the one discussed in Section 1.1.2. At lowest order, the JJ implements a 3rd-order nonlinearity that can be used to drive 4-wave-mixing interactions, with a strength determined by the characteristic current $I_* = \sqrt{2}I_c$. The quantity $L_J = \Phi_0/2\pi I_c$ is called the Josephson inductance (cf. Fig. 1.5(b)). Moreover, a second-order nonlinearity can be implemented by applying a combination of AC (I_{AC}) and DC (I_{DC}) currents to the JJ. To see this, we assume that the total current flowing through the junction is $I = I_{DC} + I_{AC}(\omega)$, where ω denotes the frequency of the AC bias current. Substituting this expression into Eq. (1.12), one finds that the inductance takes the form

$$L = L_J\left(1 + \frac{I_{DC}^2}{I_*^2} + \left(\frac{2I_{DC}}{I_*^2}\right)I_{AC} + \frac{I_{AC}^2}{I_*^2} + \cdots\right). \tag{1.14}$$

In terms of the classification introduced in Section 1.1.3, the third term in Eq. (1.14) enables 3-wave-mixing processes[9]. Moreover, by comparison with Eq. (1.2), we observe that the strength of the second-order nonlinearity, is proportional to the ratio I_{DC}/I_*.

The most common approach for fabricating a JJ is to use a stack of pure aluminum (Al) electrodes separated by an aluminum oxide (AlO_x) insulating barrier [118–120], as depicted in Fig. 1.5(a). In this method, an aluminum layer is first deposited on top of an insulating substrate and is then oxidized under a controlled oxygen pressure. Because the oxidation of aluminum is self-limiting, only the upper 2-3 nm of the film oxidize [121, 122]. A second aluminum layer is then subsequently deposited, completing the vertical JJ stack. Because of the nm-scale thickness of the oxide layer, the geometry in Fig. 1.5(a) effectively forms a parallel-plate capacitance C_J, which can be estimated using the relation $C_J \approx A \cdot 50$ fF/μm^2, where A is the area of the JJ [123, 124].

[9] This process can be interpreted as a 4-wave-mixing interaction with one of the pumps set to zero frequency.

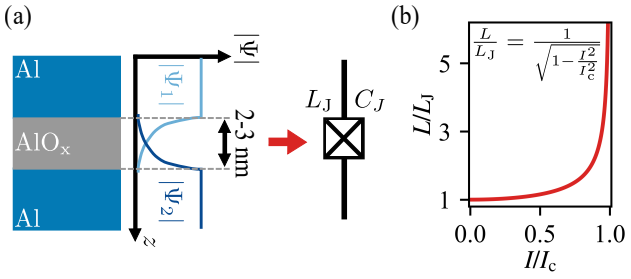

Figure 1.5: Nonlinearity of a Josephson Junction. **(a)** Schematics of a conventional Al-AlO_x-Al JJ. Transport across the Al leads occurs via tunneling of Cooper pairs, enabled by the overlap of the condensate wave functions in each lead (Ψ_i with $i = 1, 2$). **(b)** Nonlinear inductance of the JJ. As the current through the junction increases, the effective inductance rises.

1.2.3 Superconducting qubits

One of the most important milestones enabled by the nonlinearity of a JJ is the realization of a quantum bit, or qubit, by embedding the junction in a superconducting circuit [1, 6, 103]. In contrast to linear harmonic oscillators, where all energy levels are equally spaced, the nonlinearity introduced by the JJ produces an uneven spacing between adjacent energy levels. The deviation from a purely linear spectrum is quantified by the anharmonicity α, defined as

$$\alpha = (E_2 - E_1) - (E_1 - E_0), \tag{1.15}$$

where E_i with $i = 0, 1, 2$ are the energies of the ground, first excited and second excited states of the qubit, respectively.

For sufficiently large anharmonicities and low dissipation, one can selectively drive Rabi oscillations between a chosen pair of energy levels, effectively realizing a quantum two-level system. At the time of writing this thesis, several laboratories have already implemented quantum processors comprising hundreds of superconducting qubits [46–48, 125, 126]. Although this scale is still insufficient for the most ambitious quantum-computing applications, significant efforts are underway to further increase the size and performance of these processors.

Finding an optimal method to detect the signal that encodes the state of a superconducting qubit has long been one of the main motivations behind the development of parametric amplifiers. These devices are typically designed to meet the requirements needed for single-shot qubit readout. However, at the same time, superconducting qubits also serve as valuable tools for parametric amplifier characterization, as they can be seen as highly accurate power calibration sources[10]. Although the field of superconducting qubits has become increasingly broad, in this thesis we focus specifically on the type of qubits used to calibrate our parametric amplifiers. For the interested reader, Appendix C provides a detailed explanation of two different methods by which qubits can be used to calibrate the added noise of an amplifier.

[10] In the mind of a parametric amplifier engineer, the usual roles are flipped: amplifiers take the central stage, and qubits are treated as useful calibration tools.

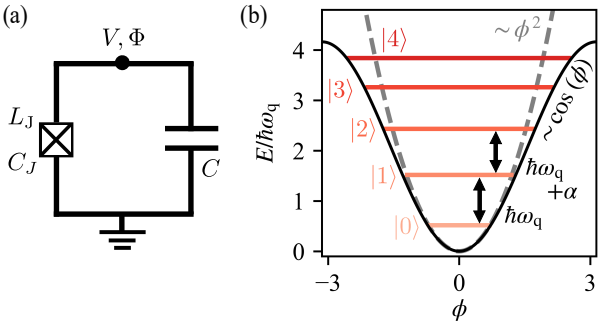

Figure 1.6: Circuit quantization of a transmon qubit. (a) Circuit diagram. A JJ with inductance L_J and capacitance C_J is shunted by with an additional capacitor C. When the total charging energy E_C and Josepshon energy E_J satisfy $E_J \gg E_C$ (cf. Eq. (1.16)), the circuit is known as a transmon qubit. **(b)** Energy spectrum of a transmon qubit with $E_C = 1$ GHz and $E_J = 30$ GHz. The nonlinear energy–phase potential (black solid line) produces an anharmonicity α defined in Eq. (1.15), which separates the two lowest energy levels to form a qubit with frequency ω_q. For comparison, the grey dashed line shows the potential of a linear harmonic oscillator.

Transmon qubit

The simplest way to fabricate a superconducting qubit is to shunt a JJ with a parallel capacitor of strength C, as shown in Fig. 1.6(a). The dynamics of this circuit can be modeled by the Hamiltonian

$$\hat{H} = 4E_C(\hat{n} - n_g)^2 - E_J \cos(\hat{\phi}), \tag{1.16}$$

where $E_C = e^2/2C_\Sigma$ is the charging energy determined by the total capacitance $C_\Sigma = C_J + C$, $\hat{n} = \hat{Q}/2e$ is the number of Cooper pairs tunneling across the junction, n_g is the offset charge produced by an external field bias and $E_J = \Phi_0^2/(4\pi^2 L_J)$ is called the Josephson energy. The potential energy $E_J \cos(\phi)$ can be derived by calculating the energy stored inside the JJ using Eq. (1.11) and Eq. (1.12).

The behavior of the system depends on the ratio E_J/E_C. When $E_J/E_C \ll 1$, the system's eigenstates correspond to the eigenstates of the charge operator. In this regime, the spectrum is highly anharmonic, but the qubit is also sensitive to charge noise, which degrades its stability and coherence. This problem can be mitigated by moving to the opposite limit, $E_J/E_C \gg 1$. In this case, the circuit is called a transmon qubit, whose dynamics are better described in the basis of the phase operator $\hat{\phi}$. The suppression of charge dispersion in the transmon, which increases exponentially with E_J/E_C, comes at the cost of a reduced anharmonicity. Nevertheless, because the anharmonicity decreases only linearly with E_J/E_C, there is an optimal ratio where one can design the circuit such that charge noise is strongly suppressed while the device still shows an anharmonicity on the order of 10-100 MHz. These values are sufficient for coherent control and readout of a transmon qubit.

In the transmon regime (cf. Fig. 1.6(b)), phase fluctuations across the JJ are small, allowing us to expand the cosine potential in Hamiltonian (1.16) to quartic order

$$\hat{H} = 4E_C(\hat{n} - n_g)^2 + \frac{1}{2}E_J\hat{\phi}^2 - \frac{1}{24}E_J\hat{\phi}^4 + \cdots, \tag{1.17}$$

where we have omitted all possible offset energies. Using the canonical quantization (cf. Eq. (1.9)), one can rewrite Eq. (1.17) and obtain

$$\hat{H}/\hbar = \omega_q \hat{a}^\dagger \hat{a} + \frac{K}{2}\hat{a}^\dagger \hat{a}^\dagger \hat{a}\hat{a}, \tag{1.18}$$

where $\hbar\omega_q = \sqrt{8E_J E_C} - E_C$ is the qubit frequency and now the nonlinearity of the circuit is denoted by the self-Kerr coefficient $K \approx E_C$, which sets the anharmonicity of the Transmon.

Generalized flux qubit

To overcome the tradeoff between charge-noise sensitivity and anharmonicity in a transmon qubit, one can instead design a Generalized Flux Qubit (GFQ) [74, 127, 128], as depicted in Fig. 1.7(a). In this architecture, the transmon's original JJ, called the α-junction is shunted by an array of N identical JJs, each with Josephson energy γE_J. The α-junction and the JJ array form a closed loop threaded by an external magnetic flux Φ_{ext}. The system is described by the Hamiltonian

$$\hat{H} = 4E_C(\hat{n} - n_g)^2 - E_J \cos(\hat{\phi}) - \gamma N E_J \cos(\hat{\phi}_L/N), \tag{1.19}$$

where the term ϕ_L represents the total superconducting phase drop across the entire array. In the limit of a large number of junctions, $\gamma/N \ll 1$, the total energy of the array can be approximated by expanding the JJ cosine potential to second order, such that $\cos(\hat{\phi}_L/N) \approx 1 + (\phi_L/N)^2$ (see Fig. 1.7(b)). Thus, the JJ array behaves as a linear inductance with inductive energy $E_L = \gamma E_J/N$, which screens offset charges and improves charge stability. Eq. (1.19) then simplifies to the Fluxonium qubit Hamiltonian [71, 129]

$$\hat{H} = 4E_C(\hat{n} - n_g)^2 - E_J \cos(\hat{\phi}) - \frac{1}{2}E_L\left(\hat{\phi} - \phi_{ext}\right)^2, \tag{1.20}$$

where we have used $\phi + \phi_L = \phi_{ext}$ and $\phi_{ext} = 2\pi\Phi_{ext}/\Phi_0$. Here, $E_L = (\Phi_0/2\pi)^2/L$ denotes the energy stored in the effective inductance $L = (N/\gamma)\, L_J$.

Conventionally, the GFQ is operated in the fluxon regime, where $E_C \approx E_J$ and $E_L < E_J$. When biased at half-flux $\Phi_{ext} = \Phi_0/2$, the potential energy has a double-well shape (see Fig. 1.7(c)). In this regime, the anharmonicity can reach the GHz scale, two orders of magnitude larger than that of a transmon, making GFQs particularly suitable for fast and high-fidelity qubit control.

1.2.4 Josephson Junction arrays

In contrast to superconducting qubits, where large anharmonicity is essential, parametric amplifiers require only a very small nonlinearity, typically with self-Kerr coefficients $K \lesssim 1$ KHz. For a single JJ, the nonlinearity can be tuned by increasing its critical current

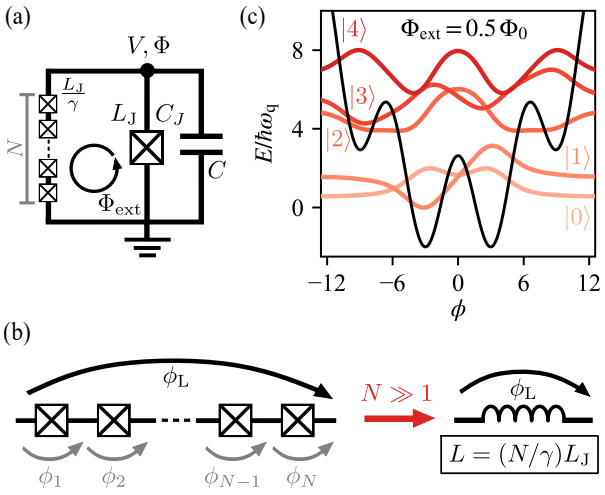

Figure 1.7: Circuit quantization of a generalized flux qubit (GFQ). **(a)** Circuit diagram of the GFQ. The transmon circuit is now shunted by an array of N identical JJs with inductance L_J/γ. The array forms a loop with the original junction (called the α-junction), allowing the qubit to be biased with an external magnetic flux Φ_{ext}. **(b)** In the long-array limit ($N \gg 1$), the phase drop across each JJ is approximately equal, such that the array behaves as a linear inductor with $L = (N/\gamma)L_J$. **(c)** Energy spectrum of a GFQ with $E_C = E_J = 1$ GHz and $E_L = 20$ GHz. When biased at $\Phi_{ext} = 0.5\Phi_0$, the circuit develops a double-well potential hosting the two lowest energy levels that define the qubit computational space. Compared to the transmon, the GFQ is less sensitive to charge noise and exhibits up to three orders of magnitude larger anharmonicity.

I_c. The value of I_c is determined by the Cooper pair tunneling rate across the insulating barrier, and can be experimentally tuned by adjusting the oxidation conditions used to form the AlO_x layer. However, increasing I_c, changes not only the nonlinearity but also the junction inductance and the circuit resonance frequency.

To reduce the self-Kerr coefficient without changing the circuit resonance frequency, a standard technique is to replace the single JJ with an array of N identical junctions, similar to the case of the GFQ. In the limit of long arrays ($N \gg 1$), the total Josephson energy can be expanded using a Taylor series. Expanding the potential of the array up to fourth order gives [21, 130]

$$-NE_J \cos(\hat{\phi}/N) \approx -NE_J + \frac{E_J}{2N}\hat{\phi}^2 - \frac{E_J}{24N^3}\hat{\phi}^4. \tag{1.21}$$

We see that the quadratic term (which fixes the resonance frequency) and the quartic term (responsible for the self-Kerr nonlinearity) can now be tuned independently through both I_c (through the dependence with E_J) and N.

Using the creation and annihilation operators defined in Section 1.2.1, the Hamiltonian in Eq. (1.6) takes the form of Eq. (1.18). For a fixed resonance frequency, the self-Kerr coefficient can now be written as

$$K = -\frac{E_J}{8\hbar N}\left(\frac{\omega_r L_J}{R_Q}\right)^2. \tag{1.22}$$

where $R_Q = \hbar/4e^2$ is the resistance quantum.

1.2.5 Open quantum systems and circuit readout

So far, we have studied the behavior of a superconducting quantum circuit assuming it is completely isolated from its environment. In a real experimental setup, however, the

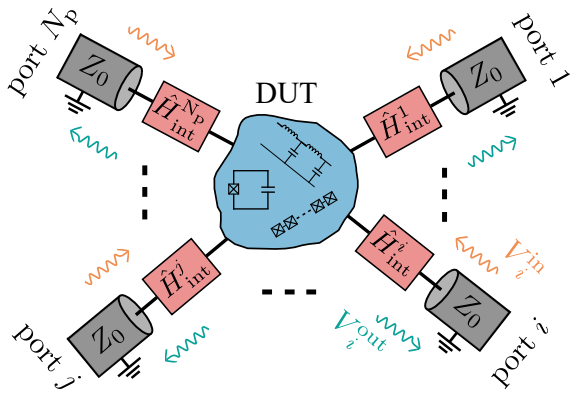

Figure 1.8: General setup used in open quantum systems. A device under test (DUT) is coupled to readout channels, used by an experimentalist to extract information, and dissipation channels, representing internal losses and which are inaccessible by the an external observer. Classically, the DUT's information can be described by scattering theory [83], while at the quantum level it requires the formalism of open quantum systems [131, 132]. The Hamiltonian of the full setup, including DUT and ports, is given by Eq. (1.26).

system is coupled to various control and readout channels. These couplings allow us to probe the circuit dynamics but also introduce unavoidable loss and decoherence.

Classically, in microwave engineering, a device under test (DUT) is treated as a black box connected to multiple ports, as shown in Fig. 1.8. An input signal at port i (with $i = 1, \cdots, N_\mathrm{p}$), represented as an excitation voltage V_i^in, interacts with the electromagnetic field inside the DUT and emerges from all ports in the form of outgoing voltages V_j^out (with $j = 1, \cdots, N_\mathrm{p}$), each carrying information about the state of the system. The ratios between incoming and outgoing voltages are known as the scattering parameters and are defined as

$$\mathrm{S}_{ji} = \left.\frac{V_j^\mathrm{out}}{V_i^\mathrm{in}}\right|_{V^\mathrm{in}_{k\neq i}=0}, \tag{1.23}$$

where S_{ii} is the reflection coefficient at port i and S_{ji} (with $i \neq j$), represents the transmission coefficient from port i to port j. By measuring the complete set of scattering coefficients at all ports, one can infer all the information about the state of the DUT [83].

Unfortunately, this classical formalism breaks down when we attempt to describe a quantum system. In the specific case of a parametric amplifier, it fails to capture the correct dynamics of quantum fluctuations and the noise that accompanies the emitted radiation. For this reason, when studying a quantum microwave circuit, one must instead use the input–output formalism, originally developed by Gardiner and Collet in 1985 [131, 133].

In this approach, the system is modeled as being coupled to one or more semi-infinite transmission lines, each acting as a reservoir. The electromagnetic field propagating along these lines is described by bosonic operators $\hat{b}_i(\omega)$ and the Hamiltonian

$$\hat{H}_\mathrm{TL}/\hbar = \sum_{i=1}^{N_\mathrm{p}} \int \hat{b}_i^\dagger(\omega)\hat{b}_i(\omega)d\omega, \tag{1.24}$$

where $[\hat{b}_i(\omega), \hat{b}_j^\dagger(\omega')] = \delta(\omega - \omega')\delta_{\mathrm{i,j}}$. In a Rotating Wave Approximation (RWA), the coupling between the transmission line and the DUT can be written as

$$\hat{H}_\mathrm{int}/\hbar = \sum_{i=1}^{N_\mathrm{p}} \hat{H}^i_\mathrm{int}/\hbar = \sum_{i=1}^{N_\mathrm{p}} \int \xi_i(\omega)\left(\hat{a}\hat{b}_i^\dagger(\omega) + \hat{b}_i(\omega)\hat{a}^\dagger\right)d\omega, \tag{1.25}$$

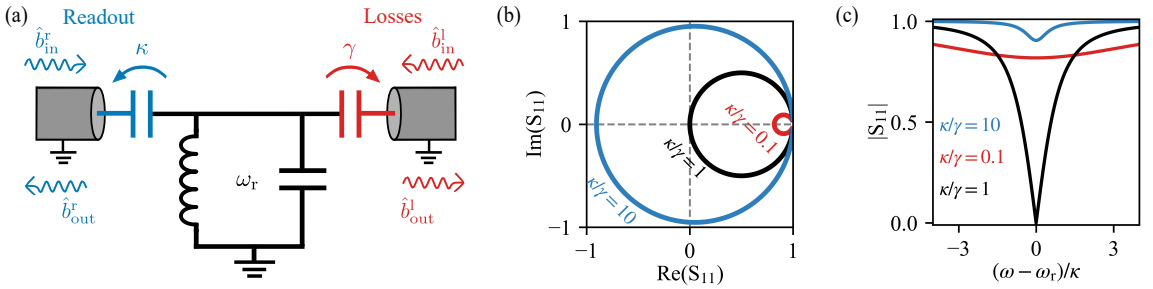

Figure 1.9: Resonance of an LC circuit in an open quantum system. **(a)** Circuit diagram of an LC resonator in a realistic experimental setup. The resonator, with frequency ω_{r}, is coupled to readout (blue) and loss (red) channels, with external and internal coupling rates κ and γ, respectively. **(b)** Complex-plane representation of the reflection coefficient S_{11} of the LC resonator from panel (a). The size of the resonance circle depends on the coupling rates. **(c)** Reflection amplitude for different κ/γ ratios. The resonance is barely visible in the undercoupled (κ/γ) $\ll 1$ and overcoupled ($\kappa/\gamma \gg 1$) regimes, while a clear dip appears at ω_{r} in the critically coupled case ($\kappa/\gamma = 1$).

where $\xi_i(\omega)$ are frequency-dependent coupling coefficients and $\hat{a}$ denotes the bosonic mode of the DUT [132]. Then the dynamics of the full system, which includes both the DUT and the semi-infinite transmission lines, is governed by the Hamiltonian,

$$\hat{H} = \hat{H}_{\mathrm{DUT}} + \hat{H}_{\mathrm{TL}} + \hat{H}_{\mathrm{int}}. \tag{1.26}$$

Readout of an LC resonator

The simplest circuit we can use to show how we derive the equations of motion of a DUT with the Hamiltonian (1.26), is again a lossless LC resonator. In this thesis we focus on devices measured in reflection, therefore we model the resonator as coupled to two transmission lines (cf. Fig. 1.9(a)): one readout line, from which we retrieve the information of the resonator, and one dissipation line, which models internal losses. Assuming the dynamics is Markovian (i.e. it has no memory effects) and the coupling strengths are weaker than the resonator frequency ω_{r}, the evolution of the resonator annihilation operator $\hat{a}$ is described by the Heisenberg–Langevin equation[11] [131],

$$\begin{aligned}\frac{d\hat{a}}{dt} &= -\frac{i}{\hbar}[a, \hat{H}_{\mathrm{DUT}}] - \left(\frac{\kappa+\gamma}{2}\right)\hat{a} + \sqrt{\kappa}\,\hat{b}^{\mathrm{r}}_{\mathrm{in}} + \sqrt{\gamma}\,\hat{b}^{\mathrm{l}}_{\mathrm{in}} \\ &= -i\omega_{\mathrm{r}}\hat{a} - \left(\frac{\kappa+\gamma}{2}\right)\hat{a} + \sqrt{\kappa}\,\hat{b}^{\mathrm{r}}_{\mathrm{in}} + \sqrt{\gamma}\,\hat{b}^{\mathrm{l}}_{\mathrm{in}},\end{aligned} \tag{1.27}$$

where $\hat{b}^{\mathrm{r/l}}_{\mathrm{in}}$ are the bosonic operators of the input radiation fields at each port, and κ and γ are the coupling strengths to the readout and loss channels, respectively.

[11] This equation can be derived from the time-dependent dynamics of the resonator and bath operators, $\hat{a}$ and $\hat{b}_{\mathrm{in}}$, starting from the total system–bath Hamiltonian in Eq. (1.26). For a pedagogical derivation, we refer the reader to Ref. [82].

By converting to the frequency domain using a Fourier transform, Eq. (1.27) can be rewritten as

$$\hat{a}(\omega) = \frac{\sqrt{\kappa}\,\hat{b}^{\mathrm{r}}_{\mathrm{in}}}{i(\omega-\omega_{\mathrm{r}})+(\kappa+\gamma)/2} + \frac{\sqrt{\gamma}\,\hat{b}^{\mathrm{l}}_{\mathrm{in}}}{i(\omega-\omega_{\mathrm{r}})+(\kappa+\gamma)/2}. \tag{1.28}$$

To retrieve information from the harmonic oscillator, one measures the radiation field emerging from the readout line. This outgoing field can be related to the input field using the input–output relation

$$\hat{b}^{\mathrm{r}}_{\mathrm{out}} = -\hat{b}^{\mathrm{r}}_{\mathrm{in}} + \sqrt{\kappa}\,\hat{a}. \tag{1.29}$$

Combining Eq. (1.28) and Eq. (1.29) allows us to obtain an expression for the reflection coefficient $\mathrm{S}_{11} = \hat{b}^{\mathrm{r}}_{\mathrm{out}}/\hat{b}^{\mathrm{r}}_{\mathrm{in}}$ at the readout port, which follows the typical response of a microwave resonator [83] and is given by

$$\mathrm{S}_{11}(\omega) = -1 + \frac{\kappa}{i(\omega-\omega_{\mathrm{r}})+(\kappa+\gamma)/2}. \tag{1.30}$$

The coupling strengths γ and κ can be related to quantities that are more commonly used in microwave electronics: the external Q_{c} and internal Q_{i} quality factors of the resonator. They are defined as

$$Q_{\mathrm{c}} = \omega_{\mathrm{r}}/\kappa, \quad Q_{\mathrm{i}} = \omega_{\mathrm{r}}/\gamma. \tag{1.31}$$

These quantities characterize how efficiently a resonator stores energy relative to the dissipation through its loss channels. Depending on the relative magnitudes of $Q_{\mathrm{i/c}}$, a resonator falls into one of three regimes, each associated with a distinct resonance-line shape, as illustrated in Fig. 1.9(b)-(c). When $Q_{\mathrm{i}} < Q_{\mathrm{c}}$ ($\gamma > \kappa$), the resonator is undercoupled, and most of the energy cannot be retrieved because it leaks mainly through the loss channel. When $Q_{\mathrm{i}} = Q_{\mathrm{c}}$ ($\gamma = \kappa$), the resonator is critically coupled, and the energy decays equally into the readout and dissipation channels. This regime is ideal for accurately extracting Q_{i}, as it minimizes Fano uncertainties originating from the measurement setup [134]. Finally, when $Q_{\mathrm{i}} > Q_{\mathrm{c}}$ ($\gamma < \kappa$), the resonator is overcoupled, and most of the radiated energy can be collected through the readout line. This is the optimal operational regime for standing-wave parametric amplifiers because, as we will see in Section 1.3.3, it minimizes the added noise.

Waveguide Quantum electrodynamics

Similar to the case of an LC resonator, a superconducting qubit can be coupled directly to a set of microwave ports. This setup is often referred to as a waveguide Quantum Electrodynamics (wQED) architecture [80, 103, 135, 136] and emulates the fluorescence of a single atom in free space (see Fig. 1.10(a)). The readout line can still be treated as a Markovian environment. However, for a qubit, several dissipation channels can exhibit "memory" effects, leading to non-Markovian behavior [137, 138]. Moreover, fully capturing the dynamics of the qubit requires tracking the evolution of its density matrix using the master-equation formalism, which is beyond the scope of this thesis. For our purposes, we

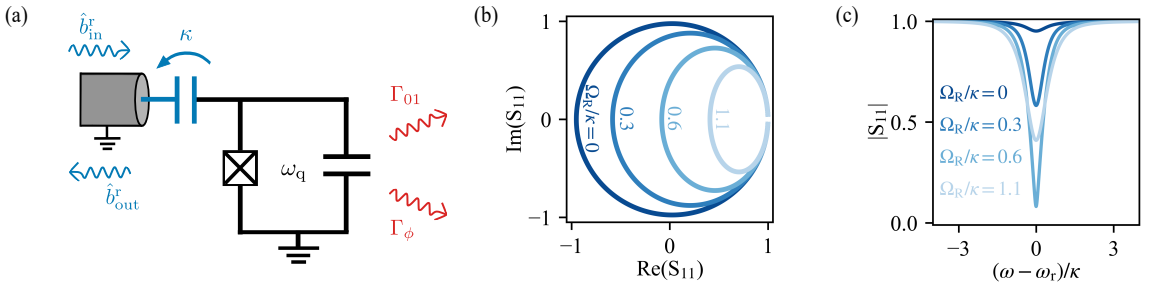

Figure 1.10: Response of a qubit in a wQED setup. **(a)** Circuit diagram of a qubit with frequency ω_{q} and coupled to a readout port with strength κ. Unwanted coupling to the environment produces energy relaxation at rate Γ_{01} and pure dephasing at rate Γ_{ϕ}. **(b)** Complex-plane representation of the reflection coefficient S_{11} in the limits $\Omega_{\mathrm{R}} \ll \alpha$ and $\Gamma_{\phi} \ll \kappa$. As the drive power is increased, Ω_{R} grows, resulting in an elliptical resonance shape. **(c)** Reflection amplitude showing the same power-dependent variation. The Rabi frequency can be used as a fitting parameter to calibrate the power at the qubit input using Eq. (1.33) (see Appendix C.4 for details).

simply analyze the resulting reflection coefficient S_{11} in the limit when the Rabi frequency Ω_{R} is smaller than the qubit anharmonicity α, as calculated by Refs. [80, 135],

$$\mathrm{S}_{11} = 1 - \kappa \frac{\Gamma_{01}\Gamma_2 - i\Gamma_{01}\left(\omega_{\mathrm{q}} - \omega\right)}{\Gamma_{01}\left[\Gamma_2^2 + \left(\omega_{\mathrm{q}} - \omega\right)^2\right] + \Gamma_2\Omega_{\mathrm{R}}}, \tag{1.32}$$

where ω_{q} and κ are the qubit frequency and external coupling strength, respectively. The quantities Γ_{01} and Γ_2 denote the qubit energy-relaxation and dephasing rates. Their inverses are called the qubit relaxation and dephasing times, $T_1 = 1/\Gamma_{01}$ and $T_2 = 1/\Gamma_2$. Moreover, the dephasing rate can be written as $\Gamma_2 = \Gamma_{01}/2 + \Gamma_{\phi}$, where Γ_{ϕ} is called the pure dephasing rate.

We observe that, in contrast to the harmonic oscillator case, the reflection coefficient of a qubit in a wQED setup depends also on the (resonant) Rabi frequency Ω_{R} (see Fig. 1.10(b)-(c)), defined as

$$\Omega_{\mathrm{R}}^2 = \frac{4\kappa P_{\mathrm{in}}}{\hbar\omega_{\mathrm{q}}}, \tag{1.33}$$

where P_{in} is the drive power at the qubit input. This implies that the qubit fluorescence can be used for an in-situ power calibration. This is crucial for parametric devices, since standard microwave calibration techniques cannot be applied inside a cryostat, where amplifiers are typically installed.

Circuit Quantum Electrodynamics

Although a qubit can be measured in a wQED architecture, a drawback of this approach is that the direct coupling to a transmission line drastically limits the qubit coherence. Since the external coupling rate κ determines the rate at which information is extracted from the qubit, achieving fast readout necessarily requires a large κ, which enhances energy relaxation and dephasing. Consequently, the wQED configuration is incompatible with

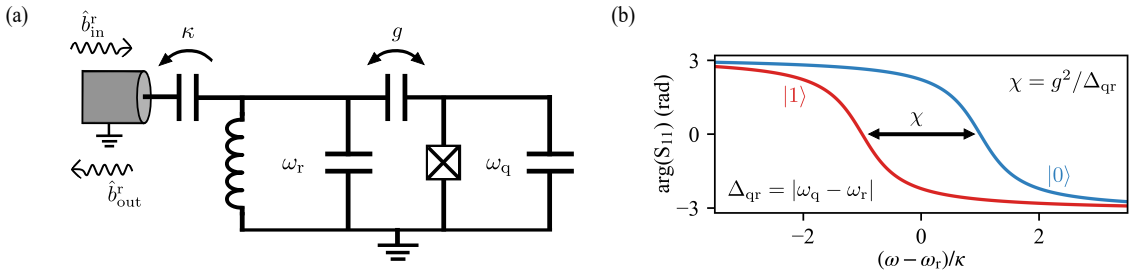

Figure 1.11: Response of a qubit in a cQED setup. **(a)** Circuit diagram of a qubit with frequency ω_{q} and coupled to a readout resonator with frequency ω_{r}. The resonator is connected to a readout port producing a damping rate κ. In the dispersive regime, the qubit-resonator coupling g induces a state-dependent shift in ω_{r}, determined by the dispersive shift $\chi \approx g^2/\Delta_{qr}$, where $\Delta_{qr} = |\omega_{\mathrm{q}} - \omega_{\mathrm{r}}|$ (cf. Eq. (1.35)). **(b)** Phase of the readout resonator reflection coefficient S_{11}, with the qubit in the ground (blue) and excited (red) state. By monitoring the resonator response, one measure the state of the qubit [103].

fast, high-fidelity, and coherent qubit measurements. To overcome this limitation, the field has largely adopted circuit Quantum Electrodynamics (cQED) architectures [103], depicted in Fig. 1.11(a). This approach is the circuit analogue of cavity QED, where a quantized electromagnetic field confined in a cavity interacts with the discrete energy levels of an atom, in this case represented by the qubit.

In cQED configuration, the qubit is coupled with strength g to a readout resonator rather than directly to a transmission line. The dynamics of the coupled system is then described by the Jaynes–Cummings Hamiltonian

$$\hat{H}/\hbar = \omega_{\mathrm{r}}\,\hat{a}^\dagger\hat{a} + \frac{\omega_{\mathrm{q}}}{2}\hat{\sigma}_{\mathrm{z}} + g\left(\hat{\sigma}_+\hat{a} + \hat{a}^\dagger\hat{\sigma}_-\right), \tag{1.34}$$

where $\hat{a}$ is the annihilation operator of the readout resonator and $\hat{\sigma}_{\mathrm{z}}$, $\hat{\sigma}_\pm$ are the Pauli operators modeling the qubit dynamics.

In the dispersive limit, when $\Delta_{\mathrm{qr}} = |\omega_{\mathrm{q}} - \omega_{\mathrm{r}}| \gg g$, the Jaynes–Cummings Hamiltonian be can diagonalized using the unitary transformation $\hat{U} = \exp\left(g/\Delta_{\mathrm{qr}}\left(\hat{\sigma}_+\hat{a} - \hat{a}^\dagger\hat{\sigma}_-\right)\right)$. Expanding up to the first order in g/Δ_{qr}, we obtain

$$\hat{H}/\hbar = \left(\omega_{\mathrm{r}} + \frac{\chi}{2}\hat{\sigma}_{\mathrm{z}}\right)\hat{a}^\dagger\hat{a} + \frac{1}{2}\left(\omega_{\mathrm{q}} + \frac{\chi}{2}\right)\hat{\sigma}_{\mathrm{z}}, \tag{1.35}$$

where $\chi \approx 2g^2/\Delta_{\mathrm{qr}}$ is called the qubit-resonator dispersive shift.

From Eq. (1.35), we can infer an important feature: the effective frequency of the readout resonator is dependent on the qubit state. This means that we can extract information about the qubit by measuring the response of the readout resonator (cf. Fig. 1.11(b)). This technique is known as dispersive readout [103] and has become the standard method for measuring superconducting qubits.

We can also regroup the terms in Eq. (1.35) in a slightly different way to obtain

$$\hat{H}/\hbar = \omega_{\mathrm{r}}\hat{a}^\dagger\hat{a} + \frac{1}{2}\left[\omega_{\mathrm{q}} + \frac{\chi}{2}\left(1 + 2\hat{a}^\dagger\hat{a}\right)\right]\hat{\sigma}_{\mathrm{z}}. \tag{1.36}$$

We now observe that, due to the coupling g, the qubit frequency ω_q is also renormalized and becomes dependent on the photon population of the readout resonator $\bar{n}_r = |\langle \hat{a}^\dagger a \rangle|$, such that

$$\omega_q(\bar{n}_r) = \omega_q(\bar{n}_r = 0) + \chi \bar{n}_r. \tag{1.37}$$

Equation (1.37) is known as the qubit AC-stark shift [139]. Since the resonator photon population can be related to the input drive power using Eq. (1.27), the AC Stark shift provides a direct method for performing power calibration (see Appendix C.3).

In addition to the AC Stark shift, fluctuations in the photon number of the readout resonator lead to an additional dephasing mechanism for the qubit. This phenomenon, called measurement-induced dephasing [139], and can be calculated in the limit of $\chi \ll \kappa$ using the following formula

$$\Delta\Gamma_\phi = \frac{2\chi^2}{\kappa} (\bar{n}_r + \bar{n}_{th}), \tag{1.38}$$

where $\bar{n}_r$ and $\bar{n}_{th}$ denote the resonator photon population due to coherent readout drive and excess thermal noise, respectively.

1.3 Superconducting parametric amplifiers

Thanks to the removal of resistive dissipation and amenable operational frequencies, superconducting microwave circuits have emerged as an ideal platform for implementing low-noise parametric amplifiers. In this subsection, we provide a brief overview of the basic features of JJ-based amplifiers. Our discussion focuses on standing-wave parametric amplifiers, as these are the devices used throughout this work. For a comprehensive review on TWPAs, we refer the reader to Ref. [13].

1.3.1 Josephson parametric amplifiers

The Josephson Parametric Amplifier (JPA) represents the minimal circuit model that captures the essential dynamics of JJ-based amplifiers. The circuit model is analogous to that of a transmon qubit and is connected similarly to the wQED setup presented in Fig. 1.10(a). The main difference lies in the relative magnitude of the circuit nonlinearity compared to the coupling rate to the readout line. For a transmon, the circuit is designed such that $\kappa \ll K$, where K is the self-Kerr coefficient defined in Eq. (1.18). In this regime, the discrete energy levels of the circuit can be addressed through the readout line. In contrast, a JPA operates in the opposite regime, $\kappa \gg K$, where the circuit behaves as a nonlinear Duffing oscillator[12] [141].

[12] Sometimes, the amplifier regime is defined when $\kappa \approx K$, in order to distinguish it from the limiting case of a purely linear oscillator with $K \to 0$ [140]. However, this definition is not entirely accurate. A more precise distinction between an amplifier and a linear resonator can be made using the analogy of a Duffing oscillator, as we propose.

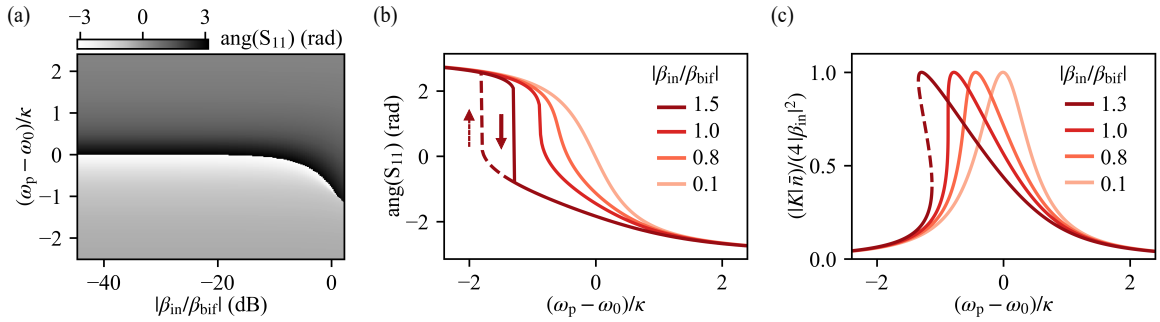

Figure 1.12: Mean-field response of a JPA. **(a)** Phase of the JPA reflection coefficient S_{11} as a function of the pump frequency ω_p and input field amplitude β_{in}. **(b)** Linecuts of panel (a) for increasing input fields. At low powers, the JPA resonance frequency ω_0 shifts proportionally to its self-Kerr coefficient K. Above a critical input field β_{bif}, the response becomes hysteretic. As shown in panel **(c)**, this behavior arises from the onset of bistability in the photon-number population $\bar{n}$, analogous to a Duffing oscillator [141]. Panels (a) and (b) are obtained using Eq. (1.42), and panel (c) by solving Eq. (1.41). In the bistable regime, the dashed lines indicate the additional solutions of the Duffing oscillator equation (cf. Eq. (1.41)).

We begin studying the behavior of a JPA by applying the Heisenberg-Langevin equations (cf. Eq. (1.27)) to derive the time evolution of the JPA bosonic operator $\hat{a}$, assuming negligible internal losses. This yields

$$\frac{d\hat{a}}{dt} = -i\omega_0\hat{a} - iK\hat{a}^\dagger\hat{a}\hat{a} - \frac{\kappa}{2}\hat{a} + \sqrt{\kappa}\,\hat{b}_{in}, \tag{1.39}$$

where ω_0 is the JPA resonance frequency. Next, we apply a pump tone at the input port, characterized by power P_p and frequency ω_p. A solution to Eq. (1.39) can then be obtained using the displacement transformation

$$\hat{a} \longrightarrow \alpha e^{-i\omega_p t} + \hat{a}, \quad \hat{b}_{in} \longrightarrow \beta_{in} e^{-i\omega_p t} + \hat{b}_{in}, \tag{1.40}$$

where $\bar{n} = |\alpha|^2$ can be interpreted as the mean-field photon number population of the JPA, and $\hat{a}$ now represents the bosonic operator of a weak probe signal entering the amplifier. The field amplitude β_{in} can be calculated from the pump power using $\beta_{in} = \sqrt{P_p/\hbar\omega_p}$. We assume a stiff pump approximation $|\langle\hat{a}\rangle| \ll \alpha$, meaning that the pump remains unaffected by the probe signal. Under these assumption, the dynamics in frequency domain of the mean-field amplitude α is described by the Duffing oscillator equation [82, 130]

$$\left((\omega_p - \omega_0)^2 + \frac{\kappa^2}{4}\right)\bar{n} - 2(\omega_p - \omega_0)K\bar{n}^2 + K^2\bar{n}^3 = \kappa|\beta_{in}|^2. \tag{1.41}$$

Using the input-output relation for the mean-field amplitudes, we can derive an analytical expression for the reflection coefficient of the JPA

$$S_{11}(\omega) = -1 + \frac{\kappa}{i(\omega_0 - \omega_p) + \kappa/2 + iK\bar{n}}. \tag{1.42}$$

Depending on the applied pump power, the JPA exhibits two markedly different dynamical regimes. At low powers, i.e. when $\bar{n} \ll \kappa/K$, the JPA behaves similarly to a linear

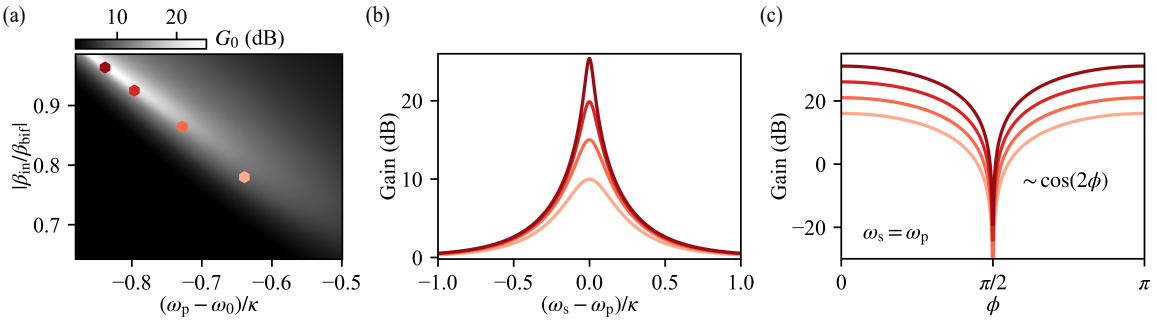

Figure 1.13: Predicted gain performance of the JPA. (a) Maximum gain G_0 as a function of the pump frequency ω_p and input field amplitude β_{in}. **(b)** Gain profiles of the JPA for the pump powers and frequencies indicated by the markers in panel (a). Each trace exhibits a Lorentzian lineshape, characteristic of standing-wave parametric amplifiers. The maximum gain increases with pump power according to Eq. (1.46), while the bandwidth is constrained by the gain–bandwidth product in Eq. (1.48). **(c)** Calculated phase-dependent gain at the degeneracy point where signal and idler coalesce ($\omega_s = \omega_i = \omega_p$). The curves vary periodically as $\cos(2\phi)$, where ϕ is the relative phase between the signal and pump tones.

LC resonator. In this regime only one real solution of Eq. (1.41) exists. As the pump power increases, the JPA experiences a frequency shift, as shown in Fig. 1.12(a)-(b). This effect, known as the Kerr shift, is a characteristic feature of amplifiers with a third-order nonlinearity. For input amplitudes β_{bif}, when the photon number $\bar{n}$ reaches the threshold value $\bar{n}_{bif} = \kappa/(\sqrt{27}K)$, the JPA enters a bifurcation point, beyond which the device dynamics become hysteretic. In this regime, Eq. (1.41) admits two real and stable solutions, giving rise to bistability in the JPA, as illustrated in Fig. 1.12(c). The bifurcation point imposes a more stringent condition for operating the JPA as an amplifier, set by the maximum number of photons that can populate the device before reaching $\bar{n}_{bif}$. In typical cQED experiments, readout requires at least ten photons, i.e. $\bar{n}_{bif} \gtrsim 10$. Therefore, a JPA can be used as an amplifier when $\kappa/K \gtrsim 10$.

By driving the JPA with powers slightly below the bifurcation point, it amplifies the input fluctuations $\hat{b}_{in}$. To show this, one needs to instead solve the Heisenberg-Langevin equations for the fluctuation field $\hat{a}$. In the frequency domain, one can show that the dynamics of $\hat{a}$ is given by

$$-\sqrt{\kappa}\,\vec{\hat{b}}_{in} = \mathbf{M}\,\vec{\hat{a}}, \tag{1.43}$$

where $\mathbf{M}$ is called the amplifier drift matrix and is given by

$$\mathbf{M} = \begin{pmatrix} i\delta_s - \frac{\kappa}{2} & -iK\alpha^2 \\ iK(\alpha^*)^2 & -i\delta_i - \frac{\kappa}{2}. \end{pmatrix}. \tag{1.44}$$

where $\delta_{s/i} = \omega_{s/i} - \omega_0 - 2\bar{n}K$ and $\omega_i = 2\omega_p - \omega_s$. We also have defined the vector operators $\vec{\hat{a}} = (\hat{a}(\omega_s), \hat{a}^\dagger(\omega_i))^T$ and $\vec{\hat{b}}_{in} = (\hat{b}_{in}(\omega_s), \hat{b}^\dagger_{in}(\omega_i))^T$.

We observe that now the bosonic operator $\hat{a}$ at frequency ω_s depends also on the dynamics of the fluctuations $\hat{a}^\dagger$ at ω_i. The latter operator denotes the idler tone generated due to

4-wave-mixing inside the JPA. Using the input-output relation Eq. (1.29), we can calculate the gain at the signal frequency ω_s, which is given by

$$G(\omega_s) = \left|\frac{\hat{b}_{out}}{\hat{b}_{in}}\right|^2 = \left|-1 + \frac{\kappa^2/2 + i\kappa\delta_i}{\delta_i\delta_s + \kappa^2/4 - i(\delta_s - \delta_i)\kappa/2 - K^2\bar{n}^2}\right|^2 . \tag{1.45}$$

In Fig. 1.13(a)-(b) we show examples of gain profiles obtained when driving a JPA close to its bifurcation point. These profiles follow the typical Lorentzian lineshape characteristic of standing-wave parametric amplifiers. Their bandwidth, defined using the full-width-at-half-maximum (FWHM), is referred to as the instantaneous bandwidth (BW). Increasing the pump power enhances the maximum gain G_0, which follows the relation

$$G_0 = \left|\frac{C_\Lambda + 1}{C_\Lambda - 1}\right|^2 , \tag{1.46}$$

where $C_\Lambda = 4K^2\bar{n}^2/\kappa^2$ is known as the squeezing cooperativity.

When the signal and idler frequencies are not equal, the JPA operates as a degenerate, phase-preserving amplifier, following the classification discussed in Section 1.1.3. If instead the signal and idler frequencies coincide, the amplifier becomes phase-sensitive. In this regime, one can show that the maximum gain varies as a function of $\cos(2\phi_s - 2\phi_p)$, where $\phi_{s/p}$ are the phases of the signal and pump tones [82] (cf. Fig. 1.13(c)). For this case, one can now find the effective Hamiltonian modeling the amplifier, using the displacement transformation in Eq. (1.40) to the transmon Hamiltonian (1.18). After performing a RWA and moving to a frame rotating at the pump frequency, one obtains

$$\hat{H}/\hbar = \Delta\, \hat{a}^\dagger\hat{a} + \frac{\Lambda}{2}e^{i\phi}\hat{a}^\dagger\hat{a}^\dagger + \text{h.c.}\,, \tag{1.47}$$

where $\Delta = \omega_p - \omega_0 - 2K\bar{n}$ is the frequency detuning, $\Lambda = K^2\bar{n}^2$ is called the single-mode squeezing strength and $\phi = 2\phi_s - 2\phi_p$ is the relative phase of the pump tone. Equation (1.47) shows that the JPA implements the Hamiltonian of the degenerate amplifier discussed by Ref.[11].

1.3.2 Gain-bandwidth tradeoff

In Fig. 1.13(b) we observe that increasing the pump power raises the maximum gain of the amplifier. However, this enhancement is accompanied by a reduction in BW. One can show that these quantities satisfy the relation

$$\sqrt{G_0} \cdot \text{BW} = \kappa. \tag{1.48}$$

Equation (1.48) is known as the gain–bandwidth (GBW) product, a generic feature of standing-wave parametric amplifiers [11, 12]. Intuitively, this arises because the amplifier requires additional time to build up the energy needed to produce gain. The higher the

gain, the longer the device takes to build up the necessary amount energy. Formally, the GBW product originates from the fact that the JPA operates near an instability point, set by its damping rate κ.

The damping rate κ plays a crucial role in stabilizing the dynamics of the JPA by preventing the system from entering an unbounded regime. Consider the hypothetical scenario in which the JPA is suddenly decoupled from its electromagnetic environment. The subsequent evolution of the bosonic operator $\hat{a}$ is then governed by the Heisenberg equations of motion (i.e. taking $\kappa = 0$ in Eq. (1.27)). Using the Hamiltonian in Eq. (1.47) in the interaction frame with respect to the free Hamiltonian, one finds that the field operator evolves as $\hat{a}(t) = \hat{a}(0)\cosh(\Lambda t) + \hat{a}^{\dagger}(0)\sinh(\Lambda t)$, which exhibits a divergent behavior in time. Naturally, this divergence cannot persist indefinitely. At sufficiently large amplitudes the approximation of a weakly anharmonic oscillator breaks down, and the full periodic cosine potential of the Josephson junction (cf. Eq. (1.16)) becomes relevant. The presence of non-negligible higher order nonlinearities then leads to a transition into chaotic motion, analogous to the trajectories exhibited by an undamped pendulum driven beyond the small-angle approximation[141].

Mathematically, the stability of the system can be analyzed by evaluating the eigenvalues of its drift matrix. This is analogous to finding the normal frequencies of small oscillations in a system of coupled mechanic harmonic oscillators. For a JPA operated at resonance, i.e. under the condition $\delta_{s/i} = 0$, the eigenvalues are given by

$$\epsilon_{\pm} = -\frac{\kappa}{2} \pm \Lambda. \tag{1.49}$$

Then we can use the Routh–Hurwitz criterion [142], which states that the dynamics of an open system is stable if the real parts of all the eigenvalues are negative. In a more intuitive picture, one can think that the imaginary part of the eigenvalues determine the *oscillations* of the electromagnetic field and the real part its *damping* or *anti-damping*. If the system is *damped*, the fields will exponentially reach a steady state of amplified oscillations. For the JPA, this requirement is satisfied when $C_\Lambda < 1$. Increasing the pump power, increases C_Λ and enhances the maximum gain G_0, but simultaneously drives the JPA closer to the instability region defined when $C_\Lambda > 1$.

1.3.3 Performance metrics

The design of microwave amplifiers is constrained by performance metrics that depend on the requirements of the target experiment. In this section, we review the key metrics relevant for the optimal readout of quantum devices.

Maximum gain

To determine the gain requirements of superconducting parametric amplifiers, we must first understand their role in the readout chain of a quantum device. In Fig. 1.14(a) we

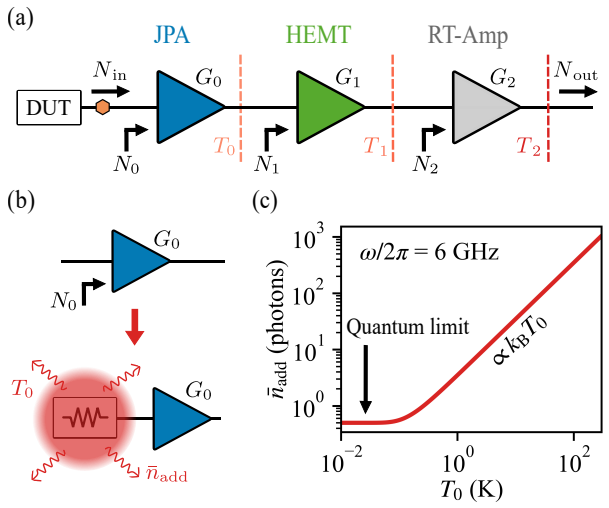

Figure 1.14: Noise performance of a readout line. **(a)** Schematics of a typical measurement chain for reading out a quantum device under test (DUT), consisting of three amplification stages: a JPA, a HEMT, and a room-temperature (RT) amplifier. Each stage provides gain G_i and introduces noise N_i (i = 0,1,2). The total output noise N_{out} is referred to the chain input (orange marker) by dividing to the total gain. In an optimized chain, the input-referred added noise N_{in} is dominated by N_0. **(b)** Noise model for a phase-preserving amplifier, where N_0 is the Johnson–Nyquist noise from a resistor thermalized at temperature T_0. **(c)** Johnson–Nyquist noise versus temperature. When $\hbar\omega \ll k_B T_0$, the noise is proportional to T_0. While, if $\hbar\omega \gg k_B T_0$, it approaches the quantum limit at $\bar{n}_{\text{add}} = 0.5$.

show a schematic of a typical measurement line used in experiments. The DUT is mounted inside a dilution refrigerator operating at temperatures ≈ 10-30 mK. The output signal carrying information about the DUT is routed through an amplification chain, with multiple amplifiers thermalized at different temperature stages of the cryostat. Each stage amplifies the signal by a gain G_i (with i = 0,1,2). However, they also add a noise power N_i. In this cascaded configuration, assuming lossless transmission between stages, the total noise referred to the input of the chain[13] is given by the formula [12, 83]

$$N_{\text{in}} = N_0 + \frac{N_1}{G_0} + \frac{N_2}{G_0 G_1}. \tag{1.50}$$

Equation (1.50) highlights the function of a parametric amplifier (i = 0) at the front of the readout line: suppress the noise added by the following stages. In standard cryogenic setups the stage i = 1 consists of a High Electron Mobility Transistor (HEMT) amplifier with a typical noise temperature of ≈ 1.5-3 K [9, 143, 144]. Gain levels of $G_0 \geq 20$ dB are sufficient to reduce the noise contribution of the HEMT by at least an order of magnitude below the level of state-of-the-art JPAs [21, 22, 145, 146].

Added noise

If the gain performance of a JPA has been optimized to reduce the noise of the amplification chain, the next metric one needs to consider is the noise of the JPA itself. For a phase-preserving amplifier, the added noise can be evaluated using the model shown in Fig. 1.14(b). Here, we model the added noise of the amplifier as originating from a hypothetical resistor at temperature T_0, placed at the input of a noiseless amplifier with gain G_0 [83]. At a

[13] For amplifiers, it is customary to report the added noise referred to their input plane. Experimentally, this means measuring the noise power at the output N_{out} (for example using a spectrum analyzer), and divide it by the amplifier gain G. Hence, $N_{\text{in}} = N_{\text{out}}/G$.

frequency ω, the random motion of the electrons in the resistor generates Johnson–Nyquist noise, which follows the spectral distribution of a perfect black-body radiator [10, 147]:

$$\bar{n}_{\mathrm{add}} = \frac{N_0}{B\hbar\omega} = \frac{1}{2}\coth\left(\frac{\hbar\omega}{2k_{\mathrm{b}}T}\right), \tag{1.51}$$

where $\bar{n}_{\mathrm{add}}$ is the added noise expressed in units of photons, and B represents the characteristic bandwidth of the setup. In the Rayleigh–Jeans limit $\hbar\omega \ll k_{\mathrm{B}}T_0$, the Johnson–Nyquist noise is proportional to T_0 and reduces to its classical form[14] $\bar{n}_{\mathrm{add}} = k_{\mathrm{B}}T_0$ (see Fig. 1.14(c)). However, in the Wien limit when $\hbar\omega \gg k_{\mathrm{B}}T_0$, the added noise is no longer dominated by thermal fluctuations and instead approaches the quantum limit set by vacuum fluctuations of the electromagnetic field. Expressed in units of photons[15], this corresponds to half a photon of noise $\bar{n}_{\mathrm{add}} = 0.5$. An amplifier operating in this regime is called a quantum-limited amplifier [14], which is the current requirement for high-fidelity readout of quantum circuits.

Analogous to the added noise, one can also define another relevant figure of merit called the amplifier quantum efficiency [28, 148, 149]. In a phase-preserving amplifier, where the noise originates from uncorrelated vacuum fluctuations of the idler, the quantum efficiency is defined as

$$\eta_{\mathrm{add}} = \frac{\bar{n}_{\mathrm{QL}}}{\bar{n}_{\mathrm{add}}}, \tag{1.52}$$

where $\bar{n}_{\mathrm{QL}} = 0.5$ denotes the quantum limit. Whereas, in a phase-sensitive amplifier, single-mode squeezing can be used to surpass the quantum limit and for one of the electromagnetic-field quadratures reach noise levels approaching $\bar{n}_{\mathrm{add}} \to 0$. In this scenario, the amplifier quantum efficiency should be renormalized to[16] $\eta_{\mathrm{add}} = \bar{n}_{\mathrm{QL}}/(\bar{n}_{\mathrm{QL}} + \bar{n}_{\mathrm{add}})$.

In the presence of internal losses, the added noise of a parametric amplifier deviates from the ideal quantum limit. For a JPA, internal losses can be modeled as arising from dissipation to an additional microwave port (cf. Fig. 1.9). Then, following the derivation explained by Ref. [150], the added noise rescales as

$$\bar{n}_{\mathrm{add}} = \bar{n}_{\mathrm{QL}}\left(1 + \frac{2\gamma}{\kappa}\right), \tag{1.53}$$

where γ is the internal loss rate. As long as $\kappa \gg \gamma$, the influence of internal losses in the added noise is negligible. This fact shows a key advantage in the fabrication of parametric amplifiers: one can counteract the effect of internal losses by increasing κ. As shown

[14] Because microwave amplifiers were initially developed for room-temperature operation, where their added noise follows the classical Johnson–Nyquist relation, the noise contribution of the amplifier was traditionally expressed in terms of an equivalent noise temperature, defined as $T_{\mathrm{noise}} = \hbar\omega\bar{n}_{\mathrm{add}}/k_{\mathrm{B}}$.

[15] In absolute temperature scale the quantum limit is frequency dependent. For an amplifier operating in the 4–12 GHz range, this corresponds to an effective noise temperature between approximately 100 mK and 300 mK, respectively.

[16] However, one should be careful when applying this alternative definition to a phase-preserving amplifier, because even a quantum-limited device can reach at most 50% efficiency. In general, it is better to specify both the type of amplifier being used and the chosen definition of quantum efficiency.

in Eq. (1.48) this also has the benefit of increasing the BW. This is in stark contrast to the fabrication of superconducting qubits, where minimizing both the loss rate γ and external coupling κ, is essential to increase their coherence properties [119, 120].

Frequency range and instantaneous bandwidth

The primary application of parametric amplifiers is in the readout of quantum systems, where the relevant information is typically encoded in microwave resonators with linewidths on the order of 1 MHz and operating between 4 to 12 GHz. For conventional standing-wave parametric amplifiers, bandwidths of approximately 10 MHz can be achieved at a gain of 20 dB, primarily limited by the GBW product. Such bandwidths are sufficient for the readout of a single qubit. Furthermore, replacing a single Josephson junction with a DC SQUID [16, 22, 151], SNAIL [21, 152], or RF SQUID [145, 153], enables tunability of the amplifier resonance frequency with a external magnetic field, allowing coverage of a broader frequency range. However, the challenge arises when the amplifier must be used for the simultaneous readout of multiple qubits, a technique known as frequency multiplexed readout [154], which has become the standard approach for large-scale superconducting processors [35, 46–48].

One could think that a simple strategy could be to increase the coupling strength κ, by matching the device impedance to that of the microwave port. However, for standing-wave amplifiers operating via 4-wave mixing, the external quality factor Q_c should satisfy the condition [155]

$$pQ_c \geq \frac{16}{\sqrt{3}}. \tag{1.54}$$

Here, $p = L_J/(L_s + L_J)$ is defined as the nonlinear inductance participation ratio, where L_s is the circuit stray inductance, including both the kinetic inductance of the superconducting leads and the geometric inductance. The above condition arises from the requirement that the circulating current in the circuit must remain below the JJ critical current I_c. Eq. (1.54) limits the value of κ to the range of 300 MHz, which, according to the GBW product, corresponds to a bandwidth of roughly 30 MHz at 20 dB gain. Slightly improved scaling can be achieved using RF-SQUID-based amplifiers [26, 145, 153], as the shunted inductance reduces the effective current flowing through the JJ. To achieve larger bandwidths, alternative strategies are required. In Chapter 4, we discuss the techniques currently employed in the field to increase the bandwidth of parametric amplifiers.

Dynamic range

An important figure of merit for parametric amplifiers is their dynamic range, which is quantified by the 1-dB compression point: the input signal power at which the amplifier gain decreases by 1 dB. This quantity, also commonly refereed to as the saturation power, arises from two primary mechanisms: (i) higher-order nonlinearities induced by the signal tone, and (ii) depletion of the pump due to the signal backaction. In the context of the

derivation in Eq. (1.45), pump depletion occurs when the stiff-pump approximation breaks down, necessitating the inclusion of the pump dynamics in the system evolution.

In general, amplifiers operating via 4-wave mixing are limited predominantly by the signal-induced Kerr shift, whereas in pure 3-wave-mixing amplifiers the saturation power is constrained by pump depletion. Ref. [152] provides analytical expressions that approximate the scaling of both contributions, which can be written as

$$P_{\text{sat}}^{\text{Kerr}} \sim \frac{\kappa^2}{K G_0^{5/4}} \hbar\omega_0, \tag{1.55}$$

and

$$P_{\text{sat}}^{\text{depl}} \sim \frac{\kappa^2}{(|g_3|^2/\omega_0) G_0^{3/2}} \hbar\omega_0, \tag{1.56}$$

where g_3 is analogous to the Kerr coefficient for 3-wave-mixing processes.

For typical microwave quantum circuits, the power required to perform the readout of a single quantum device is on the order of -130 dBm to -120 dBm, which in the cQED setup described in Section 1.2.5, corresponds to approximately 1–10 photons populating the readout resonator. This range coincides with the saturation powers of amplifiers based on a single JJ [17, 20, 152, 156, 157], which limits their applicability for multiplexed qubit readout or the higher-power readout scenarios shown in Ref. [150, 158]. Moreover, although 3-wave-mixing amplifiers can, in principle, achieve higher saturation powers, in practice residual Kerr interactions restrict their dynamic range to values comparable to single-JJ devices [44, 152].

The standard approach to increase the saturation power is to dilute the Kerr coefficient using arrays of Josephson junctions, as described in Section 1.2.4. By employing this strategy, state-of-the-art JPAs have achieved saturation powers up to -90 dBm using resonators comprising ≈ 1000 JJs, which effectively reduce the Kerr coefficient to $\lesssim$ kHz [21, 22, 24, 112, 145]. However, as we elaborate in Section 2.2, this enhancement comes at the cost of stronger interactions with the higher harmonics of the array and larger device footprints.

Minimum pump power and heat load

When designing a parametric amplifier, it is essential to consider the amount of pump power required to achieve the 20 dB gain levels needed for quantum device readout. This consideration is particularly critical because the amplifiers are typically installed at the lowest temperature stage of a cryostat, where cooling power is limited, and higher pump powers increase the total heat load. The challenge becomes more pronounced for 4-wave-mixing amplifiers as their Kerr nonlinearities are designed to enhance saturation power according to Eq. (1.55). However, this design choice implies that larger pump powers are needed to achieve 20 dB gain (cf. Eq. (1.46)). To date, this has not posed a significant issue, as the required operational powers (≈ -60 dBm [22, 49, 112]) remain several orders of

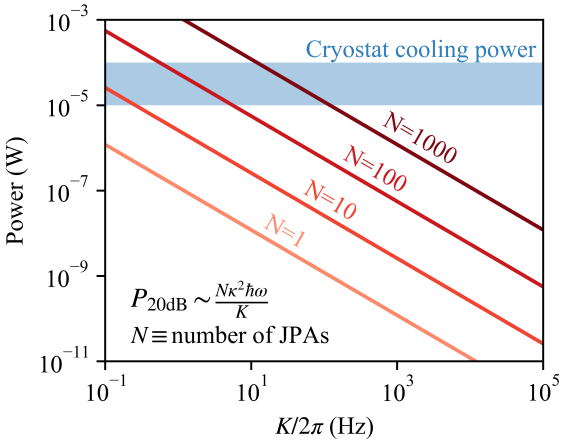

Figure 1.15: Heat load of a JPA operated with 4-wave-mixing. We assume the JPA pump power is dissipated at the mixing chamber of a commercially available dilution refrigerator [159]. Moreover, we assume the amplifier is driven close to its bifurcation point (cf. Section 1.3.1) and at a frequency of $\omega/2\pi$ = 6 GHz. Reducing the device nonlinearity, in this case given by the self-Kerr coefficient K, enhances its dynamical range but demands higher pump powers, increasing the thermal load on the cryostat. Scaling the number of JPAs (N) can eventually exceed the available cooling power, indicated by the blue area.

magnitude below the cooling capacity of commercially available dilution refrigerators (≈ 10-100 μW [159]). Yet, as quantum processors scale up, multiple amplifiers may need to operate within a single cryostat, potentially creating constraints for future applications. In Fig. 1.15, we illustrate the effects of reducing the Kerr coefficient and its impact on the scalability of amplifiers. This limitation can be alleviated by implementing 3-wave-mixing amplifiers through the application of DC bias currents [26, 50, 55, 56]. Alternative strategies have also been proposed in Refs. [153, 160]. However, at the time this thesis is written, no definitive approach exists to optimize pump power transfer in parametric amplifiers.

Magnetic field resilience

For applications involving only superconducting qubits, magnetic fields rarely exceed the militesla range. The situation is different for hybrid quantum systems such as, spin qubits [33–35], Andreev qubits [36, 37], molecular magnets [39] and dark-matter detection platforms [40–42], which typically require magnetic fields that can even exceed 1 T for proper operation. Such conditions impose a fundamental constraint on conventional JPAs, due to the intrinsic sensitivity of JJs to magnetic fields. In this section, we briefly review the dominant mechanisms that limit the performance of JPAs in high-field environments. For clarity, we restrict the discussion to the case of junctions fabricated in the standard Al-AlO_x-Al stack illustrated in Fig. 1.5(a). However, the same physical considerations apply to other types of Josephson junctions.

There are three mechanisms which could hinder JPA performance under magnetic fields. They are illustrated in Fig. 1.16. First, the application of a magnetic field to a superconductor, induces Cooper-pair breaking through Zeeman splitting and the formation of screening currents [29]. This effect is reflected in the suppression of the superconducting gap Δ, which follows the formula

$$\frac{\Delta(B)}{\Delta(0)} = \sqrt{\frac{1-\alpha(B)}{1+\alpha(B)}}, \tag{1.57}$$

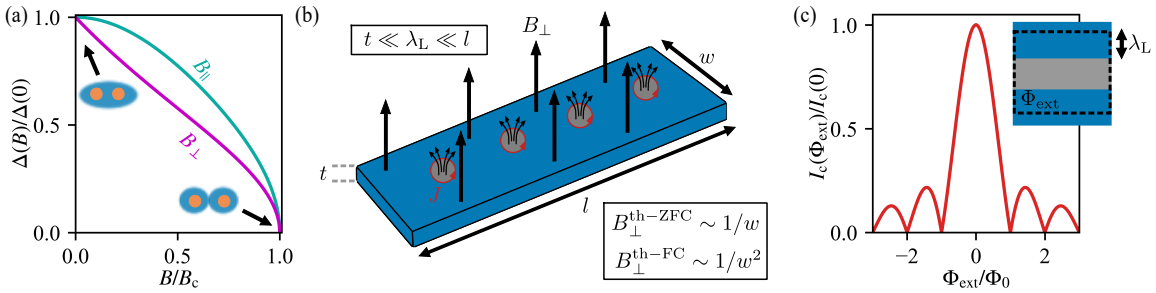

Figure 1.16: Mechanisms hindering JPA performance under magnetic field. **(a)** Suppression of the superconducting gap in the JJ electrodes under in-plane $B_{||}$ and out-of-plane $B_\perp$ fields. The magnetic field induces Zeeman splitting and screening currents, which leads to Cooper pair breaking, as depicted by the schematic drawings. **(b)** Formation of Abrikosov vortices in a thin-film superconducting strip. Each vortex hosts a circulating normal-state current J (red arrows), which can introduce dissipation when the vortex approaches the JJ or regions of high current density. In the limit $t \ll \lambda_L \ll l$, where t, l and λ_L denote the strip thickness, length, and London penetration depth, respectively. The threshold field for vortex trapping ($B_\perp^{th}$) scales as $1/w^2$ for field-cooled (FC) conditions [79, 162] and as $1/w$ under zero-field-cooling (ZFC) [140, 163], where w is the strip width. Panel adapted from Ref. [79]. **(c)** Fraunhofer interference pattern of a JJ under an in-plane magnetic field. The field modulates the critical current by threading flux Φ_{ext} through the effective cross-sectional area outlined by the dashed contour. Flux penetration into the superconducting leads is included by accounting for their London penetration λ_L.

where α is called the pair-breaking parameter and can be written as $\alpha(B) = B_{||}^2/B_c^2$ for in-plane magnetic fields $B_{||}$ and $\alpha(B) = B_\perp/B_c$ for out-of-plane magnetic fields $B_\perp$, with B_c denoting the critical field of the superconducting electrodes [29]. A decrease in the superconducting gap increases the amount of thermal quasiparticles [161], which introduces additional dissipation channels and degrades the noise performance of the amplifier.

Second, a magnetic field can lead to the formation of Abrikosov vortices in the superconducting leads [29, 164]. Although they typically occur in type-II superconductors, such vortices can also form in thin films of type-I superconductors like Al, due to the reduced ability of the film to screen magnetic fields. Since superconductivity is strongly suppressed at the vortex core, these vortices can act as quasiparticle traps [165]. Their presence might increase energy dissipation, particularly when a vortex moves close to the JJ or into regions of high current density in the circuit. For in-plane magnetic fields, this effect can be mitigated if the electrode thickness t is much smaller than the London penetration depth λ_L [29]. For out-of-plane fields, vortex formation is governed by a characteristic length scale of the film. For example, in the strip geometry shown in Fig. 1.16(b), when the thickness t and length l satisfy $t \ll \lambda_L \ll l$, the threshold field $B_\perp^{th}$ for vortex trapping scales as

$$B_\perp^{th-ZFC} \sim \frac{1}{w}, \tag{1.58}$$

under zero-field cooling (ZFC) [140, 163] and as

$$B_\perp^{th-FC} \sim \frac{1}{w^2}, \tag{1.59}$$

under field-cooling (FC) [79, 162], where w is the strip width. Thus, one can improve the magnetic field resilience of the strip by reducing w. Alternatively, one can also

engineer pinning sites to localize the vortices and prevent their uncontrolled motion in the superconducting leads [166, 167].

Lastly, applying an in-plane magnetic field modulates the JJ critical current according to the Fraunhofer pattern [29],

$$\frac{I_c(\Phi_{ext})}{I_c(0)} = \left|\frac{\sin(\pi\Phi_{ext}/\Phi_0)}{\pi\Phi_{ext}/\Phi_0}\right|, \tag{1.60}$$

where Φ_{ext} is the magnetic flux threading the JJ area shown in Fig. 1.16(c). Near the first node of the pattern, where I_c is strongly suppressed, two effects degrade JPA performance. First, as indicated by Eq. (1.22), higher-order nonlinearities can no longer be neglected, limiting the achievable gain. Second, the reduction of I_c increases the Josephson inductance and shifts the resonance frequency of the amplifier away from its designed value.

The response of JJ-based parametric amplifiers under magnetic fields has been investigated in Ref. [32], which reports that in-plane fields on the order of 100 mT and out-of-plane fields as low as 5 mT, are sufficient to drastically degrade the device performance. Comparable field sensitivities have also been observed in the coherence of transmon qubits [30, 31]. These results highlight the need for alternative amplifier technologies that are compatible with magnetic-field operation.

1.3.4 Bogoliubov class of parametric amplifiers

We conclude this chapter by discussing a relatively unexplored yet fascinating research about a type of non-conventional parametric amplifiers that can circumvent several limitations inherent to standard JPAs: the Bogoliubov class of amplifiers. The linearized Hamiltonian of the JPA, shown in Eq. (1.47) is not diagonalizable, meaning that its dynamics are unbounded and grows exponentially with the pump strength. As outlined in Section 1.3.2, the dynamical stability of the JPA relies on the damping rate κ, which inevitably leads to the GBW product of Eq. (1.48). Such constraint reduces the available BW by an order of magnitude at 20 dB gain. The question is then: how can one avoid such limitation?

The key idea is to tune some of the parameters in the device Hamiltonian so that it becomes diagonalizable. Therefore, the amplifier no longer relies in the damping rate κ to achieve dynamical stability. As discussed in the Appendix of Ref. [168], one can systematically classify Bogoliubov amplifiers according to the number of modes in the amplifier and the structure of their interactions. In what follows, we concentrate on two variants that are central to the scope of this thesis: Optimally Detuned Bogoliubov Amplifiers (ODBA) and Optimally Imbalanced Bogoliubov Amplifiers (OIBA).

We begin by explaining the operating principle of an ODBA. As shown in Eq. (1.47), the effective Hamiltonian of a phase-sensitive JPA depends on two key parameters: the frequency detuning Δ and the single-mode squeezing interaction Λ. For simplicity, we take the relative pump phase to be $\phi = 0$. When $|\Delta| < |\Lambda|$, the Hamiltonian is not

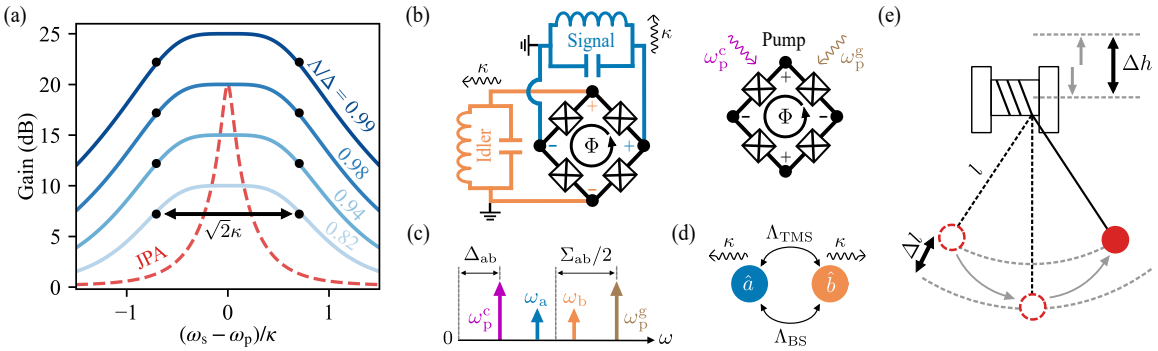

Figure 1.17: Expected gain performance and dynamics of the Bogoliubov class of parametric amplifiers. **(a)** Bandwidth (BW) enhancement predicted in Ref. [168] for an ODBA. We compute gain profiles as a function of the detuning Δ and single-mode squeezing strength Λ (cf. Eq. (1.47)), and extract the corresponding BW (black markers). Unlike a conventional JPA, the GBW product vanishes when the device is tuned to operate as an ODBA, enabling more than an order-of-magnitude BW improvement at 20 dB gain. **(b)** Circuit diagram of a Josephson Parametric Converter (JPC). Four identical JJs form a Josephson Ring Modulator (JRM), whose eigenmodes are embedded in microwave circuits. Two modes host the signal and idler, while a third mode is used for pumping. Panel adapted from Ref. [168]. **(c)** Frequency arrangement to operate the JPC as an OIBA. When biased by an external flux Φ, a gain pump applied at a frequency $\omega_p^g = \Sigma_{ab} = \omega_b + \omega_b$ generates phase-preserving (nondegenerate) amplification between the signal and idler. A second pump at $\omega_p^c = \Delta_{ab} = \omega_b - \omega_b$ enables frequency conversion between the two modes. **(d)** Effective mode structure of the double-pumped JPC. The signal and idler modes are coupled via beam-splitter (BS) and two-mode squeezing (TMS) interactions with strengths Λ_{BS} and Λ_{TMS}, respectively. Their damping rate κ comes from the coupling of the embedding resonators to microwave lines. When the interactions are properly imbalanced, the device realizes an OIBA, which exhibits a transmission gain profile similar to the ODBA. **(e)** Proposed classical analogy to the mechanism underlying an OIBA. The *Botafumeiro* of Fig. 1.2 is now imagined to have an additional "pump": its support is moved up and down within a height Δh. By synchronizing the pulls of the *tiraboleiros*, with this vertical motion, the system can sustain stable amplified oscillations without requiring a dissipative mechanism such as rope friction or air drag.

diagonalizable, and the system must rely on the damping rate κ to achieve dynamical stability. In contrast, when $|\Delta| \geq |\Lambda|$, the Hamiltonian can be diagonalized through the Bogoliubov transformation $\hat{\beta} = \cosh(r)\hat{a} + \sinh(r)\hat{a}^\dagger$, where $\tanh(r) = \Lambda/\Delta$. Under this condition, the JPA Hamiltonian can be rewritten as

$$\hat{H}/\hbar = \Theta\, \hat{\beta}^\dagger \hat{\beta}, \tag{1.61}$$

where $\Theta = \sqrt{\Delta^2 - \Lambda^2}$. Interestingly, unlike a conventional harmonic oscillator, the eigenstates of this Hamiltonian are squeezed Fock states. When the amplifier is coupled to a transmission line, the detuning parameter can be adjusted such that the energy of the Bogoliubov modes is matched to the damping rate κ i.e. $\Theta = \kappa/2$. In this regime, the gain profile gets broadened and exhibits a flat-top at the region of maximum gain G_0, as illustrated in Fig. 1.17(a). By adjusting the pump power, we can vary the single-mode squeezing term Λ, and by tuning Δ accordingly, the same broadening can be achieved for different values of G_0 (see Fig. 1.17(a)). For these amplifiers, the bandwidth becomes independent of G_0 and is given by

$$\mathrm{BW} = \sqrt{2}\kappa \tag{1.62}$$

From this expression, it is evident that the ODBA effectively eliminates the conventional GBW tradeoff. In particular, for 20 dB gain, the BW becomes ten times larger than the one obtained in a conventional JPA, as illustrated in Fig. 1.17(a).

In an ODBA, stability is achieved by varying the detuning parameter Δ. We can apply an alternative approach in a non-degenerate amplifier i.e. an amplifier with two physical modes. This strategy was originally proposed for a Josephson Parametric Converter (JPC) (see Fig. 1.17(b)). Unlike a JPA, the nonliearity in a JPC stems from a Josephson Ring Modulator (JRM), which consists of four identical JJs arranged in a loop [18, 44, 169]. Two normal modes of the JRM are embedded in superconducting resonators with an external coupling strength κ, and are used to host the signal and idler tones of the parametric process. A third mode is used to pump the amplifier (cf. Fig. 1.17(b)). By threading a magnetic flux through the JRM, the JPC can operate as a non-degenerate 3-wave-mixing amplifier when a pump tone is applied at $\omega_{\mathrm{p}}^{\mathrm{g}} = \Sigma_{\mathrm{ab}} = \omega_{\mathrm{a}} + \omega_{\mathrm{b}}$, where ω_{a} and ω_{b} are the frequencies of the signal and idler modes, respectively [44, 169, 170]. However, similar to the JPA, the JPC also develops a GBW product.

The solution to overcome the GBW tradeoff in a JPC is to introduce a second pump tone at $\omega_{\mathrm{p}}^{\mathrm{c}} = \Delta_{\mathrm{ab}} = \omega_{\mathrm{b}} - \omega_{\mathrm{a}}$, which activates frequency conversion between the signal and idler modes[17]. By applying a displacement transformation analogous to Eq. (1.40), the effective Hamiltonian of the JPC can be expressed as

$$\hat{H}/\hbar = \Lambda_{\mathrm{TMS}}\, \hat{a}^{\dagger}\hat{b}^{\dagger} + \Lambda_{\mathrm{BS}}\, \hat{b}^{\dagger}\hat{a} + \mathrm{h.c}, \tag{1.63}$$

where Λ_{BS} and Λ_{TMS} are called the beam-splitter and two-mode squeezing interactions. They quantify the strength of the conversion and amplification processes, respectively. If $\Lambda_{\mathrm{BS}} < \Lambda_{\mathrm{TMS}}$, the above Hamiltonian is not stable. However, if $\Lambda_{\mathrm{BS}} \geq \Lambda_{\mathrm{TMS}}$, we can rewrite Eq. (1.63) in a stable form using Bogoliubov transformations. Then, the JPC Hamiltonian becomes

$$\hat{H}/\hbar = \Theta\, \hat{\beta}_1^{\dagger}\hat{\beta}_2 + \mathrm{h.c}, \tag{1.64}$$

where now $\Theta = \sqrt{\Lambda_{\mathrm{BS}}^2 - \Lambda_{\mathrm{TMS}}^2}$. The dynamics in an OIBA is governed by the hopping interaction between two independent squeezed Fock states. When the strengths Λ_{BS} and Λ_{TMS} are tuned such that $\Theta = \kappa/2$, the OIBA also shows the same gain profiles as in the ODBA (cf. Fig. 1.17(a)) but now in the transmission coefficient between the signal and idler modes.

Beyond the improved bandwidth scaling, the Bogoliubov class of amplifiers provides two additional advantages. First, the added noise remains quantum-limited, even with the

[17] Although we couldn't find a classical analogy for the ODBA, we can offer an intuitive picture for the OIBA. Lets consider the example of the *Botafumeiro* in Section 1.1.1. We can introduce a second "pump" in the system by moving the upper support of the burner up and down, as depicted in Fig. 1.17(e). By carefully synchronizing the pull of the *tiraboleiros* with the vertical motion of the support, one can achieve a stable state of amplified oscillations without relying on the friction of the ropes or the burner. This analogy, however, should be taken with a grain of salt, as it may not fully capture the underlying physics of the OIBA.

introduction of a second pump, as in the case of the OIBA. Second, theoretical predictions indicate that the input power threshold at which pump depletion occurs increases by nearly two orders of magnitude. For a 3-wave-mixing amplifier, such as the JPC, this translates into an in-situ enhancement of the device saturation power.

2 Granular Aluminum: complex nonlinearity for optimal parametric processes

In this short chapter, we introduce the material of choice to fabricate our parametric amplifiers: granular aluminum (grAl). Initially considered mainly as an alternative to address the magnetic-field sensitivity of JPAs, we found during this project that grAl also possesses intrinsic properties that make it particularly well-suited for parametric devices in a broader context. We provide an overview of the key features that make grAl such a promising material.

This chapter is organized as follows. In Section 2.1, we introduce the key properties of granular aluminum, focusing on its superconductivity and microstructure. In Section 2.2, we discuss its nonlinear characteristics and review several previous applications. Finally, in Section 2.3, we compare grAl with commonly used sources of nonlinearity in superconducting circuits.

2.1 Superconducting properties of granular Aluminum

The physics of granular aluminum and its unconventional superconducting properties have been studied since the 1960s. Discussed in the review of Guy Deutscher [64], grAl was originally discovered by accident: in an effort to fabricate pure aluminum films, Abeles *et al.* [61] were unaware of oxygen contamination in their deposition chamber. As a result, they observed anomalous superconducting transition temperatures, nearly twice the one of bulk aluminum (1.2 K). In addition, the films exhibited enhanced critical magnetic fields and normal-state resistivities several orders of magnitude larger than pure Al. Transmission electron microscopy [61] revealed that these features originated from the microstructure of the film: aluminum tends to form grains of uniform size between 2–4 nm, separated by AlO_x barriers, as illustrated in Fig. 2.1(a).

These surprising observations motivated extensive theoretical and experimental efforts aimed at understanding the connection between the microstructure and the unconventional superconductivity of grAl [62, 63, 171, 172]. In the decades following the pioneering experiments of Abeles *et al.*, numerous studies based on DC transport [173, 174], scanning

tunneling microscopy [175], optical spectroscopy [66, 176, 177], and microwave measurements [65, 67, 68, 80, 81, 178–180] have significantly advanced our understanding of this material. Nevertheless, no complete consensus has yet been reached regarding the microscopic mechanisms governing grAl's superconducting properties. In this section, we provide a brief overview of the key phenomenological features of grAl. For more comprehensive reviews, we refer the reader to Refs. [64, 181].

In general, granular aluminum is a disordered superconductor characterized by a high kinetic inductance. It can be fabricated by depositing aluminum in a controlled oxygen atmosphere. By tuning the oxygen partial pressure during deposition, one can vary the oxygen content in grAl films, which in turn modifies their normal-state resistivity ρ [65]. In contrast to amorphous disordered superconductors such as NbN [182], NbTiN [183], TiN [184] or InO_x [185], where disorder arises at the atomic level, grAl exhibits a non-monotonic dependence of its superconducting transition temperature T_c vs resistivity. Numerous experiments have shown that the transition temperature forms a dome-like curve as a function of ρ [66, 174, 176], with a maximum at resistivities of approximately $\rho_{max} \approx 400$ μΩcm, as shown in Fig. 2.1(b).

Phenomenologically, this non-monotonic behavior originates from the interplay between finite-size effects and fluctuations in the phase of the superconducting condensate [64]. On the low-resistivity side of the dome ($\rho < \rho_{max}$), the aluminum grain size decreases with increasing resistivity. Reducing the grain size enhances the density of states at the Fermi level N_F, through, for example, the so-called shell effect [186]. This leads to an increase in T_c according to the BCS relation $T_c \sim \exp(-1/N_F\nu)$, where ν denotes the effective electron-electron interaction [29]. Additional evidence of the influence of finite-size effects comes from recent experiments on grAl films deposited at temperatures of 100 K and 25 K [174]. Under these conditions, the grain size shrinks; and, as illustrated in Fig. 2.1(b), the critical temperature increases even up to even 3.2 K at the top of the dome.

On the high-resistivity side of the dome ($\rho > \rho_{max}$), the grain size saturates, and further increasing the resistivity instead reduces the phase coherence of the superconducting condensate [64]. A mesoscopic measure of the resilience of superconductivity against phase fluctuations is the superfluid stiffness J, which for disordered superconductors is proportional to T_c [29, 174]. In grAl, it has been shown that the stiffness decreases approximately as $J \propto 1/\rho$ [66, 176], providing a partial explanation for the downward trend of T_c. Above resistivities $\rho_{SIT} \approx 10^4$ μΩcm, grAl experiences a superconductor-to–insulator transition (SIT) [66, 174, 176], where superconductivity at the macroscopic scale is suppressed. Interestingly, in contrast to atomically disordered films, the SIT in grAl has been proposed to resemble that of a Mott insulator [182, 187], where the transition is driven by the decoupling between the Al grains rather than the suppression of superconductivity within the grains themselves. Although it lies outside the scope of this work, we note that rich and unusual phenomena emerge near the SIT, including the appearance of collective long-range bosonic (Goldstone) excitations of the condensate. Experimental evidence for such modes has been reported in Ref. [177].

As mentioned before, grAl is also notable for its large kinetic inductance. Up to this point, we have only discussed the role of geometric inductance, which accounts for the energy

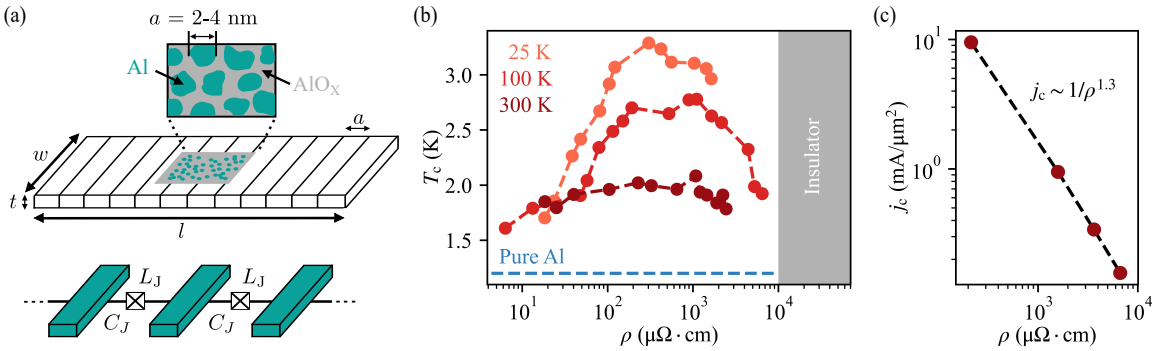

Figure 2.1: Superconducting properties of granular aluminum. **(a)** Microscopic structure of grAl. The material consists of grains of pure aluminum (Al) embedded in an AlOx matrix. The grain size is uniformly distributed around a = 2-4 nm, and varies depending on the material resistivity ρ [64, 66]. The middle and lower panels depict the JJ-array model proposed by Ref. [65]. A grAl strip of length l, width w and thickness t is partitioned into islands of same length a. Each pair of islands forms an effective JJ with inductance L_J and capacitance C_J. Panel adapted from Ref. [65]. **(b)** transition temperature T_c vs. resistivity for different deposition temperatures. The dome-like curve results from the interplay between quantum size effects and superconducting phase fluctuations in grAl [64]. The increase of T_c at lower deposition temperatures is attributed to the reduction in the Al grains size, producing an increasing shell-effect [186]. Notably, grAl's critical temperature exceeds the value of bulk Al 1.2 K (blue dashed line) by up to a factor of three. At resistivities $\gtrsim 10^4$ μΩcm, grAl experiences a phase transition where it becomes insulating, which is depicted by the grey area. Panel adapted from Ref. [174]. **(c)** Critical current density j_c as a function of ρ, as measured by Ref. [173]. The black-dashed line depicts the scaling $j_c \sim \rho^{-1.3}$. Increasing ρ from 10^2 μΩcm to 10^4 μΩcm reduces j_c by almost two orders of magnitude.

stored in the magnetic field in the circuit. However, in a superconductor an additional contribution originates from the kinetic energy stored in the motion of Cooper pairs. This additional contribution is known as the kinetic inductance and is denoted as L^k, and its origin can be understood by considering the first London equation [29],

$$\frac{d\vec{j}}{dt} = \frac{n_s q^2}{m}\vec{E}, \tag{2.1}$$

where $q = 2e$, m and n_s are the charge, mass and density of Copper pairs. The quantity $\vec{j}$ denotes the supercurrent density.

Lets suppose we have a superconducting strip with a geometry similar to the one shown in Fig. 2.1(a). In the absence of magnetic field, a voltage V applied across the ends of the strip generates a unidirectional supercurrent density $\vec{j}$. In the limit of $t \ll \lambda_L$, where λ_L is the material's London penetration depth, we can assume that the current is homogeneously distributed across the cross-section of the strip, producing a total current $I = twj$. Moreover, integrating the electric field along the length of the strip yields $E = Vl$. Substituting these expressions into Eq. (2.1), one finds that the resulting relation between I and V is analogous to Eq. (1.3), with a proportionality constant that defines the kinetic inductance

$$L^k_\square = L^k \frac{w}{l} = \frac{m}{n_s q^2 t}, \tag{2.2}$$

where $L^k_\square$ denotes the sheet inductance.

A similar expression for the kinetic inductance can be obtained from BCS theory using a formalism derived by Mattis and Bardeen [188]. This approach was developed as an approximation of the anomalous skin effect in a superconductor within the so-called local $l_s \ll \lambda_L$ and dirty $l_s \ll \chi$ limits, where l is the electron mean free path and ξ the superconducting coherence length. At temperatures well-below the transition temperature, the kinetic inductance of the superconductor can be expressed as

$$L_{\square}^{k} = \frac{R_{\square}\hbar}{\pi\Delta}, \tag{2.3}$$

where $R_{\square} = \rho/t$ is the material sheet resistance, ρ its resistivity and Δ its superconducting gap.

In a microwave circuit, the effects of kinetic inductance are appreciable only when it exceeds the geometric inductance. From the Mattis–Bardeen formula, this condition is achieved in materials with a large normal-state resistivity. For conventional superconductors such as Al or Nb, their small normal-state resistance yields a kinetic inductance of approximately 1 pH/□ [189]. By contrast, due to its high resistivity, grAl exhibits kinetic inductance values reaching the range of 1 nH/□ [75, 76], matched only by amorphous InO_x [189].

2.2 Nonlinearity of granular aluminum

Despite the rich physics underlying grAl superconductivity, the main focus of this thesis is to exploit its nonlinear properties. But where does it come from? Maleeva *et al.* [65] proposed a simple model to understand the nonlinear behavior of grAl structures, motivated by their resemblance to a JJ network (see Fig. 2.1(a)). In this model, a strip of granular aluminum is represented as an effective one-dimensional array of identical JJs, with uniformly distributed superconducting islands. The length of each island is denoted by a and was assumed to be equal to the mean size of the Al grains. Although this simplified model provided a good qualitative understanding of the Kerr nonlinearities in grAl, most of the inferred values underestimated experimental data by roughly an order of magnitude.

Later experiments suggested that the discrepancy arises from an incorrect estimation of the island size a, since Al grains tend to form clusters rather than remain isolated within the material [80, 175]. This effect is more pronounced at lower resistivities. To address this issue, Ref. [82] refined the model without an assumption of the island size and instead imposing two main conditions: (i) the critical current of the effective JJ array should match the critical current of the material I_c, and (ii) the total inductance of the strip should satisfy $L_{strip} = N_J L_J$, where N_J is the number of effective JJs and L_J their Josephson inductance. Based on this model, the total inductance of the grAl strip can be expressed in the same form as in Eq. (1.13), and the effective Kerr coefficient can be rewritten from Eq. (1.22) as

$$K = -\frac{E_J}{8\hbar N_J^3}\left(\frac{\omega_r L_{strip}}{R_Q}\right)^2 \propto \frac{\omega_r^2}{j_* N_J}, \tag{2.4}$$

where ω_r is the resonance frequency of the circuit embedding the grAl strip and $R_Q = \hbar/4e^2$ the resistance quantum. The quantity j_* characterizes the nonlinearity strength and is defined as $j_* = \sqrt{2}j_c$, with j_c denoting grAl's critical current density. Using Mattis-Bardeen formula (cf. Eq. (2.3)), the effective island size is now given by $a = l/N_J = \pi\Delta/2ej_c\rho$.

From Eq. (2.4), one identifies two primary tuning knobs for controlling the nonlinearity. First, the effective Kerr coefficient can be adjusted by modifying the total volume of the grAl structure. In the simplified case of a strip, changing the volume directly alters the effective number of Josephson junctions, N_J. In general, smaller volumes correspond to fewer effective junctions and therefore stronger nonlinearities. Second, the parameter j_* can be tuned via j_c, which in grAl is controlled by the resistivity ρ. DC transport measurements performed on a grAl nano-SQUID loop by Ref. [173], reported a scaling of the form $j_c \propto 1/\rho^{-1.3}$ (see Fig. 2.1(c)). Remarkably, the critical current of grAl varies by more than an order of magnitude before reaching the SIT.

The flexibility of grAl's nonlinearity has enabled the realization of a wide variety of microwave circuits operating across different nonlinear regimes. When $K/2\pi \lesssim 1$ Hz, the intrinsic nonlinearity of grAl is strongly suppressed. In this limit, its large kinetic inductance allows the implementation of compact superinductors. Such devices have been previously employed as microwave resonators [65, 68, 76], detectors [67], and shunt inductors in fluxonium and flux qubits [71, 74, 77]. By increasing the Kerr coefficient to the MHz range, Winkel *et al.* demonstrated that a $0.01 \times 0.2 \times 0.5\,\mu m^3$ grAl strip can function as a weak link for a transmon qubit [80]. Pushing device fabrication even further, Refs. [81, 179] used a grAl constriction of volume $\approx (20\,nm)^3$, to engineer an element that reproduces the current–phase relation expected in a conventional Al-AlO_x-Al tunnel junction (cf. Eq. (1.11)). This result suggests that the JJ-array model of grAl may also capture higher-order nonlinearities beyond the Kerr term.

2.3 Advantages of granular aluminum as a nonlinear source

In the previous sections, we presented grAl properties in a general context. However, why one would choose to use this material to build parametric devices? As being the main focus of our research, we present in this section several advantages that make grAl an interesting candidate for such applications. We discuss how grAl can overcome some of the limitations of current JJ-based devices and how even among the family of disordered superconductors, it stands out as an ideal low-loss and rich nonlinearity source to be used as a testbed for parametric devices.

Fabrication compatible with state-of-the-art quantum devices

An important aspect to consider when implementing parametric amplifiers is the use of a reproducible and reliable fabrication process. Since most research on these devices primarily focuses on microwave design and engineering, it is crucial not to introduce additional

complications at the fabrication stage. Ideally, one would like to employ techniques that are compatible with current technologies and have already been validated by previous experiments. In particular, for amplifiers, the fabrication process should introduce as little loss as possible, as this can degrade the noise performance. Fortunately, granular aluminum satisfies these requirements.

As demonstrated by several experiments [65, 67, 68, 71, 74, 76, 77], the fabrication of grAl is compatible with the processes used for conventional Al–AlOx–Al JJs. A grAl microwave structure can be patterned using standard lithographic techniques and subsequently metalized in a commercially available electron-beam evaporator. However, unlike JJ fabrication, which typically involves three separate steps [22] or requires complex multi-angle evaporations [118–120], grAl can be deposited in a single step using dynamic oxidation. In this method, a pure Al layer is evaporated while maintaining a continuous oxygen flow in the chamber. The Al evaporation rate together with the oxygen partial pressure determines the final resistivity of the film [180]. Most importantly, dynamic oxidation can be performed at zero-angle evaporation, offering great flexibility when fabricating devices with complex geometries. This has been demonstrated, for example, in Refs. [71, 74, 77], where a modified Dolan-bridge technique was employed to realize fluxonium and flux qubits incorporating grAl strips as superinductances.

Together with a flexible device fabrication, it is essential to assess whether such techniques produce high-quality grAl microwave structures. A standard proxy for material quality is the internal quality factor of an LC resonator. Higher values of Q_i indicate lower internal losses and correspondingly cleaner materials. It is important to emphasize, however, that a meaningful comparison across materials requires measurements at the same power level, preferably in the single-photon regime, where saturation processes are absent. Most conventional superconductors as Al, Nb or Ta have reported values up to $Q_\mathrm{i} \approx 10^7 - 10^8$ [189]. In grAl, Q_i is typically reduced by about an order of magnitude, with maximum values reaching only $Q_\mathrm{i} \approx 4 \cdot 10^6$ at low resistivities [180]. Ref. [189] attributes this reduction to an excess of non-equilibrium quasiparticles arising from sub-gap states introduced by disorder. Other experiments suggest that the diminished quality factor may also stem from unwanted coupling to environmental degrees of freedom whose origin remains unknown [72, 81].

Although the previous results may appear discouraging at first, the situation changes significantly when grAl is compared with other disordered superconductors. As detailed in Ref. [189], grAl provides Q_i on-par with materials such as NbN, NbTiN or TiN. In particular, amorphous InO_x, a material whose kinetic inductance is comparable to that of granular Aluminum, reports internal quality factors only up to $Q_\mathrm{i} \approx 1 \cdot 10^4$, roughly two orders of magnitude lower than those measured in grAl.

In addition, we need to recall that building a parametric amplifier has another key advantage, as one is interested mainly in the ratio between internal and external quality factors, not only in the value of Q_i itself. Amplifiers operating in the 4–12 GHz range with bandwidths exceeding several tens of megahertz require an external quality factor on the order of $Q_\mathrm{c} \approx 10 - 100$. Under these conditions, we can use Eq. (1.53), to find that even with Q_i as low as 10^5, the resulting amplifier noise would be only 2% above

the quantum limit. Therefore, although the mechanisms that degrade quality factors in grAl limit its performance in superconducting qubits, they do not pose a critical obstacle for the implementation of parametric amplifiers. This observation, together with its amenable fabrication, makes granular aluminum one of the most favorable choices for such applications.

Magnetic field resilience in the Tesla range

One of the main limitations of JJ-based amplifiers is their sensitivity to magnetic fields. Among the various mechanisms contributing to this sensitivity, the most critical is the Fraunhofer-like modulation of the critical current under in-plane magnetic fields (see Fig. 1.16(c)). Over the course of this thesis, several experiments demonstrated that this limitation can be mitigated by employing disordered superconductors such as NbN or NbTiN [49, 50, 58, 59], enabling near quantum-limited amplification at magnetic fields as high as 6 T. This naturally raises the question: can grAl be used to achieve comparable performances?

Due to the minute spacing between the Al grains in grAl, only a small cross-section contributes to the Fraunhofer interference. Instead, the dominant limitation in grAl thin films under in-plane magnetic fields arises from the suppression of the superconducting gap. When the film thickness t satisfies $t \ll \lambda_{\mathrm{L}}$, which is the case for grAl, the in-plane critical field scales as [29]

$$B_{\mathrm{c}} \sim \lambda_{\mathrm{L}}/t, \tag{2.5}$$

Hence, reducing the film thickness directly enhances the achievable critical field.

Granular aluminum field resilience has been tested by several experiments using different types of superconducting circuits. A work prior to the beginning of this project, demonstrated grAl resonators with internal quality factors on the order of $5 \cdot 10^5$ that remained unchanged up to in-plane fields of 1 T, limited only by the maximum field of the experimental apparatus [68]. Similar results were later reported for grAl-based fluxonium qubits [81]. Independent studies by Refs. [69, 75] further confirmed the potential of grAl in high-field applications. In particular, the latter work experimentally verified the scaling of Eq. (2.5), showing that reducing the thickness of a grAl nanostrip resonator from 50 nm to 20 nm, increased its critical field from 1 T to approximately 3 T. This study also demonstrated the successful integration of grAl into a hybrid semiconductor–superconductor platform, enabling strong coupling to the electronic states of a germanium quantum dot and opening a path toward grAl-based readout of spin qubits. These results established a promising route toward implementing grAl-based parametric amplifiers capable of operating in magnetic fields in the Tesla range.

Diluted nonlinearity with negligible self-capacitance

In a parametric amplifier, fine control over the circuit nonlinearities is essential for achieving optimal performance. In Section 1.3.3, we showed for example how reducing the

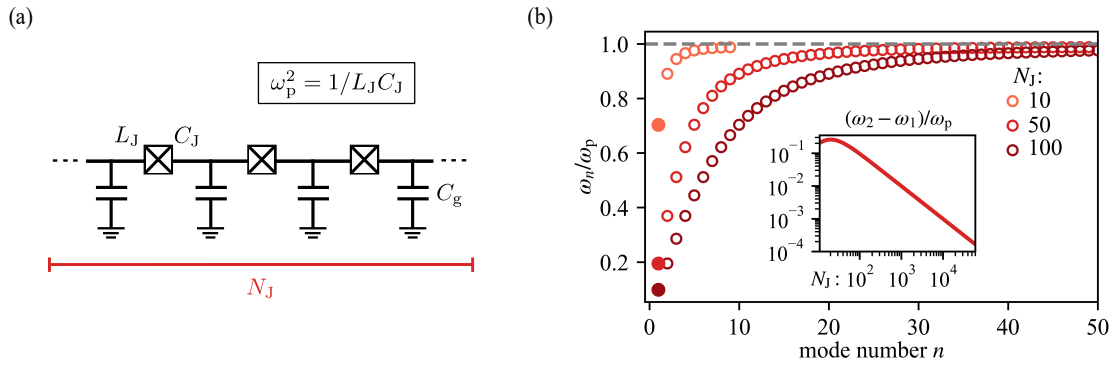

Figure 2.2: Frequency crowding in a realistic Josephson junction array. **(a)** Complete circuit diagram of a JJ array without neglecting capacitive contributions. Depending on the footprint of each JJ, two additional contributions must be included: JJ self-capacitance C_J and parasitic capacitance to the environment C_g. Their presence turns the JJ array into the electrical analogous of a phonon chain, supporting a set of N_J collective modes. In addition, C_J sets a self-resonance frequency ω_p at which every JJ behaves as an LC oscillator. **(b)** Frequency spectrum as a function of the number of junctions, N_J. We take for simplicity $C_J = C_g$. Increasing N_J, produces frequency crowding for the fundamental mode, denoted by the solid markers. Reduced spacing to neighboring modes gives rise to unwanted cross-Kerr couplings and could trigger uncontrolled mixing processes under strong pumping. In the inset we plot the frequency difference $\omega_2 - \omega_1$ between the fundamental and first excited modes, which serves as a proxy for cross-Kerr susceptibility. Increasing the number of JJs, decreases $\omega_2 - \omega_1$ and therefore the possibility of inducing uncontrolled mixing processes by applying a strong pump.

self-Kerr coefficient K in a JPA is crucial to enhance the dynamic range. Higher-order nonlinearities, arising from the expansion of the sinusoidal JJ energy–phase relation, must also be carefully controlled. If such contributions become non-negligible, the amplifier can enter a chaotic regime when driven by a pump tone. Fortunately, the use of a JJ-array also helps diluting such terms. In fact, they even have a faster scaling with the number of junctions in the array N. However, this approach introduces two notable drawbacks: (i) a larger device footprint, and (ii) spectral crowding due to the presence of higher modes of the array. Both limitations can be alleviated through the use of granular aluminum.

The fabrication of JJs is performed using lithographic techniques. Depending on the method, the minimum feature size is in the order of 1 µm for optical lithography and 200 nm for electron-beam lithography. As discussed in Refs. [21, 130], suppressing nonlinearities to the levels required for parametric amplification typically demands arrays with more than $N_J = 1000$ JJs. Even when using electron-beam lithography, this requirement leads to amplifier footprints on the order of 200 µm. In contrast, because of the nanometer-scale spacing between Al grains, a grAl strip of length ≈ 3 µm, two orders of magnitude smaller, can implement an effective array with the required number of JJs.

The smaller grain spacing in grAl brings an additional and more crucial advantage. Up to this point, we have described a JJ array by considering only its inductive contribution, an approximation valid only when capacitive effects of the junctions can be neglected. In the more general case, two capacitive contributions must be included: the Josephson capacitance C_J, defined in Section 1.2.2, and the parasitic capacitance to the environment C_g, which arises from the finite footprint of each JJ. These contributions modify the effective

circuit of the array as shown in Fig. 2.2(a). Incorporating both C_J and C_g causes the JJ array to behave as a chain of mechanical oscillators, with the inductances and capacitances playing the roles of effective spring constants and masses. As a result, the system supports a set of collective modes whose dispersion relation is illustrated in Fig. 2.2(b) and given by [190]

$$\omega_n = \omega_p \sqrt{\frac{1 - \cos(n\pi/N_J)}{1 - \cos(n\pi/N_J) + C_g/(2C_J)}}, \tag{2.6}$$

where $n \in \mathbb{N}$ denote the mode number. At low frequencies, the dispersion relation is approximately linear, analogous to the acoustic-phonon regime of a mechanical chain. However, as the frequency approaches the self-resonance of the array, known as the plasma frequency $\omega_p = 1/\sqrt{L_J C_J}$ when each individual JJ behaves as a LC resonator, the mode spacing progressively decreases. Importantly, only the fundamental mode ($n = 1$) inherits the full $1/N_J$ nonlinearity reduction derived in Eq. (1.21), while higher-frequency modes exhibit a reduced scaling.

The frequency crowding of the array spectrum can affect device operation through cross-Kerr coupling between modes. Although this intermode coupling was exploited in Refs. [21, 22] to achieve parametric amplification across a broader frequency range, it also introduces important limitations for more complex applications. For example when trying to realize a Bogoliubov class of amplifiers, multiple pumps can generate additional mixing processes, which could increase the device noise level or drive it to a chaotic regime. A closely related effect has recently been observed in superconducting qubits [191], where dynamically induced interactions were shown to limit transmon coherence[1]. Furthermore, the dense spacing of higher-order modes can complicate the design of an impedance-matching network to increase the amplifier bandwidth [192].

One must therefore seek an alternative strategy to reduce the circuit nonlinearity without introducing unwanted capacitive effects, for which grAl offers clear advantages. First, owing to the small charging volume between the Al grains, the self-capacitance of grAl is drastically reduced. Second, the much smaller physical footprint of a grAl strip suppresses parasitic capacitance to the environment. The benefits of a low self-capacitance and a cleaner frequency spectrum have already been suggested by other circuits using grAl superinductors, like fluxoniums and flux qubits, where they have consistently shown to be more resilient to higher powers and less sensitive to parasitic cross-Kerr interactions [74, 81, 150, 158].

One way to quantify the improvement provided by grAl is to compare its plasma frequency with those reported for JJ-array JPAs. In general, a higher plasma frequency implies fewer spurious modes entering the 4–12 GHz band targeted by parametric amplifiers. In the work of Winkel *et al.* [22], the JJ-array plasma frequency was engineered to lie between 13 GHz and 20 GHz. In contrast, as reported in Maleeva *et al.* [65], the plasma frequency of grAl lies in the THz range, representing an improvement of more than one order of magnitude relative to conventional JJ arrays.

[1] The authors cleverly named this effect as DUST: drive-induced unwanted state transitions.

Enhanced nonlinearity for parametric processes

The discussions above show that grAl could overcome several limitations of conventional JPAs. However, similar advantages could, in principle, be obtained using other disordered superconductors. Then, what makes grAl different? The answer comes from the strength of its nonlinearity.

Even tough the JJ-array model introduced by Maleeva *et al.* [65] allows us to predict the strength of grAl's nonlinearity, it is not immediately obvious whether the same approach applies to atomically disordered superconductors like NbN, NbTiN, TiN and InO_x. Due to their amorphous nature, these materials do not form the granular microstructure characteristic of grAl films. Nevertheless, in any superconductor, the nonlinearity of the kinetic inductance follows in general the equation

$$L_K(j) = L_K(0)\left(1 + \frac{j^2}{j_*^2} + \cdots\right), \tag{2.7}$$

where the parameter j_* is called the depairing current density and is proportional to the critical current density of the material j_c. As shown by in Annunziata *et al.* [193], the expression in Eq. (2.7) can be derived from a generalization of the Mattis–Bardeen formalism. A similar result can also be obtained using the Usadel equations [194] or, in the limit of low currents and temperatures close to the superconducting transition, from Ginzburg–Landau theory [193]. This general behavior arises because a bias current breaks the time-reversal symmetry of the condensate, effectively creating a pair-breaking mechanism [29]. Intuitively, as the current increases, the kinetic energy of the Cooper pairs rises. Once this energy becomes comparable to the condensation energy, it becomes energetically favorable for Cooper pairs to break, reducing their density n_s and therefore increasing the kinetic inductance. The primary distinction between the models is in the specific dependence of j_* with j_c. In the JJ-array model, $j_* = \sqrt{2}j_c$, whereas in the Mattis–Bardeen and Usadel formalisms, one obtains $j_* \approx 3.36 j_c$. Although the Ginzburg–Landau formalism is not strictly valid for the operational temperatures of typical microwave circuits, for completeness, it predicts $j_* \approx 1.5 j_c$.

Regardless of its microscopic origin, j_* is a key parameter which determines the strength of a material's nonlinearity. This applies for both 4-wave mixing and 3-wave mixing processes. In Fig. 2.3, we present a compilation of j_* values obtained from different disordered superconductors. Granular aluminum stands out as one of the richest sources of nonlinearity. Although for low resistivities, the depairing current is comparable to other materials, by increasing the resistivity to $\rho \approx 3000$ μΩcm we can reduce j_* below $\approx$ nA/μm^2. The only material reaching similar values is amorphous InO_x. However, its order of magnitude lower quality factors, makes it a less attractive material to be used in a parametric device.

One might argue that using a material with a lower characteristic current for a parametric amplifier could be compensated by reducing the device volume or applying a stronger pump tone. However, this approach introduces significant drawbacks. First, device miniaturizing, although possible as demonstrated in Ref. [49], increases fabrication complexity and

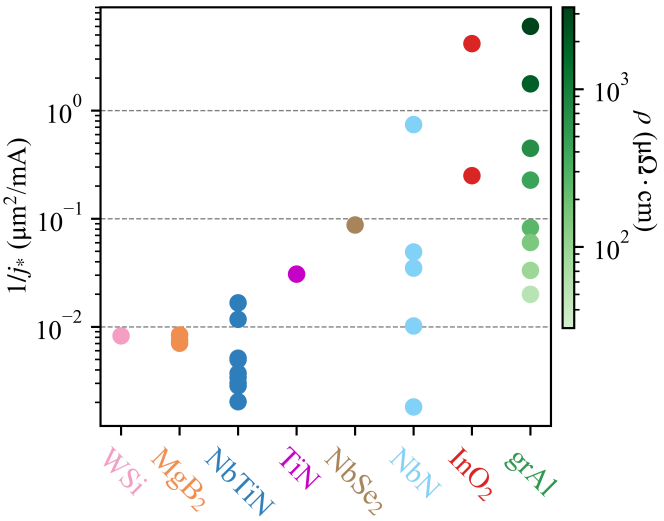

Figure 2.3: Nonlinearity of disordered superconductors. Reducing the characteristic current j_* increases the material nonlinearity. Granular Aluminum stands out as one of the richest sources of nonlinearity. By tuning the material resistivity ρ, the characteristic current j_* can be varied by nearly two orders of magnitude. Data are compiled from: [195] (WSi), [196] (MgB_2), [52–60] (NbTiN), [197] (TiN), [198] ($NbSe_2$), [49, 50, 93, 199] (NbN), [69, 91, 92] (InO_2) and [69, 80, 179, 200–202] (grAl). When only the critical current j_c was reported, we used $j_* = \sqrt{2} j_c$ for grAl and $j_* = 3.36 j_c$ for all other materials.

reduces reproducibility. Second, applying stronger pump powers leads to a higher heat load on the cryostat, as shown in Fig. 1.15. Both complications should be avoided when building the next generation of parametric amplifiers, as they can impact the scalability of future superconducting hardware.

In the following chapters, we present the realization of a granular aluminum parametric amplifier were we exploit some of the benefits presented in this section. We focus primarily on its compatibility with magnetic fields (Chapter 3) and the reduced nonlinearities in the absence of self-capacitive effects (Chapter 4). Nevertheless, we encourage the interested reader to explore the concepts and advantages introduced here, in more complex devices, which could benefit from the unique grAl properties.

3 Granular Aluminum Parametric Amplifier (grAlPA): beyond the militesla limit

In this chapter, we present the design and characterization of the central device of this work: the granular Aluminum Parametric Amplifier (grAlPA). We leverage grAl nonlinearity and low internal losses to realize a practical amplifier in the form of a Bose-Hubbard dimer. The grAlPA achieves a performance comparable to state-of-the-art implementations based in Josephson junctions: phase-preserving gain above 20 dB, signal-pump detuning $\sim$ 0.1 GHz, -110 dBm saturation power and near quantum-limited noise performance. Most importantly, all these features remain unchanged for in-plane fields up to 1 T, which demonstrates the suitability of our amplifiers for the readout of systems operating under high magnetic fields. This chapter is adapted from Ref.[94] and builds upon the initial work done by Ivan Takmakov, which is documented in Ref.[82].

The preceding discussions showed how JJ-based parametric devices suffer from an intrinsic susceptibility to magnetic fields above the militesla range, which limits their applicability in systems requiring high field operation. Thin films of disordered superconductors, offer a suitable alternative due to their resilience to fields at Tesla levels. GrAl is particularly attractive as it supports critical current densities $\lesssim$ mA/μm^2 [65, 68, 80, 179], an order of magnitude lower than most disordered superconductors[1]. Moreover, grAl structures exhibit internal quality factors among the highest achievable in disordered superconductors [189], enabling high coherence and low dissipation. These two properties recommend grAl as suitable material to realize parametric devices operating close to the Tesla range.

Along this chapter, we explain the process of designing, fabricating, and evaluating the performance of a grAl amplifier, which we call grAlPA. The chapter is organized as follows. Section 3.1 provides an overview of the Bose-Hubbard dimer model we use as a reference for designing our amplifiers, followed by a discussion in Section 3.2 of the requirements needed to achieve 20 dB non-degenerate gain. Section 3.3 introduces the layout and fabrication process of the grAlPA. Having introduced the grAlPA design, in Section 3.4 we describe the extraction of its circuit parameters. Section 3.5 presents the amplifier's gain profiles under zero field, followed by its gain performance under in-plane (Section 3.6)

[1] A detailed comparison between grAl and NbN for high-magnetic field applications can be found in Ref. [69] and is highly recommended.

and out-of-plane (Section 3.7) magnetic fields. Afterwards, in Section 3.8, we focus in the most important figure merit of the grAlPA: its noise performance. We demonstrate the near quantum-limited operation of our amplifier up to 1 T. Finally, in Section 3.9 and Section 3.10, we report the successful application of the grAlPA for single-shot readout of a superconducting qubit. We use these measurements to estimate the grAlPA's quantum efficiency.

3.1 The Bose-Hubbard dimer

The Bose–Hubbard model is a well-known quantum mechanical framework that describes the dynamics of bosonic lattices with an on-site potential K and hopping interactions J [203, 204]. It was originally conceived to explain the superfluid–insulator transition in Bose–Einstein condensates [204–207] and ultracold atomic lattices [208]. A minimal building block of this model is the Bose–Hubbard dimer (BHD) [209], in which the lattice is reduced to only two sites. This system has been realized in several experimental platforms, including semiconductor microcavities [210, 211], photonic crystals [212], and superconducting circuits [22, 58, 94, 130, 213]. It has attracted considerable interest as a testbed for studying the interplay between nonlinear physics and quantum correlations [213–215], and has been shown to exhibit phenomena such as Josephson-like dynamics[2] [204, 216], parametric self-oscillations [217, 218], and spontaneous symmetry breaking [212, 215] when driven by an external excitation.

The first discussion of the BHD as a possible source of non-degenerate amplification appeared in Ref. [219]. In the presence of both driving forces and dissipation, the system develops an instability point similar to the one discussed in Section 1.3.2. In 2014, this feature was exploited by Eichler *et al.* [112] to successfully realize a non-degenerate parametric amplifier with a BHD made of JJ resonators. More recently, the concept has been extended to multi-mode configurations, where dispersion engineering of JJ-arrays enabled broadband amplification covering the 4–12 GHz range [22]. Other implementations using kinetic inductance materials can also be found in Ref. [58].

To understand how the driven BHD gives rise to non-degenerate (ND) gain, we start by examining its key features. In Fig. 3.1(a) we show the equivalent circuit representation of the device implemented by Eichler *et al.*. It consists of two nonlinear superconducting resonators with frequencies $\omega_{\mathrm{L,R}}$, coupled via capacitive interactions of strength J. The left cavity is connected to a microwave port, resulting in an external damping rate κ, while all additional losses in the dimer are captured by the internal damping rate of the right resonator, denoted as γ. The inductive part and nonlinearity of each resonator stem from

[2] This is the reason why the BHD is sometimes referred to as the bosonic Josephson Junction, as it describes the tunneling of bosons through two macroscopically populated quantum states [204].

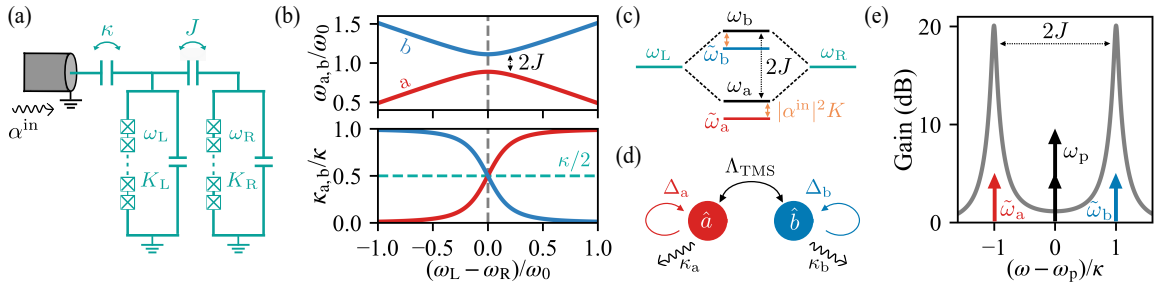

Figure 3.1: Bose-Hubbard dimer model and non-degenerate gain. **(a)** Circuit diagram of the Bose-Hubbard dimer model. A pair of resonators with frequencies and on-site potentials denoted by ω_{i} and K_{i} (i = L, R), respectively, are capacitive coupled with a hopping strength J. The non-linearity of each resonator stem from two Josephson Junction arrays. Resonator L is coupled with rate κ to an input port, through which a pump tone α^{in} is applied to activate non-degenerate gain. **(b)** Frequencies $\omega_{\text{a,b}}$ (top) and linewidths $\kappa_{\text{a,b}}$ (bottom) of the hybridized modes as a function of the detuning $(\omega_{\text{L}} - \omega_{\text{R}})/\omega_0$, where $\omega_0 = (\omega_{\text{L}} + \omega_{\text{R}})/2$. In case of perfect hybridization $\omega_{\text{L}} = \omega_{\text{R}}$, the separation of the dimer modes is given by the hopping parameter J and their linewidths fulfill $\kappa_{\text{a,b}} = \kappa/2$. **(c)** Dressed mode structure of the dimer. When driven, the hybridized modes are red shifted by $|\alpha^{\text{in}}|^2 K$ to $\tilde{\omega}_{\text{a,b}}$, where $|\alpha^{\text{in}}_{\text{tot}}|$ is proportional to the total input power and K is an effective Kerr coefficient. **(d)** Linearized mode structure in the presence of a pump tone with frequency $\omega_{\text{p}} = (\tilde{\omega}_{\text{a}} + \tilde{\omega}_{\text{b}})/2$. Each mode has a frequency detuning Δ_{j} (j = a,b) relative to the rotating frame at ω_{p}. The modes are coupled through two-mode squeezing interactions denoted by Λ_{TMS}. **(e)** Example of a non-degenerate gain profile when the BHD is driven with a pump at frequency $\omega_{\text{p}} = (\tilde{\omega}_{\text{a}} + \tilde{\omega}_{\text{b}})/2$. The arrows schematically represent the four-wave mixing process, where two pump photons (black) are converted into a signal photon (red) and an idler photon (blue), each occupying a different dimer mode.

Josephson-junction arrays with self-Kerr coefficients $K_{\text{L,R}}$. The dynamics of the system is described by the following Hamiltonian

$$\hat{H}/\hbar = \sum_{i=\text{L,R}} \left(\omega_i \hat{a}_i^\dagger \hat{a}_i + \frac{K_i}{2} \hat{a}_i^\dagger \hat{a}_i^\dagger \hat{a}_i \hat{a}_i \right) + J \hat{a}_{\text{L}}^\dagger \hat{a}_{\text{R}} + \text{h.c.}, \tag{3.1}$$

where $\hat{a}_{\text{L,R}}$ denote the annihilation operators of the bosonic modes corresponding to the two superconducting resonators.

The hopping interaction leads to the formation of hybridized modes[3] with frequencies $\omega_{\text{a,b}}$ and linewidths $\kappa_{\text{a,b}}$, which depend on the detuning between the bare grAl resonators, as illustrated in Fig. 3.1(b) and described by[4] (see. Appendix A)

$$\begin{aligned} \omega_{\text{a/b}} &= \frac{\omega_{\text{L}} + \omega_{\text{R}}}{2} \pm \sqrt{J^2 + \left(\frac{\omega_{\text{L}} - \omega_{\text{R}}}{2} \right)^2} \\ \kappa_{\text{a/b}} &= \frac{\kappa}{2} \left(1 \pm \frac{\omega_{\text{L}} - \omega_{\text{R}}}{\sqrt{4J^2 + (\omega_{\text{L}} - \omega_{\text{R}})^2}} \right). \end{aligned} \tag{3.2}$$

[3] Throughout this manuscript, we refer to the modes in the bare basis of the BHD as "resonators" to clearly distinguish them from the hybridized modes.

[4] Note that due to the asymmetric coupling of the resonators to the microwave environment, there is also a dissipative coupling between the hybridized modes, denoted by κ_{m} in Eq. (A1.30).

When the bare resonators are perfectly hybridized, i.e., $\omega_L = \omega_R = \omega_0$, the frequency separation between the dimer modes reaches its minimum given by $2J$, and the total coupling κ is equally shared between them. If $J \lesssim 2\kappa$ [82, 219], a pump applied at frequency[5] $\omega_p = (\omega_a + \omega_b)/2$ activates four-wave mixing interactions by populating both hybridized modes symmetrically. In such case, two pump photons convert into a signal and an idler photon, each living in a different dimer mode. This realizes a phase-preserving amplifier with a signal–pump detuning given by the hopping interaction J.

To better elucidate the origin of the amplification process, we rewrite the Bose–Hubbard Hamiltonian in the hybridized basis. For simplicity, we consider the case of symmetric resonators, such that $\omega_L = \omega_R = \omega_0$ and $K_L = K_R = K$ (the full Hamiltonian for asymmetric resonators can be found in Appendix A). Under these conditions we obtain

$$\hat{H}/\hbar = \omega_a \hat{a}^\dagger \hat{a} + \omega_b \hat{b}^\dagger \hat{b} + \frac{K}{4}\hat{a}^\dagger \hat{a}^\dagger \hat{a}\hat{a} + \frac{K}{4}\hat{b}^\dagger \hat{b}^\dagger \hat{b}\hat{b} + K\hat{a}^\dagger \hat{a}\hat{b}^\dagger \hat{b} + K\hat{a}^\dagger \hat{a}^\dagger \hat{b}\hat{b} + \text{h.c.}, \tag{3.3}$$

where the third and fourth terms describe the self-Kerr interactions of each dimer mode and the last two terms correspond to cross-Kerr interactions. Under the presence of a classical pump at ω_p, we can follow the same procedure as in Section 1.3.1 and linearize the Hamiltonian using the displacement transformations $\hat{a} \to \alpha e^{i\omega_p t} + \hat{a}$ and $\hat{a} \to \beta e^{i\omega_p t} + \hat{b}$. We take α and β as the mean field amplitudes of the modes a and b, respectively, which can be calculated from the mean-field Langevin equations shown in Eq. (A1.20). In a frame rotating with respect to their Kerr-shifted frequencies $\tilde{\omega}_{a/b}$, Eq. (3.3) becomes:

$$\begin{aligned}\hat{H}/\hbar = &\left(\Lambda_{S_a} e^{2i(\omega_p - \tilde{\omega}_a)t}\hat{a}^\dagger \hat{a}^\dagger + \text{h.c.}\right) + \left(\Lambda_{S_b} e^{2i(\omega_p - \tilde{\omega}_b)t}\hat{b}^\dagger \hat{b}^\dagger + \text{h.c.}\right) \\ &+ \Lambda_{TMS}\left(e^{i(2\omega_p - \tilde{\omega}_a - \tilde{\omega}_b)t}\hat{a}^\dagger \hat{b}^\dagger + \text{h.c.}\right) + \Lambda_{BS}\left(e^{i(\tilde{\omega}_b - \tilde{\omega}_a)t}\hat{a}^\dagger \hat{b} + \text{h.c.}\right),\end{aligned} \tag{3.4}$$

where $\hat{a}$ and $\hat{b}$ correspond now to the linearized bosonic modes, and $\Lambda_{S_{a,b}}$, Λ_{TMS} and Λ_{BS} correspond to single-mode squeezing, two-mode squeezing and beam splitter interaction strengths, respectively. Notice that all terms in Eq. (3.4) dependent on the circuit parameters and the pump frequency and power (see Appendix A for the full expressions).

At first glance, Eq. (3.4) appears rather complicated. However, depending on the pump configuration, some of the terms in Eq. (3.4) can be neglected in a rotating-wave approximation. For example, if $\omega_p = \tilde{\omega}_a(\tilde{\omega}_b)$, the dynamics of the BHD is dominated by the single-mode squeezing of mode $a(b)$, which effectively implements the Hamiltonian of the degenerate amplifier discussed in Section 1.3.1. On the other hand, if $\omega_p = (\tilde{\omega}_a + \tilde{\omega}_b)/2$, both $\Lambda_{S_{a,b}}$ and Λ_{BS} are now off-resonant and can be removed with a RWA. In this case the system presents the mode structure of Fig. 3.1(d) and Eq. (3.4) can be rewritten as

$$\hat{H}/\hbar = \Lambda_{TMS}\left(\hat{a}^\dagger \hat{b}^\dagger + \hat{b}\hat{a}\right), \tag{3.5}$$

which is the Hamiltonian of a non-degenerate amplifier discussed by Ref. [11], but transformed to the interaction frame with respect to the free Hamiltonian. In Fig. 3.1(e), we

[5] We use this convention here just for simplicity. Experimentally, one should account for the Kerr-shift of the dimer modes and modify the pump frequency accordingly.

present an example of ND gain curves calculated for a BHD with perfectly hybridized resonators. Around each dimer mode, the curve has the characteristic Lorentzian shape of standing-wave parametric amplifiers with maximum gain G_0 and instantaneous bandwidth BW given by (see Appendix A)

$$G_0 = \frac{16|\Lambda_{\mathrm{TMS}}|^2 + \kappa^2}{16|\Lambda_{\mathrm{TMS}}|^2 - \kappa^2}, \tag{3.6}$$

and

$$\mathrm{BW} = \frac{\kappa}{2\sqrt{G_0}}. \tag{3.7}$$

Realizing ND gain with a BHD offers several advantages over other amplifier configurations. First, unlike degenerate amplifiers, where the signal and idler tones lie within the linewidth of the same physical mode, the inherent frequency separation of the two hybridized modes in a BHD naturally facilitates filtering of the idler tone. This suppresses unwanted phase sensitivity in the amplifier's output signal arising from the non-zero measurement bandwidth of the experimental setup. Moreover, the large signal–to-pump detuning in a BHD, simplifies the design of filtering circuits for the pump tone. Finally, as demonstrated in previous implementations [22, 112], the inclusion of an additional physical mode does not introduce extra noise, allowing the device to remain near–quantum-limited.

3.2 Conditions for the existence of non-degenerate gain

In Section 3.1, we showed how the BHD can provide ND gain when pumped between its dimer modes. However, in a practical amplifier, its circuit parameters must satisfy specific criteria to produce stable amplification at the 20 dB levels required in cQED setups. For the BHD, the existence of ND gain in a subset of the pump amplitude α_{in} and frequency ω_{p} parameter space is determined mainly by two conditions:

(i) **Coupling condition,** $J \lesssim 2\kappa$. This condition ensures a non-negligible frequency overlap of the dimer modes, implying that they can be simultaneously populated when applying a pump between them.

(ii) **Perfect hybridization condition,** $\omega_{\mathrm{L}} = \omega_{\mathrm{R}}$**,** $K_{\mathrm{L}} = K_{\mathrm{R}}$. This condition ensures that $\kappa_{\mathrm{a}} = \kappa_{\mathrm{b}}$ (cf. Fig. 3.1(b)), which maximizes the amplifier bandwidth [82, 112]. Furthermore, imposing $K_{\mathrm{L}} = K_{\mathrm{R}}$, guarantees that the modes bifurcate at the same pump power, therefore increasing the operation area in the $(\omega_{\mathrm{p}}, \alpha_{\mathrm{in}})$ parameter space [82].

In Fig. 3.2 we show examples of the BHD phase space for three different cases: a system satisfying both (i) and (ii), a system satisfying only (i), and a system satisfying only (ii). We obtain these diagrams by calculating the number of linearly independent solutions for the resonator population numbers $n_{\mathrm{L,R}}$, from the BHD mean-field Langevin equations (cf. Eq. (A1.12)). The blue areas, represent regions that enable ND gain, which for the BHD are defined by the relation $n_{\mathrm{R}} > 4n_{\mathrm{L}}$ [82, 130]. The phase diagrams at the upper panel of

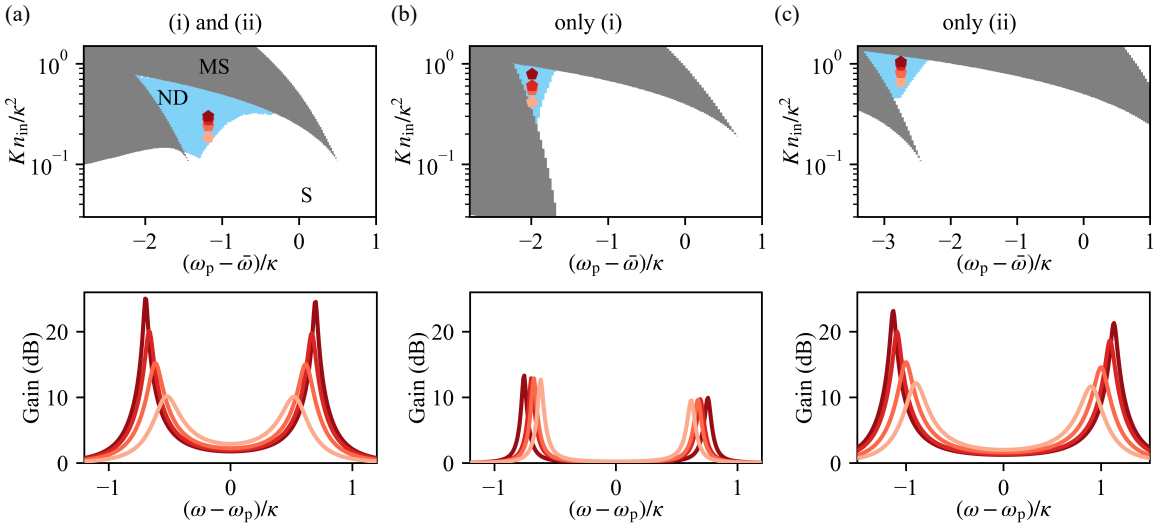

Figure 3.2: Phase space and non-degenerate gain profiles of the BHD. In the upper panels we present the calculated phase space of the BHD for three different cases: **(a)** when conditions (i) and (ii) are both satisfied, **(b)** when only condition (i) is satisfied and **(c)** when only condition (ii) is satisfied. We define the different regions of the phase space depending of the number of solutions of the mean-field Langevin equations (cf. Eq. (A1.12)) in presence of a pump tone with amplitude $\alpha_{in} = \sqrt{n_{in}}$ and frequency ω_p. When the equations have a unique solution the system is in the stable regime (S) marked by the white areas. Inside this region, when the population of the BHD resonators fulfill $n_R > 4n_L$ and the device provides at least 5 dB gain, the system is defined to be in the non-degenerate regime (ND) depicted by the blue areas. Finally, when there are multiple solutions of the Langevin equations, the system is in a multistability regime (MS), illustrated by the gray areas. We denote $\bar{\omega}$ as the average of the bare resonance frequencies $\omega_{L,R}$. Not satisfying (i) or (ii), produce a reduction of the available ND area. The lower panels show examples of non-degenerate gain profiles obtained for the pump configurations depicted by the red markers of the upper panels. Notably, even when the ND exists, it is not a warranty that the BHD can provide 20 dB gain.

Fig. 3.2(a), when both (i) and (ii) are satisfied, show that pumping between the Kerr-shifted dimer modes yields the expected double-Lorentzian gain profiles, with gain increasing as a function of the pump power α_{in}. In contrast, if either (i) or (ii) are not are satisfied, the range of α_{in} and ω_p that allow ND gain is significantly reduced and the maximum gain might stay below 20 dB (see lower panels of Fig. 3.2(b)-(c)).

Analogous to the analysis in Section 1.3.2, the BHD also supports regions with multiple solutions (MS) of $\alpha_{L,R}$. They are depicted by the gray areas on the phase diagrams in Fig. 3.2. When designing an amplifier, it is generally recommended to avoid operating in such regions, as the device may exhibit hysteretic behavior and increased added noise [220]. Nevertheless, in specific cases, a BHD in this regime can still function as a near-quantum-limited ND amplifier, as we will demonstrate in Chapter 4. Understanding the conditions required to operate the BHD in the MS regime, involves a deeper discussion of the system's dynamical stability, which we treat in the next chapter.

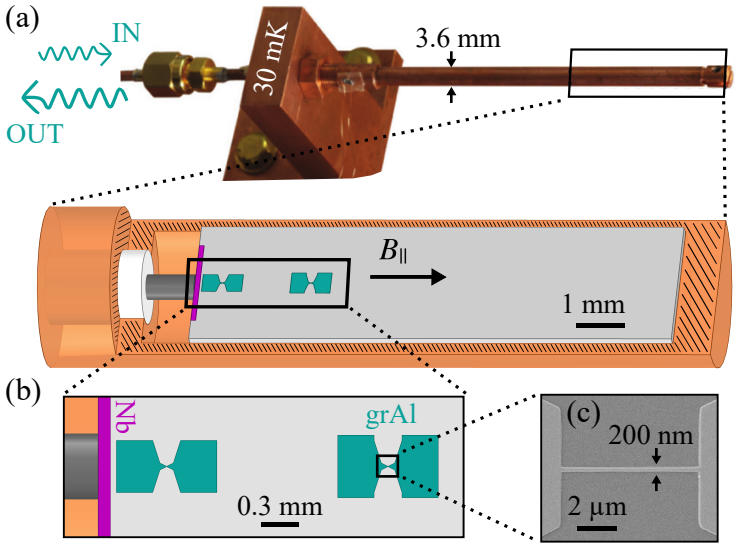

Figure 3.3: grAlPA design. **(a)** Photograph (top) and schematics (bottom) of the cylindrical waveguide used for microwave reflection measurements. The design is similar to the one employed by Refs. [68, 134, 179]. **(b)** Zoomed-in schematics of the grAlPA. It resembles the BHD shown in Fig. 3.1 and consists of a pair of lumped-element grAl resonators (green), formed by two coplanar capacitor plates connected by a central strip. To stabilize the evanescent coupling to the coaxial central pin (black) we add a Nb pad (purple) at the edge of the substrate. The black arrow depicts the magnetic field orientation (in-plane) used for gain and noise performance measurements (cf. Section 3.6 and Section 3.8). **(c)** Scanning electron beam picture of the central grAl nanostrip.

3.3 Design and fabrication

To realize the grAlPA we follow a design that resembles the BHD model and is implemented using the two grAl resonators illustrated in Fig. 3.3. The device is operated in reflection and is mounted inside the single-port cylindrical waveguide shown in Fig. 3.3(a). The waveguide is installed at the mixing chamber of a dilution refrigerator, operating at temperatures between 10 mK and 40 mK (see Appendix B.2). Thanks to its cut-off frequency close to 60 GHz, well above the common 4-12 GHz operational range of superconducting circuits, the waveguide provides a clean microwave environment for the amplifier. Coupling to the readout lines, denoted as κ in Fig. 3.1(a), is achieved via the evanescent electric field generated by the stripped pin of a coaxial cable positioned at one end of the waveguide. Each resonator is formed by two coplanar capacitor plates, which are connected by a $7{\times}0.2{\times}0.04\,\mu m^3$ grAl strip (see Fig. 3.3(b)-(c)). We choose the size of the capacitor plates to match the frequencies of the resonators and reach perfect mode hybridization. The hopping interaction J between the resonators originates from their electric dipole–dipole coupling and is primarily determined by their on-chip separation. Importantly, we maximize κ to enhance the amplifier instantaneous bandwidth and satisfy the condition $J \lesssim 2\kappa$, essential for achieving ND gain without reaching to the multistability regime. We design the grAlPA to have $\omega_L = \omega_R = 8.33$ GHz, $J/2\pi = 0.1$ GHz and $\kappa/2\pi = 60$ MHz.

For the grAlPA fabrication, we use a single step of electron-beam lithography on a c-plane sapphire wafer with a thickness of 330 µm (the complete recipe is detailed in Appendix B.1).

The substrate is spin-coated with a resist stack consisting of 800 nm MMA EL-13 and 400 nm PMMA A4, followed by an Au antistatic layer of 10 nm thickness. We use a 50 keV e-beam writer to pattern the grAl resonators, remove the Au layer with Lugol and subsequently develop the wafer in a IPA:H_2O (3:1) solution at 6°C. Before the deposition step, we place the substrate inside a Plassys MEB550S electron-beam evaporator [221] and use a Ar/O_2 descum process to clean the substrate surface from possible resist residues coming from the development step. Inside the Plassys, we use Ti gettering to improve the vacuum conditions after cleaning. Then, a granular aluminum film with thickness $t = 40$ nm and resistivity $\rho = 830$ μΩcm is deposited under dynamic oxidation via zero-angle Al evaporation at a rate of 1 nm/s. Finally, the sample is static-oxidized inside the evaporator for approximately 3 min at a fixed O_2 pressure of 10 mbar. This last step is performed to protect the grAl film against degradation when exposed to ambient conditions.

The central elements of the amplifier design are the grAl strips shown in Fig. 3.3(c), as they provide the dominant inductive contribution of each resonator and are also the source of their nonlinearity. To confirm that both assertions hold in our amplifier design, we calculate the inductive participation of the kinetic inductance arising from the grAl central line. Three main contributions are identified: the resonator's total geometric inductance L_{geo}, the kinetic inductance of the grAl strip L_{strip} and the kinetic inductance of the capacitor pads L_{pads}. An estimate of L_{strip} is obtained by calculating the grAl sheet inductance $L^{\text{k}}_{\square} = 12$ nH/□ from Mattis-Bardeen formula (cf. Eq. (2.3)) and using the measured grAl resistivity ρ and film thickness t. We estimate the superconducting gap from Ref. [66]. The grAl strip accounts for 35 squares of sheet inductance, which gives $L_{\text{strip}} = 4.20$ nH. Using finite element method (FEM) simulations we obtain $L_{\text{pads}} \approx 1$ nH and $L_{\text{geo}} \lesssim 1$ fH. Consequently, the inductance participation ratio of the grAl central line $p = L_{\text{strip}}/(L_{\text{strip}} + L_{\text{pads}} + L_{\text{geo}})$ is approximately 80%, confirming our initial claims.

We focus now on an estimation of the resonators self-Kerr non-nonlinearities K. As discussed in Section 2.2 and following Refs. [65, 82], we can estimate K by modeling the strip as an effective array of N_{J} Josephson Junctions. We use Eq. (2.4), where we calculate $I_{\text{c}}^{\text{grAl}}$ from the resistivity of the film, as explained in Ref. [82]. For the grAlPA, the JJ array model yields $N_{\text{J}} \approx 1000$ and $K/2\pi = 6$-7 kHz. From Eq. (1.21), we also determine higher order nonlinearities below the mHz level. Furthermore, unlike amplifiers based on actual JJ arrays, the low self-capacitance of grAl prevents the emergence of higher harmonic modes of the strip within the operational range of our device. In Chapter 4, we exploit this fact to realize an amplifier beyond the GBW limit.

Even though the evanescent coupling of the grAlPA to the cylindrical waveguide provides a clean microwave environment, this strategy presents a clear challenge: the coupling is exponentially sensitive to variations in the distance between the pin and the grAlPA. In order to mitigate this effect, we use a second step of optical lithography to fabricate a 40 μm wide and 40 nm thick Nb pad, at the edge of the chip. This pad acts as an on-chip extension of the coaxial cable pin, which spreads the electric field lines uniformly towards the grAl resonators. With this improvement, we can stabilize the coupling strength κ in case of misalignments occurring during the installation of the grAlPA chip and preserve

the conditions necessary to achieve non-degenerate gain. A detailed discussion about the role of the Nb pad can be found in Appendix B.3.

3.4 Circuit parameters extraction

To confirm that the grAlPA can be used as a parametric amplifier, we first asses the device performance at low powers and verify its microwave properties according to the predictions of the BHD model (see Fig. 3.1(a)). We begin by characterizing the grAlPA spectrum at zero magnetic field and for powers corresponding to single-photon population in the grAl resonators, where the effect of the self-Kerr coefficients $K_{\mathrm{L/R}}$ is negligible. For this purpose, we measure the grAlPA reflection coefficient S_{11} using a Vector Network Analyzer (VNA), connected as shown in Fig. A2.1. In the single-photon regime, both hybridized modes behave as two independent harmonic oscillators, allowing us to extract their frequencies $\omega_{a/b}$ and damping rates $\kappa_{a/b}$ and $\gamma_{a/b}$, using single-tone spectroscopy measurements and standard circle fits [222]. From these values, we calculate $\omega_{\mathrm{L/R}}$, J and κ using Eq. (3.2). The results are summarized in Table 3.1. As designed, we observe near-perfect hybridization of the grAl resonators ($\omega_{\mathrm{L}} \approx \omega_{\mathrm{R}}$) and a hopping parameter satisfying $J \approx 2\kappa$. Furthermore, the ratio between internal and external damping rates is $\gamma_{\mathrm{a/b}}/\kappa_{\mathrm{a/b}} \lesssim 0.2$, which indicates the potential for near quantum-limited noise performance of the grAlPA (see Eq. (1.53)).

Applying an in-plane magnetic field $B_{||}$ with the orientation shown in Fig. 3.3(b), modifies grAl's kinetic inductance by a change in the superconducting gap according to Eq. (1.57). Consequently, the BHD resonators undergo a frequency shift given by

$$\omega(B_{||}) = \frac{1}{\sqrt{L_{\mathrm{k}}(B_{||})C}} = \omega(0)\left(\frac{1-(B_{||}/B_{\mathrm{c}})^2}{1+(B_{||}/B_{\mathrm{c}})^2}\right)^{1/4}, \tag{3.8}$$

where C is the resonator capacitance and B_{c} is the effective in-plane critical field of the grAl film. We measure the change in frequencies from single-tone spectroscopy measurements at different $B_{||}$ and extract the corresponding grAlPA circuits parameters with the same procedure as in zero field. The magnetic field is produced by a homemade 2D vector magnet with ranges up to ≈ 100 mT and ≈ 1 T in the out-of-plane and in-plane directions, respectively. A word of caution is however necessary, as the large capacitive pads in each grAl resonator make them highly susceptible to residual out-of-plane field components,

Table 3.1: Circuit parameters of the grAlPA at zero field. The errors arise from the Fano uncertainty in the measurement setup [134].

$\omega_{\mathrm{a}}/2\pi$ (GHz)	$\omega_{\mathrm{b}}/2\pi$ (GHz)	$\kappa_{\mathrm{a}}/2\pi$ (MHz)	$\kappa_{\mathrm{b}}/2\pi$ (MHz)	$\gamma_{\mathrm{a,b}}/2\pi$ (MHz)	$\omega_{\mathrm{L}}/2\pi$ (GHz)	$\omega_{\mathrm{R}}/2\pi$ (GHz)	$J/2\pi$ (MHz)	$\kappa/2\pi$ (MHz)
8.222	8.421	26.1 ± 3	19.9 ± 2	≤ 6.3	8.321 ± 1	8.321 ± 1	99.3 ± 10	56.5 ± 5

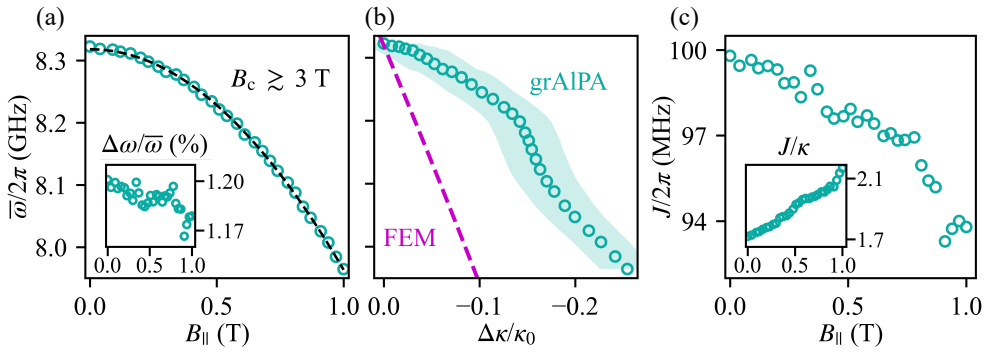

Figure 3.4: Magnetic field dependence of grAlPA resonators $\omega_{L,R}$, coupling strength κ and hopping parameter J. (a) Field dependence of the average frequency $\bar{\omega} = (\omega_L + \omega_R)/2$. Green circles are calculated from single-tone spectroscopy measurements and using Eq. (3.2). The dashed black line depicts the fit obtained from Eq. (3.8). We extract a critical field $B_c \approx 3$ T. The inset illustrates the relative frequency difference between the modes denoted as $\Delta\omega/\bar{\omega}$, with $\Delta\omega = \omega_R - \omega_L$. **(b)** Change of external coupling as a function of $\bar{\omega}$. We define $\Delta\kappa = \kappa - \kappa_0$, where $\kappa_0 = 56.5$ MHz is the coupling strength at zero field. The Fano uncertainty in the estimation of the external coupling strength κ [134] is depicted by the shaded regions. Results from FEM simulations are shown by the purple dashed line. **(c)** Magnetic field dependence of the hopping parameter J. The inset displays the field variation of J/κ, which remains close to the designed value of $J/\kappa \approx 2$.

which could lead to trapping of unwanted vortices and increased dissipation [166, 167]. To suppress this effect we align the in-plane direction following a procedure similar to Ref. [68], and detailed in Appendix B.5. With this method, we achieve an alignment accuracy better than 1% in the in-plane direction.

Fig. 3.4(a) shows the field dependence of the grAlPA average frequency $\bar{\omega} = (\omega_L + \omega_R)/2$ and total coupling strength κ. As shown in the inset of Fig. 3.4(a) the frequency difference $\Delta\omega = \omega_R - \omega_L$ vary by less than 2% up to 1 T, indicating the absence of issues related to inhomogeneous fields seen by the two resonators. Moreover, by fitting the measured data with Eq. (3.8) we extract $B_c = 3$ T, smaller than the values reported in other experiments [68, 69, 75]. We attribute this discrepancy to the large capacitor pads of the grAl resonators, for which even a small residual out-of-plane field component is sufficient to skew the fit. The experiments also show a monotonic decrease of κ with higher $B_{||}$ (see Fig. 3.4(b)). Part of this reduction can be explained by the gradual decoupling of the grAlPA resonators as their frequencies move farther from the cutoff of the cylindrical waveguide in Fig. 3.3(a). This is confirmed by FEM simulations, which indicate $\approx 50\%$ decrease in κ for the frequency range covered in the experiments. The remaining 50% is attributed to additional features in the impedance of the environment seen by the grAlPA. Such features likely originate from the frequency-dependent isolation of the circulators used in our setup (see Fig. A2.1 and the datasheets in Ref. [223]). Importantly, since the hopping strength J also changes by less than 10% over the entire field range (see Fig. 3.4(c)), we conclude that the grAlPA preserves the conditions for ND gain.

By studying the field dependence of the hybridized modes, we observe that they can be tuned by approximately 300 MHz (see Fig. 3.5(a)). Moreover, in Fig. 3.5(b) we show the dependence of the external and internal quality factors. Similar to the results of Refs. [68,

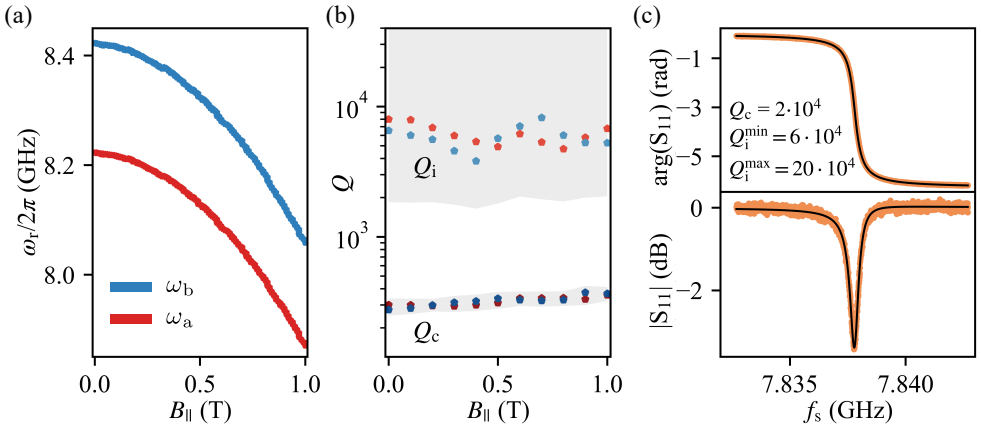

Figure 3.5: Dimer modes frequencies and quality factors $Q_{a,b}$ as a function of $B_{||}$. **(a)** Field dependence of the dimer frequencies $\omega_{a,b}$. For both modes we observe a tunability of 300 MHz. **(b)** Field dependence of the internal and external quality factors for single-photon population. Errors originating from Fano uncertainties [134] are depicted by the grey areas. Notably, Qi is at least one order of magnitude above Qc for the entire field range. **(c)** Single-tone spectroscopy of a sample with critical coupling Qi ≈ Qc. The data in panel (c) is adapted from [82].

75, 81], no additional losses are introduced in the dimer modes under the application of $B_{||}$, providing an initial evidence that the amplifier noise does not increase under in-plane magnetic fields. Notice, however, that due to the strong coupling required to operate the grAlPA as an amplifier, we can only place a lower bound for the Q_i [134]. To extract a more accurate estimation, we would need to decouple the resonators such that they become critically coupled (see Section 1.2.1). For reference, in Fig. 3.5(c) we show the resonant response of a critically coupled grAlPA previously measured by Ref [82]. They reported $Q_i = 9{\cdot}10^4$ with uncertainties $6{\cdot}10^4 < Q_i < 20{\cdot}10^4$, which is in the range of the quality factors measured with our current grAlPA.

We now turn our attention to the remaining circuit parameters: the self-Kerr coefficients $K_{L,R}$. To quantify them from the measurement data, we first derive a simplified expression for the Kerr-shifted dimer frequencies $\tilde{\omega}_{L,R}$ as a function of $K_{L,R}$. Note that the grAlPA used in our experiments shows almost perfect hybridization ($\omega_L \approx \omega_R$) (cf. Table 3.1). Due to the fact that the grAl central strips in both resonators are nominally identical, we can safely assume that $K_{L,R} = K$, such that the Kerr-shift of each mode can be written as (see Eq. (A1.22) for the general expression)

$$\tilde{\omega}_{a/b} = \omega_{a/b} + \frac{K}{2}\left(\bar{n}_a + \bar{n}_b\right), \tag{3.9}$$

where $\bar{n}_{a,b}$ are the photon number populations of the modes. If $\bar{n}_{a,b} \ll \kappa/K$ i.e. when the modes excitations are well bellow their bifurcation points, we can approximate $\bar{n}_{a,b} \approx 16P_{in}/\hbar\omega_{a,b}\kappa_{a,b}$, where P_{in} is the power calibrated at the grAlPA input (see Appendix C.4 for details about the power calibration). We calculate $\omega_{a,b}$ as a function of input power using single and two-tone spectroscopy measurements and fit the results with Eq. (3.9). The resulting fits are shown in Fig. 3.6(a), where we use the labels K_{ij} (i,j = a,b) for coefficients obtained while driving mode j and probing mode i. By averaging

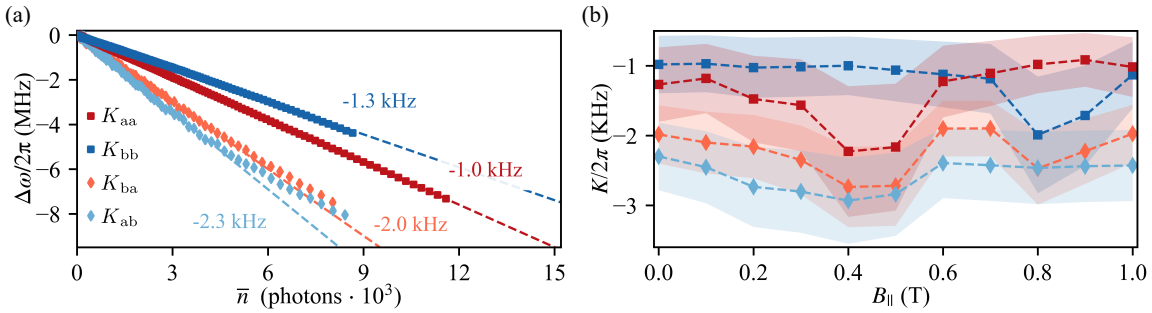

Figure 3.6: grAlPA Kerr coefficients. **(a)** Kerr-shift of the dimer mode frequencies as a function of their average photon number. The shift produced by the self-Kerr (K_{aa} and K_{bb}) and cross-Kerr (K_{ab} and K_{ba}) coefficients are measured through single-tone and two-tone spectroscopy, respectively. For photon populations below $\approx 4 \cdot 10^3$, the fruquency change follow the linear trend predicted by Eq. (3.9). Variations of K_{ab} and K_{ba} for higher powers are attributed to corrections of Eq. (3.9) **(b)** Dependence of Kerr coefficients with $B_{||}$. All coefficients remain within 1-3 kHz up to 1 T.

the measured self-Kerr coefficients, we obtain $K/2\pi = 1.65 \pm 2$ KHz, with the uncertainty dominated by the ± 2 dB error in the power calibration (see Appendix C.4). As expected, the frequencies follow the linear trend predicted by Eq. (3.9) at low photon populations. Deviations from this trend for powers above 4×10^3 photons are attributed to high-power corrections of the effective Kerr coefficients. Repeating the same procedure for increasing $B_{||}$, we obtain the results in Fig. 3.6(b), which demonstrate that the self-Kerr coefficients remain unchanged under field operation. According to Eq. (2.4), the field dependence of $\omega_{L,R}$ predicts a change of K with $B_{||}$. However, using the frequency shifts from Fig. 3.5(a), we estimate a maximum decrease of ≈ 0.1 KHz, a value below our measurement accuracy and therefore not observable.

We notice a factor of six disagreement between the measured Kerr coefficients and the initial estimates using the JJ-array model (see Section 3.3). One possible source of discrepancies come from the uncertainty in the estimation of grAl's critical current density j_c^{grAl}, obtained from Ref. [82]. These calculations interpolate a limited set of j_c^{grAl} vs resistivity points collected using DC measurements of grAl nano-SQUIDs (shown also in Fig. 2.1(c)), which can easily introduce factor of three uncertainties in j_c^{grAl} (see Supplementary Figure 6 in Ref. [65]). Nevertheless, we cannot rule out the possibility that intrinsic physical mechanisms could also contribute to these deviations. Following the discussion of Section 2.3, previous works on other kinetic inductance materials have shown similar differences between critical currents I_c measured with a DC setup and the characteristic current I_* dominating the nonlinearity of the material at microwave frequencies [54–56, 93]. In future experiments, we could compare the relation of I_c and I_* for grAl structures with different resistivities, by combining RF and DC measurements. This could provide a better model of grAl nonlinearities and provide new insights into the role of disorder in the nonlinearity of kinetic inductance materials.

3.5 Gain performance in zero field

Having characterized the circuit parameters of the grAlPA, we are now ready to check its performance as a non-degenerate amplifier. Following the discussions of Section 3.1, we apply a pump tone with frequency ω_p between the Kerr-shifted dimer modes. Given the negligible internal losses in the amplifier, we can calculate the amplifier gain as the ratio between the reflected power with the pump on and off. The resulting gain profiles are shown in Fig. 3.7(a) for different pump powers P_p. We report P_p as the power reaching the grAlPA input, taking the nominal attenuation of the microwave setup (see Fig. A2.1 in Appendix B.2). Remarkably, with our amplifiers we are able to achieve up to 30 dB non-degenerate gain before entering into the multistability regime (cf. Fig. 3.2). Moreover, the enhanced nonlinearity of grAl allows us to reach the ND gain regime with pump powers more than three orders of magnitude lower than in similar implementations based on NbN and NbTiN [224]. To extract the instantaneous bandwidth for each gain profile, we calculate their FWHM from Lorentzian fits, from which we obtain a constant GBW product $\sqrt{G_0} \cdot \mathrm{BW} = (\kappa/2)/2\pi = 22.5$ MHz (see right panel of Fig. 3.7(a)). This result agrees with the expected GBW scaling of Eq. (3.7) and the measured coupling rates $\kappa_{a/b}$ (cf. Table 3.1). Moreover, the pump tone is ~ 0.1 GHz detuned from the regions of high gain, as expected from the designed value of the hopping parameter J. The frequency shift of the gain curves with increasing pump power is due to the the Kerr-shift of the dimer modes. However, unlike $\tilde{\omega}_{a,b}$, which always move down in frequency when pumped in resonance, the gain curves must also obey the 4-wave mixing energy conservation equation $\omega_p = (\tilde{\omega}_a + \tilde{\omega}_b)/2$, which explains the splitting behavior visible in Fig. 3.7(a).

By varying ω_p and P_p, we can tune the grAlPA gain profiles. Fig. 3.7(b) illustrates the dependence of the maximum gain G_0 with P_p and f_p. Similar to Fig. 3.7(a), we calculate G_0 by performing Lorentzian fits to the gain curves. Regions with $G_0 \approx 20$ dB are marked by the white areas in Fig. 3.7(b), showing that they can be reached with various combinations of P_p and ω_p. Increasing the pump power further, pushes the amplifier to the MS region indicated with the grey area. If we recall from Section 3.2, MS is defined when the system sustains multiple solutions for the resonator's populations $n_{L,R}$. To accurately identify this region in our experiments, we should recreate grAlPA's phase space with the circuit parameters extracted in Section 3.4. However, since P_p at the grAlPA input is estimated from the nominal attenuation of the measurement setup, we expect a ± 5 dB uncertainty range in the estimation of α_{in}, which prevents a precise determination of the MS boundaries. Instead, we exploit the fact that in MS regime, and for high enough powers, the grAlPA exhibits transitions between its multiple metastable states. This manifests as additional peaks (or dips) in the gain profiles, which can be detected in our measurements (see Fig. 3.7(d)). Fig. 3.7(c) shows that by moving across the 20 dB region, we can tune the gain profile of each dimer mode by approximately 50 MHz. This feature of the grAlPA is particularly useful, as it serves as an in-situ tuning knob during experiments. We attribute the changes in the bandwidth to the frequency-dependent environmental impedance seen by the grAlPA, similar to effects reported in impedance-engineered parametric amplifiers [157].

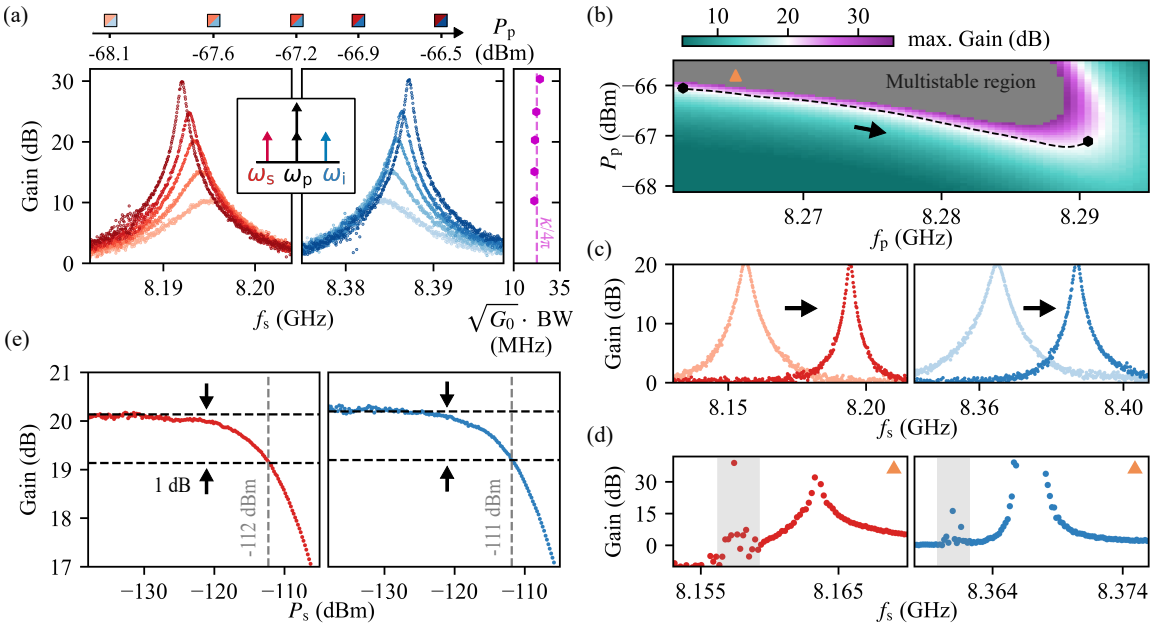

Figure 3.7: Gain performance in zero field. **(a)** GrAlPA gain profiles as a function of signal frequency f_s, for different pump powers P_p. The detuning between the pump frequency f_p = 8.29 GHz (not shown in the figure) and the regions of gain is ~ 0.1 GHz. The right panel presents the gain-bandwidth product of the grAlPA, which follows the relation $\sqrt{G_0} \cdot \text{BW} = (\kappa/2)/2\pi$ = 22.5 MHz. **(b)** Maximum gain G_0 as a function of the pump frequency and pump power. Regions with G_0 = 20 dB are highlighted by a white fringe, while the grey area represents the multistable regime. The gain profile of the grAlPA is tuned by moving the pump tone along the dashed black line, as shown in **(c)**. We achieve frequency tunability close to 50 MHz for each dimer mode. **(d)** Example of gain profiles measured in the MS region (see orange marker in panel (b)). Metastable states produce the appearance of additional gain peaks, as highlighted by the gray shaded areas. We use them to experimentally identify the MS region. **(e)** Saturation power measurements for the two modes of the grAlPA. We denote P_s as the signal power, calibrated at the grAlPA input plane. We indicate the 1-dB compression point with the lower horizontal dashed line and the grey labels indicate the corresponding signal power.

To quantify the dynamic range of the grAlPA we use the 1-dB compression point explained in Section 1.3.3, which is measured by varying the probe tone power (P_s) generated by the VNA. We calibrate P_s using the resonance fluorescence of a transmon qubit operating in the same frequency range as our amplifier (see Appendix C.4). The results in Fig. 3.7(e) present the measured 1-dB compression points for a low power gain of G_0 = 20 dB. We obtain saturation values of -111±2 dBm for both modes, similar to previous implementations using arrays of Josephson junctions [21, 22, 152, 225] and sufficient to perform readout with signal powers corresponding to hundreds of circulating photons [150]. Repeating the measurements for different G_0, allows us to determine the scaling of the 1-dB compression point, as shown in Fig. 3.8. We observe a linear scaling of the saturation power with increasing gain, as expected from a Kerr-based amplifier (cf. Eq. (1.55)).

Comparing to the dynamic range of state-of-the-art amplifiers ($\gtrsim$ 90 dBm for G_0 ≈20 dB) [26, 50, 55, 56], the grAlPA shows at least two orders of magnitude lower compression points. Being a 4-wave mixing amplifier, grAlPA's dynamic range is limited by the Kerr-shift of its modes (cf. Eq. (1.55)) and could be improved by decreasing the range of the self-Kerr

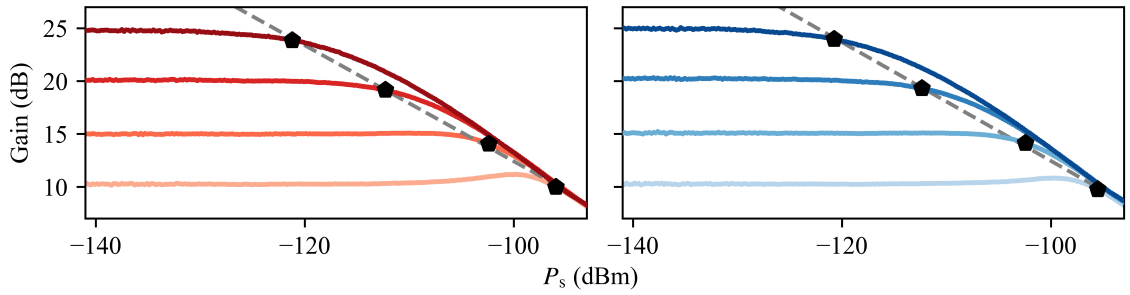

Figure 3.8: Saturation power scaling with maximum gain G_0. Saturation power measurements for G_0 = 10, 15, 20 and 30 dB for each dimer mode. The 1 dB compression points are denoted by the black markers. They follow a linear trend with increasing G_0, as predicted in Eq. (1.55) and illustrated by the gray dashed line. The small "bump" shown in the G_0 = 10 dB for input powers close to -100 dBm is attributed to the system reaching MS (cf. Fig. 3.7(b)).

coefficients $K_{L,R}$ or by designing stronger couplings κ. In practice, lower values of $K_{L,R}$ could be achieved by increasing the aspect ratio of the microstrip of each grAl resonator (see Fig. 3.3). A factor of two increase in its length and decrease in its width, would imply a fourfold improvement in the dynamical range. Moreover, a factor of ten improvement can also be accomplished by optimizing κ using for example an interdigitated coupling between the grAl resonators and the Nb coupling pad. Together, both solutions could increase the saturation power to ranges reported in Refs.[26, 50, 55, 56]. It is important to notice however, that such strategy comes at the cost of needing higher pump powers to reach 20 dB gain levels, which increases the heat load at the mixing chamber of the cryostat.

3.6 Gain performance under in-plane magnetic field

In this section, we present one of the main results of this work: the capability of the grAlPA to provide non-degenerate 20 dB gain for in-plane fields up 1 T. The measured gain profiles are shown in Fig. 3.9(a) for increasing values of in-plane magnetic field $B_{||}$. Due to the field dependence of the dimer modes (see Fig. 3.5(a)), the pump frequencies need to be adjusted for each field bias, as illustrated by the black arrows in Fig. 3.9(a). As the hopping parameter J varies by less than 10% with $B_{||}$, the signal-pump detuning remain approximately constant in the entire field range. Similarly, thanks to the negligible change in κ and the Kerr coefficient K, the pump power also remains approximately independent of $B_{||}$ and at ≈ -67 dBm. Employing Lorentzian fits to the gain profiles, we extract the change in GBW product as a function of $B_{||}$. As shown in the right-hand panel of Fig. 3.9(a), the GBW decreases by approximately 20%, in agreement with the change in κ shown in Fig. 3.4(b).

In Fig. 3.9(b) and (c) we present the gain curves and saturation power measurements for $B_{||}$ = 1 T. Remarkably, the gain performance at $B_{||}$ = 1 T remains almost unchanged compared to $B_{||}$ = 0 T. The small shoulder visible in the lineshape of the high frequency

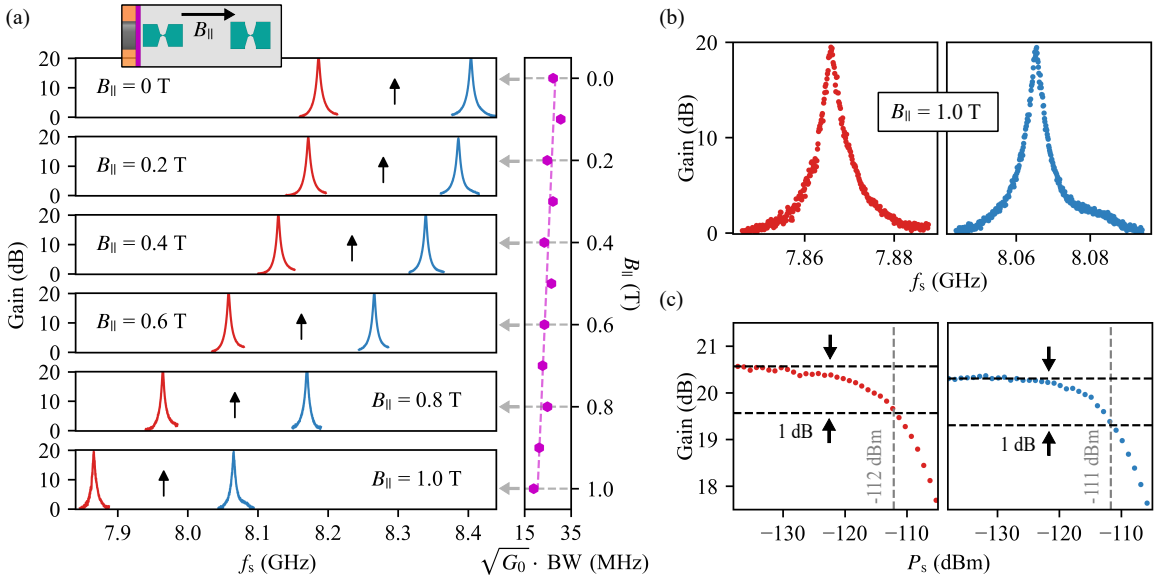

Figure 3.9: Gain performance under in-plane magnetic fields $B_{||}$. **(a)** Measured gain profiles at magnetic fields $B_{||}$ = 0, 0.2, 0.4, 0.6, 0.8, and 1.0 T. The schematics depicts the direction of the magentic field and the black arrows indicate the frequency of the pump. The right panel depicts the field dependence of the gain-bandwidth product. The observed trend is explained by the gradual decoupling of the grAlPA as the frequencies of the modes move away from the cut-off of the cylindrical waveguide in Fig. 3.3(a). Values of $\kappa/2$ measured from single-tone spectroscopy with the pump off (cf. Fig. 3.4(b)), are depicted by the dashed line. **(b)** Gain of the grAlPA at $B_{||}$ = 1 T. The shoulder visible in the gain profile of the high frequency mode originates from an imperfection in our definition of gain, as shown by Fig. 3.10. **(c)** Saturation power measurements for the two modes of the grAlPA at $B_{||}$ = 1 T. We indicate the 1-dB compression point with the lower horizontal dashed line and the grey labels indicate the corresponding signal power.

mode, originates from an artifact on our definition of gain. This effect is clearly visible in the comparison of the raw reflection amplitude $|S_{11}|$ when the pump is on and off (see Fig. 3.10). In the undriven case, we note a 1 dB dip appearing near the resonance frequency, arising from residual internal losses. This effect is less pronounced at lower magnetic fields due to the larger frequency detuning between the gain profiles and the low-power resonance of the dimer modes. When the pump is on, $|S_{11}|$ returns to a Lorentzian shape.

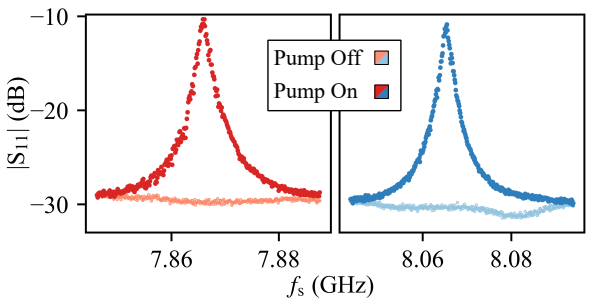

Figure 3.10: grAlPA reflection at $B_{||}$ = 1 T. Measured reflection amplitude $|S_{11}|$ close to each mode of the grAlPA, with the pump off (light blue and red lines) and on (dark red and blue lines). When the pump is on, the lineshape follows the expected Lorentzian gain profile. When the pump is off, we observe a dip at the resonance of the high frequency mode (light blue line on the right panel), which explains the additional shoulder seen in the gain profile presented in Fig. 3.9(b).

Testing the grAlPA gain performance above 1 T was not possible due to the limited range of the vector magnet in our setup. However, results reported for grAl resonators with thicknesses comparable to the grAlPA suggest that we could generate stable amplification up to ≈ 2 T [69, 75]. One approach to further increase in-plane resilience is to reduce the film thickness to approximately 20 nm. This modification could extend the operational field up to 3 T [68, 75, 81], fully meeting the requirements of most applications demanding 20 dB gain at microwave frequencies and strong resilience along one direction like in Refs. [38, 42, 226, 227].

3.7 Gain performance under out-of-plane magnetic field

Having demonstrated the successful operation of the grAlPA under in-plane magnetic fields, an important question arises: how well does it perform under out-of-plane magnetic fields $B_\perp$? Designing an amplifier with high resilience in all directions is particularly attractive, as it eliminates the need for precise alignment of the magnetic field. As discussed in Section 1.3.3, achieving out-of-plane resilience strongly depends on the sample geometry, and experimentally, one can expect to reach fields up to ~30 mT [166, 167]. Although this is smaller than the in-plane resilience, such levels are sufficient for applications like the readout of spin [33–35] or Andreev qubits [36, 37], which can highly profit form the use of the grAlPA.

In Fig. 3.11(a) we present an example of the gain performance of our amplifier with $B_\perp$ up to 22 mT. We use a grAlPA different to the one used in Fig. 3.9, but fabricated from a grAl film with the same resistivity and thickness. The main difference is a 16% increase in the capacitor plates of the grAl resonators (cf. Fig. 3.3(c)), which results in a 8% reduction of the dimer frequencies. Using this amplifier, we obtain 20 dB ND gain up to $B_\perp$ = 22 mT. However, during the experiment, we observed fluctuations of the gain profiles for out-of-plane fields as low as 20 μT. Moreover, all the gain curves were highly unstable and disappeared within a few minutes.

To investigate the mechanisms behind these effects, we heated the device above grAl's critical temperature ($T_c \approx 2$ K) and then cooled it back to ~ 20 mK without an applied field. We subsequently measured the dependence of the undriven dimer frequencies with $B_\perp$. Fig. 3.11(b) shows the result of an initial sweep with $B_\perp$ increasing from 0 mT to 22 mT. In contrast to the monotonic shifts under $B_{||}$ (cf. Fig. 3.5(a)), the application of an out-of-plane field results in a noisy spectrum across the entire field range. This effect can be traced back to the trapping of unwanted flux vortices within the resonator capacitor pads. Following the analysis of Ref. [164], above a threshold field $B_\perp^{\text{th}}$, the capacitor pads can develop instabilities known as magnetic flux avalanches, which consist in the penetration of a large number of vortices close to a defect or weak spot in the superconducting film. These avalanches generate local fluctuations in the magnetic field, causing drastic variations in the resonator inductances and, consequently, the noisy behavior of their frequencies. Once the vortices penetrate the pads, persistent current prevents their removal by simply

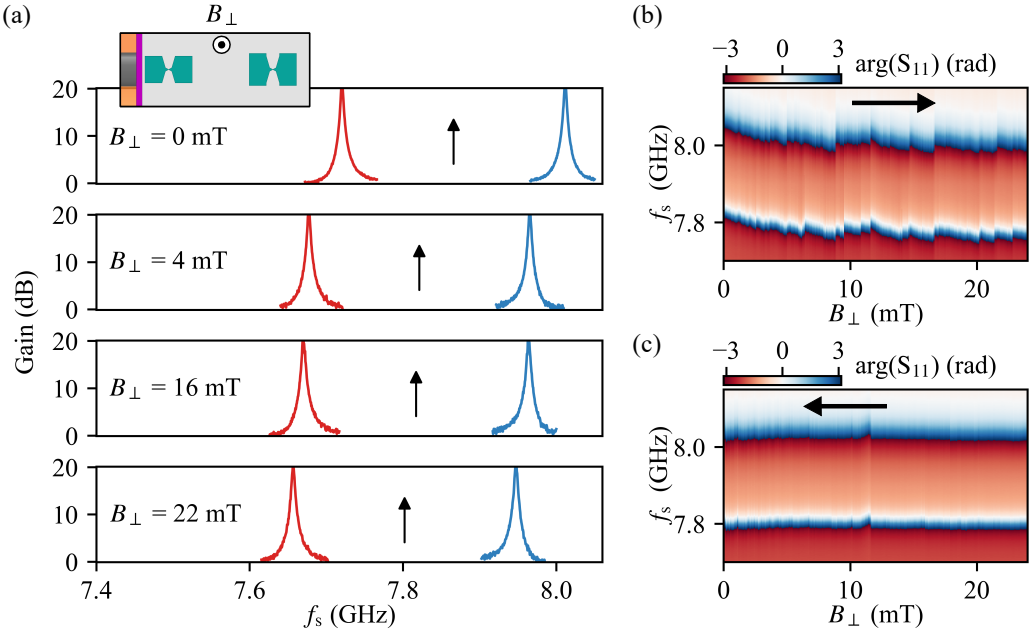

Figure 3.11: Gain performance under out-of-plane magnetic fields $B_\perp$. (a) Measured gain profiles at magnetic fields $B_\perp$ = 0, 4, 16, and 22.0 mT. The schematics depicts the direction of the magentic field and the black arrows indicate the frequency of the pump. **(b)-(c)** Single-tone spectroscopy measurements of the unpumped grAlPA for increasing and decreasing $B_\perp$, respectively. The black arrows show the directions of the field scans. Jumps of the spectrum are caused by the trapping of vortices within the capacitor plates of the grAl resonators. The hysteretic behavior is attributed to the pinning energy of the vortices.

reducing the field back to zero, therefore producing a hysteretic behavior in the resonator spectrum similar to the plot presented in Fig. 3.11(c).

An improvement of the out-of-plane resilience of the grAlPA can be accomplished by reducing the dimensions of the capacitor pads. From Eq. (1.58) and the results shown by Refs. [68, 228], we deduce that $B_\perp^{\text{th}}$ can increase from 20 µT to 1 mT by reducing the pads widths to ~ 10 µm. However, such design will come with a limitation, as the new capacitor pads also reduce the total coupling κ if we use the same setup shown in Fig. 3.3(a). Stronger couplings could be achieved with a 2D architecture, without the need for large capacitor pads. A complementary strategy consist of adding artificial pinning sites, to trap most of the vortices generated during an avalanche and therefore preventing spurious variations in the field distribution. This approach has proven to increase the $B_\perp$ resilience of large superconducting structures to 30 mT [166, 167]. Implementing these improvements would allow the grAlPA to be used directly for the readout of semiconductor spin qubits, without requiring additional alignment of the magnetic field.

3.8 Noise performance under in-plane magnetic field

We now turn our attention to the most important figure of merit of the grAlPA: its ability to improve the signal-to-noise ratio (SNR) of a readout chain. For this purpose one needs

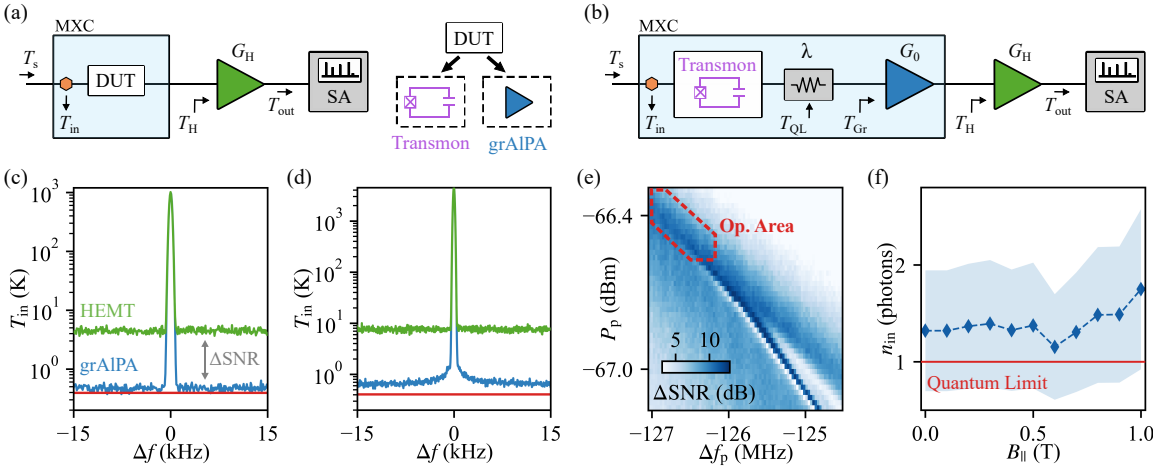

Figure 3.12: Noise performance under in-plane magnetic fields $B_{||}$. **(a)-(b)** Schematics of the setups employed to measure the SNR and input referred noise temperature T_{in} of the readout chain containing the grAlPA. We calibrate the input-line attenuation and incoming noise level T_{s} at the orange marker, using the resonance fluorescence of a flux-tunable transmon qubit. In the method of panel (a), the transmon qubit and the grAlPA are measured in separate cooldowns. The signal coming from the device under test (DUT) is amplified by a chain with a HEMT amplifier (green) as the first stage, and the total output power and noise T_{out} is measured outside the cryostat using a Spectrum Analyzer (SA). We denote G_{H} and T_{H}, as the gain and noise of the HEMT. In panel (b), we show an alternative method, where the qubit and the grAlPA are connected in the same cooldown. Here, λ denotes the insertion loss of the connections. The attenuator noise is at the quantum limit $T_{\text{QL}} \approx 400$ mK. **(c)-(d)** Input-referred noise temperature T_{in} measured at $B_{||} = 0$ T and using the method of panel (a)-(b), respectively. We plot T_{in} as a function of the detuning Δf from a power-calibrated pilot tone at $f_{\text{s}} = 8.193$ GHz. The green and blue solid lines represent measurements with the grAlPA pump off and on, respectively. When the grAlPA is off, the noise is mainly dominated by the HEMT amplifier. By driving the grAlPA, the noise approaches the standard quantum limit indicated by the solid red line. The SNR improvement (ΔSNR) is extracted from the ratio between the baselines of the green and blue curves. **(e)** ΔSNR as a function of pump power and signal-pump detuning Δf_{p}, while having the pilot tone fixed. The red countour line depicts the operational area of the grAlPA. **(c)** Input-referred noise as a function of in-plane magnetic field $B_{||}$. The quantum-limit is depicted by the red line. The blue area indicates the uncertainty propagated from the power calibration.

to measure the noise added by the amplifier. There are multiple techniques that we can use for this task, as detailed in Appendix C. Here, we employ the power calibration obtained from the resonance fluorescence of a flux-tunable transmon qubit, designed to fit the same waveguide used for the grAlPA. We then use SNR improvement measurements to extract the noise of our amplifier. As this might not be familiar to all readers, we use the next paragraph to briefly describe this technique.

The schematics of the experiment is shown in Fig. 3.12(a)-(b). A monochromatic pilot tone with power P_{s} and calibrated at the grAlPA input, is applied at a frequency f_{s}, close to one of the peaks of the gain profiles. Then, we measure the power spectral density (PSD) of the entire amplification chain by connecting a Spectrum Analyzer (SA) at its output. In contrast to the VNA, which measures scattering coefficients, the SA detects the absolute power at the output of the cryostat, within a frequency window defined by its Resolution Bandwidth (RBW). By keeping the RBW much smaller than the instantaneous bandwidth

of the amplifier, the total power measured at f_s with the grAlPA pump on and off is given by

$$\begin{aligned} P_{\text{out}}^{\text{off}} &= G_{\text{H}} P_{\text{s}} \\ P_{\text{out}}^{\text{on}} &= G_{\text{H}} G_0 P_{\text{s}}, \end{aligned} \tag{3.10}$$

where G_0 is the grAlPA gain and G_{H} is the gain of the remaining amplification chain with a HEMT connected after the grAlPA (see Fig. 3.12(a)-(b)). Similarly, at frequencies different to f_{s}, but within the RBW, the SA will detect a noise floor N_{out} given by

$$\begin{aligned} N_{\text{out}}^{\text{off}} &= G_{\text{H}} \left(N_{\text{s}} + N_{\text{H}}\right) \\ N_{\text{out}}^{\text{on}} &= G_{\text{H}} \left(G_0 \left(N_{\text{s}} + N_{\text{gr}}\right) + N_{\text{H}}\right), \end{aligned} \tag{3.11}$$

where N_{s} is the noise accompanying the pilot tone, N_{gr} is the noise added by the grAlPA, and N_{H} is the noise of the HEMT. Therefore, from the input power P_{s}, we can calculate G_{H} and G_0 with Eq. (3.10). Knowing both values, we can then use Eq. (3.11) to calculate the noise of the HEMT and the grAlPA, from the measurements of $N_{\text{out}}^{\text{on/off}}$. It is worth emphasizing that employing this technique is only possible because we have a reliable calibration of the input power P_{s}. Any uncertainty in this quantity propagates directly into the extracted HEMT and grAlPA noise. If one attempts to determine N_{gr} or N_{H} using only the nominal attenuation of the cryostat, the resulting uncertainties would likely give unphysical results. Therefore, accurately reporting the noise performance of the amplification chain requires careful and precise calibration of P_{s}.

Once we have extracted the noise and gain of the grAlPA, we can extract the SNR of the amplification chain using the formula SNR = $P_{\text{s}}/N_{\text{in}}^{\text{on/off}}$. The quantity $N_{\text{in}}^{\text{on/off}}$ is the input-referred noise, which is given by $N_{\text{in}}^{\text{on}} = N_{\text{out}}^{\text{on}}/G_0 G_{\text{H}}$ when the grAlPA is on and by $N_{\text{in}}^{\text{off}} = N_{\text{out}}^{\text{off}}/G_{\text{H}}$ when its off. From the definition of SNR, we can now also quantify how much SNR improvement (ΔSNR = $\text{SNR}_{\text{on}}/\text{SNR}_{\text{off}}$) the grAlPA provides. From Eq. (3.10) and Eq. (3.11) we can obtain an analytical expression for ΔSNR as a function of the chain parameters:

$$\Delta\text{SNR} = \frac{N_{\text{s}} + N_{\text{H}}}{N_{\text{s}} + N_{\text{gr}} + N_{\text{H}}/G_0}. \tag{3.12}$$

We measure the noise added and ΔSNR provided by the grAlPA with two different methods. In the first one, we perform the power calibration using the transmon qubit and then, in a subsequent cooldown and employing the same setup, we replace the transmon with the grAlPA to measure its added noise (see Fig. 3.12(a)). This method removes the ambiguity in the estimation of the insertion loss λ between the qubit and the amplifier, but cannot account for possible cooldown-dependent variations of the line attenuation. Therefore, we complement the measurements using a second method, as depicted in Fig. 3.12(b). Here, the transmon is connected in the same cooldown as the grAlPA, which enables the

in-situ calibration of the input power P_s. Figs. 3.12(c) and (d) show the outcome of the measurements with the two methods. We report the results in units of input refereed noise temperature $T_{in} = N_{in}/(k_B \, \mathrm{RBW})$, where k_B is the Boltzmann constant. When the grAlPA is off, the noise floor is about 4 K, close to the nominal noise of the HEMT [143]. When the grAlPA is on, we obtain 10 dB of SNR improvement and a noise floor approaching the standard quantum limit of phase preserving amplifiers [14]. During the experiments, we tuned the amplifier to provide a maximum gain of $G_0 = 20$ dB.

We now quantify the susceptibility of ΔSNR to fluctuations in the pump power and frequency. This analysis allows us to ensure that variations in the pumping conditions do not lead to suboptimal operation. The results are shown in Fig. 3.12(e). We define the operational region of the amplifier as the set of pump powers and frequencies that yield a stable $\Delta\mathrm{SNR} \geq 10$ dB, highlighted by the red contour. Deviations in the pump parameters can drive the grAlPA into the MS region, giving rise to the discontinuities visible in Fig. 3.12(e). For our device, we find that the SNR remains stable for pump-frequency variations of up to approximately 2 MHz.

To finish this section, we show in Fig. 3.12(f) the near-quantum limited noise performance of the grAlPA under in-plane magnetic fields up to $B_{||} = 1$ T. We measured the data using the setup shown in Fig. 3.12(a). For each $B_{||}$, we fix the gain of the amplifier to $G_0 = 20$ dB and tune the power-calibrated pilot tone to match the shift of the gain profiles in field. We report the input referred noise n_{in} in units of photons, calculated using the relation

$$n_{in} = k_B \overline{T}_{in}/hf_s, \tag{3.13}$$

where $\overline{T}_{in}$ is the noise floor extracted from the SNR measurements with the grAlPA on. In these units, the quantum limit is given by $n_{in} = 1$, with half a photon coming from vacuum fluctuations and half a photon of added noise from the amplifier. Remarkably, the grAlPA remains near quantum-limited up to $B_{||} = 1$ T, illustrating its utility for low-noise quantum readout in magnetic field. We attribute the small upturn visible above 0.6 T to vortices trapped in the capacitor pads.

3.9 Single-shot readout of a superconducting qubit

We have shown in the preceding sections the outstanding metrics of the grAlPA. But, how about its performance when is used in the readout of an actual quantum system? To demonstrate the grAlPA's applicability in quantum device readout, we connect a Generalized Flux Qubit (GFQ) in a cQED setup, as shown in Fig. 3.13(a) (see Appendix B.2 for a detailed description of the setup). The qubit is coupled to a readout resonator with linewidth $\kappa_r/2\pi = 1.25$ MHz and frequency $f_r = 8.1361$ GHz (for more details see device q8 in Ref. [74]). We then use the grAlPA to perform single-shot heterodyne detection of the GFQ quantum states.

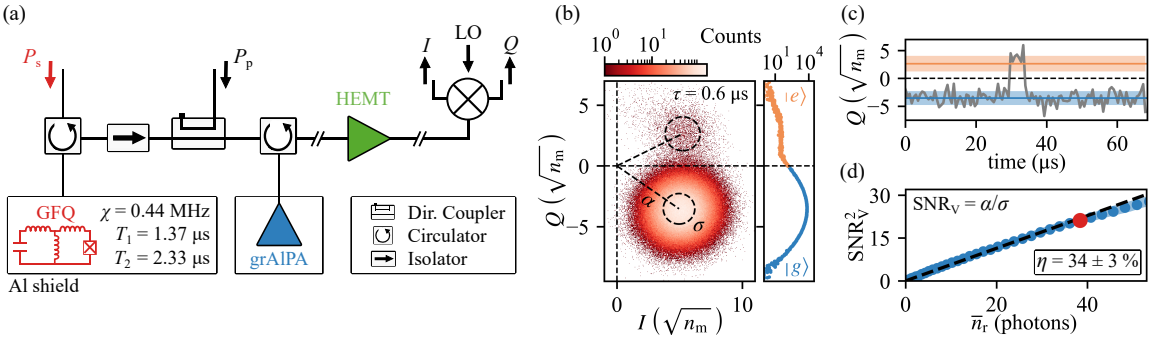

Figure 3.13: Qubit readout and quantum efficient extraction. **(a)** Qubit setup used to measure grAlPA quantum efficiency η. We use a Generalized Flux Qubit (GFQ) with coherence times $T_1 = 1.37$ µs, $T_2 = 2.33$ µs and qubit-resonator dispersive shift $\chi = 0.44 \pm 0.04$ MHz [74]. The GFQ and the grAlPA are mounted inside aluminum shields to minimize the impact of stray magnetic fields. The grAlPA pump tone is coupled via a directional coupler installed at the cryostat's mixing chamber. To prevent pump leakage into the qubit frequency band, an additional isolator is placed between the GFQ and the grAlPA. A probe tone with power P_s populates the readout resonator, and the resulting signal is amplified through a chain with the grAlPA and a HEMT as its first two stages. The output signal is then demodulated into its IQ quadratures using a mixer and a local oscillator (LO) detuned by 90 MHz above the GFQ readout resonator frequency. **(b)** IQ histogram of contiguous measurements acquired while the grAlPA provides a maximum gain of $G_0 = 25$ dB. The I and Q quadratures are scaled in units of square root of measurements photons $\sqrt{n_m} = \sqrt{\bar{n}_r \tau \kappa_r / 4}$, where $\kappa_r/2\pi = 1.25$ MHz, $\bar{n}_r = 39$ photons and $\tau = 0.6$ µs. The plot on the right panel illustrate the qubit distributions corresponding to the ground $|g\rangle$ and excited $|e\rangle$ state. **(c)** Example of a quantum-jump trace acquired while driving the grAlPA. The solid lines correspond to the ground (blue) and excited (orange) states of the qubit and the shaded regions depict one standard deviation σ obtained from the IQ-clouds in (b). **(d)** SNR_V^2 as a function of readout strength $\bar{n}_r$. The black dashed line depicts a linear fit of the data, form which we extract $\eta = 34 \pm 3$ %. The red dot represents the value of $\bar{n}_r$ used for the measurements in panels (b) and (c).

In Fig. 3.13(b) we present a histogram of 8×10^5 contiguous measurements using a readout pulse with length $\tau = 0.6$ µs and power equivalent to $\bar{n}_r = 31$ circulating photons in the resonator. The data was taken with the qubit flux-biased at its sweet spot, where it shows energy-relaxation and dephasing times of $T_1 = 1.37$ µs and $T_2^* = 2.33$ µs, respectively. The readout pulse was calibrated using the AC stark shift and measurement-induced dephasing of the GFQ (see Appendix C.3). As observed in the left panel of Fig. 3.13(b), the distribution shows two maxima corresponding to the ground ($|g\rangle$) and first excited ($|e\rangle$) states of the qubit. In Fig. 3.13(c), we also show an example of a typical quantum-jump experiment where we can clearly discriminate the qubit state within $\tau = 0.6$ µs (the length of the readout pulse), an achievement enabled only by the use of the grAlPA. From this data, we can extract a qubit temperature of $T_q = 56$ mK using formula

$$T_q = \frac{2\pi\hbar f_q}{k_B \ln\left(N_g/N_e\right)}, \tag{3.14}$$

where $N_{g,e}$ are qubit ground and first excited state populations and $f_q = 6.0195$ GHz its frequency. We neglect the contributions of higher-energy states as they account for less than 0.01% of the qubit excitations. The measured qubit temperature is slightly higher than the nominal value at the cryostat mixing chamber ($T_{MXC} \approx 20$ mK), which is attributed to non-equilibrium processes changing the qubit's thermal population [229].

We can also use the GFQ to extract the so-called readout quantum efficiency η. For this purpose, we measure the power dependence of the quadrature $\mathrm{SNR_V}$, which is defined[6] as the ratio between the magnitude α of the $|g\rangle$ pointer state and its standard deviation σ (cf. Fig. 3.13(a)). Following Refs. [28, 150], the quadrature SNR can be quantified by.

$$\mathrm{SNR_V^2} = \frac{\eta \overline{n}_\mathrm{r} \kappa_\mathrm{r} B^{-1}}{4}, \tag{3.15}$$

where $B^{-1} = 2/\kappa_\mathrm{r} + \tau$ is the measurement bandwidth and η the readout quantum efficiency. The latter quantity is related to the input referred noise photons n_in by the formula

$$\eta = \frac{n_\mathrm{in}^\mathrm{QL}}{n_\mathrm{in}}, \tag{3.16}$$

where $n_\mathrm{in}^\mathrm{QL}$ is the noise of an ideal quantum-limited readout chain. It takes the value of $n_\mathrm{in}^\mathrm{QL} = 0.5$ and $n_\mathrm{in}^\mathrm{QL} = 1$ for degenerate and non-degenerate amplifiers, respectively. In cf. Fig. 3.13(d), we present the measured and fitted $\mathrm{SNR_V}$ vs $\overline{n}_\mathrm{r}$, from which we calculate $\eta = 43 \pm 9\%$, on par with other readout chains using parametric amplifiers [145, 150]. The error range comes from the propagation of the uncertainty in the power calibration.

3.10 Budgeting the grAlPA quantum efficiency

The readout quantum efficiency η estimated in the previous section is calibrated at the input of the GFQ readout resonator. To calculate the contribution of the grAlPA added noise on η, we need to account for the different noise sources along the entire readout chain. In out setup, we identify four main contributions:

- η_r: related to added noise due to the internal losses of the GFQ readout resonator.
- η_IL: an efficiency which accounts for the insertion loss between the GFQ and the grAlPA.
- η_H: an efficiency related to the input referred noise of the HEMT, scaled by the grAlPA gain.
- η_gr: the intrisic quantum efficiency of the grAlPA, limited by internal losses and unwanted higher-order mixing processes.

Together, their product should equal to the measured readout quantum efficiency i.e. $\eta = \eta_\mathrm{r} \cdot \eta_\mathrm{IL} \cdot \eta_\mathrm{H} \cdot \eta_\mathrm{gr}$. In the following, we extract an estimation of these efficiencies based on the measurements presented throughout the chapter.

The noise at the output of a lossless readout resonator coupled to the GFQ is given by vacuum fluctuations T_QL. The coupling to internal loss channels generates an additional

[6] We can use $\mathrm{SNR_V}$ to calculate the power SNR, as defined in Section 3.8, using the formula $\mathrm{SNR}=\mathrm{SNR_V^2}$.

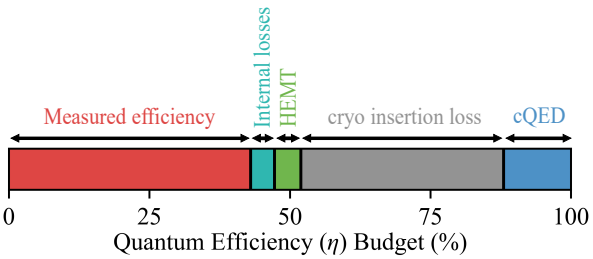

Figure 3.14: grAlPA quantum efficiency budget. We identify four contributions that reduce the readout quantum efficiency in our measurements: losses of the readout resonator in the cQED setup (blue), insertion loss in the microwave connections between the grAlPA and the cQED setup (grey), residual input-referred noise of the HEMT (green), and internal losses of the grAlPA resonators (turquoise). The red area represents the measured readout efficiency.

noise factor given by $T_r = T_{QL}\,(\gamma_r/\kappa_r)$ [82], where $\gamma_r/2\pi$ = 0.17 MHz, $\kappa_r/2\pi$ = 1.25 MHz are the resonator internal and external loss rates, respectively. In our case, the quantum efficiency at the output of the resonator is $\eta_r = T_{QL}/\left(T_{QL} + T_r\right)$ = 0.88.

We calculate η_{IL}, by modeling the losses between the grAlPA and the qubit as an effective attenuator thermalized to the mixing chamber of the cryostat, as shown in the sketch in Fig. 3.12(b). The non-zero insertion loss λ increases the noise at the output of the attenuator to $T_{IL} = \lambda T_{QL} + (1-\lambda)T_\lambda$, where T_λ is its Johnson–Nyquist noise temperature (see Appendix B.7). We use the nominal attenuation λ = -2.3 dB (see Appendix B.2) to compute $\eta_{IL} = \lambda T_{QL}/T_{IL} = 0.59 \pm 0.04$. The error corresponds to ± 0.5 dB uncertainty in the insertion loss coming from ripples in the transmission of the wiring.

The noise of the HEMT amplifier, referred to the GFQ resonator input, is given by $T_H/\lambda \cdot G_0$. In the ideal case, this contribution should be negligible and the noise should be given by the sum of vacuum fluctuations and the grAlPA quantum-limited noise ($2T_{QL}$). We extract T_H from the noise floor of the PSD shown in Fig. 3.12(d), while having the grAlPA pump off. Then, we use the relation $\eta_H = 2T_{QL}/\left(2T_{QL} + T_H/\lambda \cdot G_0\right)$ to calculate η_H = 0.91.

Combining the different contributions, we extract an intrinsic grAlPA quantum efficiency of $\eta_{gr} = 92^{+8}_{-22}\%$. Using the formula in Eq. (1.52), we calculate n_{gr} = 0.54 ± 0.13 grAlPA added noise photons, only 8% above the quantum limit at n_{QL} = 0.5. This reduction can be explained by internal losses of the dimer modes, which contribute to an additional noise factor $T_{\gamma_\pm} = T_{QL}\,(\gamma_+/\kappa_+) + T_{QL}\,(\gamma_-/\kappa_-)$ [82]. We estimate κ_- = 19.4 ± 4.1 MHz, $\gamma_- = 0.3^{+4.1}_{-0.3}$ MHz, $\kappa_+ = 25.0^{+4.9}_{-5.9}$ MHz and $\gamma_+ = 2.0^{+5.3}_{-2.0}$ MHz from single-tone spectroscopy measurements of the grAlPA. We take the errors originating from the Fano uncertainty of the measurements [134]. Then, we calculate $\eta_{\gamma_\pm} = T_{QL}/\left(T_{QL} + T_{\gamma_\pm}\right) = 0.91^{+0.09}_{-0.25}$, which confirms that internal losses might account for the ≈ 8% reduction in the grAlPA intrinsic quantum efficiency η_{gr} and should be improved in future designs. In Fig. 3.14, we illustrate a summary of the contributions that limit our readout quantum efficiency.

We can now compare the noise performance of the grAlPA obtained with the three different power calibrations used in this chapter: (I) fluorescence of a transmon qubit measured in separate cooldowns , (II) fluorescence of a transmon qubit measured in the same cooldown and (III) AC stark shift of a GFQ. We use the total measurement efficiency η, intrinsic grAlPA quantum efficiency η_{gr} and the amount of added noise photons n_{gr} as the metrics.

Table 3.2: Comparison of grAlPA added noise for three different power calibrations. (I) fluorescence of a transmon qubit measured in separate cooldowns, (II) fluorescence of a transmon qubit measured in the same cooldown and (III) AC stark shift of a GFQ. The uncertainty of the quantum efficiency is upper bounded to 100%.

	Power calibration method			
	(I) at $B_{\|\|}$ = 0 T	(I) at $B_{\|\|}$ = 1 T	(II)	(III)
η (%)	76^{+24}_{-36}	57 ± 27	62 ± 14	43 ± 9
η_{gr} (%)	70^{+30}_{-62}	46 ± 35	94^{+6}_{-71}	92^{+8}_{-22}
n_{gr}	0.71 ± 0.63	1.08 ± 0.83	0.53 ± 0.40	0.54 ± 0.13

For experiments with the transmon qubit measured in different cooldowns (cf. Fig. 3.12(a)) we calculate n_{gr}, with the formula

$$n_{\mathrm{gr}} = n_{\mathrm{in}} - n_{\mathrm{QL}} - \frac{n_{\mathrm{H}}}{G_0}, \tag{3.17}$$

where G_0 = 20 dB is the gain of the grAlPA and n_{H} the added noise of the HEMT. The latter quantity can be computed using the relation $n_{\mathrm{H}} = k_{\mathrm{B}}\overline{T}_{\mathrm{H}}/hf_{\mathrm{s}}$, where $\overline{T}_{\mathrm{H}}$ is the noise temperature floor extracted from the pump-off PSD in Fig. 3.12(c) and f_{s} the frequency of the power-calibrated pilot tone. For method (II) (cf. Fig. 3.12(b)), we use an attenuator model (see Appendix B.7) to account for the losses between the qubit and grAlPA and derive the relation

$$n_{\mathrm{in}} = n_{\mathrm{s}} + \left(\frac{1-\lambda}{\lambda}\right) n_{\mathrm{QL}} + \frac{n_{\mathrm{gr}}}{\lambda} + \frac{n_{\mathrm{H}}}{\lambda G_0}, \tag{3.18}$$

where $n_{\mathrm{s}} = n_{\mathrm{QL}}$ = 0.5 is the noise accompanying the pilot tone in units of photons and λ = -1.5 dB is estimated from the insertion loss of the microwave components (see Fig. A2.1). Similar to method (I), we calculate n_{H} from the pump-off PSD measurements in Fig. 3.12(d) and extract η_{gr} using Eq. (1.52). The results of all the calculations are summarized in Table 3.2. We find that method (III) provides the most accurate noise calibration. Nevertheless, within their respective uncertainties, all methods indicate the same conclusion: incorporating the grAlPA in the readout chain brings the input-referred noise to less than 50% from the quantum limit.

4 Doubled-pumped Granular Aluminum Amplifier: beyond the gain-bandwidth limit

This chapter presents another advantage achievable with the grAlPA: the realization of a standing-wave parametric amplifier that exhibits a non-conventional GBW limit. By applying two pump tones to the grAlPA, we simultaneously activate frequency-conversion and parametric-amplification processes. When these interactions are optimally imbalanced, they provide dynamical stability to the system, enabling the amplifier to surpass the GBW constraint typical of JPAs. Thanks to the reduced higher-order nonlinearities and negligible self-capacitance of grAl, we demonstrate a sixfold bandwidth broadening at 20 dB gain, with improved BW scaling and near-quantum-limited noise performance up to 25 dB. The results presented in this chapter are adapted from Ref. [230] and were carried out in collaboration with Anja Metelmann and Najmeh Etehadi Abari who developed the theoretical framework.

Standing-wave parametric amplifiers, such as the grAlPA, have become the preferred choice for experiments demanding noise performance within half a photon of the quantum limit. Their main advantage lies in the ability to achieve high gain and near-quantum-limited noise performance while allowing for flexible circuit design and fabrication. However, standing-wave amplifiers must operate close to an instability point, which inherently imposes a GBW tradeoff, as shown for example in Fig. 3.7(a). In practice, their operational bandwidth is typically restricted to a few tens of MHz for the gain levels required for the readout of quantum system. This restriction limits their applicability in systems requiring bandwidths approaching the GHz range, such as frequency-multiplexed qubit readout [46–48, 154], broadband quantum optics experiments in the microwave domain [113, 114, 231], and dark-matter searches [40–42, 232].

Along this chapter we will show how we can use a doubled-pumped grAlPA to overcome its GBW limitation applying the ideas in Section 1.3.4. First, in Section 4.1, we provide a brief overview of the different approaches currently employed to increase the BW of parametric amplifiers. Then, in Section 4.2, we develop the theoretical framework describing a doubled-pumped grAlPA. We proceed with an explanation of the possible pumping configurations to achieve a BW improvement, discussed in Section 4.3. In Sections 4.4 to 4.8 we put to test the theoretical predictions and present the gain performance of the grAlPA under the

application of two pumps. We explain the protocol to increase its BW for different gain levels, which can be generalized to any amplifier designed as a BHD. Finally, in Section 4.9 we discuss the current experimental challenges and outline possible improvements for future implementations.

4.1 Approaches to overcome the gain-bandwidth limit

Several efforts have been devoted in recent years to overcome the bandwidth limitation of standing-wave amplifiers. A natural first approach involves replacing nonlinear resonators with a nonlinear transmission lines, and realize a Traveling-Wave Parametric Amplifier (TWPA) [13]. In this configuration, amplification occurs through the energy transfer between waves propagating along the line, which is no longer constrained by the bandwidth of a superconducting cavity. State-of-the-art TWPAs have demonstrated bandwidths covering the entire 4–12 GHz range [25, 26, 54, 233–235]. However, the generation of dynamically enhanced sidebands within the amplifier operational range [26, 236] and the use of materials with non-negligible internal losses to match the line characteristic impedance [25, 237], have led to a degradation up to a factor of three in their noise performance compared to common JPAs. Only recently have JJ-TWPAs achieved noise performances comparable to those of standing-wave amplifiers [235]. This breakthrough required modulating the critical currents of 3000 Josephson junctions with a precision better than 5%, a technically demanding task.

An alternative strategy involves the use of impedance-engineering techniques to optimize the coupling between the amplifier and microwave readout circuitry [20, 24, 57, 157, 192, 238]. Two main methods for achieving an optimal coupling have been reported in the literature. First, one could reduce the amplifier's external quality factor Q by matching its characteristic impedance to the standard 50 Ω level of typical microwave systems [157]. However, lowering Q necessitates higher pump powers to activate parametric processes, which can create circulating currents beyond the critical current of the device and therefore increasing internal losses (cf. Eq. (1.54)). A more robust approach consist on designing a microwave circuit with a complex impedance, resulting in a coupling coefficient κ with an imaginary part that could compensate for the frequency dependent terms in the device gain profile (see Eq. (1.45)). As discussed by Naaman and Aumentado [192], techniques from microwave filter design can be adapted to tailor the environmental impedance for each specific implementation. The most recent impedance-matched amplifiers have achieved bandwidths up to 500 MHz at gain levels near 20 dB while maintaining quantum-limited noise performance [24, 57]. However, similar to TWPAs, these devices also require stringent fabrication tolerances. Even minor deviations in the impedance-matching network can significantly degrade bandwidth and introduce unwanted gain ripples or peaks [157, 239, 240]. Moreover, the use of passive impedance matching networks, imply that their operation is restricted to a fixed gain level.

An approach that has not yet been extensively explored consists of realizing one of the Bogoliubov amplifier classes [168] (cf. Section 1.3.4). A key advantage of this method is that

the bandwidth can be optimized in situ for any desired gain level by appropriately tuning the frequency and power of the pump tones driving the amplifier. Implementations of the ODBA class have been demonstrated in both JPAs [102] and kinetic-inductance-based amplifiers [227], where they have exhibited negligible GBW tradeoff for gain levels up to 10 dB. On the other hand, OIBAs have been experimentally realized in JPCs, achieving a sixfold increase in bandwidth for gains up to 15 dB and also reporting improved GBW scaling [44, 241]. Other implementations of OIBAs have also been realized in electromechanical systems [242, 243], where an enhanced GBW product has been demonstrated for gain levels up to 40 dB, although the BW was limited to the kHz range.

Although these previous realizations have confirmed the existence of the Bogoliubov amplifier classes, none have yet demonstrated operation at gain levels approaching 20 dB. As discussed in Refs. [44, 170], a major limitation of earlier implementations arises from residual higher-order nonlinearities, which pushed the system away from the ideal operation predicted by theory. Furthermore, all prior realizations have relied exclusively on 3-wave-mixing devices, either in JJ-based amplifiers biased at their Kerr-free point or in current-biased KIPAs. However, residual Kerr effects are unavoidable in any of these systems, which have further limited their gain performance. We then ask ourselves, is it at all possible to realize a Bogoliubov-class amplifier that shows improved GBW scaling at gain levels reaching 20 dB? In the following sections, we present our approach to this challenge, exploiting the fact that in the grAlPA, higher-order nonlinearities are naturally diluted, by several orders of magnitude compared with previous implementations. Moreover, we take advantage of the clean frequency spectrum in the grAlPA, enabled by grAl's low self-capacitance, to avoid activating unwanted cross-Kerr coupling and frequency mixing with the higher modes of the amplifier. In contrast to previous realizations of Bogoliubov amplifiers, our approach relies entirely on the intrinsic Kerr nonlinearity naturally present in grAl.

4.2 Ideal double-pumped Bose-Hubbard dimer

Our goal is to realize a Bogoliubov amplifier with a non-conventional GBW product using the grAlPA design (cf. Fig. 3.3). The theoretical framework introduced in Section 1.3.4 and initially developed in Ref. [168] was formulated for a Kerr-free amplifier and, therefore, is not a-priori directly applicable to the grAlPA. To address this, we need to extend the model to account for 4-wave mixing dynamics, which we will present along this section. Although the following treatment is purely theoretical, and involves several assumptions not directly related to the actual design of the grAlPA, our goal is to build initial intuition about the mechanisms that enable the realization of the Bogoliubov amplifier and to identify the experimental signatures of its emergence. Since the physics of the system becomes more intuitive in the hybridized basis, we will analyze the grAlPA in this frame for the remainder of the section.

We start by assuming the BHD is driven by two pumps with powers and frequencies $P_{g/c}$ and $\omega_{g/c}$, respectively. Each pump will populate the dimer modes with amplitudes α

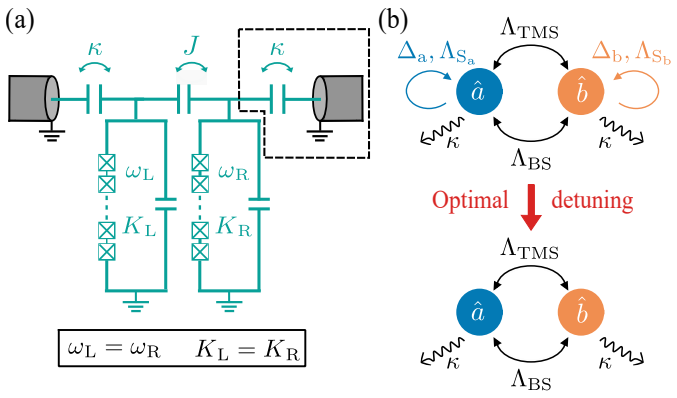

Figure 4.1: Symmetric BHD design. **(a)** Circuit diagram of a symmetric BHD design. Both resonators are coupled to different microwave ports with a strength κ. The remaining circuit parameters are similar to Fig. 3.1(a). **(b)** Dynamics of the system following Eq. (4.1). Each dimer mode has a damping rate κ, with a frequency detuning Δ_j and single-mode squeezing strength Λ_{S_j} (j = a, b). The modes are coupled by beam-splitter Λ_{BS} and two-mode squeezing Λ_{TMS} interactions. When the system is optimally detuned, the dynamics is dominated by Λ_{BS} and Λ_{TMS}.

and β, given by the mean-field Langevin equations shown in Eq. (A1.46). In a stiff pump approximation, we can calculate the effective system dynamics using the displacement transformations $\hat{a} \longrightarrow \hat{a}+\alpha$ and $\hat{b} \longrightarrow \hat{b}+\beta$, where $\hat{a}$, $\hat{b}$ are the bosonic annihilation operators of the dimer modes. In a frame rotating at frequency ω_o, close to either ω_a or ω_b, the BHD Hamiltonian in the hybridized basis takes the form (see Appendix A)

$$\begin{aligned}\hat{H}/\hbar = &-\left[\Delta_a\,\hat{a}^\dagger\hat{a} - \left(\Lambda_{S_a}\,\hat{a}^\dagger\hat{a}^\dagger + \text{h.c.}\right)\right] - \left[\Delta_b\,\hat{b}^\dagger\hat{b} - \left(\Lambda_{S_b}\,\hat{b}^\dagger\hat{b}^\dagger + \text{h.c.}\right)\right] \\ &+ \left(\Lambda_{TMS}\,\hat{a}^\dagger\hat{b}^\dagger + \text{h.c.}\right) + \left(\Lambda_{BS}\,\hat{a}^\dagger\hat{b} + \text{h.c.}\right),\end{aligned} \tag{4.1}$$

where $\Delta_{a/b} = \omega_o - \tilde{\omega}_{a/b}$ are the detunings from the Kerr-shifted dimer modes $\tilde{\omega}_{a/b}$. The terms $\Lambda_{S_{a/b}}$, Λ_{TMS} and Λ_{BS} correspond to time-dependent single-mode squeezing, two-mode squeezing and beam-splitter interactions. All parameters depend on the pump powers and frequencies as well as the circuit parameters of the BHD (see Appendix A).

In comparison to the Hamiltonian of the 3-wave-mixing OIBA in Eq. (1.64), the linearized Hamiltonian of the BHD driven by two pumps contains additional single-mode squeezing interactions. These terms tend to drive the system toward dynamical instability (like in the JPA example of Section 1.3.2), which constituted one of the main limitations in earlier 3-wave-mixing OIBA implementations [44], as no pump configuration could fully compensate the two single-mode squeezing strengths using only beam-splitter interactions. Then, we adopt a hybrid stabilization strategy that combines the principles of ODBAs and OIBAs: the destabilizing single-mode squeezing terms are partially compensated through the frequency detuning of the dimer modes, while the two-mode squeezing is balanced by the beam-splitter term. This approach has previously been implemented in JPCs, as reported by Refs. [44, 232].

Depending on the pump configuration, one can tune Λ_{BS} and $\Delta_{a/b}$ to compensate for the single and two-mode squeezing interactions and provide the system dynamical stability. To simplify the equations of the model and obtain analytical formulas, we assume a symmetrically coupled grAlPA, where each grAl resonator is coupled to a different microwave port with a damping rate κ, as shown in Fig. 4.1(a). This symmetry implies that the damping

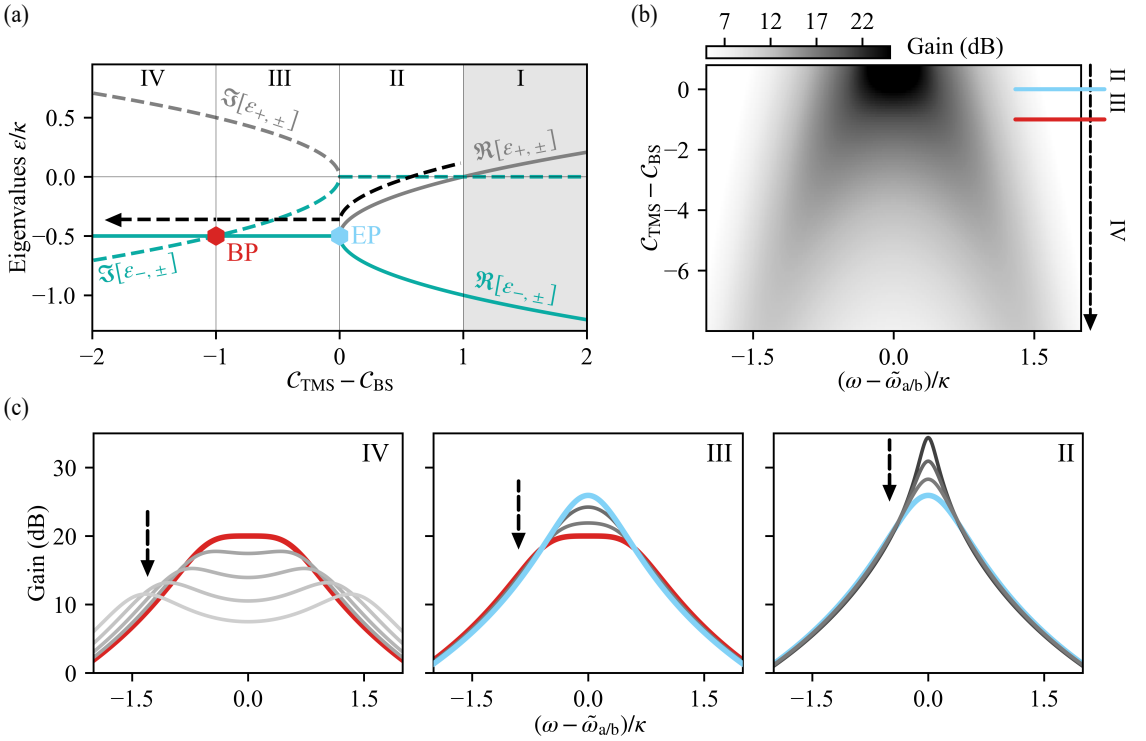

Figure 4.2: Dynamical stability and gain profiles of a double-pumped symmetric BHD with optimal detuning. **(a)** Real and imaginary parts of the eigenvalues $\epsilon_{\pm,\pm}$ (cf. Eq. (4.2)) as a function of the cooperativity difference $C_{\mathrm{TMS}} - C_{\mathrm{BS}}$. Four distinct stability regions are identified based on the system dynamics. In Region I, the photon population in the resonators diverges, preventing the generation of parametric amplification. In Region II, the amplifier behaves similar to a single-pumped (SP) BHD, with a GBW product. In Region III, the beam-splitter interactions effectively balance the two-mode squeezing terms, stabilizing the dynamics and allowing the amplifier to surpass the GBW limit. Two characteristic points define the boundaries of this region: when the cooperativities are equal, the eigenvalues coalesce and the system reaches an exceptional point (EP). When the cooperativities are optimally imbalanced, $C_{\mathrm{TMS}} - C_{\mathrm{BS}} = -1$, the system reaches the Bogoliubov point (BP), where the gain profile exhibits a flattened maximum. Below BP, in Region IV, normal-mode splitting appears around each dimer mode. **(b)-(c)** Calculated gain profiles as a function of frequency ω and $C_{\mathrm{TMS}} - C_{\mathrm{BS}}$. Following the trajectory indicated by the black dashed line in panel (a), the BW gradually increases, as shown in the line cuts of panel (c). The solid red and blue lines mark the BP and EP, respectively.

rates in the hybridized basis are also equal, i.e. $\kappa_{\mathrm{a}} = \kappa_{\mathrm{b}} = \kappa$ (see Appendix A). Furthermore, we assume that both resonators have identical frequencies $\omega_{\mathrm{L}} = \omega_{\mathrm{R}}$ and nonlinearities $K_{\mathrm{L}} = K_{\mathrm{R}}$. Under these conditions, the system can be tuned to produce a dynamics similar to the OIBA by adjusting $\Delta_a = -\Delta_b$, $\Lambda_{\mathrm{S}_a} = \Lambda_{\mathrm{S}_b} = \Lambda_{\mathrm{S}}$ and $|\Delta_{\mathrm{a}}| = |\Delta_{\mathrm{b}}| = 2|\Lambda_{\mathrm{S}}|$. The effective mode diagram of the system is then simplified, as depicted in Fig. 4.1(b).

Similar to the case of the JPA studied in Section 1.3.1, the information of the stability of the system is encoded in the amplifier's drift matrix (cf. Eq. (A1.57)). We want to find regions where the real part of the eigenvalues is negative, such that the electromagnetic field can reach a steady state of amplified oscillations. For the case of a symmetrically coupled BHD with optimal detuned pumps, the eigenvalues reduce to

$$\epsilon_{\pm,\pm} = \frac{\kappa}{2}\left(-1 \pm \sqrt{C_{\mathrm{TMS}} - C_{\mathrm{BS}}}\right), \tag{4.2}$$

where $C_{\mathrm{BS/TMS}} = 4|\Lambda_{\mathrm{BS/TMS}}|^2/\kappa^2$ are the cooperativities associated with the beam-splitter and two-mode squeezing interactions, respectively. We identify four distinct stability regions for the double-pumped BHD, which are depicted in Fig. 4.2(a). They are defined according to the sign and relative magnitude of the eigenvalues $\epsilon_{\pm,\pm}$.

In Region I, when $C_{\mathrm{TMS}} - C_{\mathrm{BS}} > 1$, the system becomes dynamically unstable, as the real part of at least one eigenvalue is positive. In this regime, the system dynamics is unbounded, and the excitations cannot be stabilized by the external damping rates of the modes. Experimentally, operating the BHD within this region would induce a chaotic behavior, in which spontaneous transitions among multiple metastable states prevent stable parametric amplification.

As $C_{\mathrm{TMS}} - C_{\mathrm{BS}}$ decreases below the instability threshold, we reach to Region II, where the amplifier behavior is analogous to the single-pump (SP) BHD described in Section 3.1. Increasing C_{TMS} produce higher photon populations in the dimer modes, which enhances the amplifier gain. In Fig. 4.2(b)-(c), we show gain profiles calculated in the quadrature representation of the hybridized basis (cf. Eq. (A1.63)). The increase of gain in this region is accompanied by a critical slow down of the system, as the beam-splitter interactions cannot fully counteract the instability driven by the two-mode squeezing term. Consequently, the BHD recovers the standard GBW tradeoff of standing-wave amplifiers.

In region III, when $-1 < C_{\mathrm{TMS}} - C_{\mathrm{BS}} < 0$, the system enters the regime we are looking for, where it can be operated as an amplifier with an unconventional GBW scaling. Two characteristic points define the boundaries of this region. The first is the exceptional point (EP), reached when $C_{\mathrm{TMS}} = C_{\mathrm{BS}}$, where there is degeneracy of the eigenvectors and the eigenvalues coalesce into a single real value, $\epsilon_{\pm,\pm}|\mathrm{EP} \longrightarrow -\kappa/2$ [44, 170, 242]. The second is the Bogoliubov point (BP), reached when $C_{\mathrm{TMS}} - C_{\mathrm{BS}} = -1$. As shown in Fig. 4.3(a)-(b), operating near the EP and BP yields two key benefits. First, since the amplifier operates away from the instability threshold, it no longer obeys the conventional GBW scaling, and second, the achievable bandwidth for a maximum gain $G_0 = 20$ dB increases up to a factor of six and ten at the EP and BP, respectively. Remarkably, at the BP, the BW even exceeds the damping rate κ, allowing the amplifier to exploit the full available frequency span of the modes. The improvement in bandwidth is also reflected at the noise level where, as shown in Fig. 4.3(c), the frequency range in which the amplifier provides quantum-limited performance increases at both EP and BP[1].

Lastly, further decreasing $C_{\mathrm{TMS}} - C_{\mathrm{BS}}$ moves the system deeper into the dynamically stable regime, reaching Region IV, where the beam-splitter interactions induce a splitting of the hybridized modes. This effect can be intuitively understood as a dynamically-enhanced hopping interaction that generates two distinct internal resonances near ω_{a} and ω_{b}. Amplifiers operating in Region IV can exhibit even larger BWs than those obtained at

[1] In a JPC Refs. [44, 170] refer to the EP and BP as GC (gain–conversion) and GCI (gain–conversion–imbalanced) modes, respectively.

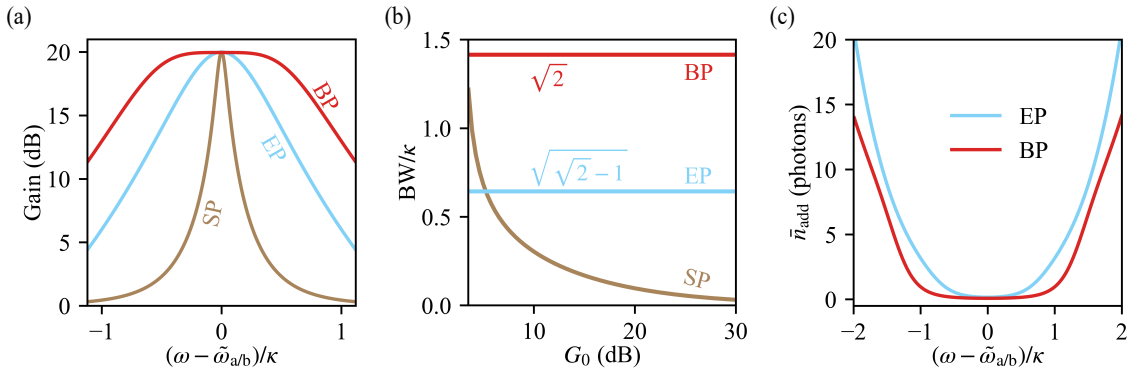

Figure 4.3: Gain and noise performance of the BHD under multi-pump operation. **(a)** Gain profiles for three possible operational modes of the BHD: single-pump (SP), double-pump at exceptional point (EP), and double-pump at Bogoliubov point (BP). The curves are calculated in the quadrature representation of the hybridized basis (see (cf. Eq. (A1.63)). **(b)** Bandwidth scaling vs maximum gain G_0 for the modes of operation in panel (b). Operating at EP or BP, the device overcomes the conventional GBW product. **(c)** Amplifier input referred added noise when biased at $G_0 = 20$ dB and operated at BP or EP. As expected, the BW improvement shown in panel (a) is also reflected in a broader range in which the amplifier approaches the quantum limit. As in the hybridized basis, the amplifier is phase-sensitive, we define the quantum limit as $\bar{n}_{add} = 0$.

the BP (cf. Fig. 4.2(c)). However, the bandwidth must now be defined as the sum of the widths of the two split peaks, rather than with respect to a single gain peak. Interestingly, if one checks the GBW product of each split-peak independently, it can be shown that it remains independent of the overall gain, emulating the behavior of the EP and BP. Such behavior was reported in Refs. [102, 227], where they confusingly called each split-peak a Bogoliubov amplifier. Nonetheless, this regime should not be confused with a true BP, as the total GBW product is reduced relative to the BP case.

For the more general case, where the resonator frequencies and damping rates are not symmetric, not all the interaction terms in Eq. (4.1) can be simultaneously balanced using only two parametric pumps. Under such conditions, the stability of the eigenmodes of the drift matrix cannot be determined directly from the negativity of their real parts, as they become time-dependent. A proper analysis of the amplifier's stability and dynamical phases, in this case, requires the application of Floquet theory, which accounts for the time-dependent modulation of the effective system parameters.

However, we can use the results of the symmetric BHD to extract some predictions on what to expect in the asymmetric case. First, residual single-mode squeezing interactions will tend to drive the system towards instability, resulting in non-constant GBW scaling (see Appendix D.1). Second, as discussed in Ref. [168] for the case of a 3-wave-mixing OIBA, asymmetric damping rates hinder the complete coalescence of the beam-splitter peaks at the BP. Consequently, the amplifier gain profile would not exhibit the flat-top behavior predicted for the ideal symmetric case shown in Fig. 4.3(a).

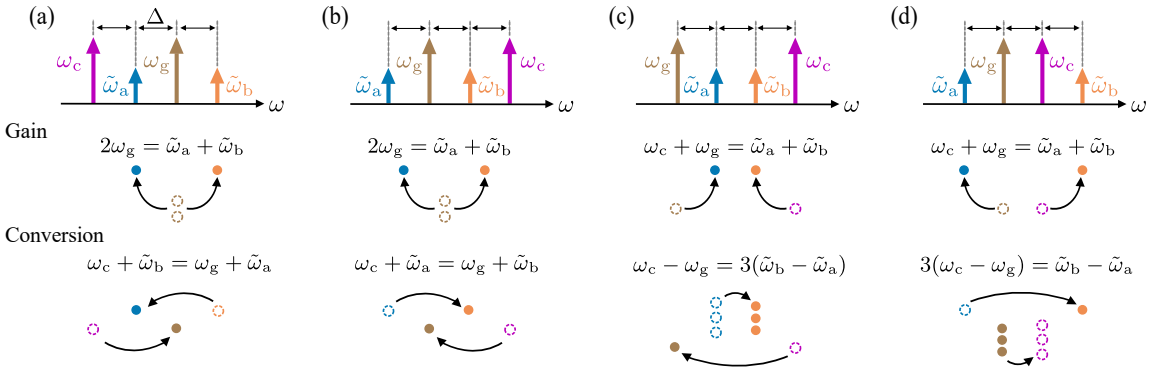

Figure 4.4: Possible configurations to obtain resonant beam-splitter interactions with two pumps. The upper panels illustrate the frequency arrangement of the Kerr-shifted modes $\tilde{\omega}_{a/b}$ and the two pump tones $\omega_{g/c}$. We assume a symmetric detuning Δ between each pair of adjacent tones. The lower panels depict an schematics of the effective gain and conversion processes at the single-photon level. Panels **(a)-(b)**, show the two possible asymmetric configurations. Here, gain pump applied between $\tilde{\omega}_a$ and $\tilde{\omega}_b$ activates phase-preserving amplification where the signal and idler occupy different dimer modes. A second pump, called the conversion pump, is applied with a red (blue) detuning from $\tilde{\omega}_b$ ($\tilde{\omega}_a$), generating frequency conversion processes mediated by the gain pump. Panels **(c)-(d)**, show the two possible symmetric configurations. Now, both pumps are applied either *inside* or *outside* the mode frequencies. In this configuration, the two pumps simultaneously contribute to both amplification and frequency conversion between $\tilde{\omega}_a$ and $\tilde{\omega}_b$.

4.3 Experiment concept

The treatment in the previous section was done assuming the system is already linearized and all the terms in its Hamiltonian were active. To realize this in the grAlPA, we need to find the correct configuration of pump frequencies that activate such terms. Resonant single-mode and two-mode squeezing can be activated using for example the ND pump used for the experiments in Chapter 3. However, we also need to be able to control beam-splitter interactions. This is by no means a trivial task. For example, a careful reader might have noticed that even for a single-pump configuration, the term Λ_{BS} appears in grAlPA's linearized Hamiltonian shown in Eq. (3.4). However, in that case, Λ_{BS} arises solely from the hybridization of the bare grAl resonators and cannot become resonant, since $\tilde{\omega}_a \neq \tilde{\omega}_b$.

To produce resonant beam-splitter interactions, frequency-conversion processes must be activated through the application of a second pump tone. Unlike 3-wave-mixing amplifiers, where the pump configuration that enables frequency conversion is uniquely defined, the grAlPA offers a wide range of possible two-pump configurations capable of driving such processes. In Fig. 4.4, we illustrate four representative configurations that can induce frequency conversion when the amplifier is driven by two pumps[2].

[2] Notice that pumping at $(\tilde{\omega}_b - \tilde{\omega}_a)/2$ can also induce frequency-conversion processes and thus also beam-splitter interactions. However, given the ≈ 200 MHz detuning between the dimer frequencies in the current grAlPA, this configuration would require a conversion pump near 100 MHz. In our present setup, such low-frequency pump cannot be applied, as it lies outside the operational bandwidth of the circulator connected before the grAlPA. Incorporating an on-chip pump line could overcome this limitation.

Depending on their configuration, we can get an intuitive understanding on the type of process each pump tone is activating. For the configuration shown in Fig. 4.4(a), where the pumps are asymmetrically spaced with respect to the dimer modes, a pump applied at frequency $\omega_g = (\tilde{\omega}_a + \tilde{\omega}_b)/2$, which we call the gain pump, generates phase-preserving gain. This means that two pump photons transform into one signal and one idler photon, split between the dimer modes. The application of a second pump at the left of $\tilde{\omega}_a$ and with frequency $\omega_c = \tilde{\omega}_a + \omega_p - \tilde{\omega}_b$, called the conversion pump, activates frequency conversion between photons at $\tilde{\omega}_a$ and $\tilde{\omega}_b$, which is mediated by photons from the gain pump. A similar process is obtained if one would apply the conversion pump at the right of $\tilde{\omega}_b$, but now the role of $\tilde{\omega}_a$ and $\tilde{\omega}_b$ are exchanged. On the other side, one could apply the pumps in a symmetric configuration as shown in Fig. 4.4(b) and (c) i.e. with both of their frequencies *inside* or *outside* the dimer modes. In this case however, both pumps simultaneously contribute to phase-preserving gain and frequency conversion, and thus cannot be uniquely associated with a single parametric process. For this reason, in our experiments, we focus in the asymmetric configuration shown in Fig. 4.4(a), as it provides a clear interpretation of the function of each pump (closely resembling the operation of a 3-wave-mixing OIBA) and enables a direct comparison between single- and double-pump operation without changing the gain-pump frequency. Nevertheless, exploring the amplifier performance under the symmetric configurations would constitute an interesting direction for future studies.

To confirm that our choice of pumps activates resonant beam-splitter interactions, we write the linearized BHD Hamiltonian without applying a rotation transformation. In the hybridized basis we obtain,

$$\begin{aligned}\hat{H}/\hbar = {} & \tilde{\omega}_a \hat{a}^\dagger \hat{a} + \tilde{\omega}_b \hat{b}^\dagger \hat{b} \\ & + \left(\left[\Lambda_{S_a}^{(1)} e^{-2i\omega_g t} + \Lambda_{S_a}^{(2)} e^{-2i\omega_c t} + \Lambda_{S_a}^{(12)} e^{-i(\omega_c+\omega_g)t} \right] \hat{a}^\dagger \hat{a}^\dagger + \text{h.c.} \right) \\ & + \left(\left[\Lambda_{S_b}^{(1)} e^{-2i\omega_g t} + \Lambda_{S_b}^{(2)} e^{-2i\omega_c t} + \Lambda_{S_b}^{(12)} e^{-i(\omega_c+\omega_g)t} \right] \hat{b}^\dagger \hat{b}^\dagger + \text{h.c.} \right) \\ & + \left(\left[\Lambda_{TMS}^{(1)} e^{-2i\omega_g t} + \Lambda_{TMS}^{(2)} e^{-2i\omega_c t} + \Lambda_{TMS}^{(12)} e^{-i(\omega_c+\omega_g)t} \right] \hat{a}^\dagger \hat{b} + \text{h.c.} \right) \\ & + \left(\Lambda_{BS} \left[e^{-i(\omega_c-\omega_g)t} + e^{i(\omega_c-\omega_g)t} \right] \hat{a}^\dagger \hat{b} + \text{h.c.} \right),\end{aligned} \tag{4.3}$$

where the exact expressions of all the interaction parameters are detailed in Appendix A. Under the conditions of asymmetric pumping, i.e. $2\omega_g = \tilde{\omega}_a + \tilde{\omega}_b$ and $\omega_g + \tilde{\omega}_a = \omega_c + \tilde{\omega}_b$, and rotating the Hamiltonian with respect to its free energy, the effective dynamics of the system is given by

$$\hat{H}/\hbar = \left(\Lambda_{S_a}^{(12)} \hat{a}^\dagger \hat{a}^\dagger + \Lambda_{TMS}^{(1)} \hat{a}^\dagger \hat{b}^\dagger + \Lambda_{BS} \hat{a}^\dagger \hat{b} + \text{h.c.} \right). \tag{4.4}$$

Thus, the strategy of realizing an OIBA relies in balancing $\Lambda_{S_a}^{12}$ by detuning from the frequency $\tilde{\omega}_a$ and canceling Λ_{TMS}^{1} with the now resonant term Λ_{BS}.

Table 4.1: Circuit parameters of the grAlPA used for double-pumping experiments. The errors arise from the Fano uncertainty in the measurement setup [134].

$\omega_a/2\pi$ (GHz)	$\omega_b/2\pi$ (GHz)	$\kappa_a/2\pi$ (MHz)	$\kappa_b/2\pi$ (MHz)	$\gamma_{a,b}/2\pi$ (MHz)	$\omega_L/2\pi$ (GHz)	$\omega_R/2\pi$ (GHz)	$J/2\pi$ (MHz)	$\kappa/2\pi$ (MHz)
8.233	8.434	14.0 ± 1	29.0 ± 3	≤ 5	8.299 ± 7	8.368 ± 7	95 ± 10	44 ± 4

4.4 Optimized parameter extraction

Before we start double-pumping the grAlPA, we first need a way to extract more accurately its circuit parameters. This is important because in order to realize a Bogoliubov amplifier, we need the fine tuning of all interaction terms in the system's linearized Hamiltonian. Therefore, if we aim to have an accurate comparison between experimental results and theoretical predictions, it is essential to estimate these terms with high precision, which effectively means accurately calculating the system's circuit parameters. The calculations must also be performed in situ, since even small variations between cooldowns can lead to significant changes in the device dynamics and a complete mismatch with theoretical predictions.

For the experiments that we will show in the following sections, we use the same grAlPA employed for the results in Chapter 3. The measurement setup, depicted in Fig. A4.3, was optimized to minimize insertion losses between the calibrated power reference and the amplifier input. The extracted circuit parameters are summarized in Table 4.1. They were obtained from single-tone spectroscopy measurements in the single-photon regime, following the procedure detailed in Section 3.4. We observe that for this cooldown, the grAl resonators are not perfectly hybridized,[3] and thus the procedure employed in Chapter 3 to extract the Kerr coefficients $K_{L,R}$ cannot be directly applied.

In this case, we extract $K_{L,R}$ by fitting the grAlPA reflection coefficient S_{11} as a function of both driving frequency ω and input power P_{in}. We derive an analytical expression of S_{11} using the mean-field Langevin equations of the grAl resonators (cf. Eq. (A1.3)) and the standard input–output formalism. We obtain

$$S_{11}(\omega) = 1 + \frac{i\kappa\,(\delta_R - i\gamma/2)}{J^2 - (\delta_R - i\gamma/2)\,(\delta_L - i\kappa/2)}, \tag{4.5}$$

where $\delta_j = \omega - \omega_j - K_j\, n_j$ (with $j = L, R$) are the Kerr-shifted detunings from the bare grAl frequencies $\omega_{L/R}$, $n_{L/R}$ their respective photon number populations and γ the effective

[3] Although the Nb pad stabilizes the grAlPA coupling strength, ensuring that the device consistently provides 20 dB non-degenerate gain across multiple cooldowns, it does not completely eliminate the residual hybridization asymmetry caused by substrate misalignments. A more robust solution would be to fabricate the grAlPA in a 2D geometry, in which the coupling strength is less sensitive to experimental imperfections.

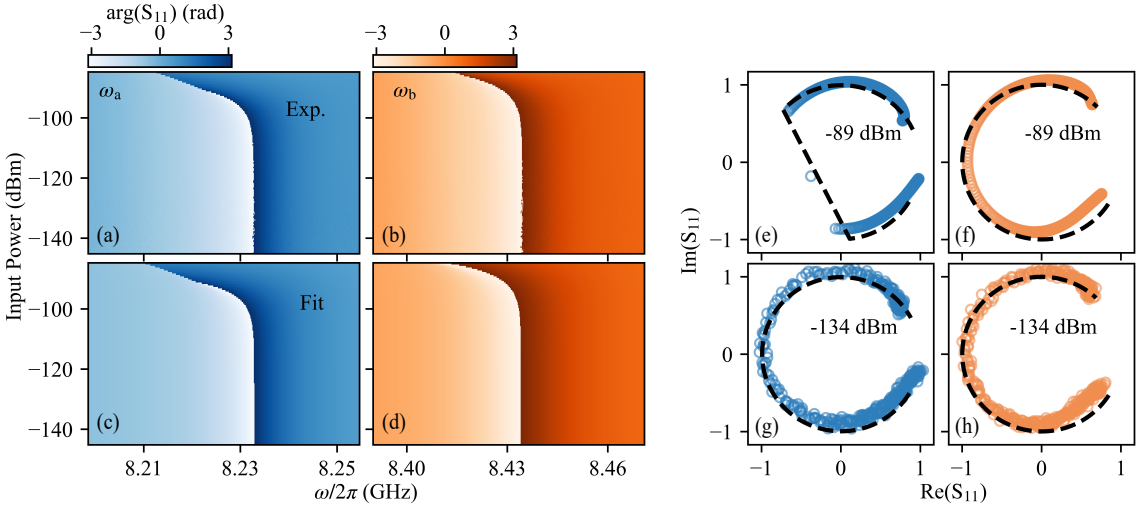

Figure 4.5: Kerr-shift of dimer modes and extraction of circuit parameters.. Measured **(a)-(b)** and fitted **(c)-(d)** single-tone spectroscopy of the grAlPA dimer modes $\omega_{a/b}$ as a function of input power. Fits are obtained using Eqs.(4.5)-(4.6). The probe power is calibrated from the measurement-induced dephasing of a superconducting qubit placed before the amplifier (see Appendix C.3). In the right panels we show linecuts at probe powers of −89 dBm (**e**-**f**) and −134 dBm (**g**-**h**). The black dashed lines depict the fit curves.

damping rate due to internal losses. We calculate $\gamma = 0.5 \pm 0.5$ MHz from the results obtained in Fig. 3.5(c). Using the steady-state Langevin equations of the bare grAl modes, we obtain also expressions for $n_{\mathrm{L/R}}$

$$
\begin{aligned}
n_{\mathrm{R}} &= n_{\mathrm{L}} \frac{J^2}{{\delta_{\mathrm{R}}}^2 + \gamma^2/4} \\
n_{\mathrm{L}} &= n_{\mathrm{in}} \frac{{\delta_{\mathrm{R}}}^2 + \gamma^2/4}{\left(J^2 - \delta_{\mathrm{R}}\delta_{\mathrm{L}} - \gamma\kappa/4\right)^2 + \left(\gamma\,\delta_{\mathrm{L}}/4 + \kappa\,\delta_{\mathrm{R}}/4\right)^2},
\end{aligned}
\tag{4.6}
$$

where n_{in} can be calculated from the power at the amplifier input P_{in} using $n_{\mathrm{in}} = P_{\mathrm{in}}/\hbar\omega\kappa$. The input-referred power is calibrated via the AC-stark shift and dephasing of a GFQ, as detailed in Appendix C.3. We fit the power-dependent spectroscopy data shown in Fig. 4.5(a)-(b) by solving Eq. (4.5) and (4.6) self-consistently, using only the Kerr coefficients $K_{\mathrm{L/R}}$ as free parameters. Above the mode bifurcation point, where the system supports multiple steady-state solutions of $n_{\mathrm{L/R}}$, we select the branch corresponding to the lowest photon population in the grAl resonators. The extracted results are presented in Fig. 4.5(c)–(h), from which we obtain $K_{\mathrm{L}}/2\pi = 2.9 \pm 1$ kHz and $K_{\mathrm{R}}/2\pi = 3.2 \pm 1$ kHz. The error intervals arise from both the Fano uncertainty of the measurement setup and the uncertainty in the calibration of the input power. Note that this optimized extraction procedure successfully reproduces the lineshape of mode ω_{a} even beyond its bifurcation point (see Fig. 4.5(e)), a regime where conventional circle-fit methods fail to capture the correct shape of the resonance.

4.5 Phase-preserving gain with two parametric pumps

Now that we have an accurate calibration of grAlPA's circuit parameters, we can move forward and apply two pumps to the amplifier, with the aim of reaching the BP. Recall that, as long as the device operates in a regime analogous to Region III in Fig. 4.2(a), we expect a significant improvement in the GBW tradeoff, and therefore an enhanced BW at 20 dB gain. This is the regime that we target for the grAlPA. As can we see from the gain profiles in Fig. 4.2(c), the experimental proxy to find Region III is the coalescence of the peaks produced by beam-splitter interactions i.e. by the addition of the conversion pump.

We begin by characterizing the gain performance of the grAlPA when driven only by a gain pump at frequency $\omega_g/2\pi$ = 8.30172 GHz. Fig. 4.6(a) shows gain profiles measured near $\tilde{\omega}_b$ for increasing pump powers P_g. The corresponding gain profiles near the other dimer mode, $\tilde{\omega}_a$, are presented in Appendix D.3. As expected for single-pump operation, the grAlPA exhibits a GBW scaling following the relation BW = $\kappa_{eq}/\sqrt{G_0}$, where G_0 is the maximum amplifier gain and $\kappa_{eq}/2\pi$ = 19.2 MHz its equivalent damping rate defined as [22, 112]

$$\kappa_{eq} = \frac{2\kappa_a\kappa_b}{(\kappa_a + \kappa_b)}. \tag{4.7a}$$

We compute κ_{eq} using the modes linewidths $\kappa_{a/b}$ presented in Table 4.1.

In contrast to the results shown in Fig. 3.7(a), where individual gain curves were fitted independently using Lorentzian functions, here all gain profiles are fitted simultaneously using the predictions of the Bose–Hubbard dimer model, with the pump-line attenuation A as the only free parameter (see Appendix D.4 for details of the fitting procedure). We obtain A = -66 ± 5 dB. The observed asymmetry of the gain profiles and the discrepancy at low pump powers can be attributed to unaccounted frequency-dependent losses in the measurement setup. We note that the relatively large uncertainty in the extracted pump-line attenuation could be reduced in future experiments by integrating an additional power calibration source directly at the amplifier input (see Appendix D.2). With this modification one could reach uncertainties below 1 dB, comparable to the ones of the input line.

To stabilize the amplifier dynamics and enhance its bandwidth, we apply a conversion pump at a frequency $\omega_c/2\pi$ = 8.078 GHz, in the asymmetric configuration shown in the upper panel of Fig. 4.6(a). As observed in Fig. 4.6(b), the addition of the conversion pump induces the desired peak-splitting behavior predicted in Fig. 4.2(c). By varying the conversion pump power P_c, we can experimentally navigate through grAlPA's parameter space equivalent to that of Fig. 4.2(a), reaching the regime where the two peaks coalesce, which is predicted to occur near the BP. We assign the BP experimentally by checking the conversion power which maximizes BW without a noticeable splitting of the gain profiles.

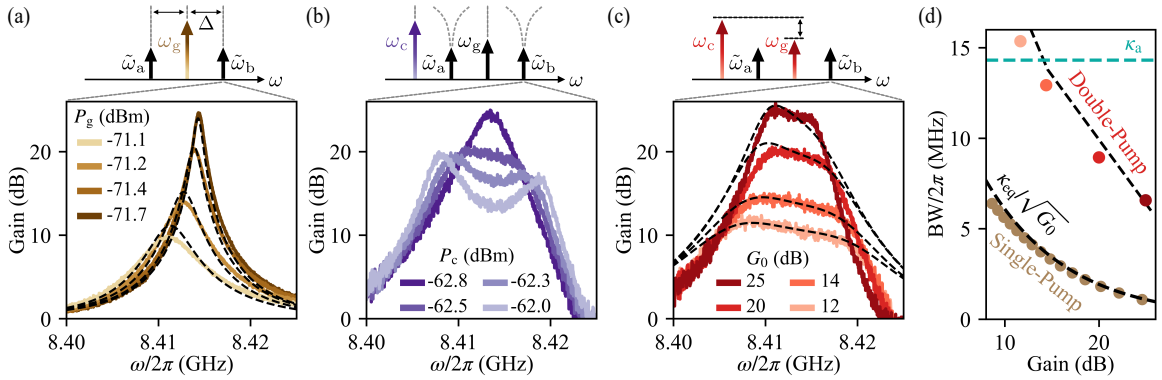

Figure 4.6: Improved gain-bandwidth scaling of the grAlPA when operated close to the BP. In panel **(a)** we show the gain performance under a single pump close to $\tilde{\omega}_b$, in panel **(b)** we show the two-pump protocol that enables optimized BW broadening, and in panel **(c)** we demonstrate the optimized operation of the amplifier close to the BP. The schematics above each panel depict the corresponding pump configurations. As visible in panel (a), the gain pump with power P_g gives rise to phase-preserving gain close to $\tilde{\omega}_b$ (and $\tilde{\omega}_a$, not shown). Applying a conversion pump with power P_c and in the configuration shown in Fig. 4.4(a), activates beam-splitter interactions between the hybridized modes. This results in the appearance of a new idler tone and a second peak in the gain profile close to $\tilde{\omega}_b$. The optimal bandwidth is achieved when the two peaks around $\tilde{\omega}_b$ coalesce near the BP, as illustrated in panel (c). For all gain curves in (c), the ratio P_c/P_g remains approximately constant. The black dashed lines in (a) and (c) depict fits obtained with the Bose-Hubbard dimer model (see Appendix D.4). **(d)** Comparison of the measured GBW product for a single- and double-pumped grAlPA. The green dashed line represents the upper limit, given by the linewidth of the low frequency hybridized mode κ_a. BWs extracted from the fits in (a) and (c) are depicted by the black dashed lines. For the single-pumped grAlPA, the BW scaling is consistent with the measured equivalent damping rate $\kappa_{eq}/2\pi = 19 \pm 4$ MHz.

Remarkably, for a maximum gain $G_0 = 20$ dB, we obtain a sixfold bandwidth improvement compared to the single-pump configuration.

To confirm that we are in fact operating close to the BP and the grAlPA is away from the dynamical instability region, we should be able to also observe the occurrence of the EP. We can test this, by further varying the conversion pump power P_c. We observe that we reproduce the behavior predicted for Region III, in Fig. 4.2. Once the amplifier surpasses the BP, the two gain peaks merge completely into a single Lorentzian profile, eventually reaching the EP. Obviously, accurately identifying the EP and thus the boundaries of Region III, requires precise calibration of all interaction parameters. Nevertheless, the close agreement between the experimental data and the theoretical predictions presented in Fig. 4.2, already confirms that we have successfully realized all the features expected from an OIBA using our Kerr-based amplifier and confirming that we can operate the grAlPA away from instability.

To reach the BP and obtain a BW enhancement for different values of G_0, we repeat the conversion-pump optimization procedure of Fig. 4.6(b), but now for different gain-pump powers and frequencies. The results are presented in Fig. 4.6(c). We observe that for $G_0 \sim 12$ dB, the BW exceeds the linewidth of the narrowest dimer mode κ_a, consistent with the theoretical predictions of operating close to the BP. Moreover, the grAlPA shows a non-conventional GBW product up to 25 dB gain (see Fig. 4.6(d)), a performance enabled

due to its strongly diluted higher order non-nonlinearities and clean frequency spectrum, that could not be achieved in previous OIBA implementations using JJs[4].

As for single-pump driving, we fit the double-pumped gain profiles using the BHD model (cf. Fig. 3.1) and the experimental parameters shown in Table 4.1 (see Appendix D.4 for details). Due to small variations in the microwave connections between single- and double-pump measurements, we take the pump powers as fitting parameters. The resulting fits, shown in Fig. 4.6(c), correspond to a pump-line attenuation consistent with that extracted from the single-pump configuration. These results validate the BHD model used for the double-pumped grAlPA. Notably, across all measurements, the ratio between the gain and conversion pump powers remains approximately constant at $P_c/P_g \approx 0.12$ (see Appendix D.4).

We identify three main discrepancies between the theoretical calculations presented in Section 4.2 and the measured gain profiles shown in Fig. 3.1(c). First, the measured bandwidth broadening at 20 dB gain is approximately a factor of two smaller than the theoretical calculation. Second, unlike the calculated flat-top gain profile in Fig. 4.3(a), the optimized gain curve exhibits a noticeable slope near its uppermost region. Finally, the GBW product of the grAlPA operated at the BP is not constant.

We attribute these discrepancies to the imperfect hybridization of the grAl resonators and the asymmetry in their coupling to the single microwave port used in our implementation. In the following sections, we will see that these non-idealities also lead to a reduction in the performance of other amplifier metrics. However, we emphasize that the current results show already the advantages of using double-pumped grAl amplifiers as a practical alternative to overcome the GBW limitation of conventional JPAs.

4.6 Phase-sensitive gain with two parametric pumps

An interesting feature of realizing an OIBA is the emergence of phase-sensitive gain around the resonance frequencies of the amplifier modes. The frequency range over which the amplifier exhibits phase sensitivity, called the squeezing bandwidth $\mathrm{BW_{sq}}$, scales according to the relation $\mathrm{BW_{sq}} = \sqrt{2}\kappa/(G_0)^{1/4}$, where κ is the damping rate of the modes and G_0 its maximum gain [168]. For a double-pumped BHD, a similar behavior is expected if one measures the gain directly in the hybridized basis. However, in our current implementation, the amplified signal is measured at the output of a single microwave port coupled only to the left resonator (see Fig. 3.3). Consequently, we probe the system dynamics in the basis of the bare grAl resonators, which lifts the degeneracy in the amplifier gain, except at highly symmetric points such as $\tilde{\omega}_a$ and $\tilde{\omega}_b$. At these frequencies, phase-sensitive gain can still be observed with our setup. Intuitively, this behavior arises because the chosen

[4] This operational mode was previously explored in the group by Patrick Winkel on the device reported in Ref. [22]. However, the results were never published, as they deviated significantly from the expected theoretical model.

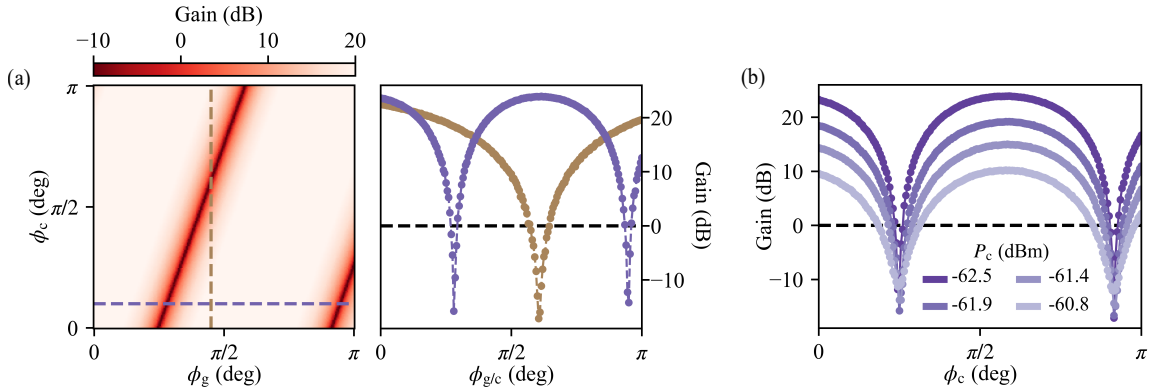

Figure 4.7: Phase-dependent gain at $\tilde{\omega}_b$ under two-pump operation. **(a)** Measured phase-dependent gain with the grAlPA biased at a maximum gain G_0 in the range of 20 dB. The left panel shows the dependence of gain with the phases of the gain pump ϕ_g and conversion pump ϕ_c. In the right panel we plot linecuts taken for fixed ϕ_g (brown) and fixed ϕ_c (purple). We obtain a mininimum deamplification of -17 dB, highlighting the potential of the grAlPA as a vacuum single-mode squeezing source. **(b)** Conversion pump power dependence of the phase-dependent gain. Varying P_c reduces G_0 (cf. Fig. 4.6(b)) and therefore also the extinction ratio.

pump-frequency configuration induces idler degeneracy at $\tilde{\omega}_a$, analogous to the behavior in single-mode parametric amplifiers under symmetric double-pumping conditions [49]. Since the two-mode squeezing interactions described in Eq. (4.3) remain active in the grAlPA, this degeneracy is also transferred to $\tilde{\omega}_b$.

We measure the phase-dependent gain of the grAlPA by pulse-pumping the amplifier. The two pump tones and a probe signal at $\tilde{\omega}_b$ are generated using an Octave-OPX+® control system (see Appendix D.2). The pulses of all tones are optimized such that we probe the amplifier once it has reached its steady-state. The quadratures of the output signal are measured using heterodyne detection, and the amplifier gain is defined as the ratio between the detected output powers when the pumps are on and off. In Fig. 4.7(a), we present the phase-dependent gain measured at $\tilde{\omega}_b$ while operating near the BP. The pump configuration provides a phase-preserving gain of ≈ 20 dB.

The linecuts in the right panel of Fig. 4.7(a) illustrate the dependence of the amplifier gain on the phases of the conversion (ϕ_c) and gain (ϕ_g) pumps. Unlike the phase-sensitive gain obtained when a single pump tone is applied on resonance at $\tilde{\omega}_b$ (see Section 1.1.3), here the phase dependence is a function of $\cos(\phi_b + 3\phi_g - \phi_c + \phi_{off})$, where $\phi_b = 0$ denotes the phase of the probe tone kept fixed during the experiments, and ϕ_{off} represents an offset phase delay introduced by the measurement setup. This dependence arises from the nonlinear mixing between the two pump tones and the probe signal. In Fig. 4.7(b), we present the evolution of the grAlPA's phase-dependent gain as a function of the conversion-pump power P_g. We observe a consistent dependence on ϕ_g across all curves, accompanied by a gradual decrease in the maximum gain with increasing P_g, in agreement with the behavior observed in the gain profiles of Fig. 4.6(b).

An important parameter to consider when characterizing phase-sensitive gain is the ratio between the maximum amplification and the minimum deamplification. This parameter is often referred to as the extinction ratio [26, 244, 245] and serves as a measure of the

amplifier ability to suppress noise in unwanted, out-of-phase quadratures. As presented in Fig. 4.7(a), the grAlPA exhibits an extinction ratio of 41 dB, which is comparable to values reported for other kinetic-inductance-based amplifiers operating at the same gain level [49, 50, 56, 58, 60]. Varying P_g modifies the extinction ratio, as shown in Fig. 4.7(b). On the other hand, the minimum deamplification level provides a useful proxy for the amplifier capability to generate single-mode vacuum-squeezed states. We measure a deamplification level of −17 dB for G_0 = 20 dB, on par with state-of-the-art kinetic inductance amplifiers, which have reported record vacuum squeezing levels of up to −8 dB [60]. This observation, recommends the grAlPA as a promising and efficient source of single-mode vacuum squeezing for future quantum optics experiments.

4.7 Saturation power under two-pump driving

Besides the improvement in bandwidth achieved in an OIBA, another appealing feature for quantum readout applications is its enhanced power-handling capability. As discussed in Section 1.3.4, the pump-depletion threshold in an OIBA can be increased by nearly two orders of magnitude compared with standard standing-wave amplifiers. When the amplifier's dynamical range is limited by pump depletion, as in pure 3-wave-mixing devices, this enhancement directly translates into an improvement in its saturation power. However, it is not a propri clear if the improvement could also be seen when using a 4-wave-mixing amplifier, as they are mainly limited by the signal-induced Kerr shifts (cf. Eq. (1.55)). In Fig. 4.8(a), we present saturation power measurements of the grAlPA operated at a gain level of $G_0 \approx 20$ dB. Contrary to expectations, the measured 1-dB compression point decreases to approximately -120 dBm, which is an order of magnitude lower than the single-pump results shown in Fig. 3.7.

To understand the reduction in saturation power under double-pump operation, we first analyze the dynamical range of the grAlPA in a single-pump configuration. In contrast to the results presented in Fig. 3.7, the current cooldown reveals a non-monotonic saturation curve with increasing probe power P_s, as shown in Fig. 4.8(a). This effect, colloquially referred to as the "shark-fin" [220], arises when the amplifier operates in a multistable regime. To confirm this scenario, we compute the photon number populations of the grAl resonators using the circuit parameters extracted in Table 4.1, the pump-line attenuation obtained from the fits in Fig. 4.6, and Eq. (4.6). The results indicate that, for the range of gain-pump powers used in our experiments, the device indeed operates within a region supporting multiple steady-state solutions of $n_{L,R}$, as illustrated in Fig. 4.8(b) and (c). Increasing the probe power P_s induces a transition to one of the metastable states with higher photon number populations, which abruptly increases the amplifier gain and produces the characteristic shark-fin feature in Fig. 4.8(a). Increasing P_s beyond this transition leads to a degradation of the amplifier's power-handling capability according to Eq. (1.55), explaining the fast gain reduction observed for probe powers above -117 dBm.

Operation of the grAlPA close to the MS regime is in conflict with the general design guidelines discussed in Section 3.2. In this case, the amplifier enters the MS regime because

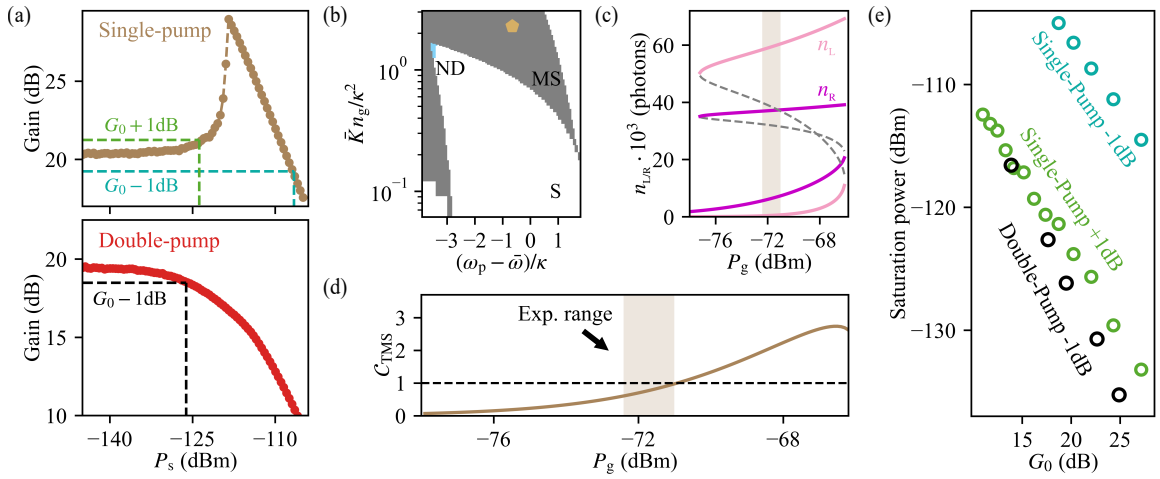

Figure 4.8: Saturation power and multistability of the grAlPA under double-pump operation. **(a)** Signal-power sweeps of the grAlPA when is driven with one (top) or two (bottom) pumps. When operated with a single pump, the grAlPA exhibits a 'shark-fin' saturation curve, indicating the existence of multistable dynamics [220]. We define two saturation powers: the conventional G_0−1 dB compression point, and the G_0+1 dB compression point, identifying the input power threshold beyond which transitions between metastable states are triggered. **(b)** Phase space of the single-pumped grAlPA, calculated using the parameters extracted in Section 4.4 and Appendix D.4. The brown marker indicates the operating point of the grAlPA. **(c)** Photon population of the grAl resonators as a function of the gain pump power P_g. The shaded area corresponds to the range of pump powers used in the experiments shown in Fig. 4.6(a), confirming grAlPA's multistability. **(d)** Dependence of the two-mode squeezing cooperativity C_{TMS} on the gain pump power. Despite the presence of multistability, the grAlPA remains below the limit of stable dynamics marked by the black dashed line. **(e)** Saturation power scaling as a function of low-power gain G_0. The double-pump −1 dB compression point closely matches the +1 dB point in the single-pump case, suggesting that the grAlPA saturation power is limited by its multistability.

the frequency asymmetry between the grAl resonators drastically reduces the available ND region (cf. Fig. 3.2). However, as briefly noted in Section 3.2, there exists a subset of the MS region where the dynamics remain non-chaotic, allowing the device to still function as a stable parametric amplifier. Within this subset, the condition to operate the grAlPA as a ND amplifier must instead be determined from its dynamical stability, evaluated through the eigenvalues of the drift matrix. For a single-pump BHD, the eigenvalues are given by Eq. (A1.34) and dynamical stability is ensured when $C_{TMS} = 4|\Lambda_{TMS}|/\kappa_a\kappa_b < 1$. As shown in Fig. 4.8(d), within the pump-power range in our experiments, this stability condition is satisfied[5], explaining why the grAlPA continues to operate as a stable ND amplifier even when is driven into the MS regime.

When the device operates in a multistable regime, we can define two characteristic saturation powers: the conventional G_0−1 dB compression point, and the G_0+1 dB compression

[5] Following the discussions in Section 3.2, we can now add a third requirement for the operation of the grAlPA as a non-degenerate amplifier:

(iv) **Dynamical stability condition** $C_{TMS} < 1$. This condition ensures that even when the amplifier operates in MS, it avoids reaching a chaotic and unbounded regime.

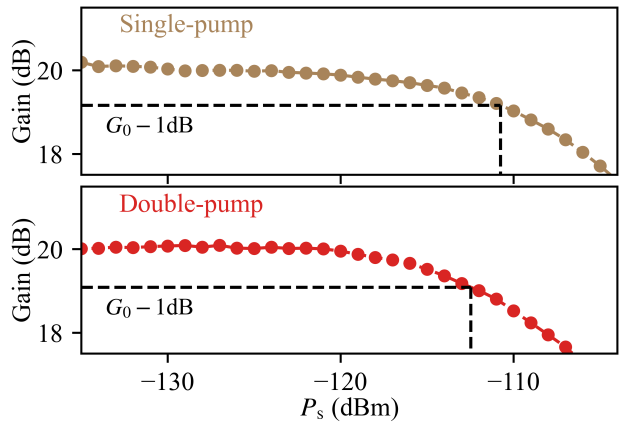

Figure 4.9: Saturation power of a grAlPA with symmetric frequencies. Due to the symmetry in the resonators frequencies, the amplifier is no longer operated in a multistable regime, which eliminates the 'shark-fin' shown in Fig. 4.8(a). under double-pump operation is comparable to that obtained for the single-pump case. The circuit parameters of the grAlPA used for these experiments are summarized in Table A4.2.

point, which quantifies the probe power above which transitions between metastable states occur [220]. We measure −1 dB compression points near −106 dBm for the single-pump configuration (consistent with Fig. 3.7) and −126 dBm for the double-pump case. Strikingly, the single-pump +1 dB point coincides with the double-pump −1 dB point, as shown in Fig. 4.8(e). A similar trend is observed across different gain levels, indicating that the dynamic range under two-pump operation is currently limited by the onset of multistability in the amplifier.

The saturation power of the amplifier can be improved by reducing the asymmetry between the grAl resonators. In Fig. 4.9, we show saturation power measurements obtained by double-pumping the same grAlPA during a cooldown in which the resonator frequencies differed by less than 1% (see Appendix D.5), and where the device was operated away from the MS region. We adjusted the scale of P_s so that the 1-dB compression point of the amplifier matches the one reported in Fig. 3.7, since a calibrated power reference was not connected during this cooldown. As shown in Fig. 4.9, operating the device outside of the MS regime leads to an improved saturation power under double-pump operation, even recovering the value obtained when using a single pump.

Although the latter result is promising, we note that even after minimizing the resonator asymmetry, we do not observe the enhanced power-handling capability originally predicted for operation at the BP. This suggests that the saturation power of the double-pumped grAlPA is not limited by pump depletion, but rather by imbalanced Kerr nonlinearities, which is also consistent with observations reported in JPCs [44]. Future work could extend the analytical framework introduced by Ref. [168] to explicitly include the contribution of Kerr nonlinearities, and enabling a more accurate estimation of the saturation power limits in a double-pumped grAlPA.

4.8 Phase-preserving noise performance

A key question to address is whether the noise performance of the grAlPA degrades when we apply the conversion pump. To investigate this, we evaluate the amplifier noise visibility, defined as the excess noise power observed in the readout line when the grAlPA is

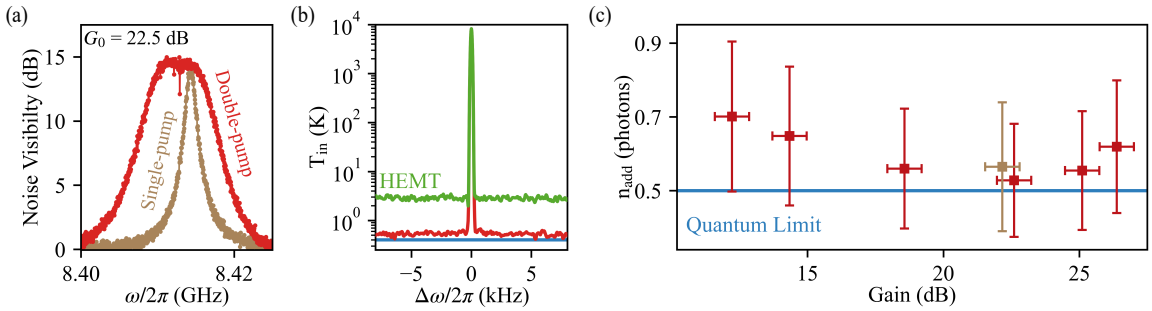

Figure 4.10: Phase-preserving noise performance when the grAlPA is operated close to BP. (a) grAlPA noise visibility when driven by a single pump (brown) and two pumps (red), at a maximum gain G_0 = 22.5 dB. **(b)** Input-referred noise temperature as a function of detuning $\Delta\omega$ from a power-calibrated tone at $\omega/2\pi$ = 8.412 GHz. The green and red solid lines correspond to measurements with both pumps off and on, respectively. When both driving tones are on, the noise approaches the standard quantum limit for phase-preserving amplification depicted by the solid blue line. **(c)** grAlPA added noise as a function of gain. The quantum limit is defined as half a photon of noise from vacuum fluctuations. Error bars represent the uncertainty propagated from the power calibration. The brown point was measured when the grAlPA was driven by a single-pump.

turned on. The total output noise power is measured using a spectrum analyzer connected at room temperature (see Appendix D.2). The noise visibility can then be calculated from the measured noise powers with the amplifier on and off, according to

$$\Delta P_{\text{vis}} = \frac{N_{\text{out}}^{\text{on}}}{N_{\text{out}}^{\text{off}}} = \frac{AG_0(N_{\text{QL}} + N_{\text{gr}}) + N_{\text{H}}}{N_{\text{QL}} + N_{\text{H}}}, \tag{4.8a}$$

where G_0 and N_{gr} are the amplifier gain and added noise respectively, N_{H} is the noise contribution from the subsequent amplification stages in the readout line (dominated by the noise of a HEMT amplifier), N_{QL} represents the vacuum noise at the grAlPA input and A is the insertion loss between the grAlPA and the HEMT. For a near quantum limited amplifier and a HEMT with a typical noise temperature between 1.5 K to 3 K, we expect a noise visibility between 9 to 15 dB, when $AG_0 \geq 20$ dB. We find that operating the grAlPA at 22.5 dB gain yields a noise level within the range expected for a near-quantum limited amplifier. Most, importantly, this noise level is unaffected by the activation of the conversion pump, as shown in Fig. 4.10(a).

Although the noise visibility provides a first qualitative indication of the amplifier performance, a more accurate estimation of the added noise requires a dedicated calibration procedure. In our experiments, we employ a pilot tone calibrated using the AC-Stark shift and dephasing of a GFQ (see Appendix C.3) to extract the input-referred noise temperature of the readout line using SNR improvement measurements. The results are plotted in Fig. 4.10(b). The pilot tone is detuned by 5 MHz above $\tilde{\omega}_{\text{b}}$ to probe the noise performance of the grAlPA in phase-preserving mode. As shown in Fig. 4.10(b), when both pumps are off, the measured noise floor corresponds to the 3 K noise temperature of the HEMT connected after the grAlPA. When the grAlPA is double-pumped and operated

at a gain of 22.5 dB, the input-referred noise approaches the standard quantum limit for phase-preserving amplifiers [14], indicated by the blue line. We calculate the number of added noise photons, n_{add}, using relation $n_{\mathrm{add}} = n_{\mathrm{in}} + n_{\mathrm{s}}$, where n_{in} is obtained from Eq. (3.13) and $n_{\mathrm{s}} = 0.5$ represents the noise accompanying the pilot tone. As presented in Fig. 4.10(c), n_{add} initially decreases with increasing gain, which we attribute to the saturation of noise in the amplification stages following the grAlPA. However, beyond 18 dB, the added noise approaches again the quantum limit. The upturn in n_{add} observed above 25 dB likely arises from excess noise associated with metastable states that appear when the amplifier operates deeper in the multistable regime [220].

4.9 Challenges and future improvements

Although the advantageous nonlinear properties of grAl have enabled the realization of an OIBA with a non-conventional GBW product using the grAlPA, several improvements could be implemented to further enhance the device's practicality and suitability for follow-up applications.

Increasing BW beyond the MHz range

Despite the impressive grAlPA gain performance presented in Fig. 4.6, the maximum BW still remains below the 100 MHz range typically reported for impedance-engineered amplifiers [20, 57, 146, 157]. One possible route to broaden the BW is to introduce more conversion pumps, which leads to the formation of additional idler tones and corresponding peaks in the gain profiles. When these peaks coalesce, the amplifier effective BW increases, similar to the behavior illustrated in Fig. 4.2 and Fig. 4.6. In Appendix D.6, we present preliminary measurements of the grAlPA operated with two conversion pumps, in a configuration combining those of Fig. 4.4(a) and (b). Although this approach yields the tenfold bandwidth improvement expected from an ideal OIBA, it is accompanied by a factor of three increase in the amplifier noise level (cf. Fig. A4.7). This degradation is likely caused by the non-negligible noise contribution from the additional idler tones generated by the second conversion process [170].

A more effective strategy to increase the amplifier bandwidth is to enhance the coupling κ between the grAlPA and its microwave environment. In the current design (cf. Fig. 3.3), systematically increasing κ to reach bandwidths in the 100 MHz range is challenging as the coupling remains highly sensitive to setup imperfections, even with the addition of the Nb pad. Historically, this setup was adopted because it was compatible with the only available cryostat with a magnet reaching 1 T. However, having now demonstrated grAlPA's magnetic field resilience, we can redesign the device using a 2D architecture, similar to the one shown in Fig. 4.11(a). In this configuration, the grAl resonators are embedded in a coplanar waveguide (CPW) circuit that can be wirebonded directly to a coaxial transmission line and mounted in a sample box. In this geometry, κ can be controlled by varying the distance between the CPW feedline and the left grAl resonator (see Fig. 4.11(b)),

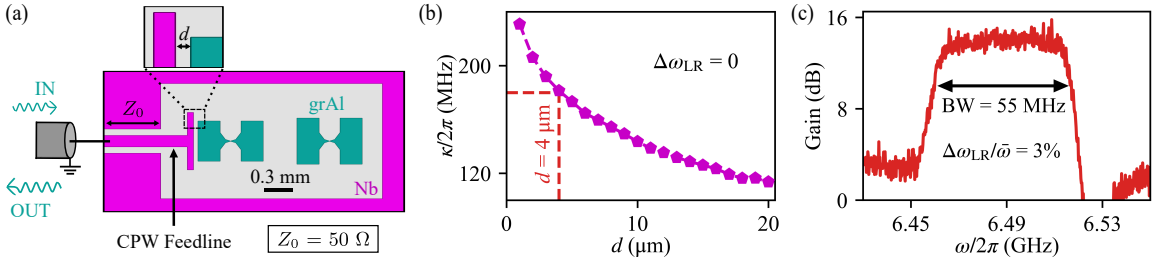

Figure 4.11: Design and preliminary results of a 2D grAlPA. (a) Optimized grAlPA design using a CPW geometry. The grAl resonators (green) are embedded inside a enclosure of a CPW line (purple). We use a feedline with characteristic impedance $Z_0 = 50\ \Omega$ to couple capacitively to the left resonator. On the other end, the feedline is coupled to a microwave port, which we use to characterize the grAlPA. **(b)** Total coupling strength κ as a function of the distance d between the feedline and the left resonator. The data was obtained using FEM simulations with the design of panel (a) and assuming perfectly hybridized grAl resonators ($\Delta\omega_{LR} = \omega_L - \omega_R = 0$). **(c)** Gain performance of a doubled-pumped grAlPA fabricated in a 2D arquitecture and with $d = 4$ μm. With the new design we increase the BW by an order of magnitude in comparison to the results in Fig. 4.6. The discrepancy with the expected bandwidth (depicted by the red line in panel b) is explained by a 3% asymmetry between the grAl resonators.

which remains fixed after fabrication. In Fig. 4.11(c), we present results from a preliminary fabrication batch using the layout shown in Fig. 4.11(a). The CPW ground plane and feedline were patterned from a 30 nm-thick Nb film. For this prototype, we observe a BW of approximately 50 MHz at 15 dB gain, representing a tenfold improvement compared to the results shown in Fig. 4.6. The device is currently limited by the ≈3% frequency asymmetry between the grAl resonators. If we reduce this asymmetry, we expect the device to exhibit a bandwidth close to 100 MHz, as predicted from FEM simulations. This performance would place the grAlPA on par with state-of-the-art standing-wave impedance-matched amplifiers.

Improving frequencies asymmetries

As previously alluded to, an important limitation of the current grAlPA design arises from the frequency asymmetry between the bare grAl resonators. This asymmetry originates from inhomogeneities in the resistivity of the grAl film. While a 2% variation in grAl resistivity, and consequently in its kinetic inductance, has negligible impact on most device applications, for the grAlPA such variation represents a significant limitation to its overall performance. First, the amplifier bandwidth is determined by the equivalent damping rate κ_{eq}, defined in Eq. (4.7). Using Eq. (3.2), we can express κ_{eq} as a function of the frequency asymmetry $\Delta\omega_{LR} = |\omega_L - \omega_R|$, such that

$$\kappa_{eq} = \frac{\kappa}{2}\left(1 - \frac{(\Delta\omega_{LR})^2}{4J^2 + (\Delta\omega_{LR})^2}\right). \tag{4.9a}$$

From this relation, we find that increasing $\Delta\omega_{\mathrm{LR}}$ leads to a reduction in κ_{eq} and, consequently, in the maximum achievable BW. Secondly, a non-zero $\Delta\omega_{\mathrm{LR}}$ contributes to the residual slope observed at the top of the gain profiles when the grAlPA is operated near the BP (see Fig. 4.6(c)).

It is therefore important to identify possible strategies to mitigate the frequency asymmetry after device fabrication. An initial approach consists in employing a post-fabrication tuning step in which part of the resonator capacitor pads is etched to adjust their frequencies according to the asymmetry measured during a preliminary cooldown. During this thesis, an alternative approach was tested, where we trimmed the capacitor pads using laser ablation. However, as shown in Appendix D.7, the resolution of this technique is insufficient to consistently reduce the frequency asymmetry below the required 2% level.

A third strategy involves reducing $\Delta\omega_{\mathrm{LR}}$ by modifying the device packaging. A simple implementation would be to integrate tuning screws into the grAlPA sample box, enabling independent adjustment of the ground capacitance of each resonator. In Appendix D.8, we present FEM simulations of this approach for a 2D grAlPA design adapted to the sample box used by Ref. [22]. Within the machining precision available at the KIT mechanical workshop, we find that the resonator frequencies can be tuned below a 2% asymmetry. The residual imbalance could be further minimized by replacing the nanostrip of Fig. 3.3(c) with a grAl loop, allowing in-situ frequency tuning via magnetic flux. This strategy has been successfully demonstrated in NbN resonators [246] and has shown promising preliminary results in grAl devices [247].

Measuring in the hybridized basis

Another limitation of the current grAlPA design is the asymmetric coupling of the grAl resonators to the microwave environment, which contributes to the reduced BW broadening when operated at the BP. This asymmetry introduces a quasi-damping rate κ_{m} (see Eq. (A1.30)), which cannot be tuned by the parametric pumps and leads to additional instability to the system dynamics. A straightforward strategy to mitigate this effect would be to include an additional microwave port, similar to the configuration illustrated in Fig. 4.1. However, a more effective improvement would be to engineer coupling ports that directly couple to the grAlPA hybridized modes, rather than to the bare resonators. Such hybrid ports would enable direct control over the coupling strengths $\kappa_{\mathrm{a/b}}$, while eliminating the unwanted quasi-damping rate κ_{m}.

In Figs. 4.12 and 4.13, we illustrate two possible strategies to extend the grAlPA concept and implement the desired hybrid ports. To clearly show the operating principle of both approaches, we redraw the grAlPA circuit diagram so that it closely resembles the experimental layout and explicitly includes all circuit nodes and parasitic ground capacitances. In the first approach, two additional feedlines are coupled to one capacitor pad in each grAl resonator. The feedlines are then routed to a 180° hybrid coupler, which separates the incoming signals into their common and differential components. This configuration enables selective coupling to each hybridized mode of the amplifier. The

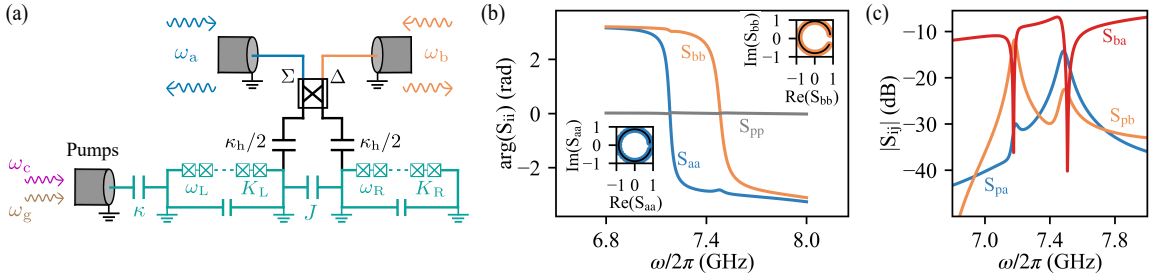

Figure 4.12: Proposed design for a grAlPA with hybrid ports. **(a)** Circuit diagram of the proposed design. Two nodes of the grAl resonators are symmetrically coupled, with coupling strength κ_h, to the ends of two independent feedlines. The opposite ends of these feedlines are connected to a 180° hybrid coupler, which separates the signals associated with the two hybridized modes of the grAlPA, $\omega_{a/b}$. The common (Σ) and differential (Δ) ports of the coupler are each connected to independent microwave environments, allowing the reflection response of $\omega_{a/b}$ to be measured individually. The grAlPA is pumped through an additional port designed to satisfy $\kappa \ll \kappa_h$, minimizing the internal damping rate of the hybridized modes as seen from each hybrid port. In this geometry, the external damping rates of the modes satisfy $\kappa_{a/b} = 2\kappa_h$. **(b)-(c)** Microwave response of a grAlPA implementing the design shown in panel (a). The data were extracted from FEM simulations using the layout presented in Fig. A4.10. Panel (b) shows the phase of the reflection coefficients S_{ii} (with i = a, b, p) for each port in the circuit. As expected, each hybrid port captures the resonance roll-off of only one dimer mode. Moreover, both modes are weakly coupled to the pump port, as evidenced by the absence of resonances in S_{pp} and by the size of the circles fits in the insets. Panel (c) shows the transmission $|S_{ij}|$ (with $i \neq j$) between each pair of ports. We observe an insertion loss of approximately 30 dB between the hybrid and pump ports, indicating that the design also reduces pump leakage.

grAlPA is pumped through the original microwave port, which remains coupled only to the left resonator. Note that in this design the pump port should be only weakly coupled (i.e., $\kappa \ll \kappa_{a/b}$), to minimize the losses of each mode as seen from the perspective of the hybrid ports. In Fig. 4.12, we present FEM simulations of a possible implementation of this design (see Appendix D.9 for details). As expected, the signals emerging from each port carry information of only a single hybridized mode (see Fig. 4.12(b)). A circle fit of the reflection coefficient at each hybrid port reveals that the ratio between external and internal quality factors satisfy the condition $Q_c/Q_i < 10$, consistent with the expected weak coupling to the pump port. The external quality factors for both modes are found to be nearly identical, with $Q_c \approx 30$. Furthermore, the transmission between the pump port and each hybrid port, as shown in Fig. 4.12(c), indicates that with the new design we can also obtain a significant reduction in pump leakage (assuming the pumps are applied in the asymmetric configuration shown in Fig. 4.4(a)).

The design presented in Fig. 4.12, although promising, comes with a caveat: the use of the hybrid coupler introduces an unavoidable −3 dB insertion loss at the amplifier input. Consequently, half of the signal from a quantum system connected to the hybrid port would be lost or reflected before reaching the amplifier. To overcome this limitation, we propose the alternative design shown in Fig. 4.13(a), which closely resembles a band-pass Purcell filter used for superconducting qubits. In this configuration, an extended λ-resonator is connected at each end to one of the capacitor plates in each grAl resonator. A segment of microwave line, open at both ends, supports resonances at frequencies $\omega_n/2\pi = n(v_p/2l)$, where l is the total line length and v_p its phase velocity [83]. The fundamental ($\lambda/2$) mode

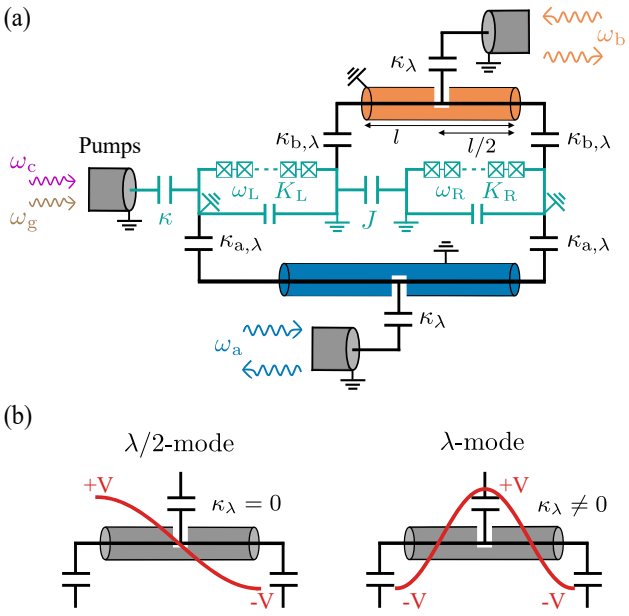

Figure 4.13: Proposed design for a grAlPA with Purcell-like ports. (a) Circuit diagram of the proposed design. Two segments of a transmission line are capacitively coupled, with coupling strength $\kappa_{a/b,\lambda}$, to one node of each grAl resonator. Feedlines connected to microwave ports are coupled, with strength κ_λ, to the transmission line segments at half of their total length l. As illustrated in panel **(b)**, the symmetry of this coupling configuration suppresses the interaction between the microwave ports and the fundamental $\lambda/2$-modes of the lines. Instead, each port couples to the first excited mode, referred to as the λ-resonator, which enables selective coupling to a single hybridized mode of the grAlPA. When the λ-resonator and the dimer modes hybridize, the effective damping rates $\kappa_{a/b}$ are given by the convolution of $\kappa_{a/b,\lambda}$ and κ_λ. A possible layout implementing this design is shown in Fig. A4.11.

generates the electric-field distribution shown in Fig. 4.13(b), while the first excited (λ) mode produces a field pattern with the same polarity at both ends. This symmetry allows selective coupling to a single hybridized mode of the amplifier.

Since the λ-mode also exhibits an antinode at the midpoint of the line, we can exploit this property to couple to an additional microwave port and realize the desired hybrid port. By tuning the length l, the resonance frequency of the λ-mode can be aligned to one of the grAlPA's dimer modes. In this scheme, the linewidth of each dimer mode is determined by the convolution of two couplings: the coupling between the λ-resonator and the external port (κ_λ) and the coupling between the λ-resonator and the corresponding grAlPA mode ($\kappa_{a/b,\lambda}$). Importantly, because the $\lambda/2$-resonator of the line has an electric node at its center, our design suppresses parasitic coupling to other resonances in the grAlPA (see Fig. 4.13(b)). Moreover, by tuning κ_λ, the λ-resonator can also act as an additional filter for the pump tones.

The design of Fig. 4.13 also come with additional advantages. First, it enables the independent design of impedance-matching networks for each hybridized mode. This would open the possibility to explore the performance of impedance-matched grAlPAs under double-pumping. Moreover, because the quadratures of the hybridized basis are now directly accessible, the new design could allow the implementation of back-action evasion protocols in a double-pumped grAlPA, potentially enhancing its sensitivity for axion-detection experiments [232].

It is important however to mention a final consideration for the Purcell-like design. Since the extended transmission-line has higher harmonic resonances, they could contribute to extra noise under double-pump operation. A generalization of the theory presented

in Section 4.2 to the case of multi-mode parametric amplifiers will therefore be essential to accurately engineer and optimize the hybrid ports.

5 Conclusions & Outlook

This thesis is dedicated to exploiting the nonlinearity of granular aluminum to fabricate parametric amplifiers that overcome the limitations of conventional JPAs. Owing to its magnetic-field resilience, low self-capacitance, and compatibility with state-of-the-art circuit fabrication, grAl stands out as an ideal material for implementing a wide range of parametric processes. Moreover, in comparison to other disordered superconductors, we found that grAl offers one of the richest and most flexible sources of nonlinearity available today. We put these assertions to test by developing a grAl-based amplifier, the grAlPA, which we used to demonstrate the two main results of this thesis: magnetic-field–resilient near quantum-limited amplification, and in situ bandwidth enhancement for gain levels up to 25 dB.

In Chapter 3, we presented the working principle of the grAlPA and demonstrated its successful operation as a magnetic-field-resilient, phase-preserving amplifier. Building on previous amplifier designs [22, 112], we fabricated the grAlPA using a Bose–Hubbard dimer model consisting of two lumped-element grAl resonators coupled via capacitive interactions. This design allowed us to achieve non-degenerate gain above 20 dB with a convenient signal–pump detuning of approximately 100 MHz. By tuning the self-Kerr nonlinearity of the grAlPA to $K \approx 3$ kHz, the device reached saturation powers of -111 dBm, on par with earlier implementations based on Josephson-junction arrays, and with a clear path toward matching state-of-the-art JPAs through minor adjustments to the current design. Furthermore, we engineered the grAlPA to exhibit a bandwidth of $\approx$ 2-3 MHz at 20 dB gain, which was proven to be sufficient for performing single-shot readout of a generalized flux qubit. Most importantly, thanks to grAl's magnetic-field resilience, the grAlPA remained near quantum limited under in-plane magnetic fields of up to 1 T, well beyond the typical operational range of conventional JPAs. Although this performance is impressive, fully exploiting grAl's resilience requires the amplifier to maintain stable operation under magnetic fields applied in all directions. For the grAlPA, we showed that although 20 dB gain is achievable also for out-of-plane magnetic fields up to 22 mT, the accidental trapping of vortices in the device structure leads to unwanted fluctuations and instabilities in the gain profiles. We suggest that reducing the effective dimensions of the current design and incorporating vortex-pinning sites in the pads could mitigate this issue. Such improvements would place the grAlPA in an excellent position for use in the readout of, for example, semiconductor and molecular spin qubits.

In Chapter 3, we exploited the balance between reduced higher-order nonlinearities and mitigated frequency crowding, enabled by the low self-capacitance of grAl, to realize a Bogoliubov amplifier with a non-conventional gain–bandwidth product at gain levels up

to 25 dB. To achieved this, we apply two parametric pumps that simultaneously activated phase-preserving gain and frequency conversion between the modes of the grAlPA. By tuning the relative effects of the pumps, we obtained a broadening of the gain profiles, achieving a tenfold bandwidth improvement at 20 dB gain and surpassing the performance reported for JPCs. Importantly, we observed that the added noise remains unchanged upon introducing the second pump. However, we find that the bandwidth improvement depends drastically on the asymmetry in the frequencies and damping rates of the grAlPA resonators. A similar trend appears in the saturation power. For highly asymmetric resonators, we observed an order of magnitude reduction relative to the single-pumped grAlPA, while the expected saturation level of approximately −110 dBm is recovered once the asymmetry is reduced to below 1%. It is also worth noting that we did not observe an improvement in the pump-depletion threshold predicted by Ref. [168], which we attributed to the fact that the grAlPA saturation power is limited by signal-induced Kerr effects. The results presented in this chapter demonstrate that a double-pumped grAlPA is a viable alternative for overcoming the bandwidth limitations of conventional JJ-based amplifiers, and could be further enhanced when combined with impedance-matching techniques [192].

Outlook and future perspectives

While the results presented throughout this manuscript provide an initial indication of the advantages of using grAl for parametric devices, we expect that several follow-up experiments could offer even stronger evidence for this case. In particular, although the diluted higher-order nonlinearities and the clean frequency spectrum enabled the realization of the Bogoliubov amplifier presented in Chapter 4, a more quantitative study of these effects and a comparison with other amplifiers, are still needed. One way to assess this would be to measure the so-called intermodulation products by applying multiple signal tones to the grAlPA [24, 54, 83, 152]. This technique is rapidly becoming a standard characterization method in the community and would be highly valuable for determining the applicability of grAl amplifiers in contexts such as qubit-multiplexed readout [248] and novel parametric qubit-qubit coupling schemes [249].

In addition, the role of disorder in determining grAl's nonlinearity remains an open question. As discussed in Chapter 2, a key parameter for characterizing the nonlinear strength of a superconducting film is the characteristic current j_*. Finding ways to improve this quantity is crucial for the engineering of future parametric devices. Based on its microstructure, one might assume that in grAl this parameter can be modeled using the uniformly distributed JJ-array model, which predicts the relation $j_* = \sqrt{2} j_c$. This relation has been validated, for example, in the case of grAl nano-constrictions, as shown in Ref. [179]. However, more recent measurements on extended grAl resonators shown by Ref. [202], found the relation $j_* \approx 3.3 j_c$, surprisingly similar to the Mattis-Bardeen prediction. We speculate that the discrepancy between these experiments originates from the role of disorder in the effective grAl volume responsible for the circuit's nonlinearity. In extended structures, such as the resonators used in Ref. [202], the uniformly distributed JJ-array model may be an oversimplification of the material microscopic dynamics. A

more refined model should account for potential inhomogeneities within the grAl film, for example, by considering a JJ network with a distribution of critical currents rather than a single uniform value. Future experiments, using the measurement method shown by Ref. [202], but performed on grAl resonators with different dimensions and resistivities, could provide deeper insights into this discrepancy. Such studies would also greatly benefit from complementary theoretical investigations of the nonlinear properties of inhomogeneous JJ arrays and networks.

Finally, granular aluminum parametric devices could also serve as efficient sources of non-classical states of light. In quantum optics, it has long been known that a parametric amplifier can generate single-mode or two-mode vacuum squeezing when operated in phase-sensitive or phase-preserving mode, respectively [86]. These states are characterized by having quadrature correlations below the standard quantum limit. Experiments using various types of parametric amplifiers have already demonstrated the generation of such states in the microwave domain [60, 110–114, 241, 250]. They hold great promise to be used also in quantum teleportation experiments [104], enhanced quantum sensing [102, 227] and quantum links between distant qubits [105, 231]. However, it has been reported that JJ-based amplifiers have an intrinsic limitations arising from higher-order nonlinearities in the circuit [105, 250–252]. This observation suggests that grAl could be a promising alternative also for squeezing at microwave frequencies.

Appendix

A Bose-Hubbard dimer model: extended calculations

In this appendix, we show the calculations for the theory of the Bose-Hubbard dimer.

A.1 Dynamics in the absence of pump tones

Bare basis

The dynamics of the Bose-Hubbard dimer shown in Fig. 3.1(a) is described by the following Hamiltonian [22, 130]

$$\hat{H}/\hbar = \sum_{i=\mathrm{L,R}} \left(\omega_i \hat{a}_i^\dagger \hat{a}_i + \frac{K_i}{2} \hat{a}_i^\dagger \hat{a}_i^\dagger \hat{a}_i \hat{a}_i \right) + J \hat{a}_\mathrm{L}^\dagger \hat{a}_\mathrm{R} + \mathrm{h.c.}, \tag{A1.1}$$

where $\hat{a}_{\mathrm{L,R}}$ are the annihilation operators of each superconducting resonator, and $\omega_{\mathrm{L,R}}$ and $K_{\mathrm{L,R}}$ denote their respective resonance frequencies and self-Kerr nonlinearities. The hopping coefficient J arises from the capacitive coupling between the bare resonators.

When a signal enters through the microwave port with an amplitude $\hat{a}_\mathrm{in}$, produces a variation of the operators $\hat{a}_{\mathrm{L,R}}$. Their time evolution can be calculated using the Heisenberg-Langevin equation (see Eq. (1.27)), which for our model can be written as

$$\begin{aligned} \frac{d\hat{a}_\mathrm{L}}{dt} &= -i\omega_\mathrm{L}\hat{a}_\mathrm{L} - iK_\mathrm{L}\hat{a}_\mathrm{L}^\dagger\hat{a}_\mathrm{L}^2 - iJ\hat{a}_\mathrm{R} - \kappa\frac{\hat{a}_\mathrm{L}}{2} - \sqrt{\kappa}\,\hat{a}_\mathrm{in}, \\ \frac{d\hat{a}_\mathrm{R}}{dt} &= -i\omega_\mathrm{R}\hat{a}_\mathrm{R} - iK_\mathrm{R}\hat{a}_\mathrm{R}^\dagger\hat{a}_\mathrm{R}^2 - iJ\hat{a}_\mathrm{L} - \gamma\frac{\hat{a}_\mathrm{R}}{2}, \end{aligned} \tag{A1.2}$$

where κ is the external ramping rate of the left resonator and γ the loss rate in the right resonator. Applying a Fourier transform to Eq. (A1.2), we can then derive the equations

$$\begin{aligned} 0 &= i\delta_\mathrm{L}\hat{a}_\mathrm{L} - iJ\hat{a}_\mathrm{R} - \kappa\frac{\hat{a}_\mathrm{L}}{2} - \sqrt{\kappa}\,\hat{a}_\mathrm{in}, \\ 0 &= i\delta_\mathrm{R}\hat{a}_\mathrm{R} - iJ\hat{a}_\mathrm{L} - \gamma\frac{\hat{a}_\mathrm{R}}{2}, \end{aligned} \tag{A1.3}$$

where $\delta_j = \omega - \omega_j - K_j\, n_\mathrm{j}$ (with $j = \mathrm{L, R}$) are the Kerr-shifted detunings from the bare grAl frequencies $\omega_{\mathrm{L/R}}$ and $n_{\mathrm{L/R}} = |\left\langle \hat{a}_{\mathrm{L/R}} \right\rangle|^2$ their respective photon number populations.

For the case of the Bose-Hubbard dimer, the input-output relations follow

$$\hat{a}_{\mathrm{out}} = -\hat{a}_{\mathrm{in}} + \sqrt{\kappa}\,\hat{a}_{\mathrm{L}}. \tag{A1.4}$$

We can therefore use Eq. (A1.3) and Eq. (A1.4), to get an analytical expression of the reflection coefficient $\mathrm{S}_{11} = a_{\mathrm{out}}/a_{\mathrm{in}}$, which is given by

$$\mathrm{S}_{11}(\omega) = -1 + \frac{i\kappa\,(\delta_{\mathrm{R}} - i\gamma/2)}{J^2 - (\delta_{\mathrm{R}} - i\gamma/2)\,(\delta_{\mathrm{L}} - i\kappa/2)}, \tag{A1.5}$$

Taking the approximations $J = K_{\mathrm{L,R}} = 0$, Eq. (A1.5) reduces to the expected reflection coefficient of a lossless linear harmonic oscillator (cf. Eq. (1.30)) for the left resonator.

Hybridized basis

Due to the hopping interaction J, the energy levels of the system get hybridized. The linear part of the Hamiltonian (A1.1) can be diagonalized if we introduce a pair of hybridized modes, given by

$$\begin{aligned} \hat{a} &= -\sin(\theta)\,\hat{a}_{\mathrm{L}} + \cos(\theta)\,\hat{a}_{\mathrm{R}} \\ \hat{b} &= \cos(\theta)\,\hat{a}_{\mathrm{L}} + \sin(\theta)\,\hat{a}_{\mathrm{R}}, \end{aligned} \tag{A1.6}$$

with resonance frequencies

$$\omega_{\mathrm{a/b}} = \frac{(\omega_{\mathrm{L}} + \omega_{\mathrm{R}})}{2} \pm \sqrt{J^2 + \left(\frac{\Delta\omega_{\mathrm{LR}}}{2}\right)^2}, \tag{A1.7}$$

where $\tan(2\theta) = 2J/\Delta\omega_{\mathrm{LR}}$ and $\Delta\omega_{\mathrm{LR}} = \omega_{\mathrm{R}} - \omega_{\mathrm{L}}$. We can then rewrite the Hamiltonian in terms of the hybridized modes, such that we obtain

$$\begin{aligned} \hat{H}/\hbar = {} & \omega_{\mathrm{a}}\hat{a}^\dagger\hat{a} + \omega_{\mathrm{b}}\hat{b}^\dagger\hat{b} + \frac{K_{\mathrm{aa}}}{2}\hat{a}^\dagger\hat{a}^\dagger\hat{a}\hat{a} + \frac{K_{\mathrm{bb}}}{2}\hat{b}^\dagger\hat{b}^\dagger\hat{b}\hat{b} \\ & + \frac{K_{\mathrm{ab}}}{8}\left(\hat{a}^\dagger\hat{a}^\dagger\hat{b}\hat{b} + \mathrm{h.c.}\right) + \frac{K_{\mathrm{ab}}}{2}\hat{a}^\dagger\hat{a}\hat{b}^\dagger\hat{b} \\ & - \frac{K_{\mathrm{ab}}}{4}\left[\mu_-\left(\hat{a}^\dagger\hat{a}^\dagger\hat{a}\hat{b} + \mathrm{h.c.}\right) + \mu_+\left(\hat{b}^\dagger\hat{b}^\dagger\hat{b}\hat{a} + \mathrm{h.c.}\right)\right]. \end{aligned} \tag{A1.8}$$

where K_{aa}, K_{bb}, and K_{ab} denote the collective self-Kerr and cross-Kerr coefficients and are given by

$$K_{ab} = \frac{J^2\,(K_L + K_R)}{J^2 + \Delta\omega_{LR}^2},$$

$$K_{aa} = \frac{1}{4}K_{ab}\left(1 + \frac{2\Delta\omega_{LR}^2}{J^2}\right) - \frac{(K_L - K_R)\;\Delta\omega_{LR}}{2\sqrt{J^2 + \Delta\omega_{LR}^2}}, \tag{A1.9}$$

$$K_{bb} = \frac{1}{4}K_{ab}\left(1 + \frac{2\Delta\omega_{LR}^2}{J^2}\right) + \frac{(K_L - K_R)\;\Delta\omega_{LR}}{2\sqrt{J^2 + \Delta\omega_{LR}^2}}.$$

Additionally, the coefficients $\mu_\pm$, which quantify the frequency shift induced by the nonlinear hopping interactions ($\propto a^\dagger a^\dagger ab + b^\dagger b^\dagger ba + \text{h.c.}$), are given by

$$\mu_\pm = \sqrt{1 + \frac{\Delta\omega_{LR}^2}{J^2}}\,\frac{(K_L - K_R)}{(K_L + K_R)} \pm \frac{\Delta\omega_{LR}}{J}. \tag{A1.10}$$

A.2 Dynamics in the presence of a single pump

Bare basis

In presence of a pump tone applied at frequency ω_g, we can decompose the operators $\hat{a}_{L,R}$ into a classical mean-field amplitude $\alpha_{L,R}$ and a fluctuation operator, such that

$$\hat{a}_{L/R} \rightarrow \alpha_{L/R}e^{-i\omega_g t} + \hat{a}_{L/R}. \tag{A1.11}$$

Then, we can likewise divide the equations of motion (cf. Eq. (A1.3)) into a mean-field part, modeling the dynamics of the pump, and a quantum part, which determines the time evolution of the fluctuations. Applying a stiff pump approximation $|\hat{a}_{L,R}| \ll |\alpha_{L,R}|$ and neglecting internal losses ($\gamma = 0$), we obtain

$$\begin{aligned} \alpha_R\delta_R &= J\alpha_L, \\ \alpha_L\left(\delta_L + i\frac{\kappa}{2}\right) &= J\alpha_R - i\sqrt{\kappa}\,\alpha_{in}. \end{aligned} \tag{A1.12}$$

where $\delta_{L/R} = \omega_g - \omega_{L/R} - K_{L/R}\,|\alpha_{L/R}|^2$ and $|\alpha_{in}|^2 = P_g/(\hbar\omega_g)$. We denote P_g as the pump power at the amplifier input. Moreover, for the fluctuation operators we derive the following equations of motion

$$\frac{d\vec{\hat{a}}_B}{dt} = \mathbf{M}_B\,\vec{\hat{a}}_B - \mathbf{K}_B\,\vec{\hat{a}}_{B,in}, \tag{A1.13}$$

where $\vec{\hat{a}}_{\mathrm{B}} = \left(\hat{a}_{\mathrm{L}}, \hat{a}_{\mathrm{R}}, \hat{a}_{\mathrm{L}}^{\dagger}, \hat{a}_{\mathrm{R}}^{\dagger}\right)^{T}$, and $\vec{\hat{a}}_{\mathrm{B,in}} = \left(\hat{a}_{\mathrm{L,in}}, \hat{a}_{\mathrm{R,in}}, \hat{a}_{\mathrm{L,in}}^{\dagger}, \hat{a}_{\mathrm{R,in}}^{\dagger}\right)^{T}$. Moreover, $\mathbf{M}_{\mathrm{B}}$ is called the system drift matrix, which is given by

$$\mathbf{M}_{\mathrm{B}} = \begin{pmatrix} i\delta_{\mathrm{L}} - \frac{\kappa}{2} & -i\,J & -i\,K_{\mathrm{L}}\alpha_{\mathrm{L}}^{2} & 0 \\ -i\,J & i\delta_{\mathrm{R}} & 0 & -i\,K_{\mathrm{R}}\alpha_{\mathrm{R}}^{2} \\ i\,K_{\mathrm{L}}\alpha_{\mathrm{L}}^{2} & 0 & -i\delta_{\mathrm{L}} - \frac{\kappa}{2} & i\,J \\ 0 & i\,K_{\mathrm{R}}\alpha_{\mathrm{R}}^{2} & i\,J & -i\delta_{\mathrm{R}} \end{pmatrix}. \tag{A1.14}$$

We also call $\mathbf{K}_{\mathrm{B}}$ the system damping matrix, which is given by

$$\mathbf{K}_{\mathrm{B}} = \begin{pmatrix} \sqrt{\kappa} & 0 & 0 & 0 \\ 0 & 0 & 0 & 0 \\ 0 & 0 & \sqrt{\kappa} & 0 \\ 0 & 0 & 0 & 0 \end{pmatrix}. \tag{A1.15}$$

We can now transform the system into the frequency domain using the following Fourier transform

$$\hat{a}_{\mathrm{L/R}}(t) = \frac{1}{\sqrt{2\pi}} \int d\Delta\, \hat{a}_{\mathrm{L/R}}(\Delta)\, \mathrm{e}^{-i\Delta t}, \tag{A1.16}$$

where $\Delta = \omega - \omega_{\mathrm{g}}$ and ω denote the frequency of the input signal. Combining this transformation with the input-output relation (A1.4), we can calculate the system scattering matrix in terms of the input and output fluctuations $\vec{a}_{\mathrm{B,in/out}} = \left(a_{\mathrm{L,in/out}}(\omega_{\mathrm{s}}), 0, a_{\mathrm{L,in/out}}^{\dagger}(\omega_{\mathrm{i}}), 0\right)^{T}$. We denote ω_{s} and $\omega_{\mathrm{i}} = 2\omega_{\mathrm{g}} - \omega_{\mathrm{s}}$ as the signal and idler frequencies, respectively. For the single-pumped BHD, the scattering matrix is given by

$$\mathrm{S}(\omega) = \mathbf{K}_{\mathrm{B}}\Big(\pm i\Delta \mathbf{1}_4 + \mathbf{M}_{\mathrm{B}}\Big)^{-1}\mathbf{K}_{\mathrm{B}} + \mathbf{1}_4. \tag{A1.17}$$

Therefore, the amplifier gain at the signal frequency is defined by

$$G(\omega) = |S_{11}(\omega)|^{2}. \tag{A1.18}$$

Hybridized basis

In the hybridized basis, we can separate the dynamics of the dressed modes into a mean-field amplitudes α, β and quantum fluctuations, such that

$$\begin{aligned} \hat{a} &\rightarrow \alpha \mathrm{e}^{-i\omega_{\mathrm{g}}t} + \hat{a}, \\ \hat{b} &\rightarrow \beta \mathrm{e}^{-i\omega_{\mathrm{g}}t} + \hat{b}. \end{aligned} \tag{A1.19}$$

We can connect the mean-field amplitudes in the bare and hybridized basis using the relations

$$\begin{aligned} \alpha &= -\sin(\theta)\, \alpha_{\mathrm{L}} + \cos(\theta)\, \alpha_{\mathrm{R}}, \\ \beta &= \cos(\theta)\, \alpha_{\mathrm{L}} + \sin(\theta)\, \alpha_{\mathrm{R}}. \end{aligned} \tag{A1.20}$$

Applying the displacement transformations of Eq. (A1.20), we can linearize Hamiltonian Eq. (A1.8) and obtain

$$\begin{aligned}\hat{H}/\hbar = \tilde{\omega}_{\mathrm{a}}\hat{a}^{\dagger}\hat{a} + \left(\Lambda_{\mathrm{S_a}}(t)\hat{a}^{\dagger}\hat{a}^{\dagger} + \mathrm{h.c.}\right) + \tilde{\omega}_{\mathrm{b}}\hat{b}^{\dagger}\hat{b} + \left(\Lambda_{\mathrm{S_b}}(t)\hat{b}^{\dagger}\hat{b}^{\dagger} + \mathrm{h.c.}\right) \\ + \left(\Lambda_{\mathrm{BS}}(t)\hat{a}^{\dagger}\hat{b} + \mathrm{h.c.}\right) + \left(\Lambda_{\mathrm{TMS}}(t)\hat{a}^{\dagger}\hat{b}^{\dagger} + \mathrm{h.c.}\right),\end{aligned} \tag{A1.21}$$

where $\tilde{\omega}_{\mathrm{a/b}}$ are the Kerr-shifted dimer frequencies. The terms $\Lambda_{\mathrm{S_{a/b}}}$, Λ_{BS} and Λ_{TMS} denote single-mode squeezing, beam-splitter and two-mode squeezing interactions. All these quantities can be written as a function of the mean-field amplitudes $\alpha_{\mathrm{L,R}}$, such that

$$\begin{aligned}\tilde{\omega}_{\mathrm{a}} &= \omega_{\mathrm{a}} + 2K_{\mathrm{L}}\left|\alpha_{\mathrm{L}}\right|^2\sin^2(\theta) + 2K_{\mathrm{R}}\left|\alpha_{\mathrm{R}}\right|^2\cos^2(\theta), \\ \tilde{\omega}_{\mathrm{b}} &= \omega_{\mathrm{b}} + 2K_{\mathrm{L}}\left|\alpha_{\mathrm{L}}\right|^2\cos^2(\theta) + 2K_{\mathrm{R}}\left|\alpha_{\mathrm{R}}\right|^2\sin^2(\theta),\end{aligned} \tag{A1.22}$$

$$\begin{aligned}\Lambda_{\mathrm{S_a}}(t) &= K_{\mathrm{L}}\alpha_{\mathrm{L}}^2\mathrm{e}^{-2i\omega_{\mathrm{g}}t}\sin^2(\theta) + K_{\mathrm{R}}\alpha_{\mathrm{R}}^2\mathrm{e}^{-2i\omega_{\mathrm{g}}t}\cos^2(\theta), \\ \Lambda_{\mathrm{S_b}}(t) &= K_{\mathrm{L}}\alpha_{\mathrm{L}}^2\mathrm{e}^{-2i\omega_{\mathrm{g}}t}\cos^2(\theta) + K_{\mathrm{R}}\alpha_{\mathrm{R}}^2\mathrm{e}^{-2i\omega_{\mathrm{g}}t}\sin^2(\theta),\end{aligned} \tag{A1.23}$$

$$\Lambda_{\mathrm{TMS}}(t) = -\frac{\mathrm{e}^{-2i\omega_{\mathrm{g}}t}}{2}\left(K_{\mathrm{L}}\alpha_{\mathrm{L}}^2 - K_{\mathrm{R}}\alpha_{\mathrm{R}}^2\right)\sin(2\theta), \tag{A1.24}$$

$$\Lambda_{\mathrm{BS}}(t) = -\left(K_{\mathrm{L}}|\alpha_{\mathrm{L}}|^2 - K_{\mathrm{R}}|\alpha_{\mathrm{R}}|^2\right)\sin(2\theta). \tag{A1.25}$$

We transform Eq. (A1.13) into the hybridized basis using the relations

$$\begin{aligned}\frac{d\vec{\hat{a}}_{\mathrm{H}}}{dt} = \frac{d(\mathbf{T}\vec{\hat{a}}_{\mathrm{B}})}{dt} &= \mathbf{T}\mathbf{M}_{\mathrm{B}}\,\vec{\hat{a}}_{\mathrm{B}} - \mathbf{T}\mathbf{K}_{\mathrm{B}}\,\vec{\hat{a}}_{\mathrm{B,in}} \\ &= (\mathbf{T}\mathbf{M}_{\mathrm{B}}\mathbf{T}^{T})(\mathbf{T}\,\vec{\hat{a}}_{\mathrm{B}}) - (\mathbf{T}\mathbf{K}_{\mathrm{B}}\mathbf{T}^{T})(\mathbf{T}\,\vec{\hat{a}}_{\mathrm{B,in}}) \\ &= \mathbf{M}_{\mathrm{H}}\,\vec{\hat{a}}_{\mathrm{H}} - \mathbf{K}_{\mathrm{H}}\,\vec{\hat{a}}_{\mathrm{H,in}},\end{aligned} \tag{A1.26}$$

where $\vec{\hat{a}}_{\mathrm{H}} = \left(\hat{a}, \hat{b}, \hat{a}^{\dagger}, \hat{b}^{\dagger}\right)^{T}$ and $\vec{\hat{a}}_{\mathrm{H,in}} = \left(\hat{a}_{\mathrm{in}}, \hat{b}_{\mathrm{in}}, \hat{a}_{\mathrm{in}}^{\dagger}, \hat{b}_{\mathrm{in}}^{\dagger}\right)^{T}$ and $\mathbf{T}$ is the transformation matrix defined by

$$\mathbf{T} = \begin{pmatrix} \cos(\theta) & \sin(\theta) & 0 & 0 \\ -\sin(\theta) & \cos(\theta) & 0 & 0 \\ 0 & 0 & \cos(\theta) & \sin(\theta) \\ 0 & 0 & -\sin(\theta) & \cos(\theta) \end{pmatrix}, \tag{A1.27}$$

The drift and damping matrices in the hybridized basis take the form

$$\mathbf{M}_{\mathrm{H}} = \begin{pmatrix} -\frac{\kappa_{\mathrm{a}}}{2} + i\delta_{\mathrm{a}} & \frac{\kappa_{\mathrm{m}}}{2} + i\Lambda_{\mathrm{BS}} & -2i\Lambda_{\mathrm{S_a}} & i\Lambda_{\mathrm{TMS}} \\ \frac{\kappa_{\mathrm{m}}}{2} + i\Lambda_{\mathrm{BS}} & -\frac{\kappa_{\mathrm{b}}}{2} + i\delta_{\mathrm{b}} & i\Lambda_{\mathrm{TMS}} & -2i\Lambda_{\mathrm{S_b}} \\ 2i\Lambda_{\mathrm{S_a}}^{*} & -i\Lambda_{\mathrm{TMS}}^{*} & -\frac{\kappa_{\mathrm{a}}}{2} - i\delta_{\mathrm{a}} & -\frac{\kappa_{\mathrm{m}}}{2} - i\Lambda_{\mathrm{BS}} \\ -i\Lambda_{\mathrm{TMS}}^{*} & 2i\Lambda_{\mathrm{S_b}}^{*} & -\frac{\kappa_{\mathrm{m}}}{2} - i\Lambda_{\mathrm{BS}} & -\frac{\kappa_{\mathrm{b}}}{2} - i\delta_{\mathrm{b}} \end{pmatrix}, \tag{A1.28}$$

and

$$\mathbf{K}_{\mathrm{H}} = \begin{pmatrix} \sqrt{k_{\mathrm{a}}} & 0 & 0 & 0 \\ 0 & \sqrt{k_{\mathrm{b}}} & 0 & 0 \\ 0 & 0 & \sqrt{k_{\mathrm{a}}} & 0 \\ 0 & 0 & 0 & \sqrt{k_{\mathrm{b}}} \end{pmatrix}, \tag{A1.29}$$

where $\delta_{a/b} = \omega_g - \tilde{\omega}_{a/b}$ and the damping rates $\kappa_{a/b}$ and κ_m can be written as

$$\begin{aligned} \kappa_a &= \kappa \sin^2(\theta), \\ \kappa_b &= \kappa \cos^2(\theta), \\ \kappa_m &= \frac{\kappa_L - \kappa_R}{2} \sin(2\theta) = \frac{\kappa}{2} \sin(2\theta). \end{aligned} \tag{A1.30}$$

We denote $\kappa_{L/R}$ as the damping rates of the bare grAl resonators, which for the design in Fig. 3.1(a) take the values $\kappa_L = \kappa$ and $\kappa_R = 0$. Interestingly, this asymmetry gives rise to a non-zero "quasi"-damping rate κ_m. This term arises from the energy exchange between the dimer modes, enabled due to the absence of other damping mechanisms like internal losses or coupling to additional microwave ports.

By applying the Fourier transform defined in Eq. (A1.15) and using the input-output relations, we can calculate the scattering matrix in terms of the input fluctuations in the hybridized basis. We obtain

$$\mathbf{S}^H(\omega) = \mathbf{K}_H \Big(\pm i\Delta \mathbf{1}_4 + \mathbf{M}_H \Big)^{-1} \mathbf{K}_H + \mathbf{1}_4. \tag{A1.31}$$

Then, the frequency dependent gain close to each dimer mode follows the formula

$$G_{a/b}(\omega) = |S^H_{11/22}(\omega)|^2 = \left| \frac{4|\Lambda_{TMS}|^2 - \Big[i\kappa_{a/b} - 2(\omega - \tilde{\omega}_{a/b}) \Big] \Big[i\kappa_{b/a} + 2\left(\omega + \tilde{\omega}_{b/a} - 2\omega_g\right) \Big]}{4|\Lambda_{TMS}|^2 + \Big[i\kappa_{a/b} + 2(\omega - \tilde{\omega}_{a/b}) \Big] \Big[i\kappa_{b/a} + 2\left(\omega + \tilde{\omega}_{b/a} - 2\omega_g\right) \Big]} \right|^2 . \tag{A1.32}$$

When $2\omega_g = \tilde{\omega}_a + \tilde{\omega}_b$, the formula above describes a Lorentzian shape centered at each $\tilde{\omega}_{a,b}$, in agreement with the experimental curves shown in Fig. 3.7(a). The maximum gain is obtained when $\omega = \tilde{\omega}_{a,b}$, and is given by

$$G_0 = \left| \frac{C_{TMS} + 1}{C_{TMS} - 1} \right|^2 . \tag{A1.33}$$

where $C_{TMS} = 4|\Lambda_{TMS}|^2/\kappa_a\kappa_b$ is the cooperativity of the two-mode squeezing interactions. Eq. (A1.33) is very similar to the results obtained for a degenerate JPA in Eq. (1.46). Increasing the pump amplitude leads to an increase in Λ_{TMS}, which in turn results in higher gain levels.

Dynamical stability

To determine the stability of the system, we use the Routh–Hurwitz criterion [142] mentioned in Section 1.3.2. Therefore, we calculate the eigenvalues of the matrix in Eq. (A1.28), such that we obtain

$$\begin{aligned} \epsilon_{1/2} &= -\frac{i}{2}\big(\delta_a - \delta_b\big) - \frac{1}{4}\big(\kappa_a + \kappa_b\big) \pm \frac{i}{4}\sqrt{\big[2\big(\delta_a + \delta_b\big) - i\big(\kappa_a - \kappa_b\big)\big]^2 - 16\,|\Lambda_{TMS}|^2}, \\ \epsilon_{3/4} &= \frac{i}{2}\big(\delta_a + \delta_b\big) - \frac{1}{4}\big(\kappa_a + \kappa_b\big) \pm \frac{i}{4}\sqrt{\big[2\big(\delta_a - \delta_b\big) + i\big(\kappa_a - \kappa_b\big)\big]^2 - 16\,|\Lambda_{TMS}|^2}. \end{aligned} \tag{A1.34}$$

One can show that for all eigenvalues, their real part remain negative if $C_{\mathrm{TMS}} < 1$.

A.3 Dynamics in the presence of two pumps

Bare basis

When we apply two pumps at frequencies ω_{g} and ω_{c}, we can decompose again the bosonic operators $\hat{a}_{\mathrm{L/R}}$ into mean-field amplitudes $\alpha^{\mathrm{g/c}}_{\mathrm{L/R}}$ and quantum fluctuations, such that

$$\hat{a}_{\mathrm{L/R}} \rightarrow \alpha^{\mathrm{g}}_{\mathrm{L/R}} \mathrm{e}^{-i\omega_{\mathrm{g}}t} + \alpha^{\mathrm{c}}_{\mathrm{L/R}} \mathrm{e}^{-i\omega_{\mathrm{c}}t} + \hat{a}_{\mathrm{L/R}}. \tag{A1.35}$$

We can now use a stiff pump approximation and linearize Hamiltonian Eq. (A1.1) using the displacement transformation in Eq. (A1.35). We obtain then

$$\begin{aligned} \hat{H}/\hbar = \tilde{\omega}_{\mathrm{L}}(t)\, \hat{a}^{\dagger}_{\mathrm{L}}\hat{a}_{\mathrm{L}} + \tilde{\omega}_{\mathrm{R}}(t)\, \hat{a}^{\dagger}_{\mathrm{R}}\hat{a}_{\mathrm{R}} + J\left(\hat{a}^{\dagger}_{\mathrm{L}}\hat{a}_{\mathrm{R}} + \mathrm{h.c.}\right) \\ + \left(\tilde{K}_{\mathrm{L}}(t)\, a^{\dagger}_{\mathrm{L}}a^{\dagger}_{\mathrm{L}} + \mathrm{h.c.}\right) + \left(\tilde{K}_{\mathrm{R}}(t)\, \hat{a}^{\dagger}_{\mathrm{R}}\hat{a}^{\dagger}_{\mathrm{R}} + \mathrm{h.c.}\right), \end{aligned} \tag{A1.36}$$

where the Kerr-induced frequency shifts of the bare resonators are given by

$$\begin{aligned} \tilde{\omega}_{\mathrm{L/R}}(t) = \omega_{\mathrm{L/R}} + 2K_{\mathrm{L/R}}|\alpha_{\mathrm{L/R}}(t)|^2 = \omega_{\mathrm{L/R}} + 2K_{\mathrm{L,R}}\left(|\alpha^{\mathrm{g}}_{\mathrm{L/R}}|^2 + \alpha^{\mathrm{c}}_{\mathrm{L,R}}|^2\right) \\ + 2\,K_{\mathrm{L/R}}\left(\alpha^{\mathrm{g}}_{\mathrm{L/R}}{\alpha^{\mathrm{c}}_{\mathrm{L/R}}}^{*}\,\mathrm{e}^{-i\Delta_p t} + \mathrm{h.c.}\right), \end{aligned}$$

where $\Delta_{\mathrm{p}} = \omega_{\mathrm{g}} - \omega_{\mathrm{c}}$. Moreover, the effective time-dependent Kerr coefficients take the form

$$\begin{aligned} \tilde{K}_{\mathrm{L/R}}(t) = \frac{K_{\mathrm{L/R}}}{2}\alpha^2_{\mathrm{L/R}}(t) = \frac{K_{\mathrm{L/R}}}{2}\Big((\alpha^{\mathrm{g}}_{\mathrm{L/R}})^2\,\mathrm{e}^{-2i\omega_g t} + (\alpha^{\mathrm{c}}_{\mathrm{L/R}})^2\,\mathrm{e}^{-2i\omega_c t} \\ + 2\,\alpha^{\mathrm{c}}_{\mathrm{L/R}}\,\alpha^{\mathrm{g}}_{\mathrm{L/R}}\,\mathrm{e}^{-i(\omega_g+\omega_c)t}\Big). \end{aligned}$$

We simplify Hamiltonian (A1.36), by applying a rotating frame transformation at a frequency[1] $\tilde{\omega}_{\mathrm{a}} = (\omega_{\mathrm{g}} + \omega_{\mathrm{c}})/2$, such that $\hat{a}_{\mathrm{L}} \rightarrow \hat{a}_{\mathrm{L}}\mathrm{e}^{-i\tilde{\omega}_{\mathrm{a}}t}$, and $\hat{b}_{\mathrm{R}} \rightarrow \hat{b}_{\mathrm{R}}\mathrm{e}^{-i\tilde{\omega}_{\mathrm{a}}t}$. Hence, Eq. (A1.36) can be rewritten as

$$\begin{aligned} \hat{H}/\hbar = \left(\tilde{\omega}_{\mathrm{L}} - \tilde{\omega}_{\mathrm{a}} + K_{1,\mathrm{L}}\,\mathrm{e}^{-i\Delta_{\mathrm{p}}t} + K_{2,\mathrm{L}}\,\mathrm{e}^{i\Delta_{\mathrm{p}}t}\right)\hat{a}^{\dagger}_{\mathrm{L}}\hat{a}_{\mathrm{L}} \\ + \left(\tilde{\omega}_{\mathrm{R}} - \tilde{\omega}_{\mathrm{a}} + K_{1,\mathrm{R}}\,\mathrm{e}^{-i\Delta_{\mathrm{p}}t} + K_{2,\mathrm{R}}\,\mathrm{e}^{i\Delta_{\mathrm{p}}t}\right)\hat{a}^{\dagger}_{\mathrm{R}}\hat{a}_{\mathrm{R}} \\ + \frac{1}{2}\Big[\left(K_{3,\mathrm{L}}\,\mathrm{e}^{-i\Delta_{\mathrm{p}}t} + K_{4,\mathrm{L}}\,\mathrm{e}^{i\Delta_{\mathrm{p}}t} + K_{5,\mathrm{L}}\right)\hat{a}^{\dagger}_{\mathrm{L}}\hat{a}^{\dagger}_{\mathrm{L}} + \mathrm{h.c.}\Big] \\ + \frac{1}{2}\Big[\left(K_{3,\mathrm{R}}\,\mathrm{e}^{-i\Delta_{\mathrm{p}}t} + K_{4,\mathrm{R}}\,\mathrm{e}^{i\Delta_{\mathrm{p}}t} + K_{5,\mathrm{R}}\right)\hat{a}^{\dagger}_{\mathrm{R}}\hat{a}^{\dagger}_{\mathrm{R}} + \mathrm{h.c.}\Big], \end{aligned}$$

[1] Note that this rotating frame is chosen only to simplify the calculations when fitting the theoretical model to the experimental data. Since no rotating-wave approximation is applied, the chosen frame of rotation has no impact on the physical results.

where the effective Kerr-coefficients $K_{i,\mathrm{L/R}}$ ($i \in 1, ..., 5$) are given by

$$\begin{aligned}
K_{1,\mathrm{L/R}} &= 2K_{\mathrm{L/R}}\, \alpha^{\mathrm{g}}_{\mathrm{L/R}} {\alpha^{\mathrm{c}}_{\mathrm{L/R}}}^{*}, \\
K_{2,\mathrm{L/R}} &= K^{*}_{1,\mathrm{L/R}} = 2K_{\mathrm{L/R}}\, {\alpha^{\mathrm{g}}_{\mathrm{L/R}}}^{*} \alpha^{\mathrm{c}}_{\mathrm{L/R}}, \\
K_{3,\mathrm{L/R}} &= K_{\mathrm{L/R}}\, (\alpha^{\mathrm{g}}_{\mathrm{L/R}})^2, \\
K_{4,\mathrm{L/R}} &= K_{\mathrm{L/R}}\, (\alpha^{\mathrm{c}}_{\mathrm{L/R}})^2, \\
K_{5,\mathrm{L/R}} &= 2K_{\mathrm{L/R}}\, \alpha^{\mathrm{g}}_{\mathrm{L/R}} \alpha^{\mathrm{c}}_{\mathrm{L/R}}.
\end{aligned} \tag{A1.37}$$

Similarly, we can now decompose the Heisenberg-Langevin equations (cf. Eq. (A1.3)), such that the mean-field amplitudes follow

$$\begin{aligned}
\alpha^{\mathrm{g/c}}_{\mathrm{R}}\, \delta^{\mathrm{g/c}}_{\mathrm{R}} &= J\alpha^{\mathrm{g/c}}_{\mathrm{L}}, \\
\alpha^{\mathrm{g/c}}_{\mathrm{L}} \left(\delta^{\mathrm{g/c}}_{\mathrm{L}} + i\frac{\kappa}{2}\right) &= J\alpha^{\mathrm{g/c}}_{\mathrm{R}} - i\sqrt{\kappa}\, \alpha^{\mathrm{g/c}}_{\mathrm{in}},
\end{aligned} \tag{A1.38}$$

where $|\alpha^{\mathrm{g/c}}_{\mathrm{in}}|^2 = P_{\mathrm{g/c}}/(\hbar\, \omega_{\mathrm{g/c}})$, with $P_{\mathrm{g/c}}$ denoting the power of the pump tones, and

$$\begin{aligned}
\delta^{\mathrm{g}}_{\mathrm{L}} &= \omega_{\mathrm{g}} - \omega_{\mathrm{L}} - K_{\mathrm{L}} \left(|\alpha^{\mathrm{g}}_{\mathrm{L}}|^2 + 2|\alpha^{\mathrm{c}}_{\mathrm{L}}|^2\right), \\
\delta^{\mathrm{c}}_{\mathrm{L}} &= \omega_{\mathrm{c}} - \omega_{\mathrm{L}} - K_{\mathrm{L}} \left(2|\alpha^{\mathrm{g}}_{\mathrm{L}}|^2 + 2|\alpha^{\mathrm{c}}_{\mathrm{L}}|^2\right), \\
\delta^{\mathrm{g}}_{\mathrm{R}} &= \omega_{\mathrm{g}} - \omega_{\mathrm{R}} - K_{\mathrm{R}} \left(|\alpha^{\mathrm{g}}_{\mathrm{R}}|^2 + 2|\alpha^{\mathrm{c}}_{\mathrm{R}}|^2\right), \\
\delta^{\mathrm{c}}_{\mathrm{R}} &= \omega_{\mathrm{c}} - \omega_{\mathrm{R}} - K_{\mathrm{R}} \left(2|\alpha^{\mathrm{g}}_{\mathrm{R}}|^2 + |\alpha^{\mathrm{c}}_{\mathrm{R}}|^2\right).
\end{aligned} \tag{A1.39}$$

The equations of motion of the fluctuation operators are now given by

$$\begin{aligned}
\frac{d\hat{a}_{\mathrm{L}}}{dt} &= i\left(\Delta_{\mathrm{L}} + i\frac{\kappa}{2}\right) \hat{a}_{\mathrm{L}} - iJ\hat{a}_{\mathrm{R}} - iK_{5,\mathrm{L}}\, \hat{a}^{\dagger}_{\mathrm{L}} - iK_{1,\mathrm{L}}\, \mathrm{e}^{-i\Delta_{\mathrm{p}}t}\, \hat{a}_{\mathrm{L}} - iK_{2,\mathrm{L}}\, \mathrm{e}^{i\Delta_{\mathrm{p}}t}\, \hat{a}_{\mathrm{L}} \\
&\quad - iK_{3,\mathrm{L}}\, \mathrm{e}^{-i\Delta_{\mathrm{p}}t}\, \hat{a}^{\dagger}_{\mathrm{L}} - iK_{4,\mathrm{L}}\, \mathrm{e}^{i\Delta_{\mathrm{p}}t}\, \hat{a}^{\dagger}_{\mathrm{L}} - \sqrt{\kappa}\, \hat{a}_{\mathrm{L,in}}, \\
\frac{d\hat{a}_{\mathrm{R}}}{dt} &= i\Delta_{\mathrm{R}}\, \hat{a}_{\mathrm{R}} - iJ\hat{a}_{\mathrm{L}} - iK_{5,\mathrm{R}}\, \hat{a}^{\dagger}_{\mathrm{R}} - iK_{1,\mathrm{R}}\, \mathrm{e}^{-i\Delta_{\mathrm{p}}t}\, \hat{a}_{\mathrm{R}} - iK_{2,\mathrm{R}}\, \mathrm{e}^{i\Delta_{\mathrm{p}}t}\, \hat{a}_{\mathrm{R}} \\
&\quad - iK_{3,\mathrm{R}}\, \mathrm{e}^{-i\Delta_{\mathrm{p}}t}\, \hat{a}^{\dagger}_{\mathrm{R}} - iK_{4,\mathrm{R}}\, \mathrm{e}^{i\Delta_{\mathrm{p}}t}\, \hat{a}^{\dagger}_{\mathrm{R}},
\end{aligned} \tag{A1.40}$$

where $\Delta_{\mathrm{L/R}} = (\omega_{\mathrm{g}} + \omega_{\mathrm{c}})/2 - \tilde{\omega}_{\mathrm{L/R}}$. Applying a Fourier transform of the form

$$\hat{a}_{\mathrm{L/R}}(t) = \frac{1}{\sqrt{2\pi}} \int d\omega\, \hat{a}_{\mathrm{L/R}}(\omega)\, \mathrm{e}^{-i\omega t}, \tag{A1.41}$$

where ω is the frequency of the input signal, we obtain

$$\begin{aligned}
-i\omega\, \hat{a}_{\mathrm{L}}(\omega) &= i\left(\Delta_{\mathrm{L}} + i\frac{\kappa}{2}\right) \hat{a}_{\mathrm{L}}(\omega) - iJ\, \hat{a}_{\mathrm{R}}(\omega) - iK_{5,\mathrm{L}}\, \hat{a}^{\dagger}_{\mathrm{L}}(-\omega) - iK_{1,\mathrm{L}}\, \hat{a}_{\mathrm{L}}(\omega - \Delta_{\mathrm{p}}) - iK_{2,\mathrm{L}}\, \hat{a}_{\mathrm{L}}(\omega + \Delta_{\mathrm{p}}) \\
&\quad - iK_{3,\mathrm{L}}\, \hat{a}^{\dagger}_{\mathrm{L}}(-\omega + \Delta_{\mathrm{p}}) - iK_{4,\mathrm{L}}\, \hat{a}^{\dagger}_{\mathrm{L}}(-\omega - \Delta_{\mathrm{p}}) - \sqrt{\kappa}\, \hat{a}_{\mathrm{L,in}}(\omega), \\
-i\omega\, \hat{a}_{\mathrm{R}}(\omega) &= i\Delta_{\mathrm{R}}\, \hat{a}_{\mathrm{R}}(\omega) - iJ\, \hat{a}_{\mathrm{L}}(\omega) - iK_{5,\mathrm{R}}\, \hat{a}^{\dagger}_{\mathrm{R}}(-\omega) - iK_{1,\mathrm{R}}\, \hat{a}_{\mathrm{R}}(\omega - \Delta_{\mathrm{p}}) - iK_{2,\mathrm{R}}\, \hat{a}_{\mathrm{R}}(\omega + \Delta_{\mathrm{p}}) \\
&\quad - iK_{3,\mathrm{R}}\, \hat{a}^{\dagger}_{\mathrm{R}}(-\omega + \Delta_{\mathrm{p}}) - iK_{4,\mathrm{R}}\, \hat{a}^{\dagger}_{\mathrm{R}}(-\omega - \Delta_{\mathrm{p}}).
\end{aligned} \tag{A1.42}$$

In contrast with the equations of motion under single-pump operation (see Eq. (A1.13)), applying a second pump activates interactions between additional sidebands at frequencies $\omega \pm \Delta_\mathrm{p}$. This implies that, even though the system scattering matrix is still defined as in Eq. (A1.17), the drift matrix is no longer bounded to fluctuations only at the signal and idler frequencies. Considering interactions with all sidebands, $\mathbf{M}_\mathrm{B}$ is now written as in Eq. (A1.45). Also the fluctuations vector $\vec{a}$ has to be redefined as

$$\begin{aligned}\vec{\hat{a}}_\mathrm{B} = \big(\cdots, &\hat{a}_\mathrm{R}^\dagger(-\omega+2\Delta_\mathrm{p}), \hat{a}_\mathrm{L}^\dagger(-\omega+2\Delta_\mathrm{p}), \hat{a}_\mathrm{R}^\dagger(-\omega-2\Delta_\mathrm{p}), \hat{a}_\mathrm{L}^\dagger(-\omega-2\Delta_\mathrm{p}),\\ &\hat{a}_\mathrm{R}^\dagger(-\omega+\Delta_\mathrm{p}), \hat{a}_\mathrm{L}^\dagger(-\omega+\Delta_\mathrm{p}), \hat{a}_\mathrm{R}^\dagger(-\omega-\Delta_\mathrm{p}), \hat{a}_\mathrm{L}^\dagger(-\omega-\Delta_\mathrm{p}),\\ &\hat{a}_\mathrm{R}^\dagger(-\omega), \hat{a}_\mathrm{L}^\dagger(-\omega), \hat{a}_\mathrm{L}(\omega), \hat{a}_\mathrm{R}(\omega),\\ &\hat{a}_\mathrm{L}(\omega-\Delta_\mathrm{p}), \hat{a}_\mathrm{R}(\omega-\Delta_\mathrm{p}), \hat{a}_\mathrm{L}(\omega+\Delta_\mathrm{p}), \hat{a}_\mathrm{R}(\omega+\Delta_\mathrm{p}),\\ &\hat{a}_\mathrm{L}(\omega-2\Delta_\mathrm{p}), \hat{a}_\mathrm{R}(\omega-2\Delta_\mathrm{p}), \hat{a}_\mathrm{L}(\omega+2\Delta_\mathrm{p}), \hat{a}_\mathrm{R}(\omega+2\Delta_\mathrm{p}), \cdots\big)^T.\end{aligned} \tag{A1.43}$$

Similar to the single-pumped case we can calculate the amplifier gain at the signal frequency using Eq. (A1.18).

Although finding analytical solutions for the scattering matrix using the drift matrix of Eq. (A1.45), is in principle possible, a more practical approach consists of solving Eq. (A1.17) numerically by truncating the drift and damping matrices up to a certain order of sidebands (i.e. sidebands up to $\pm\omega \pm n\Delta_\mathrm{p}$ for a finite $n \in \mathbb{N}$). We use this procedure to fit the gain profiles shown in Fig. 4.6(c), as detailed in Appendix D.4. Interestingly, the additional interactions with the newly created sidebands do not increase the added noise of the amplifier (see Fig. 4.10). This suggests the existence of destructive interference processes between the sidebands. It would be interesting, to extend the calculations to further investigate their impact on the single- and two-mode squeezing expected in the grAlPA.

Hybridized basis

In the hybridized basis, we can again separate the dynamics of the hybridized modes into mean-field amplitudes $\alpha^{\mathrm{g,c}}$, $\beta^{\mathrm{g,c}}$ and quantum fluctuations, such that

$$\begin{aligned}\hat{a} &\to \alpha^\mathrm{g} \mathrm{e}^{-i\omega_\mathrm{g} t} + \alpha^\mathrm{c} \mathrm{e}^{-i\omega_\mathrm{c} t} + \hat{a},\\ \hat{b} &\to \beta^\mathrm{g} \mathrm{e}^{-i\omega_\mathrm{g} t} + \beta^\mathrm{c} \mathrm{e}^{-i\omega_\mathrm{c} t} + \hat{b}.\end{aligned} \tag{A1.44}$$

$$
\mathbf{M}_{\mathrm{B}} = \begin{pmatrix}
\ddots & \vdots & \vdots & \vdots & \vdots & \vdots & \vdots & \vdots & \vdots & \vdots & \vdots & \vdots & \ddots \\
\cdots & iK_{2,\mathrm{R}} & 0 & iK_{1,\mathrm{R}} & 0 & i(\Delta_{\mathrm{R}} - i\frac{\kappa}{2}) & iJ & 0 & iK_{5,\mathrm{R}} & 0 & iK_{4,\mathrm{R}} & 0 & iK_{3,\mathrm{R}} & \cdots \\
\cdots & 0 & iK_{2,\mathrm{L}} & 0 & iK_{1,\mathrm{L}} & iJ & i(\Delta_{\mathrm{L}} - i\frac{\kappa}{2}) & iK_{5,\mathrm{L}} & 0 & iK_{4,\mathrm{L}} & 0 & iK_{3,\mathrm{L}} & 0 & \cdots \\
\cdots & 0 & -iK_{3,\mathrm{L}} & 0 & -iK_{4,\mathrm{L}} & 0 & -iK_{5,\mathrm{L}} & i(\Delta_{\mathrm{L}} + i\frac{\kappa}{2}) & -iJ & -iK_{1,\mathrm{L}} & 0 & -iK_{2,\mathrm{L}} & 0 & \cdots \\
\cdots & -iK_{3,\mathrm{R}} & 0 & -iK_{4,\mathrm{R}} & 0 & -iK_{5,\mathrm{R}} & 0 & -iJ & i(\Delta_{\mathrm{R}} + i\frac{\kappa}{2}) & 0 & -iK_{1,\mathrm{R}} & 0 & -iK_{2,\mathrm{R}} & \cdots \\
\ddots & \vdots & \vdots & \vdots & \vdots & \vdots & \vdots & \vdots & \vdots & \vdots & \vdots & \vdots & \vdots & \ddots
\end{pmatrix}
\tag{A1.45}
$$

where again can connect the mean-field amplitudes in the bare and hybridized basis using the relations

$$\begin{aligned}\alpha^{\mathrm{g/c}} &= -\sin(\theta)\,\alpha_{\mathrm{L}}^{\mathrm{g/c}} + \cos(\theta)\,\alpha_{\mathrm{R}}^{\mathrm{g/c}},\\ \beta^{\mathrm{g/c}} &= \cos(\theta)\,\alpha_{\mathrm{L}}^{\mathrm{g/c}} + \sin(\theta)\,\alpha_{\mathrm{R}}^{\mathrm{g/c}}.\end{aligned} \tag{A1.46}$$

We can linearize Hamiltonian Eq. (A1.8) and obtain

$$\begin{aligned}\hat{H}/\hbar = {}& \tilde{\omega}_{\mathrm{a}}(t)\,\hat{a}^{\dagger}\hat{a} + \tilde{\omega}_{\mathrm{b}}(t)\,\hat{b}^{\dagger}\hat{b}\\ &+ \left[\left(\Lambda_{\mathrm{S_a}}^{(1)}\,\mathrm{e}^{-2i\omega_{\mathrm{g}}t} + \Lambda_{\mathrm{S_a}}^{(2)}\,\mathrm{e}^{-2i\omega_{\mathrm{c}}t} + \Lambda_{\mathrm{S_a}}^{(12)}\,\mathrm{e}^{-i(\omega_{\mathrm{g}}+\omega_{\mathrm{c}})t}\right)\hat{a}^{\dagger}\hat{a}^{\dagger} + \mathrm{h.c}\right]\\ &+ \left[\left(\Lambda_{\mathrm{S_b}}^{(1)}\,\mathrm{e}^{-2i\omega_{\mathrm{g}}t} + \Lambda_{\mathrm{S_b}}^{(2)}\,\mathrm{e}^{-2i\omega_{\mathrm{c}}t} + \Lambda_{\mathrm{S_b}}^{(12)}\,\mathrm{e}^{-i(\omega_{\mathrm{g}}+\omega_{\mathrm{c}})t}\right)\hat{b}^{\dagger}\hat{b}^{\dagger} + \mathrm{h.c}\right]\\ &+ \left[\left(\Lambda_{\mathrm{TMS}}^{(1)}\,\mathrm{e}^{-2i\omega_{\mathrm{g}}t} + \Lambda_{\mathrm{TMS}}^{(2)}\,\mathrm{e}^{-2i\omega_{\mathrm{c}}t} + \Lambda_{\mathrm{TMS}}^{(12)}\,\mathrm{e}^{-i(\omega_{\mathrm{g}}+\omega_{\mathrm{c}})t}\right)\hat{a}^{\dagger}\hat{b}^{\dagger} + \mathrm{h.c}\right]\\ &+ \left[\Lambda_{\mathrm{BS}}^{(0)} + \left(\Lambda_{\mathrm{BS}}^{(12)}\,\mathrm{e}^{-i(\omega_{\mathrm{g}}-\omega_{\mathrm{c}})t} + \mathrm{h.c}\right)\right]\left(\hat{a}^{\dagger}\hat{b} + \hat{b}^{\dagger}\hat{a}\right),\end{aligned} \tag{A1.47}$$

where all the terms in the Hamiltonian can be written again as a function of the mean-field amplitudes $\alpha_{\mathrm{L,R}}$, such that

$$\begin{aligned}\tilde{\omega}_{\mathrm{a}} = {}& \omega_{\mathrm{a}} + 2K_{\mathrm{L}}\left[|\alpha_{\mathrm{L}}^{\mathrm{g}}|^2 + |\alpha_{\mathrm{L}}^{\mathrm{c}}|^2 + 2\left(\alpha_{\mathrm{L}}^{\mathrm{g}}\alpha_{\mathrm{L}}^{\mathrm{c}\,*}\,\mathrm{e}^{-i\Delta_p t} + \mathrm{h.c.}\right)\right]\sin^2(\theta)\\ &+ 2K_{\mathrm{R}}\left[|\alpha_{\mathrm{R}}^{\mathrm{g}}|^2 + |\alpha_{\mathrm{R}}^{\mathrm{c}}|^2 + 2\left(\alpha_{\mathrm{R}}^{\mathrm{g}}\alpha_{\mathrm{R}}^{\mathrm{c}\,*}\,\mathrm{e}^{-i\Delta_p t} + \mathrm{h.c.}\right)\right]\cos^2(\theta),\\ \tilde{\omega}_{\mathrm{b}} = {}& \omega_{\mathrm{b}} + 2K_{\mathrm{L}}\left[|\alpha_{\mathrm{L}}^{\mathrm{g}}|^2 + |\alpha_{\mathrm{L}}^{\mathrm{c}}|^2 + 2\left(\alpha_{\mathrm{L}}^{\mathrm{g}}\alpha_{\mathrm{L}}^{\mathrm{c}\,*}\,\mathrm{e}^{-i\Delta_p t} + \mathrm{h.c.}\right)\right]\cos^2(\theta)\\ &+ 2K_{\mathrm{R}}\left[|\alpha_{\mathrm{R}}^{\mathrm{g}}|^2 + |\alpha_{\mathrm{R}}^{\mathrm{c}}|^2 + 2\left(\alpha_{\mathrm{L}}^{\mathrm{g}}\alpha_{\mathrm{L}}^{\mathrm{c}\,*}\,\mathrm{e}^{-i\Delta_p t} + \mathrm{h.c.}\right)\right]\sin^2(\theta),\end{aligned} \tag{A1.48}$$

$$\begin{aligned}\Lambda_{\mathrm{S_a}}^{(1)} &= K_{\mathrm{L}}(\alpha_{\mathrm{L}}^{\mathrm{g}})^2\sin^2(\theta) + K_{\mathrm{R}}(\alpha_{\mathrm{R}}^{\mathrm{g}})^2\cos^2(\theta),\\ \Lambda_{\mathrm{S_a}}^{(2)} &= K_{\mathrm{L}}(\alpha_{\mathrm{L}}^{\mathrm{c}})^2\sin^2(\theta) + K_{\mathrm{R}}(\alpha_{\mathrm{R}}^{\mathrm{c}})^2\cos^2(\theta),\\ \Lambda_{\mathrm{S_a}}^{(12)} &= 2\left(K_{\mathrm{L}}\alpha_{\mathrm{L}}^{\mathrm{g}}\alpha_{\mathrm{L}}^{\mathrm{c}}\sin^2(\theta) + K_{\mathrm{R}}\alpha_{\mathrm{R}}^{\mathrm{g}}\alpha_{\mathrm{R}}^{\mathrm{c}}\cos^2(\theta)\right),\end{aligned} \tag{A1.49}$$

$$\begin{aligned}\Lambda_{\mathrm{S_b}}^{(1)} &= K_{\mathrm{L}}(\alpha_{\mathrm{L}}^{\mathrm{g}})^2\cos^2(\theta) + K_{\mathrm{R}}(\alpha_{\mathrm{R}}^{\mathrm{g}})^2\sin^2(\theta),\\ \Lambda_{\mathrm{S_b}}^{(2)} &= K_{\mathrm{L}}(\alpha_{\mathrm{L}}^{\mathrm{c}})^2\cos^2(\theta) + K_{\mathrm{R}}(\alpha_{\mathrm{R}}^{\mathrm{c}})^2\sin^2(\theta)\\ \Lambda_{\mathrm{S_b}}^{(12)} &= 2\left(K_{\mathrm{L}}\alpha_{\mathrm{L}}^{\mathrm{g}}\alpha_{\mathrm{L}}^{\mathrm{c}}\cos^2(\theta) + K_{\mathrm{R}}\alpha_{\mathrm{R}}^{\mathrm{g}}\alpha_{\mathrm{R}}^{\mathrm{c}}\sin^2(\theta)\right),\end{aligned} \tag{A1.50}$$

$$\begin{aligned}\Lambda_{\mathrm{TMS}}^{(1)} &= -\frac{1}{2}\left(K_{\mathrm{L}}(\alpha_{\mathrm{L}}^{\mathrm{g}})^2 - K_{\mathrm{R}}(\alpha_{\mathrm{R}}^{\mathrm{g}})^2\right)\sin(2\theta),\\ \Lambda_{\mathrm{TMS}}^{(2)} &= -\frac{1}{2}\left(K_{\mathrm{L}}(\alpha_{\mathrm{L}}^{\mathrm{c}})^2 - K_{\mathrm{R}}(\alpha_{\mathrm{R}}^{\mathrm{c}})^2\right)\sin(2\theta),\\ \Lambda_{\mathrm{TMS}}^{(12)} &= -\left(K_{\mathrm{L}}\alpha_{\mathrm{L}}^{\mathrm{g}}\alpha_{\mathrm{L}}^{\mathrm{c}} - K_{\mathrm{R}}\alpha_{\mathrm{R}}^{\mathrm{g}}\alpha_{\mathrm{R}}^{\mathrm{c}}\right)\sin(2\theta),\end{aligned} \tag{A1.51}$$

$$\begin{aligned}\Lambda_{\mathrm{BS}}^{(0)} &= -\left[K_{\mathrm{L}}\left(|\alpha_{\mathrm{L}}^{\mathrm{g}}|^2 + |\alpha_{\mathrm{L}}^{\mathrm{c}}|^2\right) - K_{\mathrm{R}}\left(|\alpha_{\mathrm{R}}^{\mathrm{g}}|^2 + |\alpha_{\mathrm{R}}^{\mathrm{c}}|^2\right)\right]\sin(2\theta),\\ \Lambda_{\mathrm{BS}}^{(12)} &= -\left(K_{\mathrm{L}}\alpha_{\mathrm{L}}^{\mathrm{g}\,*}\alpha_{\mathrm{L}}^{\mathrm{c}} - K_{\mathrm{R}}\alpha_{\mathrm{R}}^{\mathrm{g}\,*}\alpha_{\mathrm{R}}^{\mathrm{c}}\right)\sin(2\theta).\end{aligned} \tag{A1.52}$$

Rotating the Hamiltonian with respect to a frame at frequency ω_o, certain interaction terms become dominant, and oscillating contributions can be neglected. Under this condition, the Hamiltonian (A1.47) can be rewritten into a the following time-independent form

$$\begin{aligned}\hat{H}/\hbar = &-\Delta_a\,\hat{a}^\dagger\hat{a} - \Delta_b\,\hat{b}^\dagger\hat{b} \\ &+ \left(\Lambda_{S_a}\,\hat{a}^\dagger\hat{a}^\dagger + \text{h.c.}\right) + \left(\Lambda_{S_b}\,\hat{b}^\dagger\hat{b}^\dagger + \text{h.c.}\right) \\ &+ \left(\Lambda_{TMS}\,\hat{a}^\dagger\hat{b}^\dagger + \text{h.c.}\right) + \left(\Lambda_{BS}\,\hat{a}^\dagger\hat{b} + \text{h.c.}\right),\end{aligned} \tag{A1.53}$$

where $\Delta_{a/b} = \omega_o - \tilde{\omega}_{a/b}$. Rotating the Hamiltonian with frequency $\omega_o = (\omega_g + \omega_c)/2$, the main coupling interactions are governed by the set $\{\Lambda_{S_a}^{(12)}, \Lambda_{S_b}^{(12)}, \Lambda_{TMS}^{(12)}, \Lambda_{BS}^{(0)}\}$. On the other hand, rotating the Hamiltonian with frequency $\omega_o = \omega_g$, the main coupling interactions are now $\{\Lambda_{S_a}^{(1)}, \Lambda_{S_b}^{(1)}, \Lambda_{TMS}^{(1)}, \Lambda_{BS}^{(0)}\}$.

We study the dynamics of the system by analyzing the evolution of the quadrature operators

$$\begin{aligned}\hat{x}_a &= \frac{\hat{a}^\dagger + \hat{a}}{2},\ \hat{p}_a = i\frac{\hat{a}^\dagger - \hat{a}}{2}, \\ \hat{x}_b &= \frac{\hat{b}^\dagger + \hat{b}}{2},\ \hat{p}_b = i\frac{\hat{b}^\dagger - \hat{b}}{2}\end{aligned} \tag{A1.54}$$

Hamiltonian (Eq. (A1.53)) can then be rewritten as

$$\begin{aligned}\hat{H}/\hbar = &-\sum_{i=a,b}\left\{\left(\frac{\Delta_i}{2} + \Lambda_{S_i}\right)\hat{x}_i^2 + \left(\frac{\Delta_i}{2} - \Lambda_{S_i}\right)\hat{p}_i^2\right\} \\ &+ (\Lambda_{BS} + \Lambda_{TMS})\,\hat{x}_a\,\hat{x}_b + (\Lambda_{BS} - \Lambda_{TMS})\,\hat{p}_a\,\hat{p}_b,\end{aligned} \tag{A1.55}$$

The equations of motion in terms of the quadrature operators take now the form

$$\frac{d\vec{\hat{X}}}{dt} = \mathbf{M}_{xp}\,\vec{\hat{X}} + \mathbf{K}_{xp}\,\vec{\hat{X}}_{in}, \tag{A1.56}$$

where $\vec{\hat{X}} = (\hat{x}_a, \hat{p}_a, x_b, \hat{p}_b)^T$ and $\vec{\hat{X}}_{in} = (\hat{x}_{a,in}, \hat{p}_{a,in}, \hat{x}_{b,in}, \hat{p}_{b,in})^T$. Moreover, the drift $\mathbf{M}_{xp}$ and damping $\mathbf{K}_{xp}$ matrices are now defined as

$$\mathbf{M}_{xp} = \begin{pmatrix} -\kappa_a/2 & -\left(\Delta_a + 2\Lambda_{S_a}\right) & 0 & \Lambda_{TMS} - \Lambda_{BS} + i\kappa_m/2 \\ \Delta_a - 2\Lambda_{S_a} & -\kappa_a/2 & \Lambda_{TMS} + \Lambda_{BS} - i\kappa_m/2 & 0 \\ 0 & \Lambda_{TMS} - \Lambda_{BS} + i\kappa_m/2 & -\kappa_b/2 & -\left(\Delta_b + 2\Lambda_{S_b}\right) \\ \Lambda_{TMS} + \Lambda_{BS} - i\kappa_m/2 & 0 & \Delta_b - 2\Lambda_{S_b} & -\kappa_b/2 \end{pmatrix}, \tag{A1.57}$$

and

$$\mathbf{K}_{xp} = \begin{pmatrix} \sqrt{\kappa_a} & 0 & 0 & 0 \\ 0 & \sqrt{\kappa_a} & 0 & 0 \\ 0 & 0 & \sqrt{\kappa_b} & \\ 0 & 0 & 0 & \sqrt{\kappa_b} \end{pmatrix}, \tag{A1.58}$$

For the BHD dimer design in Fig. 3.1(a), where only the left resonator is coupled to the microwave environment, the damping rates follow Eq. (A1.30). In case of perfect hybridization of the bare resonators (i.e. $\omega_{\mathrm{L}} = \omega_{\mathrm{L}}$), they can be rewritten as $\kappa_{\mathrm{a/b}} = \kappa/2$ and $\kappa_{\mathrm{m}} = \kappa/2$. However, for a BHD with symmetric coupling of the bare resonators, as depicted in Fig. 4.1(a), we obtain $\kappa_{\mathrm{a/b}} = \kappa$ and $\kappa_{\mathrm{m}} = 0$. Under such conditions the BHD can be tuned to match the dynamics of the OIBA discussed in Section 1.3.4.

Dynamical stability

Similar to the case when the amplifier is driven by a single-pump, we can analyze its dynamical stability by applying the Routh–Hurwitz criterion [142] to the eigenvalues $\epsilon_{\pm,\pm}$ of the matrix in Eq. (A1.57). For simplicity, we assume from now on a BHD with the symmetric design shown in Fig. 4.1(a) (i.e. we set $\kappa_{\mathrm{m}} = 0$). Then, we obtain

$$\begin{aligned}\epsilon_{\pm,+} &= -\frac{\kappa}{2} \pm \sqrt{\Lambda_{\mathrm{TMS}}^2 - \Lambda_{\mathrm{BS}}^2 + 2\left(\Lambda_{\mathrm{S_a}}^2 + \Lambda_{\mathrm{S_b}}^2\right) - \frac{(\Delta_{\mathrm{a}}^2 + \Delta_{\mathrm{b}}^2)}{2} + \frac{\epsilon\epsilon}{2}}, \\ \epsilon_{\pm,-} &= -\frac{\kappa}{2} \pm \sqrt{\Lambda_{\mathrm{TMS}}^2 - \Lambda_{\mathrm{BS}}^2 + 2\left(\Lambda_{\mathrm{S_a}}^2 + \Lambda_{\mathrm{S_b}}^2\right) - \frac{(\Delta_{\mathrm{a}}^2 + \Delta_{\mathrm{b}}^2)}{2} - \frac{\epsilon\epsilon}{2}},\end{aligned} \tag{A1.59}$$

where

$$\begin{aligned}\epsilon\epsilon = \Big\{ &\left[(\Delta_{\mathrm{a}}^2 - \Delta_{\mathrm{b}}^2) - 4\left(\Lambda_{\mathrm{S_a}}^2 - \Lambda_{\mathrm{S_b}}^2\right)\right]^2 + 4\Lambda_{\mathrm{BS}}^2\left[(\Delta_{\mathrm{a}} + \Delta_{\mathrm{b}})^2 - 4(\Lambda_{\mathrm{S_a}} - \Lambda_{\mathrm{S_b}})^2\right] \\ &- 4\Lambda_{\mathrm{TMS}}^2\left[(\Delta_{\mathrm{a}} - \Delta_{\mathrm{b}})^2 - 4(\Lambda_{\mathrm{S_a}} + \Lambda_{\mathrm{S_b}})^2\right] + 32\Lambda_{\mathrm{BS}}\,\Lambda_{\mathrm{TMS}}\left(\Lambda_{\mathrm{S_a}}\,\Delta_{\mathrm{b}} + \Lambda_{\mathrm{S_b}}\,\Delta_{\mathrm{a}}\right)\Big\}^{1/2}.\end{aligned}$$

Optimally detuned BHD

When the double-pumped BHD is optimally detuned i.e. $\Lambda_{\mathrm{S_a}} = \Lambda_{\mathrm{S_b}} = \Lambda_{\mathrm{S}}$ and $\Delta_{\mathrm{a}} = -\Delta_{\mathrm{b}} = -2\Lambda_{\mathrm{S}}$, we obtain a simplified version of the eigenvalues in Eq. (A1.59). such that

$$\epsilon_{\pm,\pm} = \frac{\kappa}{2}\left(-1 \pm \sqrt{C_{\mathrm{TMS}} - C_{\mathrm{BS}}}\right), \tag{A1.60}$$

where $C_\zeta = 4|\Lambda_\zeta|^2/\kappa^2$ with $\zeta \in \{\mathrm{BS}, \mathrm{TMS}, \mathrm{S}\}$, are the cooperatives of the beam-splitter, two-mode squeezing and single-mode squeezing interactions, respectively.

For an optimally detuned BHD, then Hamiltonian (A1.55), reduces to

$$\hat{H}/\hbar = (\Lambda_{\mathrm{BS}} + \Lambda_{\mathrm{TMS}})\,\hat{x}_{\mathrm{a}}\,\hat{x}_{\mathrm{b}} + (\Lambda_{\mathrm{BS}} - \Lambda_{\mathrm{TMS}})\,\hat{p}_{\mathrm{a}}\,\hat{p}_{\mathrm{b}}, \tag{A1.61}$$

Moreover, we can apply the Fourier transform of Eq. (A1.41) into Eq. (A1.56), and together with the input-output relations of the quadrature operators

$$\vec{\hat{X}}_{\mathrm{out}}(\omega) = \vec{\hat{X}}_{\mathrm{in}}(\omega) + \mathbf{K}_{\mathrm{xp}}\,\vec{\hat{X}}(\omega), \tag{A1.62}$$

we can calculate the quadrature scattering matrix defined as

$$\mathbf{S}_{\mathrm{xp}}^{\mathrm{H}}(\omega) = \mathbf{K}_{\mathrm{xp}}\, \mathbf{M}^{-1}(\omega)\, \mathbf{K}_{\mathrm{xp}} + \mathbf{1}_4. \tag{A1.63}$$

We use Eq. (A1.63) to calculate the gain profiles shown in Fig. 4.3(a). If we account for the phases of the pump tones (denoted as $\phi_{\mathrm{g/c}}$ in Section 4.6), we can verify that the BHD behaves as a phase-sensitive amplifier over the entire frequency range.

The amplifier noise performance can be calculated using the symmetrized noise spectral density

$$\bar{n}^{(\mathrm{out})}_{\mathrm{F}_i,\mathrm{F}_j}(\omega) = \frac{1}{2}\int \frac{d\Omega}{2\pi}\, \left\langle \left\{ \hat{F}_{i,\mathrm{out}}(\omega), \hat{F}_{j,\mathrm{out}}(\Omega) \right\} \right\rangle, \tag{A1.64}$$

where $\hat{F}_{i/j,\mathrm{out}} \in \{\hat{x}_{\mathrm{a,out}}, \hat{p}_{\mathrm{a,out}}, \hat{x}_{\mathrm{b,out}}, \hat{p}_{\mathrm{b,out}}\}$. Then, we calculate the added noise by referring the noise spectral density to the BHD input plane, such that

$$\bar{n}_{\mathrm{add}}(\omega) = \frac{\bar{n}^{(\mathrm{out})}_{\mathrm{p_a},\mathrm{x_a}}(\omega)}{G(\omega)} - \frac{1}{2}, \tag{A1.65}$$

where $G(\omega) = |(S^{\mathrm{H}}_{\mathrm{xp}})_{21}(\omega)|^2$ and the factor $1/2$ is subtracted because the BHD in the hybridized basis is phase-sensitive.

We use Eq. (A1.65) to calculate the noise curves shown in Fig. 4.3(c). The increase of n_{add} with frequency ω arises only from the definition of noise employed here. As ω increases, the effective interaction between the quadratures that generate the gain G, decreases. For frequencies beyond the linewidths of the dimer modes $\kappa_{a/b}$, this interaction effectively vanishes (i.e. $G \longrightarrow 0$). However, the spectral density in Eq. (A1.64) is bounded by a lower limit at $1/2$, which leads to the divergent behavior observed in Fig. 4.3(c). This unphysical divergence is removed by calculating n_{add} in terms of the fluctuation operators rather than their quadratures.

B grAlPA

In this Appendix, we provide more detailed information about the results shown in Chapter 3.

B.1 Detailed fabrication recipe

Here, we provide a detailed recipe for the grAlPA fabrication. All fabrication steps are organized in Table A2.1.

Table A2.1: Fabrication recipe for grAl resonators and Nb coupling pad. PEC refers to Proximity Error Correction. Thin-film deposition was carried out in a two-chamber Plassys electron-beam evaporator.

	grAl resonators	**Nb Pad**
	Resist application	
Preheating	115°C, 3 mins	115°C, 3 mins
Resist	EL-13 (800 nm) + PMMA A4 (400 nm)	S1805 (500 nm, positive)
Coating	2000 rpm, 100 s, 1000 rpm/s (×2)	4500 rpm, 60 s, 500 rpm/s
Backing	200°, 5 min (×2)	115°, 3 min
Au coating	~ 10 nm, sputtered	–
	Exposure	
Type	electron-beam	optical, mask-aligner
Specs.	acceleration voltage: 50 kV	500 W Xe-lamp $\lambda = 365$ nm
Dose	Central strips: 567.25 μC/cm^2, 2D PEC Capacitor pads: 567.25 μC/cm^2	13 mW/cm^2, 4 s
	Development	
Au remover	Lugol solution, 10 s + 30 s H_2O rinse	–
Developer	IPA:H_2O (3:1) at 6°, 120 s	AZ dev.:H_2O (2:3), 45 s
Rinsing	IPA 30 s + N_2 blow dry	H_2O 30 s + N_2 blow dry
	Thin film deposition	
Descum	O_2/Ar (10 sccm/5 sccm), 200 V, 10 mA	same as grAl
Vacuum	~3×10^{-7} mbar + Ti getter	~1×10^{-7} mbar + Ti getter
Evap.	40 nm, 1.0 nm/s, 5.6 sccm O_2 flow	40 nm, 1.2 nm/s
Post oxid.	static 10 mbar, 3 min	–
	Lift-off	
Solvent	NEP (~3 h) + Acetone +IPA + N_2 blow dry	NEP (~12 h) + Acetone + IPA + N_2 blow dry

B.2 Measurement setups

In this section, we provide a more detailed explanation of the three different experimental setups used for the results discussed in Chapter 3. Detailed schematics of the setups are shown in Fig. A2.1.

For the results presented in Sections 3.4-3.7 and in Figs. 3.12(c), (e), and (f), we employ the setup shown in Fig. A2.1(a). Measurements were performed inside a SionLudi dilution refrigerator version L, adapted to perform both microwave characterization of the grAlPA under magnetic fields and power calibration using the fluorescence of a flux-tunable transmon qubit (see Appendix C.4). The response of each device under test (DUT) is characterized in separate cooldowns using single-port reflection measurements. A signal generated by a Vector Network Analyzer (VNA) is attenuated by two -30 dB attenuators thermalized at the 4 K and 30 mK stages of the refrigerator, respectively. A 12 GHz cutoff low-pass filter is connected at the base plate to suppress the impact of high frequency. The input signal is routed to the sample and through an output line using a cryogenic circulator. At the mixing chamber (MXC) stage, in the output line we use a 2-stage isolator and one additional low-pass filter to remove the noise traveling back from the higher temperature stages. Between the MXC and the 4 K plate, the output signal is transmitted through a NbTi superconducting cable with negligible insertion loss and then amplified by a HEMT with added noise temperature close to 3 K. Outside the refrigerator, we use a room temperature amplifier to further improve the SNR of the measurements. Finally, we split the output signal using a two-ports Wilkinson power divider, and direct the resulting components to the receiving ports of the VNA and a Spectrum Analyzer. The pump tone is synthesized by a microwave generator and coupled to the input signal at room temperature via a 16 dB directional coupler. This setup is equipped with a 2D vector magnet, which is thermalized at 4 K, to allow high magnetic field operation without heating the MXC. The magnet is designed to produce in-plane magnetic fields up to 1 T and out-of-plane magnetic fields up to 100 mT.

We employ the setup in Fig. A2.1(b) to characterize grAlPA noise performance while having the transmon qubit connected in the same cooldown, which allows an in-situ calibration of the input power (cf. Figs. 3.12(d)-(e)). Both devices are mounted in two

Table A2.2: Insertion loss of the components connected at the MXC plates. The connections are presented in Fig. A2.1(c) and (d).

	Insertion Loss (dB)
Cryogenic circulator (at 77 K) [223]	0.2
Cryogenic isolator (at 77 K) [223]	0.2
Cryogenic directional coupler (at 10 mK) [253]	0.5
Coaxial cables (per meter at 300 K) [254]	2

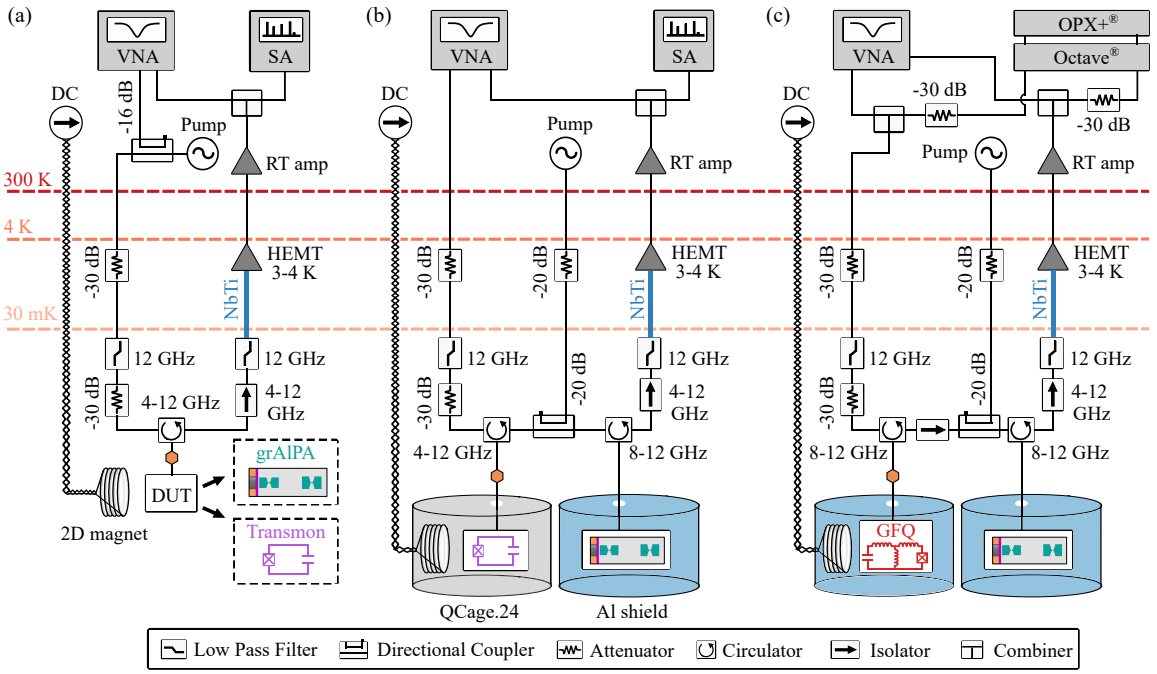

Figure A2.1: Experimental setups used in Chapter 3. Each component is thermalized to the temperature stage indicated by the nearest dashed line. **(a)** Schematics of the set up employed for the grAlPA measurements under magnetic fields. We align the field generated by a homemade 2D vector magnet using the calibration shown in Appendix B.3. In this setup, a transmon qubit used for power calibration and the grAlPA are measured in separate cooldowns. The grAlPA pump is combined through a directional coupler at room temperature with the signal from a vector network analyzer (VNA). A power divider located outside the dilution refrigerator splits the output signal to the receiving port of the VNA and to a spectrum analyzer (SA). **(b)** Setup employed for in-situ power calibration of the input line using a flux-tunable transmon. The grAlPA is connected via a circulator to the qubit. The pump tone is coupled at the base plate of the cryostat using a cryogenic directional coupler. In this setup we estimate a total insertion loss between the transmon and the grAlPA of 1.5 dB. **(c)** Setup employed for the single-shot detection of a GFQ. Compared to the setup in panel (b), we added an isolator and ≈ 30 cm of microwave cables between the GFQ and the grAlPA, which add 0.8 dB insertion loss. The orange markers in the panels indicate the input power calibration plane.

separate sample holders located at the base plate of a Bluefors L cryostat, each having its own magnetic shielding. The microwave signal reaching the MXC is now routed to the readout line by two cryogenic circulators connected at the input of the qubit and the grAlPA, respectively. Moreover, we apply the pump tone using a separate input line, with only one 30 dB attenuator connected at the 4 K flange of the refrigerator. The tone is then coupled to the input signal with a cryogenic directional coupler with 20 dB attenuation in its coupling port. We estimate the attenuation λ between the qubit and the grAlPA, from the insertion loss provided by the manufacturers of the microwave components and cables, which are summarized in Table A2.2. We extract in this case a total attenuation $\lambda \approx 1.5$ dB. In this setup, only the qubit is biased by a homemade coil connected at the base plate of the cryostat.

We use the setup in Fig. A2.1(c) to perform single-shot readout of the GFQ and extract the quantum efficiency of the grAlPA. Inside the cryostat, the setup is similar to Fig. A2.1(b), with the only two important differences being the addition of a cryogenic isolator between

the GFQ and the grAlPA, and the replacement of the qCage with a homemade Al shield. In this setup we estimate $\lambda \approx 2.3$ dB, due to the 0.2 dB insertion loss of the isolator and ≈ 0.6 dB attenuation of additional microwave connections (with ≈ 30 cm total length). We perform heterodyne measurements using an Octave-OPX+® system. We connect a homemade band-pass filter at the output of the fridge (not shown in Fig. A2.1(c)), to prevent the pump tone to reach the room temperature electronics. Finally, we also connect 30 dB attenuators at the Octave® input and output ports, as additional protection from the pump.

B.3 Stabilizing dimer symmetry with Nb coupling pad

A central element used for the optimization of the grAlPA design was the addition of the Nb coupling pad shown in Fig. 3.3(c). In this appendix, we provide further details on how this pad stabilizes both the coupling strength κ and the frequency symmetry of the grAl resonators $\omega_{L,R}$. As outlined in Section 3.3, the pad was designed to act as an on-chip extension of the coaxial cable pin that couples to the grAlPA (cf. Fig. 3.3). Its main effect is to enlarge the effective area over which the electric field generated from the pin is distributed. In Fig. A2.2(b), we show the on-chip distribution of this electric field obtained from FEM simulations in the absence of the grAl resonators. The simulations use an 8 GHz excitation and an input power corresponding to a grAlPA population of ~ 10 photons. In the prescence of the Nb pad, the electric field lines are more evenly distributed along the lower edge of the substrate. This strategy reduces the susceptibility of the resonators' hybridization in case of misalignments during the chip installation.

We consider two possible misalignments: lateral displacements (Δd) due to incorrect dimensions of the substrate, and pin thermal contractions (Δr) during the cooldown (see Fig. A2.2(b)). If we recall from Section 3.1, in case of perfect hybridization, the total coupling strength κ is equally shared by the dimer modes, $\kappa_a = \kappa_b = \kappa/2$. If $\omega_L \neq \omega_R$, their linewidths will show an asymmetry $\Delta\kappa_{a,b} = |\kappa_a - \kappa_b|$ (cf. Fig. 3.1(b)). This makes $\Delta\kappa_{a,b}$ a practical proxy for determining the degree of hybridization. Fig. A2.2(c)-(d) present FEM simulation results showing how $\Delta\kappa_{a,b}$ varies with the misalignments depicted in Fig. A2.2(b). We find that with the Nb pad we increase the stability of $\Delta\kappa_{a,b}$ to larger values of Δr and Δd. Linewidth fluctuations remain below $\sim 6\%$ of κ, an empirical threshold beyond which stable 20 dB gain was not achievable in the grAlPA.

Experimentally, we verified the stabilizing role of the Nb pad by testing several grAlPAs. Table A2.3 summarizes the circuit parameters of two representative samples, one fabricated with and one without the coupling pad. We present results measured across several cooldowns. As expected, the grAlPA with the Nb pad consistently achieved gain ≥ 20 dB in all cooldowns, whereas the sample without the pad exhibited non-degenerate gain in only one out of three cooldowns.

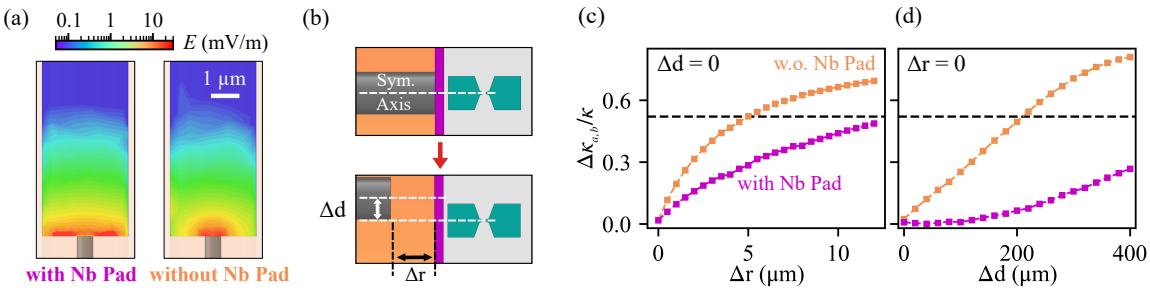

Figure A2.2: Finite element simulations of grAlPA chips with and without Nb pads. **(a)** Electric field distribution across the surface of a sapphire chip with and without the Nb pad. **(b)** Schematic representation of the two misalignments considered: thermal retraction Δr of the coaxial pin and lateral displacement Δd with respect to the symmetry axis of the waveguide (indicated by the white dashed line). **(c)**, **(d)** Coupling asymmetry $\Delta\kappa_\pm/\kappa$ as a function of Δd and Δr, respectively. The black dashed line represents an empirical limit above which 20 dB non-degenerate gain is not achievable.

Table A2.3: Summary of the linear characterization of grAlPAs with and without Nb coupling pad. The uncertainty in $\gamma_\pm$ arises from the Fano uncertainty in the setup [134]. We estimate 10% uncertainty in $\kappa_\pm$ coming from the same effect.

	with Nb Pad				without Nb Pad		
Cooldown #	1	2	3	4	1	2	3
$\omega_+/2\pi$ (GHz)	8.41	8.38	8.42	8.40	9.35	9.67	9.56
$\omega_-/2\pi$ (GHz)	8.21	8.18	8.22	8.22	8.38	8.92	8.90
$\kappa_+/2\pi$ (MHz)	23.1	28.2	28.4	26.1	91.9	5.8	85.0
$\kappa_-/2\pi$ (MHz)	34.6	38.4	28.1	19.9	15.6	26.1	29.5
$\gamma_+/2\pi$ (MHz)	$\leq$ 5.0	$\leq$ 8.0	$\leq$ 7.4	$\leq$ 6.3	$\leq$ 20.6	$\leq$ 1.3	$\leq$ 21.1
$\gamma_-/2\pi$ (MHz)	$\leq$ 6.7	$\leq$ 10.9	$\leq$ 6.8	$\leq$ 4.4	$\leq$ 2.8	$\leq$ 5.4	$\leq$ 6.5
$\omega_L/2\pi$ (GHz)	8.29	8.27	8.32	8.33	9.21	9.06	9.39
$\omega_R/2\pi$ (GHz)	8.33	8.30	8.32	8.30	8.52	9.53	9.07
$J/2\pi$ (MHz)	91.0	90.0	99.0	85.0	261.0	224.0	235.0
$\kappa/2\pi$ (MHz)	57.7	66.6	56.5	46.0	107.5	31.9	114.5
$\Delta\kappa_\pm/\kappa$	0.20	0.15	0.01	0.14	0.71	0.64	0.48
max. G_0 (dB)	$\geq$ 20	$\geq$ 20	$\geq$ 20	$\geq$ 20	None	None	12

B.4 Alternative design with symmetric coupling

In Section 3.1, we discussed that a crucial requirement for achieving 20 dB non-degenerate gain is the symmetry of the linewidths of the dimer modes $\kappa_{a,b}$, obtained when the bare resonators are fully hybridized ($\omega_L = \omega_L$). In the original grAlPA design, only the left resonator experiences a significant capacitive contribution due to its strong coupling to the stripped pin of the coaxial cable. Since this coupling is evanescent, even small chip displacements can induce non-negligible frequency mismatches between ω_L and ω_R. To address this issue, we incorporated the Nb coupling pad, as shown in Fig. 3.3 and analyzed in Appendix B.3. However, what if instead both grAl resonators were coupled

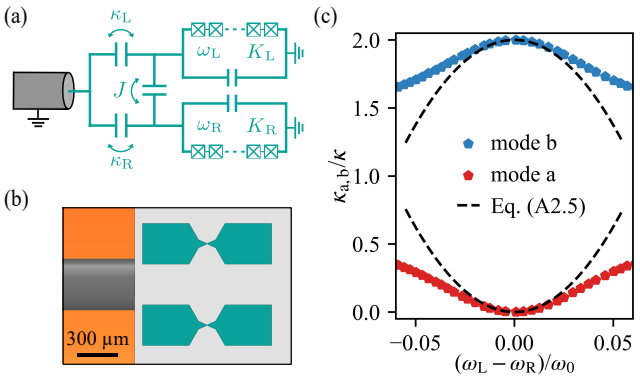

Figure A2.3: grAlPA design with symmetric coupling. **(a)-(b)** Circuit design and layout of the grAlPA with symmetric coupling to the microwave environment. The resonators have external damping rates given by κ_L and κ_R, respectively. **(c)** Linewidths of the dimer modes $\kappa_{a,b}$ as a function of the detuning $(\omega_L - \omega_R)/\omega_0$, where $\omega_0 = (\omega_L + \omega_R)/2$. The scatter data correspond to FEM simulations using the layout shown in panel (b), while the black dashed line represents a fit using Eq. (A2.4). Notably, under perfect hybridization ($\omega_L = \omega_R$), only one of the dimer modes couples to the microwave environment, with an effective coupling strength $\kappa = (\kappa_a + \kappa_b)/2$.

symmetrically to the coaxial pin? In this section, we investigate the implications of this alternative strategy for the grAlPA design.

Fig. A2.3(a) and (b) show the effective design with both resonators symmetrically coupled. In contrast to the Bose-Hubbard dimer model illustrated in Fig. 3.1(a), we assume here that each resonator is directly coupled to the microwave environment with strengths κ_L and κ_R, respectively. For simplicity, we consider only the linear part of the Bose-Hubbard Hamiltonian in Eq. (3.1) and we assume negligible internal losses in both resonators. Applying a Markov approximation to the couplings $\kappa_{L,R}$, we can derive the corresponding Heisenberg-Langevin equations for the bosonic operators $\hat{a}_{L,R}$ of each resonator (a complete derivation can be found in Ref. [132]),

$$\frac{d\hat{a}_i}{dt} = -i\omega_i\hat{a}_i - iJ\hat{a}_j - \kappa_i\frac{\hat{a}_i}{2} - \sqrt{\kappa_i\kappa_j}\frac{\hat{a}_j}{2} - \sqrt{\kappa_i}\hat{a}_{in}, \tag{A2.1}$$

where i, j = L, R and $\hat{a}_{in}$ is the input field transmitting trough the microwave port. Furthermore, the input-output relation of the propagating fields takes the form:

$$\hat{a}_{out} = -\hat{a}_{in} + \sqrt{\kappa_L}\,\hat{a}_L + \sqrt{\kappa_R}\,\hat{a}_R. \tag{A2.2}$$

Applying a Fourier transform to Eq. (A2.1), and using Eq. (A2.2), we can derive the following formula for the reflection coefficient S_{11} as a function of frequency ω,

$$S_{11}(\omega) = -1 - i\left[\frac{\kappa_L\left(\Delta_R - i\frac{\kappa_R}{2}\right) + \kappa_R\left(\Delta_L - i\frac{\kappa_L}{2}\right) - 2\sqrt{\kappa_L\kappa_R}\left(J - i\frac{\sqrt{\kappa_L\kappa_R}}{2}\right)}{\left(\Delta_L - i\frac{\kappa_L}{2}\right)\left(\Delta_R - i\frac{\kappa_R}{2}\right) - \left(J - i\frac{\sqrt{\kappa_L\kappa_R}}{2}\right)^2}\right], \tag{A2.3}$$

where $\Delta_i = \omega_i - \omega$ (i = L, R). By taking the approximations $\kappa_R = 0$ the above equation reduces to the reflection coefficient of the Kerr-free BHD reflection presented in Eq. (A1.5).

We are interested in the case where both modes are symmetrically coupled such that $\kappa_L = \kappa_R = \kappa$. In this case, Eq. (A2.3) becomes

$$S_{11}(\omega) = -1 - i\frac{\kappa(\Delta_R + \Delta_L - 2J)}{\Delta_L\Delta_R - i\frac{\kappa}{2}(\Delta_L + \Delta_R - 2J) - J^2}, \tag{A2.4}$$

We now analyze the behavior of the dimer modes linewidths $\kappa_{a,b}$ in two limiting cases. When $J \ll |\omega_L - \omega_R|$, the resonators are effectively decoupled, and both linewidths converge to κ. In the opposite limit, $J \gg |\omega_L - \omega_R|$, we can extract an analytical expression for the linewidths by approximating Eq. (A2.4) close to $\omega_{a,b}$. We obtain

$$\begin{aligned} \kappa_a &= \kappa\frac{(\omega_L - \omega_R)^2}{8J^2}, \\ \kappa_a &= \kappa\left(2 - \frac{(\omega_L - \omega_R)^2}{8J^2}\right). \end{aligned} \tag{A2.5}$$

Similar to Section 3.1, in Fig. A2.3(c) we plot the dependence of $\kappa_{a,b}$ on the detuning of the bare resonator frequencies. In contrast to Fig. 3.1(b), we find that under perfect hybridization the total coupling to the microwave environment is not equally shared between the dimer modes and one mode becomes effectively decoupled. FEM simulations confirm this behavior, as shown in Fig. A2.3(c). This effect arises because the microwave port couples now to the total electric dipole of the hybridized modes, which restricts excitations of only the common mode. One might expect that moving away from perfect hybridization could restore the conditions to achieve non-degenerate gain. However, as shown in Fig. 3.1(b), imperfect hybridization increases the spacing between the dimer frequencies, preventing equal population when pumping between them. From these observations, we conclude that symmetric single-port coupling cannot achieve non-degenerate gain. Nevertheless, the selective coupling of the new design suggests a potential upgrade for the grAlPA: a double-port design that physically separates the hybridized modes. The central question is whether such a design can meet the requirements for achieving non-degenerate gain. In Appendix D.9, we explore this possibility.

B.5 Protocol to align the in-plane magnetic field

As discussed in Section 3.7, the current grAlPA design suffers from a strong susceptibility to out-of-plane magnetic fields $B_\perp$. Even fields as low as 20 μT are enough to trap unwanted vortices in the capacitor pads of the grAl resonators (cf. Fig. 3.3). To mitigate the effect of residual $B_\perp$ when ramping the in-plane component $B_{||}$, we calibrate the orientation of the magnetic field following a protocol similar to Refs. [68, 75]. We fix $B_{||}$ and sweep $B_\perp$ in a small range below the critical field 20 μT. Simultaneously, we monitor the phase of the reflection coefficient S_{11} at a fixed frequency close to the resonance of one dimer mode. The phase should follow a quadratic variation with $B_\perp$, where the maximum indicates

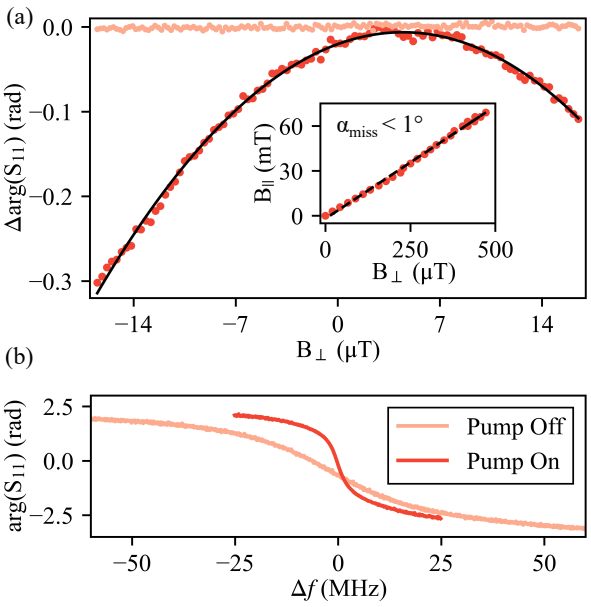

Figure A2.4: Calibration of the magnetic field orientation. **(a)** Example of a compensation sweep to calibrate the unwanted $B_\perp$, at $B_{||}$ = 0 T. We sweep $B_\perp$ and measure the phase response $\Delta\arg(S_{11})$ close to the resonance of the low-frequency dimer mode. A clear quadratic trend is observed only when driving the grAlPA. The compensation field $B_\perp$ is calcualted by fitting the data (black solid line) and extracting the field that maximizes $\Delta\arg(S_{11})$. The inset displays the compensation fields measured for different $B_{||}$. The black dashed line depicts a linear fit of the data. The slope of this line provides an estimation of the misalignment angle of the in-plane component. **(b)** Phase of the reflection coefficient S_{11} as a function of the detuning Δf from the resonance frequency f_r, while having the grAlPA on and off. By operating the grAlPA at G_0 = 18 dB, we observe a factor of 8 reduction in the mode linewidth.

the required compensation field [68, 75]. However, as shown in Fig. A2.4(a), we observe a negligible variation of the phase response using this procedure.

To correctly calibrate the field orientation for our measurements, we instead take advantage of its gain-bandwidth product. By driving the grAlPA with a non-degenerate pump tone, the linewidths of the dimer modes decrease according to $\sqrt{G_0} \cdot \mathrm{BW} = \kappa_{\mathrm{eq}}$ (cf. Eq. (4.7)), which for G_0 = 18 dB effectively reduces the linewidth of the modes by a factor of 8 (see Fig. A2.4(b)). We therefore enhance the sensitivity of the phase to $B_\perp$, facilitating the measurement of the compensation field. In Fig. A2.4(a) we present the effect of the pump-on compensation sweep at $B_{||}$ = 0 T and measured at the low-frequency mode. We observe the expected quadratic trend in the phase only when we activate the pump. Repeating the same procedure for different in-plane fields yields the dependence of the compensation field with $B_{||}$, which follows a linear trend as depicted in the inset of Fig. A2.4(a). By calculating the slope of the linear response we can then determine the misalignment angle of the in-plane magnetic field, which in our experiments was $\alpha_{\mathrm{miss}} < 1°$.

B.6 Magnetic field resilience of other devices

In Fig. A2.5, we present the gain performance of two additional grAlPAs under in-plane magnetic fields. For both samples, the field orientation was calibrated using the pump-off version of the procedure described in Appendix B.5, which explains their reduced resilience to $B_{||}$. The gain profiles in Fig. A2.5(a) were obtained with the same grAlPA used for the results in Fig. 3.11. Remarkably, the gain profiles in Fig. A2.5(b) exhibit an instantaneous bandwidth of ≈ 7 MHz, achieved by fabricating the grAlPA closer to the coupling pin of the cylindrical waveguide (cf. Fig. 3.3). However, because this sample was fabricated without a Nb coupling pad, the results could not be reproduced in subsequent cooldowns.

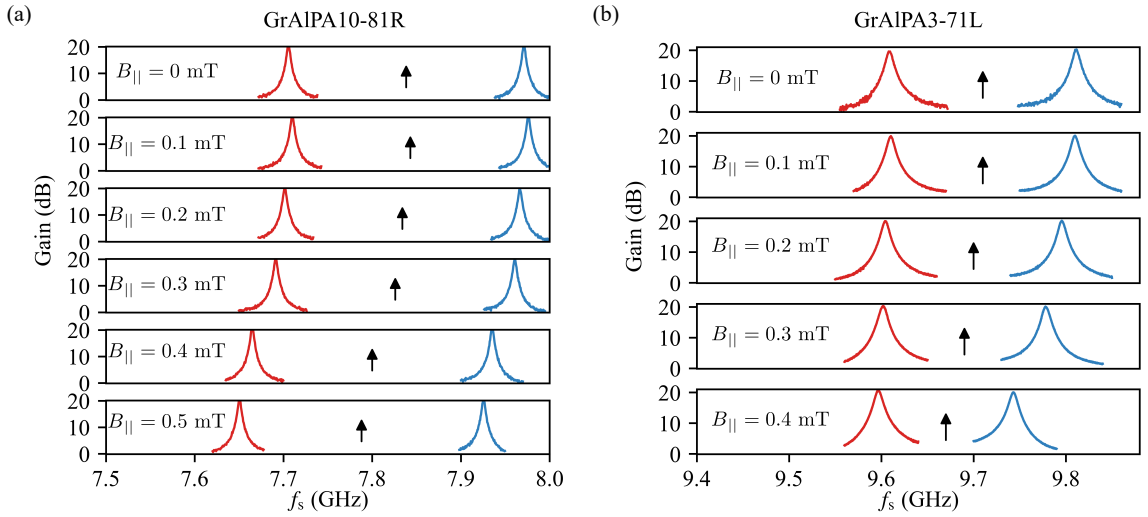

Figure A2.5: Gain performance of other grAlPAs under in-plane magnetic field. In both panels the field orientation was calibrated with the pump-off version of the procedure shown in Appendix B.5. The gain curves of panel **(a)** were obtain with the same grAlPA used for the results in Fig. 3.11. Using Lorentzian fits of the profiles in panel **(b)** we extract an instantaneous bandwidth of 7 MHz.

B.7 Attenuator model for insertion loss

We estimate the added noise (N_λ) of a lossy microwave component or transmission line by modeling it as an attenuator with an equivalent resistance R and thermalized at a temperature T [83]. We first consider the classical limit, where the noise of the attenuator is dominated by thermal fluctuations. In this regime, the total output noise of the component is simply given by the Johnson-Nyquist noise $k_\mathrm{b}T$, where k_b is the Boltzmann constant. Referring the noise to the input of the attenuator, we have $N_\mathrm{out}/\lambda = Bk_\mathrm{b}T/\lambda = N_\mathrm{in} + N_\lambda$ where $N_\mathrm{in/out}$ is the noise at the input/output of the component and B the measurement bandwidth. Without loss of generality, we assume that N_in is generated by a white-noise source with impedance R and also thermalized at T, such that $N_\mathrm{in/out} = Bk_\mathrm{b}T$. From this, we derive

$$N_\lambda = \left(\frac{1-\lambda}{\lambda}\right) Bk_\mathrm{b}T. \tag{A2.6}$$

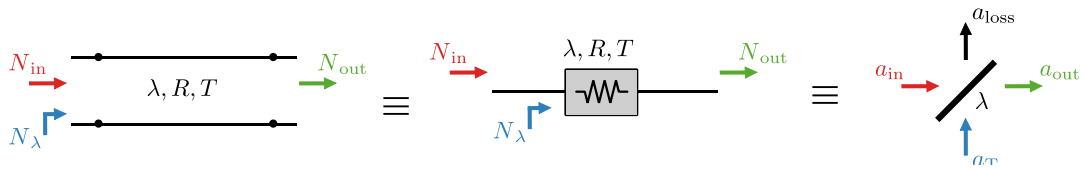

Figure A2.6: Classical and quantum models of a lossy microwave component. At the classical level, a microwave component or transmission line (left panel) can be modeled as an attenuator with insertion loss λ, effective resistance R, and thermalized at a temperature T (middle panel). The noise contribution of this effective attenuator, N_λ, is described by Eq. (A2.6). At the quantum level, the same lossy component can be represented as a beam splitter with transmittance λ (right panel).

To calculate the quantum mechanical equivalence of Eq. (A2.6), we model the effective attenuator as a beam-splitter with transmittance λ [237], as shown in Fig. A2.6. We assume that one of the input ports has incoming photons described by the bosonic annihilation operator $\hat{a}_{\text{in}}$, while the other input port is assumed to receive radiation $\hat{a}_{\text{T}}$ originating from a blackbody at temperature T. Then the bosonic field at the output of the beam-splitter $\hat{a}_{\text{out}}$ is given by

$$\hat{a}_{\text{out}} = \lambda \hat{a}_{\text{in}} + (1 - \lambda)\, \hat{a}_{\text{T}}, \tag{A2.7}$$

The noise at the output of the attenuator then can be calculated using the symmetrized noise spectral density of the bosonic operators [147], which results in

$$N_{\text{out}} = \lambda N_{\text{in}} + (1 - \lambda)\, N_{\text{T}}, \tag{A2.8}$$

where $N_{\text{T}} = B\hbar\omega n_{\text{T}}$ and n_{T} is the generalized Johnson-Nyquist noise in units of photons (cf. Eq. (1.51)). In this model, the added noise originates because part of the information is lost through photons leaving the other output port of the Beam-splitter, described by the bosonic mode $\hat{a}_{\text{loss}}$ in Fig. A2.6.

B.8 Noise level comparison with Dimer Josephson Junction Array Amplifier (DJJAA)

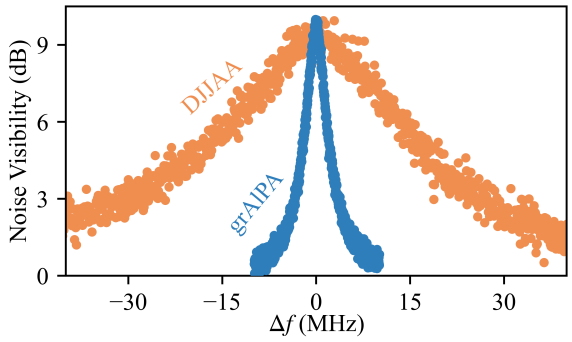

Figure A2.7: Comparison of noise visibility of the grAlPA and the DJJAA. The datasets were obtained using the setup shown in Fig. A2.1(a), with the amplifiers biased to provide a maximum gain of 20 dB. Both amplifiers exhibit comparable noise levels, with the DJJAA showing a broader noise profile due to its larger instantaneous bandwidth.

In this section, we compare the noise level of the grAlPA with that of a Dimer Josephson Junction Array Amplifier (DJJAA) [22]. The DJJAA is connected using the same experimental setup as for the grAlPA measurements (cf. Fig. A2.1(a)). In Fig. A2.7, we present the noise visibility results obtained with both amplifiers operated at 20 dB gain. We observe that both devices exhibit comparable noise performance. The small differences are likely coming from the insertion loss in the device packaging.

C Power and noise calibration methods

Throughout the main chapters of this thesis, we have demonstrated several outstanding amplifier metrics achieved with the grAlPA, such as a saturation power close to -110 dBm and added noise approaching the quantum limit. To reliably measure these quantities, it is essential to obtain an accurate calibration of the power at both the input and output planes of the amplifier. However, as with all superconducting parametric amplifiers, performing such calibrations can be challenging, since one must account for all additional cabling and components inside the cryostat. This limitation becomes particularly critical when estimating the amplifier's added noise, because it is expected to be smaller than any other noise contribution in the setup. Consequently, we need a very precise calibration of every noise source to draw strong conclusions about the amplifier's noise performance.

In this section, we provide a brief overview of some of the methods currently used in the community to accurately calculate the performance of parametric amplifiers. We focus in the methods used in this thesis and which are readily available in our laboratory: Y-factor noise calibration and power calibration with a superconducting qubits in cQED and wQED architectures. For information about another method commonly used in the literature, which involve the use of shot-noise tunnel junctions (SNTJs) [255], we refer to the comprehensive review provided by Ref. [149]. Another interesting approach, similar to SNTJs, which consist of using hot-electron shot noise of a current biased metallic nanowire can be found in Ref. [256].

C.1 Calibration inside a cryostat

To measure the performance of a parametric amplifier, we use a cryostat equipped with microwave connections like for example the one illustrated in Appendix B.2. The setup consists of input and output lines, which effectively act as attenuation and amplification chains, respectively. In general, if impedance mismatches between components along these lines are negligible, the dynamics can be simplified and described by the model shown Fig. A3.1. We model the input line as an effective attenuator with insertion loss A, characterized by the total attenuation of the chain. Typically, the input line is designed such that the dominant noise contribution $N_{\mathrm{A}}^{\mathrm{T}}$ originates from the final stage of attenuation, which is thermalized at a temperature $T \approx$ 30-40 mK. So that, we can get a good estimate of this noise using the blackbody radiation formula[2] Eq. (1.51). Similarly, we model the output line as an amplifier with gain G and input-referred added noise N_{G}.

Experimentally, we can directly measure the powers $P_{\mathrm{in/out}}$ of the incoming and outgoing signals outside the cryostat. Likewise we can also measure the noise $N_{\mathrm{in/out}}$ accompanying these signals with for example an FPGA board or a spectrum analyzer. These quantities are

[2] This assumption, however, should be verified a-posteriori.

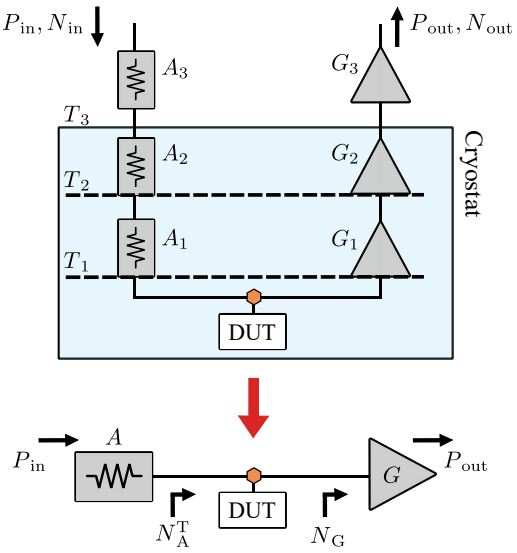

Figure A3.1: Equivalent circuit model for power and noise calibration. Schematics of the microwave setup used for superconducting quantum device measurements. The power P_{in} and noise N_{in} of an input signal are lowered by a series of attenuators before reaching the device under test (DUT) mounted at the lowest temperature stage of the cryostat. The DUT response is routed through an output line with amplifiers, producing a total output power P_{out} and noise N_{out}. Assuming negligible impedance mismatches, the input and output lines can be modeled as an effective attenuator with total insertion loss $A = \Pi_i A_i$ and as an amplifier with total gain $G = \Pi_i G_i$. The total noise referred to the input plane of the DUT (orange marker) is the sum of the input-referred noise of the amplification chain N_G, plus the Johnson–Nyquist noise N_A^T of the last attenuator in the input line.

related to the effective attenuation and gain of the input and output lines by the following equations

$$\begin{aligned} P_{out} &= GAP_{in}, \\ N_{out} &= G\left(N_A^T + N_G\right). \end{aligned} \tag{A3.1}$$

The central challenge lies in determining both the power and noise at the input of the amplification chain (marked by the orange marker in Fig. A3.1), which corresponds to the location where a quantum system under test would be mounted. Knowing any one of the parameters A, G, or N_G, allows us to infer the others through Eq. (A3.1). The essence of each calibration method is therefore to provide a precise estimate of one of these quantities, from which the remaining parameters can be accurately determined.

C.2 Y-factor method

A widely adopted method, thanks to its flexibility and simplicity of implementation, is the so-called Y-factor technique [149]. As illustrated in Fig. A3.2(a), two terminated attenuators thermalized at temperatures T_{cold} and T_{hot} are connected to the amplifier through a microwave switch. The noise measured at the output of the amplification chain, N_{out}, depends on which attenuator is selected. Since the noise added by the amplifier is independent of this choice, we can use Eq. (A3.1) to estimate N_G with the formula

$$N_G = \frac{N_A^{T_{hot}} - Y N_A^{T_{cold}}}{Y - 1}, \tag{A3.2}$$

where $Y = N_{out}^{hot}/N_{out}^{cold}$ is called the noise Y-factor and N_A^T corresponds to the output noise of each attenuator, which can be calculated using the blackbody radiation formula

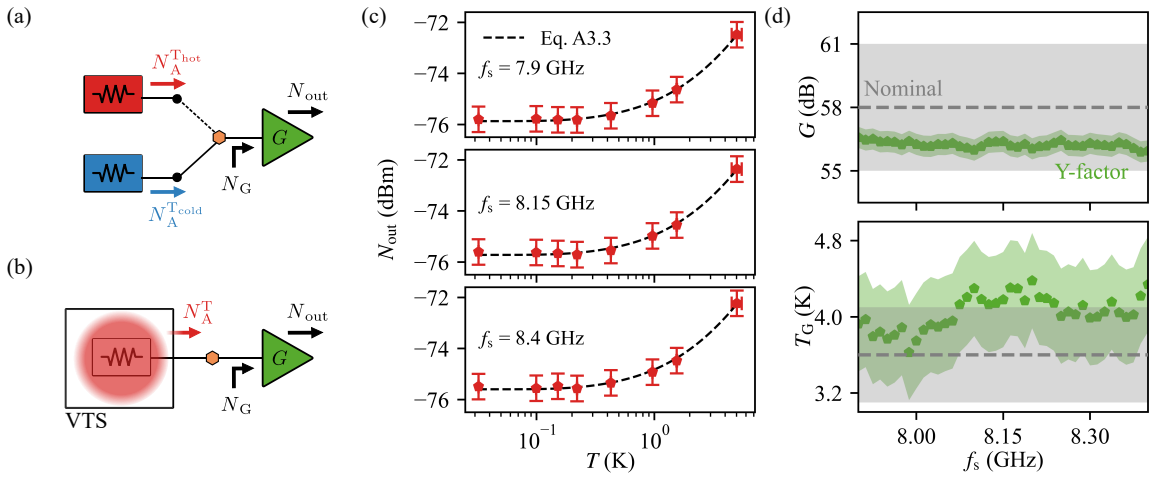

Figure A3.2: Noise calibration using the Y-factor method. **(a)** Schematic of the Y-factor method. Two terminated attenuators, thermalized at different temperatures $T_{\mathrm{hot/cold}}$, are connected before an amplifier with gain G and input-referred noise N_{G}. By switching between the attenuators and measuring the output noise N_{out}, we can extract G and N_{G} using Eq. (A3.2). **(b)** Continuous version of the Y-factor calibration. A terminated attenuator is thermalized on a variable-temperature stage (VTS). By varying the stage temperature, the measured N_{out} is fitted with Eq. (A3.3) to obtain G and N_{G}. The orange markers in panels (a) and (b) indicate the plane at which the noise calibration is performed. **(c)** Experimental N_{out} vs. temperature curves at three different frequencies, measured with the setup in Fig. A2.1(a). We implement the method in panel (b) by gradually increasing the cryostat mixing-chamber temperature. The grAlPA is turned off during the measurement, making the HEMT at the 4 K stage the first amplifier in the output line. The black dashed lines are fits to Eq. (A3.3). **(d)** Gain G (top) and input-referred noise temperature T_{G} (bottom) extracted from the fits of Eq. (A3.3). Both quantities agree with the nominal values [143], depicted by black dashed lines. Error bars for the measured data arise mainly from uncertainties in the temperature readings. A ±5 dB uncertainty is assigned to the nominal G and propagated to estimate the corresponding uncertainty in T_{G} via Eq. (A3.1).

in Eq. (1.51). As shown in Eq. (A3.2), this method has no explicit frequency dependence, making it suitable for broadband calibration of N_{G}. Furthermore, applying Eq. (A3.1) also allows us to extract an estimate of output line gain G. Once both quantities are known, the attenuation of the input line can be determined by simply switching the amplifier chain to the desired connection.

A similar method consists of connecting the amplifier to an attenuator mounted on a variable-temperature stage (see Fig. A3.2(b)). In this case, the output noise is measured continuously as the attenuator temperature T is varied[3]. If the stage is thermally isolated from the amplifier, N_{G} remains constant, and using again the blackbody radiation formula (cf. Eq. (1.51)) and Eq. (A3.1) we can derive an equation to fit the measured data,

$$N_{\mathrm{out}}(T) = G\left(\frac{B\hbar\omega}{2}\coth\left(\frac{\hbar\omega}{2k_{\mathrm{b}}T}\right) + N_{\mathrm{G}}\right), \tag{A3.3}$$

[3] For this reason, this method is sometimes referred to as the continuous Y-factor method.

where B is the measurement bandwidth[4] and k_b the Boltzman constant.

As an example, we apply this method to calibrate the noise of the output lines in one of our cryostats. The setup used is shown in Fig. A2.1(a), with the grAlPA pump turned off while the entire mixing-chamber stage is heated. As presented in Fig. A3.2(c), the measured noise follows the expected trend of Eq. (A3.3). Moreover, by fitting the data with N_G as the fitting parameter, we can calculate the input referred noise temperature $T_G = N_G/GBk_b$, which remains approximately constant over a frequency range between 7.5 GHz to 8.4 GHz (see Fig. A3.2(d)). This value is consistent with the nominal noise temperature of the HEMT amplifier (~3.6 K), serving in these experiments as the first stage of the amplification line. It also agrees with the noise values reported in Fig. 3.12, obtained using the method described later in Appendix C.4. The uncertainty ranges originate from the accuracy of the thermometers used in the setup.

Although this method provides a straightforward way to calibrate the amplifier noise over a broad frequency range, it comes with some limitations. First, it depends on precise measurements of the attenuator temperatures. Any uncertainty arising from the incorrect calibration of the thermometers or temperature gradients across the cryostat base plate, can lead to significant variations in the calculated noise. This problem is particularly acute for coaxial attenuators, which may develop thermal gradients between their inner pin and the outer body. To mitigate this issue, attenuators are commonly substituted with 50 Ω terminations, which provide effective thermalization of the coaxial inner conductor. Alternatively, one can use attenuators fabricated from materials with high thermal conductivity, as it was reported by Ref. [257]. The second limitation is that this calibration provides the noise at the output of the attenuator, rather than directly at the input of the amplification chain. Any lossy or insufficiently thermalized component located between these planes can result in an underestimation of N_G. Finally, the current methodology does not permit direct extraction of the grAlPA's intrinsic noise, as the entire mixing chamber is heated during the measurement. Accurate characterization of the grAlPA's noise would require a setup incorporating an optimized variable-temperature stage, such as the one described by Refs. [25, 149].

C.3 Qubit in a cQED setup

A second calibration method uses a qubit embedded in a cQED setup (see Fig. 1.11). As discussed in Section 1.2.5, a qubit coupled to a linear cavity experiences an AC Stark shift $\Delta\omega_q$ and measurement-induced dephasing $\Delta\Gamma_\phi$, both dependent on the cavity photon population. Close to the single-photon regime and in the small dispersive shift limit, $\Delta\omega_q$ and $\Delta\Gamma_\phi$ can be calculated using Eq. (1.37) and Eq. (1.38). In typical setups, the cryostat input line is designed such that the thermal photon contribution to the cavity population is below 10^{-3}. As a consequence, the population depends solely on the coherent drive

[4] For measurements performed with a spectrum analyzer, VNA or FPGA board, B corresponds to the resolution bandwidth, the IF bandwidth, and the inverse of the integration time, respectively.

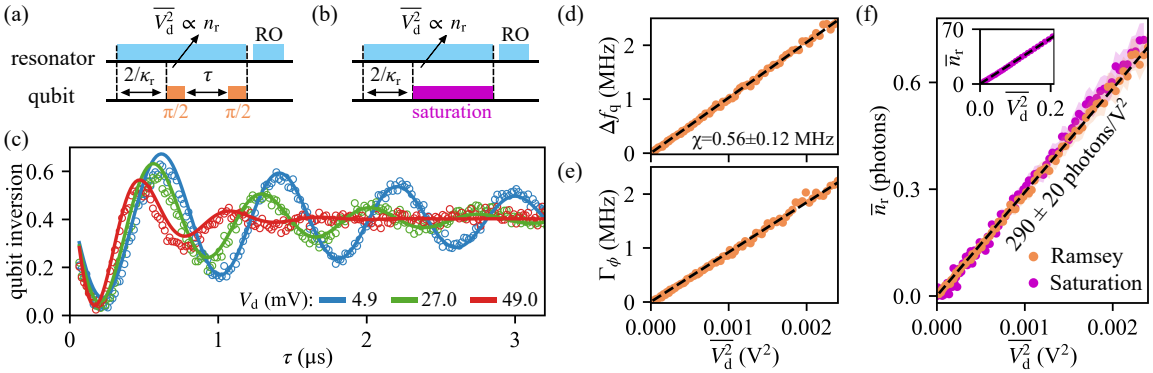

Figure A3.3: Power calibration using a GFQ with a resonant cavity drive. **(a)-(b)** Pulse sequences used to measured the AC stark shift of the GFQ using Ramsey interferometry and Two-tone spectroscopy, respectively. To reach steady-state, the resonator is populated $2/\kappa_r = 260$ ns before the start of the qubit manipulation. We use a readout pulse (RO) with a power equivalent to 30 circulating photons in the resonator. **(c)** Ramsey fringes obtained using the pulse sequence shown in panel (a) for three different readout voltages V_d. The solid lines are fits using a sinusoidal function with an exponential decaying envelope. **(d)-(e)** AC stark shift Δf_q and dephasing rate Γ_ϕ as a function of $\overline{V_d^2}$ obtained from Ramsey experiments. The black dashed lines represent fits of Eq. (A3.5). We calculate $\chi = 0.56 \pm 0.12$ MHz and $c = 290 \pm 35$ photons/V^2. **(d)** Resonator occupation number $\overline{n}_r$ as a function of $\overline{V_d^2}$, calculated from Ramsey interferometry (orange) and two-tone spectroscopy (purple). The black dashed line comes from the fits shown in panels (d) and (e). The inset shows that the power calibration remains valid up to $\overline{n}_r \approx 70$.

contribution $\bar{n}_r$. Now, we can relate this value to the power at the input of the readout resonator through the formula

$$P_s = \hbar\omega_r\kappa_r\bar{n}_r/4, \tag{A3.4}$$

where ω_r and κ_r are the resonator's frequency and linewidth, respectively. Then, by comparing P_s with the power outside the cryostat P_{in}, we can extract an estimation of the input-line attenuation A. Finally, we can use Eq. (A3.1), to calculate N_G within the linewidth of the readout resonator.

To show how this calibration method works, we employ single-shot heterodyne detection to measure the AC Stark shift and induced dephasing of the GFQ shown in Fig. 3.13(a). We use two different pulse sequences[5], as illustrated in Fig. A3.3(a) and (b). In the first sequence, we carry out Ramsey interferometry while driving the readout resonator with a room-temperature voltage amplitude V_d. From Eq. (1.37) and Eq. (1.38), we can write,

$$\begin{aligned} \Delta\omega_q &= \chi\bar{n}_r = \chi\left(c\overline{V_d^2}\right), \\ \Delta\Gamma_\phi &= \frac{2\chi^2}{\kappa}\left(c\overline{V_d^2}\right). \end{aligned} \tag{A3.5}$$

[5] For the present experiments, the population pulse was applied during both $\pi/2$-pulses due to the long ring-up time of the readout resonator relative to the GFQ decoherence time T_2. As a result, the $\pi/2$-pulses must be calibrated for each value of $\bar{n}_r$. For sufficiently short ring-up times, the population pulse can instead be confined to the interval between the $\pi/2$-pulses, as demonstrated by Ref. [22].

where χ is the dispersive shift of the readout resonator and c is the proportionality constant constant relating $\bar{n}_\mathrm{r}$ and $\overline{V_\mathrm{d}^2}$. We calculate $\kappa_\mathrm{r}/2\pi$ = 1.25 ± 0.25 MHz from single-tone spectroscopy experiments of the readout resonator. The results of the Ramsey experiments for three different voltages V_d are shown in Fig. A3.4(b), where the solid lines represent fits using a sinusoidal function with an exponential decaying envelope, from which we extract[6]. $\Delta\omega_\mathrm{q}$ and $\Delta\Gamma_\phi$. In Fig. A3.3(d)-(e) we plot the extracted values of $\Delta\omega_q$ and $\Delta\Gamma_\phi$ as a function of $\overline{V_\mathrm{d}^2}$. We fit both quantities simultaneously using Eq. (A3.5) to obtain χ = 0.56 ± 0.12 MHz and c = 290 ± 35 photons/V^2. The errors come from the Fano uncertainty of κ.

To extract an estimation of the input-line attenuation A, we use Eqs. (A3.1), (A3.4) and (A3.5) to derive the equation

$$A = c\left(\frac{Z_0\hbar\omega_\mathrm{r}\kappa_\mathrm{r}}{4}\right), \tag{A3.6}$$

where Z_0 = 50 Ω is the port impedance of the microwave generator. We employ Eq. (A3.6) and the fitted value of c to obtain A = -128 ± 0.5 dB. We use this result for the measurements presented in Section 3.9.

As can be observed in Fig. A3.3(c) the calibration using Ramsey experiments is limited to photon numbers below $\overline{n}_\mathrm{r} \approx 1$, as the qubit T_2 time decreases below the resolution time of the readout electronics at higher readout powers. To overcome this limitation we use two-tone spectroscopy with a qubit saturation pulse while populating the resonator with $\overline{n}_\mathrm{r}$ photons, as illustrated in Fig. A3.3(b). As shown in Fig. A3.3(f), for low readout powers, the two calibration methods agree. Moreover, the inset of Fig. A3.3(f) shows that the calibration is valid up to $\overline{n}_\mathrm{r} \approx 70$.

So far we have assumed that the readout cavity is driven on resonance and the dispersive shift is much smaller than the cavity linewidth. But, when the drive is detuned from the cavity frequency, both the AC Stark shift and the measurement-induced dephasing acquire corrections that depend on the detuning $\Delta\omega_\mathrm{r} = \omega_\mathrm{d} - \omega_\mathrm{r}$, where ω_d is the readout driving frequency. Applying Eq. (A3.5) under these conditions can underestimate the input-line attenuation by up to a factor of four (see Fig. A3.4), potentially resulting in an unphysical estimation of the added noise below the quantum limit. A similar result occurs when $\kappa_\mathrm{r} \lesssim \chi$. To avoid such issues, it is preferable to measure $\Delta\omega_\mathrm{q}$ and $\Delta\Gamma_\phi$ as functions of the detuning $\Delta\omega_\mathrm{r}$ and fit the results using the following corrected expressions [139, 235]

[6] Keep in mind that $\Gamma_\phi = 1/T_2^*$ is in units of angular frequency i.e. in units of ω.

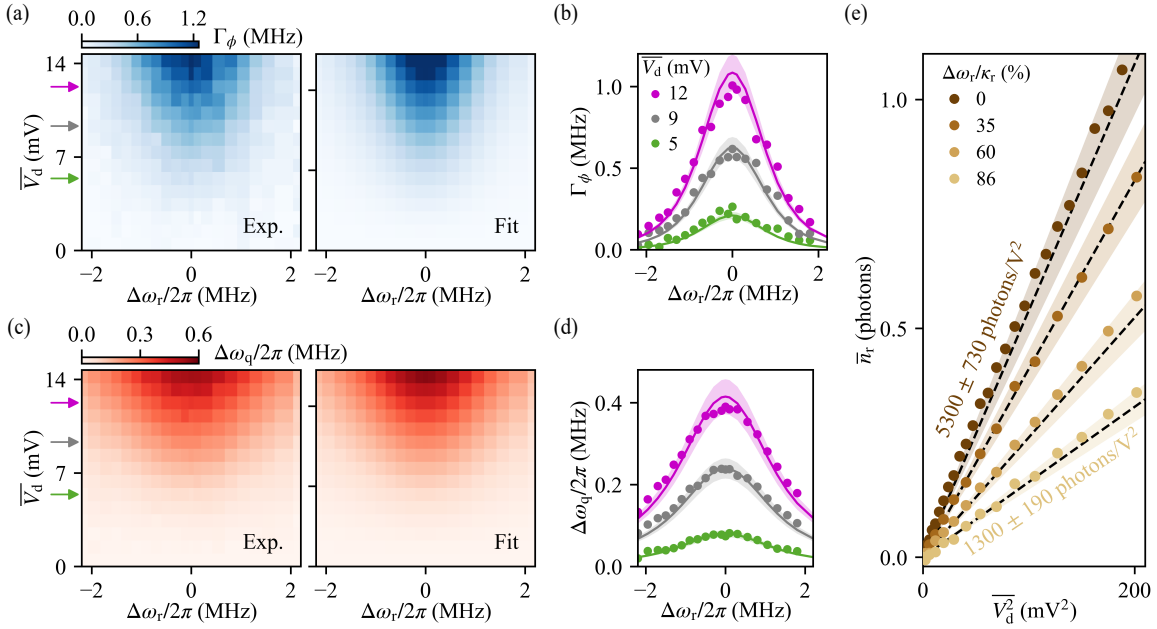

Figure A3.4: Power calibration using a GFQ with a frequency dependent cavity drive. We measure the qubit AC stark shift $\Delta\omega_q$ and dephasing rate Γ_ϕ using the Ramsey sequence illustrated in Fig. A3.3(a). **(a), (c)** Measured (left) and fitted (right) qubit dephasing and AC stark shift as a function of readout voltage $\overline{V_d}$ and readout detuning $\Delta\omega_r$. **(b), (d)** Linecuts of Γ_ϕ and $\Delta\omega_q$ for three different readout voltages. The solid lines correspond to the resulting fits using Eq. (A3.7). **(d)** Resonator occupation number $\bar{n}_r$ as a function of $\overline{V_d^2}$ for four different detunings $\Delta\omega_r/\kappa_r$ = 0, 0.35, 0.60 and 0.86. The dashed lines correspond to the resulting fits using Eq. (A3.7).

$$\bar{n}_r = \frac{c\overline{V_d^2}}{2}\left(\frac{\kappa_r^2+\chi^2}{\kappa_r^2+(2\Delta\omega_r+\chi)^2}+\frac{\kappa_r^2+\chi^2}{\kappa_r^2+(2\Delta\omega_r-\chi)^2}\right),$$

$$\Delta\omega_q = \chi\bar{n}_r\left(\frac{\kappa_r^2+(2\Delta\omega_r)^2-\chi^2}{\kappa_r^2+(2\Delta\omega_r)^2+\chi^2}\right), \tag{A3.7}$$

$$\Delta\Gamma_\phi = \frac{2\bar{n}_r\kappa_r\chi^2}{\kappa_r^2+\chi^2+(2\Delta\omega_r)^2}.$$

Fig. A3.4 presents an example of the improved power calibration obtained in the setup used for the results shown in Chapter 4. Similar to Fig. A3.3, we estimate χ and c from fits using Eq. (A3.7).

We can then employ again Eq. (A3.4) to derive a more general formula of the attenuation A at $\Delta\omega_r = 0$, using now Eq. (A3.7). In this more general case, we obtain

$$A = c\left(\frac{Z_0\hbar\omega_r(\kappa_r+\chi)^2}{4\kappa_r}\right). \tag{A3.8}$$

By taking again the value of c, extracted from the fits in Fig. A3.4 and insert it in Eq. (A3.8), we calculate A = -110.70 ± 0.63 dB.

Compared to the Y-factor technique, this method significantly reduces the uncertainty in the power calibration, making it widely regarded as the optimal approach to assess the noise performance of parametric amplifiers. However, it also does not account for the insertion loss between the amplifier and the readout cavity. Accurately determining this loss is challenging and leads to increased uncertainties when reporting noise calibrated at a plane other than the cavity input. One possible solution is to integrate the cQED system and the parametric amplifier on the same chip. This approach, however, would require the implementation of an on-chip microwave circulator to shield the qubit from the strong amplifier pump.

Additionally, this method is constrained by the linewidth of the readout resonator, which is typically $\leq$ 10 MHz in most experiments. Consequently, it cannot be easily extended to cover the entire 4–12 GHz range. Notice that to implement this method with the Ramsey pulse sequence in Fig. A3.3(a), the qubit must have a coherence time $T_2 \gg \tau_{\text{min}}$, where τ_{min} is the minimum integration time allowed by the microwave electronics[7]. If this condition is not satisfied, extracting $\Delta\omega_{\text{q}}$ and $\Delta\Gamma_\phi$ is not possible using standard Ramsey measurements.

A key advantage of employing a qubit in a cQED architecture is that it allows us to directly calculate the readout quantum efficiency η. In Section 3.9, we described how η can be estimated from measurements of power-dependent IQ clouds. A more precise determination of η can be obtained by measuring the backaction produced by the amplifier on the qubit [148]. However, performing such experiments requires a cQED system satisfying the relation $2/\kappa_{\text{r}} \ll \tau \ll T_1$, where τ is the readout pulse length and T_1 is the qubit energy relaxation time.

C.4 Qubit in a wQED setup

An alternative approach to calibrate the attenuation in a cryogenic microwave setup, is based on the resonance fluorescence produced by a qubit in a wQED architecture, as illustrated in Fig. 1.10. In this configuration, the qubit is directly coupled to a microwave port, resulting in a radiative decay rate κ. For sufficiently low powers, where the Rabi frequency Ω_{R} remains much smaller than the qubit anharmonicity α, the reflection coefficient S_{11} follows Eq. (1.32). Furthermore, if the qubit relaxation is Purcell-limited i.e. when the energy relaxation rate is dominated by κ, pure dephasing can be neglected, and S_{11} simplifies to

$$S_{11} = 1 - \frac{2\kappa}{\Gamma} \frac{1 + 2i\Delta_{\text{q}}/\Gamma}{1 + \left(2\Delta_{\text{q}}/\Gamma\right)^2 + 2\left(\Omega_{\text{R}}/\Gamma\right)^2}, \tag{A3.9}$$

[7] In an OPX+®, the minimum is 16 ns.

where $\Delta_q = \omega - \omega_q$ is the detuning between the drive frequency and the qubit frequency ω_q and we can use the approximation $\Gamma = \kappa + \gamma$, where γ denotes the qubit internal loss rate. In the single-photon regime, Eq. (A3.9) resembles the response of a linear resonator, enabling the extraction of ω_q, κ, and γ via a standard circle fit. At higher drive powers, the same equation can be used to fit the qubit response with Ω_R as the only free parameter. This procedure allows us to determine the power at the qubit input and, consequently, the input-line attenuation through the Rabi frequency (cf. Eq. (1.33)).

In contrast to the cQED setup, where the calibration is restricted to the linewidth of the readout resonator, the wQED approach enables estimation of the input line attenuation over a broader frequency range by employing a flux-tunable qubit. Furthermore, this method does not require qubits with long coherence times, offering greater flexibility in device design and fabrication. For instance, the qubit can be engineered to fit the same packaging used for a parametric amplifier, therefore eliminating uncertainties associated with insertion loss between connecting components. In practice, this allows calibration directly at the amplifier input plane, either by employing microwave switches or through successive cooldowns, as employed in Fig. 3.12(a).

We employ this method to calibrate the noise of the grAlPA for different in-plane magnetic fields (cf. Fig. 3.12). We use the flux-tunable transmon qubit shown in Fig. A3.5(a). The qubit is designed to fit within the cylindrical sample holder used for the grAlPA. It consists of a single SQUID junction shunted by a coplanar capacitor with $C_p \approx 77$ fF. The capacitor plates employ a fractal geometry to mitigate flux trapping under an applied out-of-plane magnetic field. Device fabrication is carried out using two steps of optical lithography, followed by sequential zero-angle evaporations of 30 nm and 40 nm of pure Al. Prior to the second evaporation, the native oxide on the first Al layer is removed by Ar ion milling [260], after which the sample undergoes static oxidation for 30 min at an oxygen partial pressure of 30 mbar.

The Josephson junctions formed from the overlap of the two Al layers, have an area of $\approx$ 3.8x3.8 μm^2. The SQUID loop, shown in the inset of Fig. A3.5(a), has an area of $\approx$ 4x2 μm^2. From the junctions geometry we expect a capacitance of C_J =722 fF and total SQUID capacitance $C_{SQ} = 2C_J$ =1444 fF. Considering the contribution from the capacitor plates, the total charging energy is $E_C/2\pi$ = 13 MHz. We calculate the Josephson energy $E_J/2\pi$ from the qubit frequency $\omega_q/2\pi = f_{ge} = \sqrt{8E_C E_J} - E_C$, from which we obtain $E_J/2\pi$ = 712 GHz. This value indicates that the device operates deeply in the transmon regime. By increasing the drive power of the qubit we observe the appearance of the second transition frequency $f_{gf}/2$, from which we extract an anharmonicity of $\alpha \approx 18$ MHz. The magnetic-field dependence of ω_q presented in Fig. A3.5(b), confirms that we can operate this transmon in the same frequency range as the grAlPA.

In Fig. A3.5(d)-(f) we show typical transmon qubit fluorescence measurements. For each driving power we fit the fluorescence of the transmon using Eq. (A3.9). The values of $\kappa/2\pi = 0.82 \pm 0.16$ MHz and $\gamma/2\pi = 0.16 \pm 0.08$ MHz are extracted from the fitting at powers close to the single-photon regime. The error ranges comes from the Fano uncertainty in the measurement setup, which is propagated in the estimation of Ω_R. We estimate this error using a bootstrap method, where we fit Eq. (A3.9) for 1000 different values of κ and

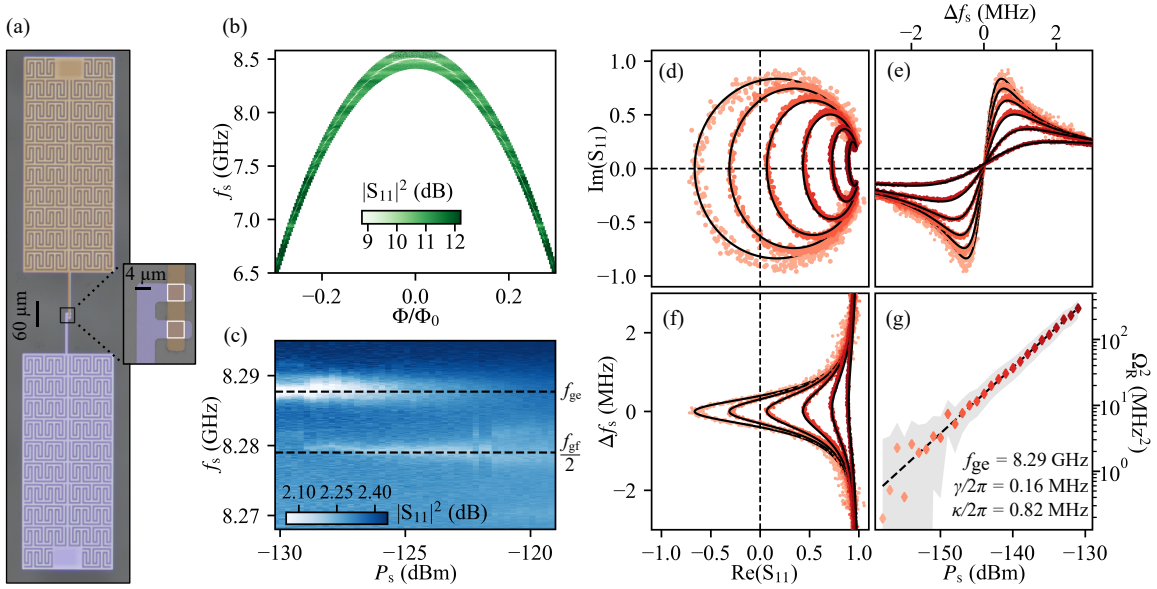

Figure A3.5: Resonance fluorescence of a transmon qubit. **(a)** False-colored image of the flux tunable transmon qubit, designed to fit the waveguide shown in Fig. 3.3(a). The device is fabricated using 2 steps of optical lithography (brown and purple layers). In the inset, we show a magnified image of the squid loop. The Josephson junctions are highlighted by the white contours. **(b)** Flux dependence of the qubit spectrum. **(c)** Single-tone spectroscopy of the transmon qubit as a function of input power P_s. Form the first (f_{ge}) and second transition ($f_{gf}/2$) frequencies, we extract an anharmonicity $\alpha \approx 18$ MHz. **(d)** Quadrature plane of the reflection coefficient S_{11} close to the qubit frequency at f_{ge}= 8.287 GHz. At low powers S_{11} follows a circular shape similar to the response of a linear resonator, from which we extract $\kappa/2\pi$ = 828 KHz and $\gamma/2\pi$ = 155 KHz through a standard circle fit procedure [222]. As power increases, the shape transforms into an ellipse, characteristic of the resonance fluorescence of a two-level system [80, 82, 258, 259]. **(e)**, **(f)** Real and imaginary part of the reflection coefficient as a function of the detuning from the qubit frequency Δf_s. Black solid lines are fits of the measurement data using Eq. (A3.9). For the fits, we use the Rabi frequency Ω_R as the only free parameter. **(g)** Input power dependence of Ω_R. The shaded area indicates the Fano uncertainty of the measurement setup. The obtained fit using Eq. (A3.10) is depicted by the black dashed line. We calculate an input attenuation of -89.3 ± 2 dB.

γ, within their respective uncertainty range. We extract the attenuation A = -89.3 ± 2 dB at 8.287 GHz, by fitting the dependence of Ω_R with driving power at room temperature P_{RT}, using the formula

$$\Omega_R^2 = A\frac{4\kappa P_{RT}}{\hbar\omega_q}. \tag{A3.10}$$

The frequency tunability of the transmon qubit enables power calibration across the entire operational range of the grAlPA, as shown in Fig. A3.6. We achieve an error interval of 2 dB, only limited by the Fano uncertainty in the measurements, which could be improved by adjusting the κ/γ ratio. As shown in Fig. A3.6, the attenuation exhibits a frequency dependence, which can be attributed to the inherent frequency-dependent insertion loss of the coaxial cables. Additionally, we observe an overall decrease in attenuation of approximately 5 dB from room temperature to 30 mK. This effect can be explained by the resistivity changes of the coaxial cables. The power calibration at lower frequencies was

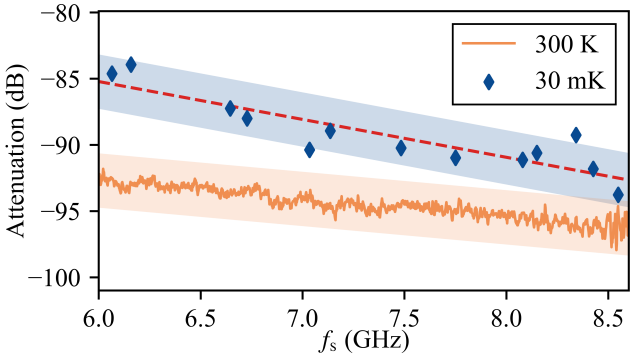

Figure A3.6: Power calibration using a transmon qubit in a wQED configuration. The blue scatter points are obtained from the fluorescence of the transmon qubit shown in Fig. A3.5. The red dashed line represents a linear fit, used to estimate the low-temperature input-line attenuation. The error intervals arise from the Fano uncertainties of the measurements. For comparison, the orange line shows the input-line attenuation measured at room temperature. The shaded region indicates the corresponding error range.

not possible with this transmon, as increased flux noise induces a fluctuating behavior in the device, preventing reliable measurements.

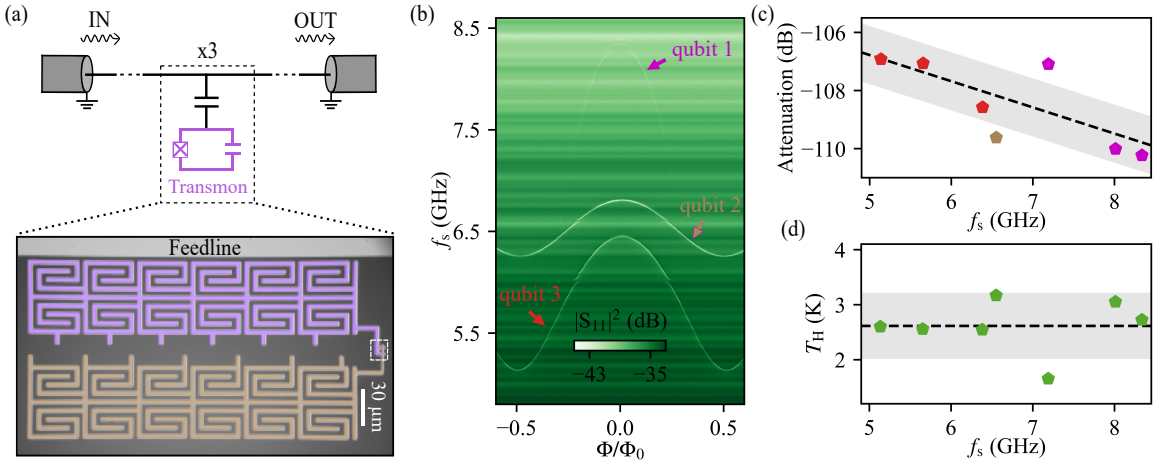

Figure A3.7: Power calibration using a multi-qubit chip in a wQED configuration. **(a)** Schematic of the multi-qubit chip used for broadband power calibration. Three transmon qubits, implemented in a notch-like geometry, are coupled to the microwave environment via a common feedline. The qubits are designed with zero-flux frequencies of 4, 6, and 8 GHz, respectively. The false-colored micrograph highlights the qubit layout, fabricated using the same process as in Fig. A3.5(a). The contour areas indicate the SQUID loop regions. **(b)** Flux dependence of the multi-qubit chip. The qubit resonance frequencies appear as dips in the reflection amplitude $|S_{11}|$. The non-monotonic flux dependence observed in qubits 2 and 3 indicates an asymmetry between the Josephson junctions in their SQUID loops. **(c)** Low-temperature attenuation extracted from the resonance fluorescence of the multi-qubit chip. The color code corresponds to data from different qubits. A linear fit of the attenuation is shown as a black dashed line. The shaded region indicates the propagated Fano uncertainty. **(d)** HEMT noise temperature T_H, calculated using the power calibration from panel (c) and Eq. (A3.1). The black dashed line shows the mean T_H obtained by averaging the scatter data, while the shaded region represents the propagated uncertainty of the power calibration. The measured T_H exceeds the nominal 1.8 K noise specified by the manufacturer [144], which we attribute to the ≈ 1.6 dB insertion loss between the multi-qubit chip and the HEMT.

We can extend the concept of the device shown in Fig. A3.5 to cover a broader frequency range by employing multiple qubits, as illustrated in Fig. A3.7(a). In this configuration, the qubits are designed in a notch-like geometry, coupled to a common feedline connected at

both ends to microwave ports. Each qubit is engineered with distinct capacitances, such that their zero-flux frequencies are 4, 6, and 8 GHz, respectively. The spectrum of the qubits is presented in Fig. A3.7(b), where the non-monotonic decay of the two lower-frequency modes arises from the asymmetry between the junctions in the SQUID. By measuring the qubits' resonance fluorescence we can calculate the input-line attenuation across their entire operational frequency range, as illustrated in Fig. A3.7(c). With this calibration we estimate the noise of the output line in one of our cryostats (see Fig. A3.7(d)). In this experiment, no grAlPA was connected at the first amplification stage, such that the line noise is dominated by the HEMT amplifier located at the 4 K stage. The discrepancy between the measured input noise and the expected HEMT noise of $\approx$ 1.8 K [144] is explained by the $\approx$ 1.6 dB insertion loss between the HEMT and the qubit chip.

With this method, the input-line attenuation can, in principle, be measured continuously across the entire operational range of the transmon qubits. However, in our current implementation, a limiting factor was the relatively large area of the Josephson junctions, which introduced unwanted coupling to environmental two-level systems. A similar limitation was also reported by Ref. [258]. To mitigate this issue, one could employ electron-beam lithography to fabricate sub-μm^2 junctions. Complementarily, RF-SQUIDs could also be used, as they offer two flux-noise-insensitive sweet spots and can cover a larger frequency span.

C.5 Comparison of calibration methods

All methods discussed in this chapter come with advantages and drawbacks, as summarized in Table A3.1. The choice of which method is suitable for an experiment depends on the resources available in the laboratory and the amplifier we would like to characterize. In general, if fabrication capabilities are accessible, we strongly recommend using techniques based on superconducting qubits, as they provide the most accurate estimation of an amplifier noise performance. Moreover, as demonstrated in Fig. A3.7, the wQED design enables calibration of amplifier's metrics across the full 4–8 GHz range.

Table A3.1: Comparison of different power and noise calibration methods. The accuracy of the methods is referenced with respect to the results presented throughout this chapter. Since a qubit in a wQED design can be adapted to fit the setup of a parametric amplifier, we assign the calibration plane at the input of the amplifier.

	Calibration method		
Metric	Y-factor	Qubit in cQED	Qubit in wQED
Range	1-30 GHz	~ 1 MHz (linewidth of readout cavity)	1-30 GHz
Accuracy	± 2 dB	± 0.5 dB	± 1 dB
Error source	temperature reading	Fano uncertainty of readout cavity	Fano uncertainty of qubit
Cal. plane	attenuator output	readout cavity input	amplifier input

D Double-pumped grAlPA

In this Appendix, we provide more detailed information about the results shown in Chapter 4.

D.1 Gain profiles for imbalanced single-mode squeezing interactions

In Section 4.2, we established that realizing an OIBA with the grAlPA requires a precise balance between the single-mode squeezing interactions $\Lambda_{S_{a/b}}$ and the frequency detuning terms $\Delta_{a/b}$. But, what is the impact of imbalanced $\Lambda_{S_{a/b}}$ on the gain performance of a double-pumped grAlPA? In Fig. A4.1, we present the evolution of the gain profiles as Λ_{S_b} is tuned away from the ideal balance condition, while keeping all other parameters fixed as for operation at the BP. We observe two main effects arising from this imbalance. First, the gain peaks associated with the idler tones generated by the beam-splitter interactions no longer coalesce. This removes the characteristic flat-top gain profile expected for an ideal BP. Second, the amplifier no longer exhibits a constant GBW product, partially explaining the residual GBW scaling observed experimentally in Fig. 4.6(d).

Interestingly, moving $\Lambda_{S_{a/b}}$ away from the perfect balance condition qualitatively reproduces the dynamics observed during saturation power measurements. Increasing the probe power P_s, enhances the photon number population of the grAl resonators $n_{L/R}$. Since the probe is applied close to resonance of the high frequency dimer mode ω_b, its main effect is to modify the effective values of Λ_{S_b} and Δ_b. As shown in Fig. A4.2, we observe a qualitative agreement between the BHD-model calculations and the measured gain profiles of the grAlPA under increasing probe power. We emphasize that this correspondence should be regarded only as qualitative. A more rigorous analysis would require calculating the back-action of the probe on the pump dynamics, which is beyond the scope of the simplified treatment presented here.

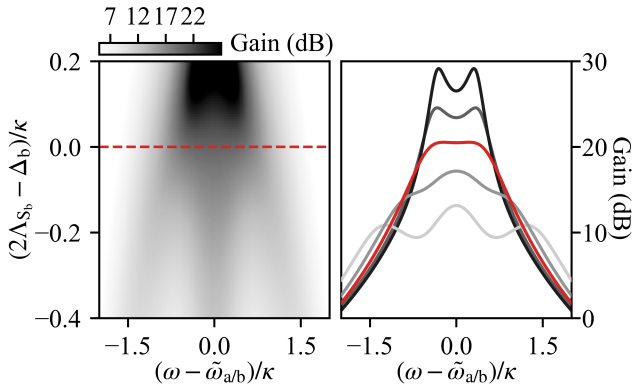

Figure A4.1: Gain profiles of a double-pumped symmetric BHD without optimal detuning. We calculate the variation of the gain profiles with respect to the BP when the interaction term $2\Lambda_{S_b}$ is not compensated by the detuning Δ_b. All other interactions in Eq. (4.1) are kept fixed to satisfy the conditions for operation at the BP. As shown by the linecuts in the left panel, an uncompensated single-mode squeezing interaction leads to a reduction of the amplifier bandwidth and the disappearance of the flat-top gain profile, even when all other parameters remain tuned to the BP conditions.

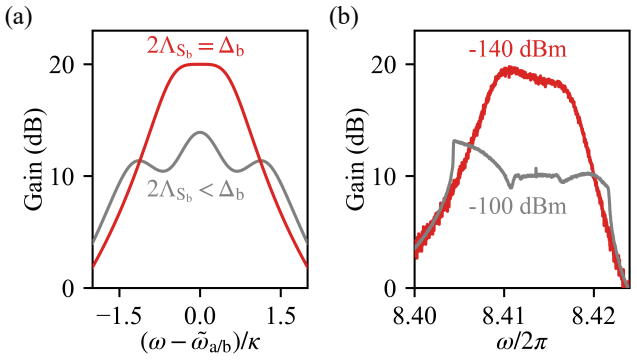

Figure A4.2: GrAlPA gain as a function of probe power when tuned at the BP. **(a)** Calculated and **(b)** measured gain profiles for increasing probe tone powers. By increasing the power of the probe tone, as for example during saturation power measurements, the total photon population in the grAlPA resonators grows, modifying Λ_{S_b} and Δ_b. This drives the system away from the ideal BP conditions, leading to a gain reduction and the appearance of additional features in the gain profile. This behavior is qualitatively reproduced by the theory of a symmetric double-pumped BHD (cf. Section 4.2), as shown in panel (a).

D.2 Setup for optimized power calibration

For the experiments presented in Chapter 4, we use the two experimental setups illustrated in Fig. A4.3. They differ from those employed for the magnetic-field characterization of the grAlPA (see Appendix B.2) in that all connections between the GFQ, the grAlPA, and the HEMT are now made with NbTi superconducting cables. This modification reduces the insertion loss between the GFQ and the amplifier chain, improving the accuracy of the power calibration. Moreover, to suppress pump-tone leakage into the room-temperature electronics, we employ a series of homemade notch filters with sub-1 dB insertion loss in the passband.

For the phase-dependent gain measurements shown in Section 4.6, the probe and the two pump tones are synthesized from the same OPX-Octave® output line. Using common local oscillators (LOs) and mixers for the up- and down-conversion of all tones was crucial to maintain proper phase synchronization. To further suppress unwanted spurious tones in the generated signals, we insert two homemade band-stop filters centered at the pump frequencies.

The power calibration performed in this setup is referenced to the input of the GFQ readout resonator. Consequently, to extract the noise metrics shown in Fig. 4.10, we must account for the total insertion loss between the GFQ and the amplifier. We estimate an upper bound of 0.6 dB using the values reported in Table A2.2. In addition, since in this configuration the frequency of the GFQ readout resonator lies outside the operational band of the grAlPA (detuned by approximately 200 MHz), we expect an additional uncertainty arising from standing-wave ripples in the microwave connections. Based on the results shown in Fig. A3.6, we assign a 1 dB uncertainty to the final power calibration, which propagates into the error bars of the extracted grAlPA added noise.

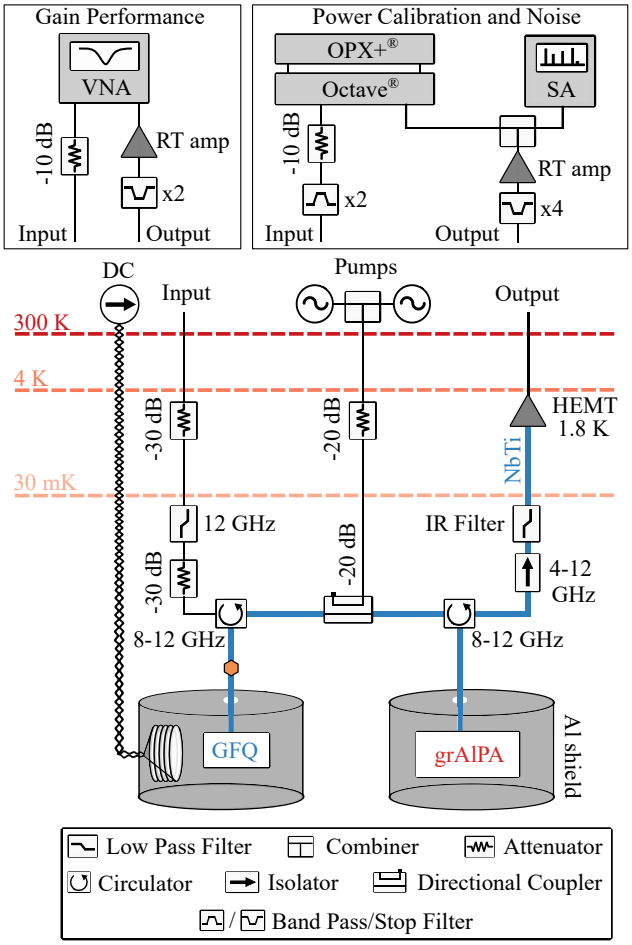

Figure A4.3: Setup used for experiments with a double-pumped grAlPA. Each component is thermalized at the temperature stage indicated by the nearest dashed line. Gain performance is characterized using a Vector Network Analyzer (VNA). For grAlPA noise measurements, we employ a combination of Quantum-Machines OPX-Octave® electronics and a Spectrum Analyzer (SA). Pump tones are generated by independent microwave sources, except for the phase-sensitive gain measurements, where they are synthesized by the OPX-Octave® system..

D.3 Gain profiles close to both hybridized modes

In Fig. A4.4 and Fig. A4.5, we present the measured gain profiles near $\omega_{a/b}$ for the single-pumped and double-pumped grAlPA, respectively. The color maps in Fig. A4.4(c)–(d) and the black dashed lines in Fig. A4.4(d) correspond to fits obtained using the Bose–Hubbard dimer model (see Appendix D.4). The asymmetry observed in the gain profiles around ω_a and ω_b, originates from the asymmetric coupling of the bare grAl resonators. By tuning the frequencies of the pump tones, we can increase the maximum gain near ω_a, as shown in Fig. A4.6. However, this adjustment reduces the effective gain at ω_b, resulting in gain profiles similar to those in Fig. A4.5, but with the roles of ω_a and ω_b exchanged. Neither of the configurations shown in Fig. 4.4(a) and (b) produced symmetric gain profiles near the dimer modes. However, when using the configuration illustrated in Fig. 4.4(c), we observed a bandwidth enhancement with identical gain levels at both ω_a and ω_b. Unfortunately, the corresponding data were not recorded during the experiment, and we were unable to reproduce this behavior in subsequent cooldowns.

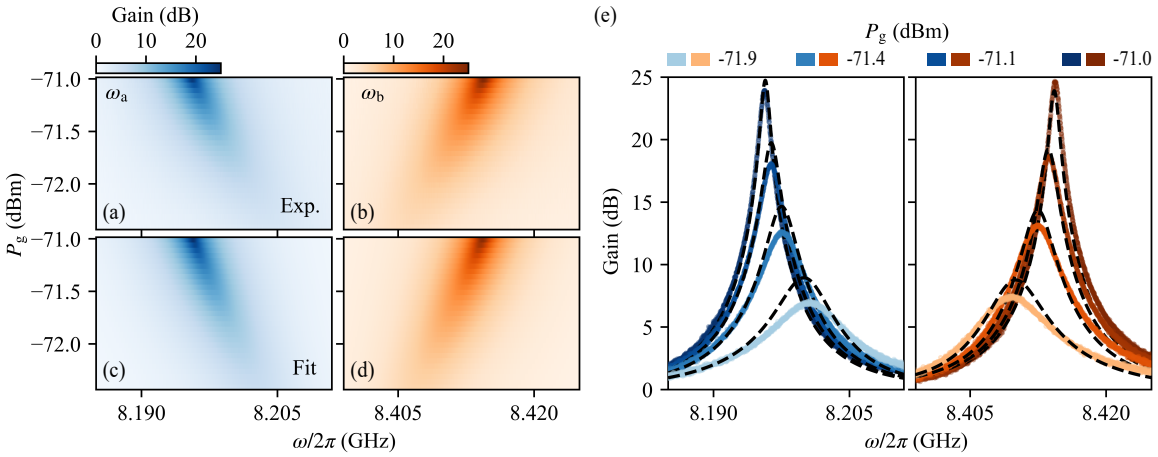

Figure A4.4: Power dependent gain profiles for the single-pump grAlPA. Measured **(a)-(b)** and fitted **(c)-(d)** gain profiles of the grAlPA dimer modes $\omega_{a/b}$ as a function of P_g. We keep ω_g fixed. Fits are obtained using the procedure explained in Appendix D.4 with the pump line attenuation as the only fitting parameter. **(e)** Linecuts at different pump powers. The black dashed lines are the fitted curves.

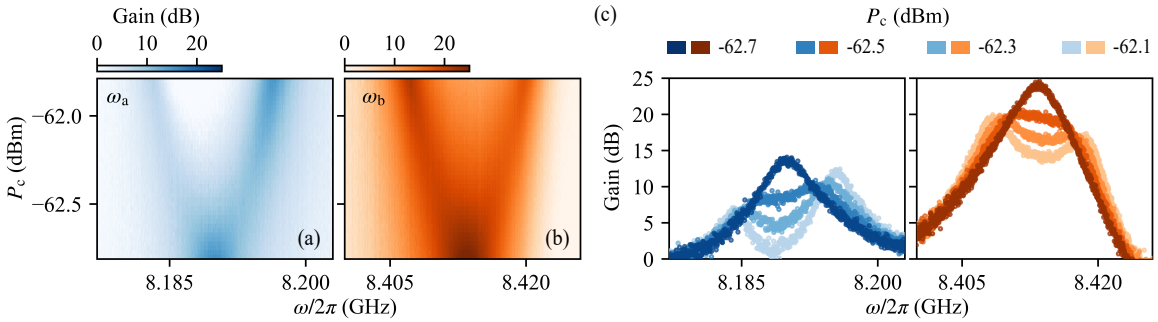

Figure A4.5: Power dependent gain profiles for the double-pump grAlPA.. Measured **(a)-(b)** gain profiles of the grAlPA dimer modes $\omega_{a/b}$ as a function of P_c. We keep ω_g, ω_c and P_g fixed. **(e)** Linecuts at different pump powers.

D.4 Fits of Gain Profiles based on Bose-Hubbard dimer model

We fit the experimental gain profiles using the results of the BHD model (see Appendix A) and the parameters extracted in Section 4.4. For the single-pump grAlPA, we calculate first the average pump fields $\alpha_{L/R}$ from the mean-field Langevin equations (see Eq. (A1.12)). Since the amplifier operates in a multistable regime, multiple solutions of $\alpha_{L/R}$ exist for the same input field α^g_{in}. We select the solution corresponding to the lowest photon population in the grAl resonators. The frequency-dependent gain is then obtained from Eq. (A1.18). This procedure is repeated iteratively, using only the pump-line attenuation as a fitting parameter. The results, shown in Fig. A4.4, are consistent with a pump-line attenuation of -66.4 ± 5 dB. The observed asymmetry of the gain profiles and the discrepancy at low pump powers can be attributed to unaccounted frequency-dependent losses in the measurement setup.

Under two-pump operation, we cannot continuously fit the gain profiles as in Fig. A4.4, due to the increased complexity of the BHD model. Instead, each gain profile shown in Fig. 4.6(c)

Table A4.1: Fitting results for double-pumped gain profiles. The gain and conversion pump powers are calculated using the data in Fig. 4.6(c) and the procedure detailed in Appendix D.4. All pump powers are consistent with the pump-line attenuation extracted from the fits of the single-pumped grAlPA (cf. Fig. A4.4).

	Maximum gain G_0			
Quantity	10 dB	15 dB	20 dB	25 dB
P_g (dBm)	-71.50	-71.54	-71.76	-71.93
P_c (dBm)	-62.61	-62.64	-62.50	-62.40
P_c/P_g	0.13	0.13	0.12	0.11

is fitted independently by solving Eq. (A1.38) and Eq. (A1.18) self-consistently, using the pump powers as fitting parameters. The measured Kerr-shifted frequencies $\tilde{\omega}_{a/b}$ are used to obtain an initial estimate of the populations of the grAl resonators via Eq. (A1.37). We then calculate the frequency-dependent gain by truncating the scattering matrix of Eq. (A1.45), such that we consider only up to the 4th order sidebands (i.e. we consider the interactions $\omega \pm n\Delta_p$ only up to $n = 4$). We iteratively adjust the photon numbers until the simulated profiles match the experimental data. Finally, we extract the equivalent pump powers using Eq. (A1.38). In Table A4.1 we summarize the calculated pump powers corresponding to each gain profile in Fig. 4.6(c). All values fall within the uncertainty range determined for the pump-line attenuation from the single-pump calibration. Moreover, the ratio between the conversion and gain pump powers remains approximately constant for different gain levels.

D.5 Gain profiles with symmetric grAl resonators

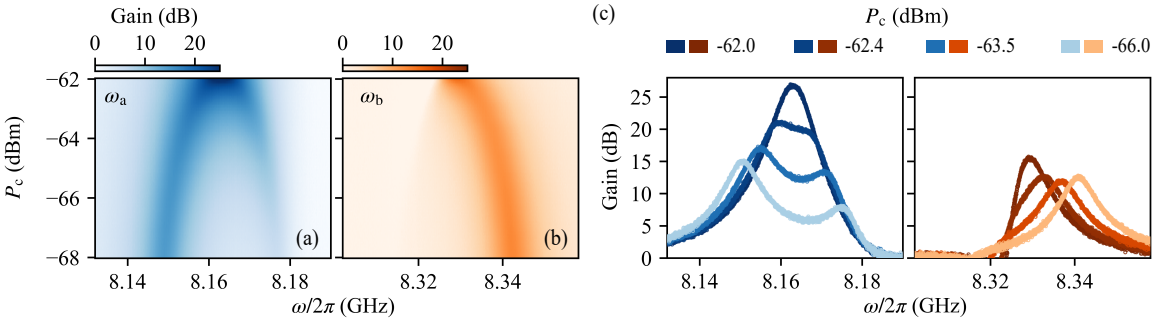

Figure A4.6: Power dependent gain profiles for the double-pump grAlPA with symmetric resonators. Measured **(a)-(b)** gain profiles of the grAlPA dimer modes $\omega_{a/b}$ as a function of P_c. We keep ω_g, ω_c and P_g fixed. **(e)** Linecuts at different pump powers.

In Fig. A4.6, we present the gain performance measured during a cooldown in which the grAl resonators exhibited negligible frequency asymmetry. The corresponding circuit parameters, extracted from the low-power response of the grAlPA, are summarized in Table A4.2. The gain and conversion pumps were applied in the same configuration as in Fig. 4.6, but were tuned to produce a BW broadening centered around ω_a rather

than ω_b. We observe the same peak-splitting behavior predicted in Section 4.2. However, in contrast to Fig. 4.6, the amplifier exhibits a larger bandwidth at the BP.

D.6 Results with tripled-pumped grAlPA

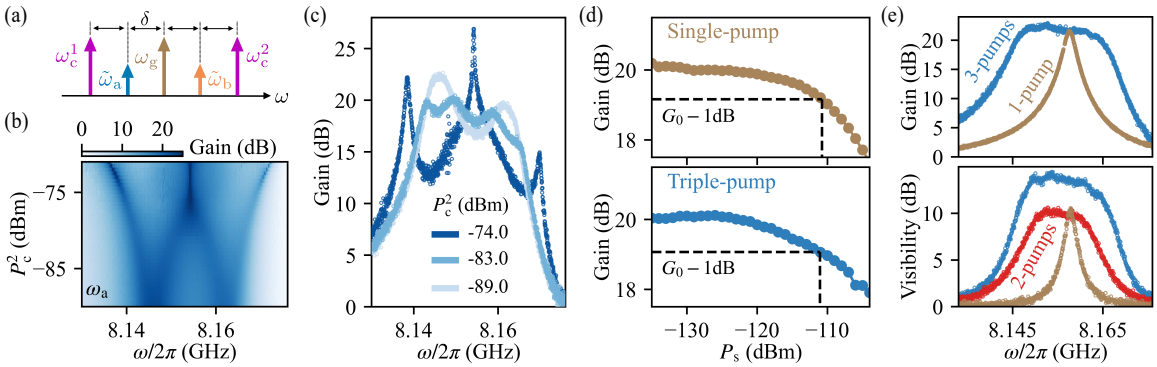

Figure A4.7: Performance of tripled-pumped grAlPA. **(a)** Frequency configuration of the gain pump (ω_g), the two conversion pumps ($\omega_c^{1/2}$) and the Kerr-shifted dimer modes ($\tilde{\omega}_{a/b}$). **(b)** Measured gain profiles close to $\tilde{\omega}_a$ for increasing power of the second conversion pump P_c^2. The powers and frequencies of the other pumps are kept fixed. By tuning, P_c^2 we observe the emergence of an additional normal-mode peak splitting. **(c)** Linecuts of panel (b) at different pump powers P_c^2. **(d)-(e)** Comparison of measured saturation powers, gain profiles and noise performance for a single- (brown), double- (red) and triple- (blue) pumped grAlPA. We optimize P_c^2 to recover the tenfold BW improvement predicted in Fig. 4.3. This improvement comes without a decrease in the saturation power. However, it produces ≈ 5 dB additional noise, coming from the formation of extra idler tones.

In this section we present the results obtained while applying three parametric pumps to the grAlPA. We use the configuration shown in Fig. A4.7(a), where we apply two conversion pumps at frequencies which combine the approaches of Fig. 4.4(a) and (b). The data was recorded in the same cooldown as the results shown in Fig. 4.9 and Fig. A4.6. The application of the second conversion pump generates the appearance of additional idler tones, that lead to the formation of a second peak splitting in the gain profiles (see Fig. A4.7(b) and (c)). Similar to results obtained with a unique conversion pump (cf. Fig. 4.6(b)), the BW increases at the coalescence point of all the peaks. Importantly, grAlPA's dynamic range is not hindered by the application of the second conversion pump, as shown in Fig. A4.7(d). By comparing the gain profiles obtained when operating the amplifier with one and three pumps (see Fig. A4.7(e)), we observe that in the latter case we

Table A4.2: Circuit parameters of the grAlPA with symmetric resonators frequencies. The errors arise from the Fano uncertainty in the measurement setup [134].

$\omega_a/2\pi$ (GHz)	$\omega_b/2\pi$ (GHz)	$\kappa_a/2\pi$ (MHz)	$\kappa_b/2\pi$ (MHz)	$\gamma_{a,b}/2\pi$ (MHz)	$\omega_L/2\pi$ (GHz)	$\omega_R/2\pi$ (GHz)	$J/2\pi$ (MHz)	$\kappa/2\pi$ (MHz)
8.221	8.421	28.1 $\pm$ 3	28.3 $\pm$ 3	≤ 5	8.320 $\pm$ 7	8.320 $\pm$ 7	100 $\pm$ 10	57 $\pm$ 5

recover the tenfold BW improvement at G_0 = 20 dB predicted for an ideal OIBA. However, noise visilibty measurements indicate that under triple-pump operation the grAlPA noise level increases by ≈ 5 dB (i.e. almost a factor of three). We attribute this effect to extra noise produced by the idler tones generated from the second conversion pump. Importantly, this effect is not present when only one conversion pump is applied, as plotted in the lower panel of Fig. A4.7(e).

D.7 Tuning of resonance frequencies with laser ablation

One approach to reduce the frequency asymmetry of the bare grAl resonators consists in trimming their capacitor pads using a laser ablation technique. A grAlPA fabricated in a 2D architecture, with a box similar the one used by Ref. [22], is mounted in the positioning stage of the instrument, which has a displacement precision of 2 µm. The sample is aligned at the focal plane of a laser with 250 W power and wavelength λ = 940 nm. By activating the laser, we locally melt portions of the grAl capacitor pads with a nominal resolution of 5 µm. In Fig. A4.8(a) we show images of a capacitor pad after a first trimming procedure. We observe that the ablation process is not fully homogeneous, as residues remain visible along the borders of the trimmed regions. These edges cannot be removed by subsequent trimming steps because the oxygen concentration, increased by local heating produced during the initial cut, prevents further absorption of the laser energy. However, as demonstrated in Fig. A4.8(b), these residues do not degrade the resonators performance, since no clear changes in the modes internal quality factors were observed after multiple trimming iterations.

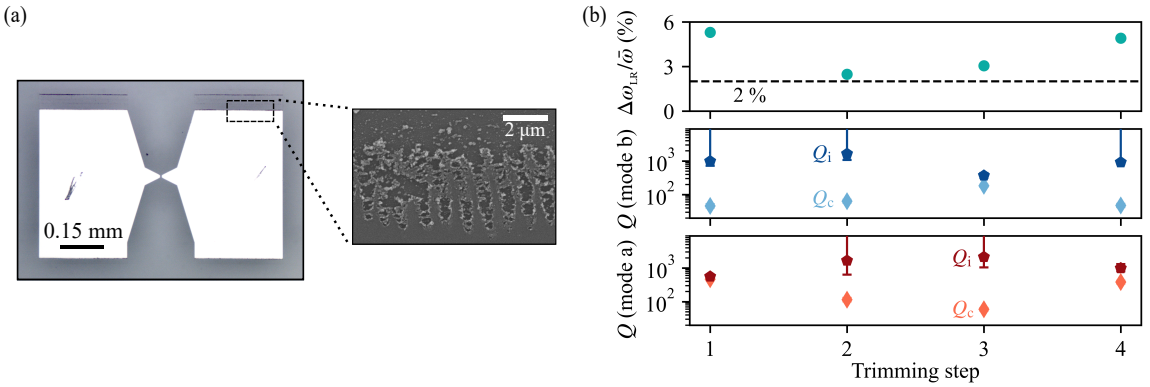

Figure A4.8: Results of laser ablation for the tuning of grAlPA's resonators frequencies. **(a)** Optical (left) and scanning electron beam (right) pictures of a grAl resonator with trimmed capacitor plates. A cut of approximately 30 µm was performed at the uppermost edge of both plates. The black lines visible within the cutting region are oxidized grAl residues, which cannot be removed with subsequent trimming steps. As shown at the right picture, this technique produces inhomogeneous edges on the capacitor plates. **(a)** Measured resonators asymmetries $\Delta\omega_{L,R}/\bar{\omega}$ and modes internal and external quality factors for the same grAlPA after four trimming procedures. Although the internal quality factors are not affected, using laser ablation to reduce the size of the capacitor pads does not allow tuning the frequency asymmetry $\Delta\omega_{L,R}/\bar{\omega}$ below 2%. The error bars in Q_i and Q_c come from the Fano uncertainty of the measurement setup [179].

Despite the high precision of the laser and the positioning stage, we were unable to consistently reduce the frequency asymmetry of the resonators below the 2% level, as shown in Fig. A4.8(b). The main limitation arises from the low resolution of the alignment camera used to match the laser coordinates with the sample. This restricts the effective spatial precision to 200 µm. Employing a higher-resolution camera would therefore be essential to optimize this technique.

D.8 Tuning of resonance frequencies with box microwave engineering

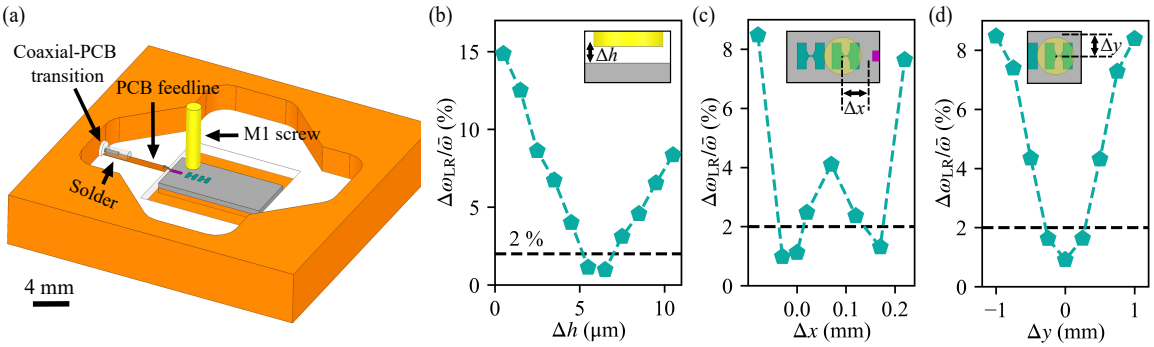

Figure A4.9: FEM simulations for frequency tuning with an M1-sized screw. **(a)** Layout used for FEM simulations. A grAlPA (green) is designed in a microstrip geometry, using the same sample box of Ref. [22]. The grAlPA is coupled to an on-chip coupling pad, which is bonded to a PCB feedline. The PCB is connected at the other end to a coaxial cable. An M1-sized screw, mounted on the lid of the sample holder, is positioned in close proximity of one grAl resonator, increasing its frequency. **(a)-(d)** Frequency asymmetry $\Delta\omega_{\mathrm{L,R}}$ in three possible tuning scenarios: variation of the substrate-to-chip distance h and in-plane horizontal Δx and vertical Δy displacements. With this tuning technique we could reduce $\Delta\omega_{\mathrm{L,R}}$ below the 2%.

In this subsection, we describe how the frequency asymmetry of the grAlPA resonators can be reduced by modifying the device packaging. In Fig. A4.9(a), we present the design used in FEM simulations. A grAlPA with the same parameters as in Table 4.1, is assumed to be mounted inside a sample box similar to the one used by Ref. [22]. The frequency of the left resonator is tuned by varying the distance of a M1-sized screw attached to the lid of the holder. The tuning step is set to match the minimum thread precision achievable by the KIT mechanical workshop (1 µm). As shown in Fig. A4.9(b)-(d), this approach allows us to reduce the resonator asymmetry below 2%. Moreover, this improvement remains robust against lateral displacements of the screw.

D.9 Layout and design of hybrid Ports

In this section, we provide details about the possible designs that enable the physical separation of the grAlPA dimer modes. The grAlPA is implemented in a 2D microstrip geometry, adapted to fit the sample box used for Dimer Josephson Junction Array Amplifiers (DJJAAs) [22]. In Fig. A4.10, we show the layout employed for FEM simulations in Ansys HFSS 2024R2, corresponding to the design presented in Fig. 4.12(a). To simulate the

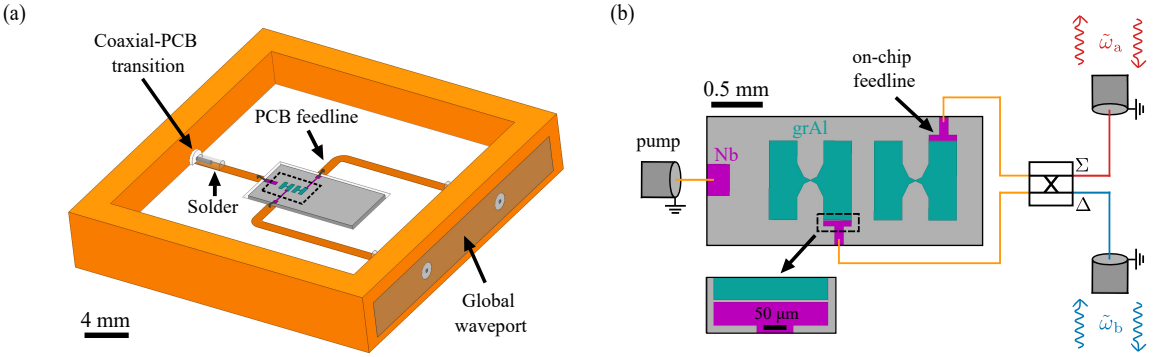

Figure A4.10: Layout used in FEM simulations of a grAlPA with hybrid ports. A sapphire chip containing the grAlPA is placed inside a sample box similar to Fig. A4.9(b), as shown in panel **(a)**. We define a global waveport at one of the outer surfaces of the box, from which we can calculate the common and differential excitations of two signals coming from each PCB feedline. In panel **(b)** we show a zoom-in drawing of the grAlPA area depicted by black dashed contour in panel (a). We use on-chip feedlines resembling the circuit model in Fig. 4.12(a). In the FEM solver we define the feedlines and the grAlPA structures, as perfect conductors and impedance boundaries, respectively.

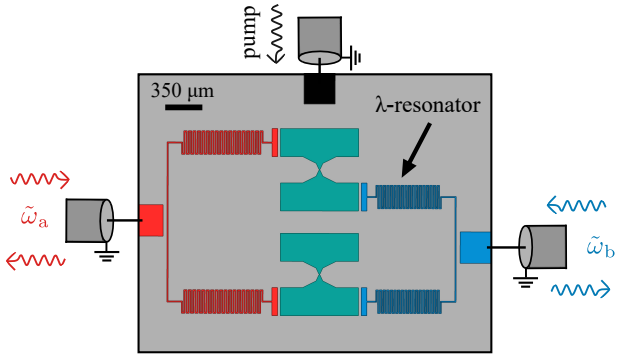

Figure A4.11: Layout of a grAlPA in a design with Purcell-like ports. The meanders in the λ-resonators are added to match the frequency of the dimer modes. With this design, one could implement an impedance matching network of each hybrid port, which could further increase the device BW.

behavior of the 180° hybrid coupler, we connect the ends of two coaxial lines to a global waveport, which we configure to provide their common and differential excitations. At the opposite ends, the central conductors of the coaxial lines are connected to a printed circuit board (PCB) through perfect conductor solder joints. The PCB feedlines are designed in a microstrip geometry using the substrate TMM10i from Rogers Corporation, which has a dielectric constant of $\varepsilon_r = 9.9$ and loss tangent of $\tan\delta = 2 \cdot 10^{-3}$ [261]. On-chip feedlines are modeled as perfect conductors and represent Nb superconducting films. The grAl resonators are modeled using the *impedance boundary* option in HFSS, with the same kinetic inductance as in the experiments (cf. Section 3.3). We use this layout to obtain the results in Fig. 4.12(b)-(c).

For completeness, we also present a proposal for a device capable of implementing the Purcell-like design of Fig. 4.13. The meander structures of each coupling resonator were tuned to match the frequencies of the hybridized modes, as confirmed by FEM simulations. However, simulations of the complete design were not performed as they were computationally demanding. We encourage the interested reader to further check this design, and optimize the simulation parameters to verify whether the proposed layout achieves the expected performance for the hybrid ports.

D.10 Driven-dissipative pendulum model

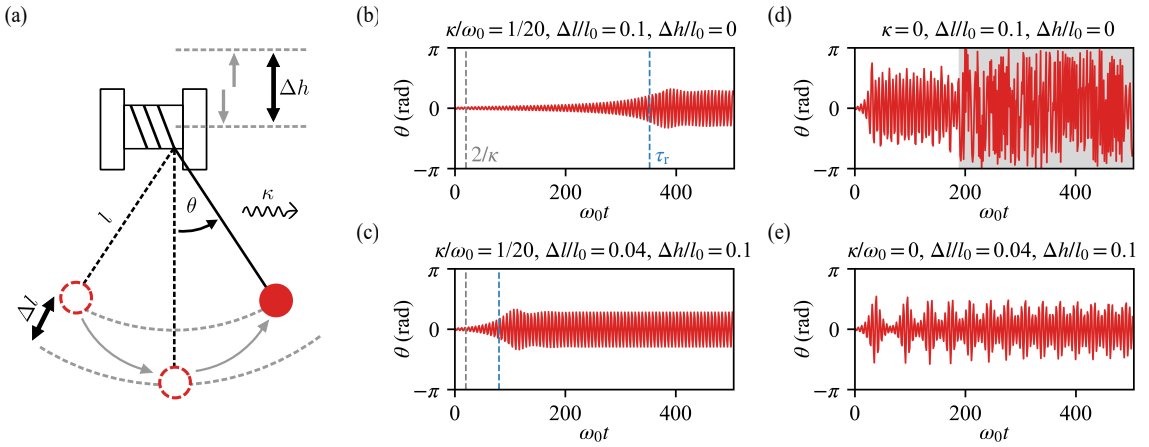

Figure A4.12: Dynamics of a double-pumped driven-dissipative pendulum. **(a)** Schematic of a driven–dissipative pendulum. The periodic vertical motion of the upper support (Δh) and the modulation of the pendulum's length (Δl) act as parametric pumps. Both drives are applied at twice the natural frequency of the pendulum $\omega_0 = \sqrt{g/l_0}$, where l_0 is the equilibrium length. Air drag and friction in the rope give rise to a dissipation rate κ. The time evolution of the angular displacement θ is computed using Eqs. (A4.1) and (A4.2) for four distinct scenarios: **(b)** single-pump operation with finite dissipation, **(c)** double-pump operation with finite dissipation, **(d)** single-pump operation with negligible dissipation, and **(e)** double-pump operation with negligible dissipation. In the absence of dissipation ($\kappa = 0$), single-pump driving leads to unbounded dynamics and chaotic motion, highlighted by the gray shaded region in panel (d). Dissipation stabilizes the dynamics and enables a steady state of amplified oscillations with an increased response time τ_r (blue dashed lines) compared to the undriven response time $2/\kappa$ (gray dashed lines). Panels (c) and (e) illustrate that introducing a second pump reduces the response time and allows for stable amplified oscillations even in the absence of dissipation.

In this section, we elaborate on the analogy between the OIBA and the doubly pumped driven–dissipative pendulum model shown in Fig. A4.12(a). Following the results of Baker and Blackburn [87], the time evolution of the pendulum's angular displacement θ can be modeled by the equation

$$\frac{d^2\theta}{dt^2} + \left(\frac{2}{l}\frac{dl}{dt} + \kappa\right)\frac{d\theta}{dt} + \frac{\left[g - \Delta h\,\omega_h^2 \cos\left(\omega_h t + \phi_{off}\right)\right]}{l}\sin\left(\theta\right) = 0, \tag{A4.1}$$

where g is the gravitational acceleration, κ is the dissipation rate arising from rope friction and air drag, $\omega_{l/h}$ are the frequencies of the two pumping mechanisms, ϕ_{off} is the relative phase offset between the pumps, and l is the pendulum length, given by

$$l\left(t\right) = \left(l_0 - \frac{\Delta l}{2}\right) + \frac{\Delta l}{2}\cos\left(\omega_r t\right). \tag{A4.2}$$

Here, l_0 denotes the equilibrium length of the pendulum. For simplicity, we assume $\phi_{off} = \pi/2$ and $\omega_{l/h} = 2\omega_0$, where $\omega_0 = \sqrt{g/l_0}$ is the natural frequency of the pendulum.

In Fig. A4.12(b)–(e), we present the calculated time evolution of the angular displacement θ under single-pump and double-pump operation, both in the presence and absence

of dissipation. For a dissipationless pendulum ($\kappa = 0$) driven by a single pump, the dynamics of θ become unbounded and rapidly evolve into a chaotic regime, as illustrated in Fig. A4.12(d). Introducing dissipation stabilizes the system and allows the pendulum to reach a steady state characterized by amplified oscillations of θ. However, the response time of the pendulum τ_r increases in comparison to the undriven case, which is given by $2/\kappa$ (see Fig. A4.12(b)). This increase in response time implies a narrowing of the pendulum's spectral density, analogous to the GBW tradeoff of single-pumped parametric amplifiers (cf. Section 1.3.2). When a second pump is applied, the response time is reduced by approximately a factor of four (see Fig. A4.12(c)), leading to a broadening of the spectral density. This behavior partially resembles the dynamics of an OIBA i.e. we can decrease the system response time by a adding a second pump. Remarkably, under double-pump operation, the pendulum reaches stable oscillations even in the absence of dissipation. However, the interference between the two pumping mechanisms gives rise to the beating pattern visible in Fig. A4.12(e).

Bibliography

[1] P. Krantz, M. Kjaergaard, F. Yan, T. P. Orlando, S. Gustavsson, and W. D. Oliver, "A quantum engineer's guide to superconducting qubits", Appl. Phys. Rev. **6** (2019) (cit. on pp. 1, 9, 13).

[2] C. D. Bruzewicz, J. Chiaverini, R. McConnell, and J. M. Sage, "Trapped-ion quantum computing: Progress and challenges", Appl. Phys. Rev. **6** (2019) (cit. on p. 1).

[3] C. Couteau, S. Barz, T. Durt, T. Gerrits, J. Huwer, R. Prevedel, J. Rarity, A. Shields, and G. Weihs, "Applications of single photons to quantum communication and computing", Nat. Rev. Phys. **5**, 326–338 (2023) (cit. on p. 1).

[4] M. Aspelmeyer, T. J. Kippenberg, and F. Marquardt, "Cavity optomechanics", Rev. Mod. Phys. **86**, 1391–1452 (2014) (cit. on p. 1).

[5] A. Chatterjee, P. Stevenson, S. De Franceschi, A. Morello, N. P. de Leon, and F. Kuemmeth, "Semiconductor qubits in practice", Nat. Rev. Phys. **3**, 157–177 (2021) (cit. on p. 1).

[6] A. Blais, S. M. Girvin, and W. D. Oliver, "Quantum information processing and quantum optics with circuit quantum electrodynamics", Nat. Phys. **16**, 247–256 (2020) (cit. on pp. 1, 9, 13).

[7] M. H. Devoret, J. M. Martinis, and J. Clarke, "Measurements of Macroscopic Quantum Tunneling out of the Zero-Voltage State of a Current-Biased Josephson Junction", Phys. Rev. Lett. **55**, 1908–1911 (1985) (cit. on pp. 1, 10).

[8] K. Husna Hamza and D. Nirmal, "A review of GaN HEMT broadband power amplifiers", AEU Int. J. Electron. Commun. **116**, 153040 (2020) (cit. on p. 2).

[9] E. Cha, "InP High Electron Mobility Transistors for Cryogenic Low-Noise and Low-Power Amplifiers", PhD thesis (Chalmers University of Technology, 2020) (cit. on pp. 2, 27).

[10] A. A. Clerk, M. H. Devoret, S. M. Girvin, F. Marquardt, and R. J. Schoelkopf, "Introduction to quantum noise, measurement, and amplification", Rev. Mod. Phys. **82**, 1155–1208 (2010) (cit. on pp. 2, 10, 28).

[11] A. Roy and M. Devoret, "Introduction to parametric amplification of quantum signals with Josephson circuits", C. R. Phys. **17**, 740–755 (2016) (cit. on pp. 2, 6, 8–10, 25, 52).

[12] J. Aumentado, "Superconducting Parametric Amplifiers: The State of the Art in Josephson Parametric Amplifiers", IEEE Microwave Mag. **21**, 45–59 (2020) (cit. on pp. 2, 5, 6, 8, 9, 25, 27).

[13] M. Esposito, A. Ranadive, L. Planat, and N. Roch, "Perspective on traveling wave microwave parametric amplifiers", Appl. Phys. Lett. **119** (2021) (cit. on pp. 2, 6, 8, 22, 76).

[14] C. M. Caves, "Quantum limits on noise in linear amplifiers", Phys. Rev. D **26**, 1817–1839 (1982) (cit. on pp. 2, 28, 69, 94).

[15] H. Zimmer, "Parametric Aamplification of Microwaves in Superconducting Josephson Tunnel Junctions", Appl. Phys. Lett. **10**, 193–195 (1967) (cit. on p. 2).

[16] M. A. Castellanos-Beltran and K. W. Lehnert, "Widely tunable parametric amplifier based on a superconducting quantum interference device array resonator", Applied Physics Letters **91** (2007) (cit. on pp. 2, 29).

[17] T. Yamamoto, K. Inomata, M. Watanabe, K. Matsuba, T. Miyazaki, W. D. Oliver, Y. Nakamura, and J. S. Tsai, "Flux-driven Josephson parametric amplifier", Appl. Phys. Lett. **93**, 042510 (2008) (cit. on pp. 2, 30).

[18] B. Abdo, F. Schackert, M. Hatridge, C. Rigetti, and M. Devoret, "Josephson amplifier for qubit readout", Appl. Phys. Lett. **99** (2011) (cit. on pp. 2, 35).

[19] C. Macklin, K. O'Brien, D. Hover, M. E. Schwartz, V. Bolkhovsky, X. Zhang, W. D. Oliver, and I. Siddiqi, "A near–quantum-limited Josephson traveling-wave parametric amplifier", Science **350**, 307–310 (2015) (cit. on p. 2).

[20] T. Roy, S. Kundu, M. Chand, A. M. Vadiraj, A. Ranadive, N. Nehra, M. P. Patankar, J. Aumentado, A. A. Clerk, and R. Vijay, "Broadband parametric amplification with impedance engineering: Beyond the gain-bandwidth product", Appl. Phys. Lett. **107**, 262601 (2015) (cit. on pp. 2, 30, 76, 94).

[21] V. V. Sivak, S. Shankar, G. Liu, J. Aumentado, and M. H. Devoret, "Josephson array-mode parametric amplifier", Phys. Rev. Appl. **13**, 024014 (2020) (cit. on pp. 2, 16, 27, 29, 30, 44, 45, 62).

[22] P. Winkel, I. Takmakov, D. Rieger, L. Planat, W. Hasch-Guichard, L. Grünhaupt, N. Maleeva, F. Foroughi, F. Henriques, K. Borisov, J. Ferrero, A. V. Ustinov, W. Wernsdorfer, N. Roch, and I. M. Pop, "Nondegenerate parametric amplifiers based on dispersion-engineered josephson-junction arrays", Phys. Rev. Appl. **13**, 024015 (2020) (cit. on pp. 2, 27, 29, 30, 42, 45, 50, 53, 62, 86, 88, 96, 101, 105, 128, 133, 147, 148).

[23] L. Planat, A. Ranadive, R. Dassonneville, J. Puertas Martínez, S. Léger, C. Naud, O. Buisson, W. Hasch-Guichard, D. M. Basko, and N. Roch, "Photonic-Crystal Josephson Traveling-Wave Parametric Amplifier", Phys. Rev. X **10**, 021021 (2020) (cit. on p. 2).

[24] R. Kaufman, T. White, M. I. Dykman, A. Iorio, G. Sterling, S. Hong, A. Opremcak, A. Bengtsson, L. Faoro, J. C. Bardin, T. Burger, R. Gasca, and O. Naaman, "Josephson parametric amplifier with Chebyshev gain profile and high saturation", Phys. Rev. Appl. **20**, 054058 (2023) (cit. on pp. 2, 30, 76, 102).

[25] A. Ranadive, M. Esposito, L. Planat, E. Bonet, C. Naud, O. Buisson, W. Guichard, and N. Roch, "Kerr reversal in Josephson meta-material and traveling wave parametric amplification", Nat. Commun. **13**, 1–9 (2022) (cit. on pp. 2, 76, 132).

[26] V. Gaydamachenko, C. Kissling, and L. Grünhaupt, "rf-SQUID-based traveling-wave parametric amplifier with input saturation power of −84 dBm across more than one octave in bandwidth", Phys. Rev. Appl. **23**, 064053 (2025) (cit. on pp. 2, 29, 31, 62, 63, 76, 89).

[27] V. R. Joshi, S. Hazra, A. Z. Ding, A. Miano, W. Dai, G. Umasankar, A. Kottandavida, G. Liu, L. Frunzio, and M. H. Devoret, "Lumped-element broadband SNAIL parametric amplifier with on-chip pump filter for multiplexed readout", Phys. Rev. Appl. **24**, 044003 (2025) (cit. on p. 2).

[28] R. Vijay, D. H. Slichter, and I. Siddiqi, "Observation of Quantum Jumps in a Superconducting Artificial Atom", Phys. Rev. Lett. **106**, 110502 (2011) (cit. on pp. 2, 9, 28, 71).

[29] M. Tinkham, *Introduction to Superconductivity* (2004) (cit. on pp. 2, 10, 11, 31–33, 38, 39, 43, 46).

[30] A. Schneider, T. Wolz, M. Pfirrmann, M. Spiecker, H. Rotzinger, A. V. Ustinov, and M. Weides, "Transmon qubit in a magnetic field: Evolution of coherence and transition frequency", Phys. Rev. Res. **1**, 023003 (2019) (cit. on pp. 2, 33).

[31] J. Krause, C. Dickel, E. Vaal, M. Vielmetter, J. Feng, R. Bounds, G. Catelani, J. M. Fink, and Y. Ando, "Magnetic Field Resilience of Three-Dimensional Transmons with Thin-Film Al/AlO_x/Al Josephson Junctions Approaching 1 T", Phys. Rev. Appl. **17**, 034032 (2022) (cit. on pp. 2, 33).

[32] L. M. Janssen, G. Butseraen, J. Krause, A. Coissard, L. Planat, N. Roch, G. Catelani, Y. Ando, and C. Dickel, "Magnetic-field dependence of a Josephson traveling-wave parametric amplifier and integration into a high-field setup", arXiv (2024) (cit. on pp. 2, 33).

[33] Z. Wang, L. Balembois, M. Rančić, E. Billaud, M. Le Dantec, A. Ferrier, P. Goldner, S. Bertaina, T. Chanelière, D. Esteve, D. Vion, P. Bertet, and E. Flurin, "Single-electron spin resonance detection by microwave photon counting", Nature **619**, 276–281 (2023) (cit. on pp. 2, 31, 65).

[34] S. Schaal, I. Ahmed, J. A. Haigh, L. Hutin, B. Bertrand, S. Barraud, M. Vinet, C.-M. Lee, N. Stelmashenko, J. W. A. Robinson, J. Y. Qiu, S. Hacohen-Gourgy, I. Siddiqi, M. F. Gonzalez-Zalba, and J. J. L. Morton, "Fast Gate-Based Readout of Silicon Quantum Dots Using Josephson Parametric Amplification", Phys. Rev. Lett. **124**, 067701 (2020) (cit. on pp. 2, 31, 65).

[35] V. Elhomsy, L. Planat, D. J. Niegemann, B. Cardoso-Paz, A. Badreldin, B. Klemt, V. Thiney, R. Lethiecq, E. Eyraud, M. C. Dartiailh, B. Bertrand, H. Niebojewski, C. Bäuerle, M. Vinet, T. Meunier, N. Roch, and M. Urdampilleta, "Broadband parametric amplification for multiplexed SiMOS quantum dot signals", arXiv (2023) (cit. on pp. 2, 29, 31, 65).

[36] M. Pita-Vidal, A. Bargerbos, R. Žitko, L. J. Splitthoff, L. Grünhaupt, J. J. Wesdorp, Y. Liu, L. P. Kouwenhoven, R. Aguado, B. van Heck, A. Kou, and C. K. Andersen, "Direct manipulation of a superconducting spin qubit strongly coupled to a transmon qubit", Nat. Phys. **19**, 1110–1115 (2023) (cit. on pp. 2, 31, 65).

[37] M. Hays, V. Fatemi, D. Bouman, J. Cerrillo, S. Diamond, K. Serniak, T. Connolly, P. Krogstrup, J. Nygård, A. L. Yeyati, A. Geresdi, and M. H. Devoret, "Coherent manipulation of an Andreev spin qubit", Science **373**, 430–433 (2021) (cit. on pp. 2, 31, 65).

[38] T. Luschmann, P. Schmidt, F. Deppe, A. Marx, A. Sanchez, R. Gross, and H. Huebl, "Mechanical frequency control in inductively coupled electromechanical systems", Sci. Rep. **12**, 1–7 (2022) (cit. on pp. 2, 65).

[39] C. Godfrin, A. Ferhat, R. Ballou, S. Klyatskaya, M. Ruben, W. Wernsdorfer, and F. Balestro, "Operating Quantum States in Single Magnetic Molecules: Implementation of Grover's Quantum Algorithm", Phys. Rev. Lett. **119**, 187702 (2017) (cit. on pp. 2, 31).

[40] S. K. Lamoreaux, K. A. van Bibber, K. W. Lehnert, and G. Carosi, "Analysis of single-photon and linear amplifier detectors for microwave cavity dark matter axion searches", Phys. Rev. D **88**, 035020 (2013) (cit. on pp. 2, 31, 75).

[41] K. M. Backes, D. A. Palken, S. A. Kenany, B. M. Brubaker, S. B. Cahn, A. Droster, G. C. Hilton, S. Ghosh, H. Jackson, S. K. Lamoreaux, A. F. Leder, K. W. Lehnert, S. M. Lewis, M. Malnou, R. H. Maruyama, N. M. Rapidis, M. Simanovskaia, S. Singh, D. H. Speller, I. Urdinaran, L. R. Vale, E. C. van Assendelft, K. van Bibber, and H. Wang, "A quantum enhanced search for dark matter axions", Nature **590**, 238–242 (2021) (cit. on pp. 2, 31, 75).

[42] C. Braggio, G. Cappelli, G. Carugno, N. Crescini, R. Di Vora, M. Esposito, A. Ortolan, L. Planat, A. Ranadive, N. Roch, and G. Ruoso, "A haloscope amplification chain based on a traveling wave parametric amplifier", Rev. Sci. Instrum. **93** (2022) (cit. on pp. 2, 31, 65, 75).

[43] P. Jung, S. Butz, M. Marthaler, M. V. Fistul, J. Leppäkangas, V. P. Koshelets, and A. V. Ustinov, "Multistability and switching in a superconducting metamaterial", Nat. Commun. **5**, 1–6 (2014) (cit. on p. 2).

[44] T.-C. Chien, O. Lanes, C. Liu, X. Cao, P. Lu, S. Motz, G. Liu, D. Pekker, and M. Hatridge, "Multiparametric amplification and qubit measurement with a Kerr-free Josephson ring modulator", Phys. Rev. A **101**, 042336 (2020) (cit. on pp. 2, 30, 35, 77, 78, 80, 92).

[45] J. Cohen, A. Petrescu, R. Shillito, and A. Blais, "Reminiscence of Classical Chaos in Driven Transmons", PRX Quantum **4**, 020312 (2023) (cit. on p. 2).

[46] S. Krinner, N. Lacroix, A. Remm, A. Di Paolo, E. Genois, C. Leroux, C. Hellings, S. Lazar, F. Swiadek, J. Herrmann, G. J. Norris, C. K. Andersen, M. Müller, A. Blais, C. Eichler, and A. Wallraff, "Realizing repeated quantum error correction in a distance-three surface code", Nature **605**, 669–674 (2022) (cit. on pp. 2, 13, 29, 75).

[47] T. White, “Readout of a quantum processor with high dynamic range Josephson parametric amplifiers”, Appl. Phys. Lett. **122** (2023) (cit. on pp. 2, 13, 29, 75).

[48] Google Quantum AI, “Suppressing quantum errors by scaling a surface code logical qubit”, Nature **614**, 676–681 (2023) (cit. on pp. 2, 13, 29, 75).

[49] M. Xu, R. Cheng, Y. Wu, G. Liu, and H. X. Tang, “Magnetic Field-Resilient Quantum-Limited Parametric Amplifier”, PRX Quantum **4**, 010322 (2023) (cit. on pp. 2, 6, 30, 43, 46, 47, 89, 90).

[50] S. Frasca, C. Roy, G. Beaulieu, and P. Scarlino, “Three-wave-mixing quantum-limited kinetic inductance parametric amplifier operating at 6 T near 1 K”, Phys. Rev. Appl. **21**, 024011 (2024) (cit. on pp. 2, 6, 31, 43, 47, 62, 63, 90).

[51] F. Faramarzi, S. Sypkens, R. Stephenson, B. H. Eom, H. LeDuc, S. Chaudhuri, and P. Day, “Near-quantum-limited subgigahertz TiN kinetic inductance traveling-wave parametric amplifier operating in a frequency-translating mode”, Phys. Rev. Appl. **23**, 024063 (2025) (cit. on pp. 2, 6).

[52] A. Giachero, M. R. Vissers, J. D. Wheeler, M. Malnou, J. E. Austermann, and J. Hubmayr, “Characterization of NbTiN Films With Thicknesses Below 20 nm for Low Power Kinetic Inductance Amplifiers”, IEEE Trans. Appl. Supercond. **33**, ArticleSequenceNumber:1700905 (2023) (cit. on pp. 2, 47).

[53] S. Shu, N. Klimovich, B. H. Eom, A. D. Beyer, R. B. Thakur, H. G. Leduc, and P. K. Day, “Nonlinearity and wide-band parametric amplification in a (Nb,Ti)N microstrip transmission line”, Phys. Rev. Res. **3**, 023184 (2021) (cit. on pp. 2, 47).

[54] L. Howe, A. Giachero, M. Vissers, P. Campana, J. Wheeler, J. Gao, J. Austermann, J. Hubmayr, A. Nucciotti, and J. Ullom, “Kinetic Inductance Traveling Wave Parametric Amplifiers Near the Quantum Limit: Methodology and Characterization”, arXiv, 10.48550/arXiv.2507.07706 (2025) (cit. on pp. 2, 47, 60, 76, 102).

[55] M. Malnou, M. R. Vissers, J. D. Wheeler, J. Aumentado, J. Hubmayr, J. N. Ullom, and J. Gao, “Three-Wave Mixing Kinetic Inductance Traveling-Wave Amplifier with Near-Quantum-Limited Noise Performance”, PRX Quantum **2**, 010302 (2021) (cit. on pp. 2, 6, 31, 47, 60, 62, 63).

[56] D. J. Parker, M. Savytskyi, W. Vine, A. Laucht, T. Duty, A. Morello, A. L. Grimsmo, and J. J. Pla, “Degenerate Parametric Amplification via Three-Wave Mixing Using Kinetic Inductance”, Phys. Rev. Appl. **17**, 034064 (2022) (cit. on pp. 2, 6, 31, 47, 60, 62, 63, 90).

[57] C.-C. Hung, H. Kutsuma, C. W. S. Chang, A. F. van Loo, and Y. Nakamura, “Broadband Kinetic-Inductance Parametric Amplifiers with Impedance Engineering”, arXiv, 10.48550/arXiv.2504.17145 (2025) (cit. on pp. 2, 47, 76, 94).

[58] A. Mohamed, E. Zohari, J. J. Pla, P. E. Barclay, and S. Barzanjeh, “Selective single- and double-mode quantum-limited amplifier”, Phys. Rev. Appl. **21**, 064052 (2024) (cit. on pp. 2, 43, 47, 50, 90).

[59] M. Khalifa and J. Salfi, "Nonlinearity and Parametric Amplification of Superconducting Nanowire Resonators in Magnetic Field", Phys. Rev. Appl. **19**, 034024 (2023) (cit. on pp. 2, 43, 47).

[60] A. Vaartjes, A. Kringhøj, W. Vine, T. Day, A. Morello, and J. J. Pla, "Strong Microwave Squeezing Above 1 Tesla and 1 Kelvin", arXiv (2023) (cit. on pp. 2, 47, 90, 103).

[61] B. Abeles, R. W. Cohen, and W. R. Stowell, "Critical Magnetic Fields of Granular Superconductors", Phys. Rev. Lett. **18**, 902–905 (1967) (cit. on pp. 2, 37).

[62] G. Deutscher, H. Fenichel, M. Gershenson, E. Grünbaum, and Z. Ovadyahu, "Transition to zero dimensionality in granular aluminum superconducting films", J. Low Temp. Phys. **10**, 231–243 (1973) (cit. on pp. 2, 37).

[63] G. Deutscher, Y. Imry, and L. Gunther, "Superconducting phase transitions in granular systems", Phys. Rev. B **10**, 4598–4606 (1974) (cit. on pp. 2, 37).

[64] G. Deutscher, "Granular Superconductivity: a Playground for Josephson, Anderson, Kondo, and Mott", J. Supercond. Novel Magn. **34**, 1699–1703 (2021) (cit. on pp. 2, 37–39).

[65] N. Maleeva, L. Grünhaupt, T. Klein, F. Levy-Bertrand, O. Dupre, M. Calvo, F. Valenti, P. Winkel, F. Friedrich, W. Wernsdorfer, A. V. Ustinov, H. Rotzinger, A. Monfardini, M. V. Fistul, and I. M. Pop, "Circuit quantum electrodynamics of granular aluminum resonators", Nature Communications **9**, 3889 (2018) (cit. on pp. 2, 6, 38–42, 45, 46, 49, 56, 60).

[66] F. Levy-Bertrand, T. Klein, T. Grenet, O. Dupré, A. Benoît, A. Bideaud, O. Bourrion, M. Calvo, A. Catalano, A. Gomez, J. Goupy, L. Grünhaupt, U. v. Luepke, N. Maleeva, F. Valenti, I. M. Pop, and A. Monfardini, "Electrodynamics of granular aluminum from superconductor to insulator: Observation of collective superconducting modes", Phys. Rev. B **99**, 094506 (2019) (cit. on pp. 2, 38, 39, 56).

[67] F. Henriques, F. Valenti, T. Charpentier, M. Lagoin, C. Gouriou, M. Martínez, L. Cardani, M. Vignati, L. Grünhaupt, D. Gusenkova, J. Ferrero, S. T. Skacel, W. Wernsdorfer, A. V. Ustinov, G. Catelani, O. Sander, and I. M. Pop, "Phonon traps reduce the quasiparticle density in superconducting circuits", Appl. Phys. Lett. **115**, 212601 (2019) (cit. on pp. 2, 38, 41, 42).

[68] K. Borisov, D. Rieger, P. Winkel, F. Henriques, F. Valenti, A. Ionita, M. Wessbecher, M. Spiecker, D. Gusenkova, I. M. Pop, and W. Wernsdorfer, "Superconducting granular aluminum resonators resilient to magnetic fields up to 1 tesla", Applied Physics Letters **117** (2020) (cit. on pp. 2, 38, 41–43, 49, 55, 58, 65, 66, 125, 126).

[69] C. Roy, S. Frasca, and P. Scarlino, "Study of Magnetic Field Resilient High Impedance High-Kinetic Inductance Superconducting Resonators", arXiv, 10.48550/arXiv.2503.13321 (2025) (cit. on pp. 2, 43, 47, 49, 58, 65).

[70] K. J. Ramos, I. Curci, E. Potosí, I. Lobato, L. S. Alarcón, H. Pastoriza, and L. Tosi, "Microwave characterization of superconducting coplanar resonators made out of granular aluminium", arXiv (2025) (cit. on p. 2).

[71] L. Grünhaupt, M. Spiecker, D. Gusenkova, N. Maleeva, S. T. Skacel, I. Takmakov, F. Valenti, P. Winkel, H. Rotzinger, W. Wernsdorfer, A. V. Ustinov, and I. M. Pop, "Granular aluminium as a superconducting material for high-impedance quantum circuits", Nat. Mater. **18**, 816–819 (2019) (cit. on pp. 2, 15, 41, 42).

[72] M. Spiecker, *Two-level system hyperpolarization with a quantum Szilard engine*, [Online; accessed 19. Nov. 2025], 2024 (cit. on pp. 2, 11, 42).

[73] F. Kaap, C. Kissling, V. Gaydamachenko, L. Grünhaupt, and S. Lotkhov, "Demonstration of dual Shapiro steps in small Josephson junctions", Nat. Commun. **15**, 8726 (2024) (cit. on p. 2).

[74] S. Geisert, S. Ihssen, P. Winkel, M. Spiecker, M. Fechant, P. Paluch, N. Gosling, N. Zapata, S. Günzler, D. Rieger, D. Bénâtre, T. Reisinger, W. Wernsdorfer, and I. M. Pop, "Pure kinetic inductance coupling for cQED with flux qubits", Appl. Phys. Lett. **125**, 064002 (2024) (cit. on pp. 2, 15, 41, 42, 45, 69, 70).

[75] M. Janík, K. Roux, C. Borja-Espinosa, O. Sagi, A. Baghdadi, T. Adletzberger, S. Calcaterra, M. Botifoll, A. Garzón Manjón, J. Arbiol, D. Chrastina, G. Isella, I. M. Pop, and G. Katsaros, "Strong charge-photon coupling in planar germanium enabled by granular aluminium superinductors", Nat. Commun. **16**, 1–9 (2025) (cit. on pp. 2, 40, 43, 58, 65, 125, 126).

[76] M. Khorramshahi, M. Spiecker, P. Paluch, S. Geisert, N. Gosling, N. Zapata, L. Brauch, C. Kübel, S. Dehm, R. Krupke, W. Wernsdorfer, I. M. Pop, and T. Reisinger, "High-impedance granular-aluminum ring resonators", Phys. Rev. Appl. **24**, 024066 (2025) (cit. on pp. 2, 40–42).

[77] D. Bénâtre, M. Féchant, N. Zapata, N. Gosling, P. Paluch, T. Reisinger, and I. M. Pop, "Simultaneous sweet-spot locking of gradiometric fluxonium qubits", Phys. Rev. Appl. **24**, 054031 (2025) (cit. on pp. 2, 41, 42).

[78] J. Basset, O. Stanisavljević, J. Gabelli, M. Aprili, and J. Estève, "Fast and Continuous Detection of Single Microwave Photons via Photo-assisted Quasiparticle Tunneling to a Superconducting Island", arXiv, 10.48550/arXiv.2511.17470 (2025) (cit. on p. 2).

[79] A. Nambisan, S. Günzler, D. Rieger, N. Gosling, S. Geisert, V. Carpentier, N. Zapata, M. Field, M. V. Milošević, C. A. D. Lopez, C. Padurariu, B. Kubala, J. Ankerhold, W. Wernsdorfer, M. Spiecker, and I. M. Pop, "Quantum Coherence in Superconducting Vortex States", arXiv (2025) (cit. on pp. 2, 32).

[80] P. Winkel, K. Borisov, L. Grünhaupt, D. Rieger, M. Spiecker, F. Valenti, A. V. Ustinov, W. Wernsdorfer, and I. M. Pop, "Implementation of a Transmon Qubit Using Superconducting Granular Aluminum", Phys. Rev. X **10**, 031032 (2020) (cit. on pp. 3, 19, 20, 38, 40, 41, 47, 49, 138).

[81] S. Günzler, J. Beck, D. Rieger, N. Gosling, N. Zapata, M. Field, S. Geisert, A. Bacher, J. K. Hohmann, M. Spiecker, W. Wernsdorfer, and I. M. Pop, "Spin environment of a superconducting qubit in high magnetic fields", Nat. Commun. **16**, 9564 (2025) (cit. on pp. 3, 38, 41–43, 45, 59, 65).

[82] I. Takmakov, "Minimizing the discrimination time for quantum states of an artificial atom", 47.12.01; LK 01, PhD thesis (Karlsruher Institut für Technologie (KIT), 2022), 94 pp. (cit. on pp. 3, 18, 23, 25, 40, 49, 52, 53, 56, 59, 60, 72, 138).

[83] D. M. Pozar, *Microwave Engineering* (Wiley, Chichester, England, UK, Apr. 2012) (cit. on pp. 3, 4, 17, 19, 27, 97, 102, 127).

[84] *Hertz's useless discovery*, [Online; accessed 14. Nov. 2025], Nov. 2025 (cit. on p. 4).

[85] A. S. Gilmour, *Microwave Tubes* (Artech House, 1986) (cit. on p. 5).

[86] R. Loudon, *The Quantum Theory of Light* (OUP, Oxford, England, UK, Sept. 2000) (cit. on pp. 5, 9, 103).

[87] G. L. Baker and J. A. Blackburn, *The Pendulum: A Case Study in Physics* (Oxford University Press, Oxford, England, UK, June 2005) (cit. on pp. 5, 150).

[88] F. J. Hyde, "Varactor-diode parametric amplifiers", Electron. Power **10**, 197–198 (1964) (cit. on pp. 5, 6).

[89] X. de Galicia, *Acércate a conocer uno de los símbolos más reconocibles de la catedral de Santiago de Compostela: el incensario más grande del mundo.* [Online; accessed 24. Nov. 2025], Nov. 2025 (cit. on p. 6).

[90] E. I. Rosenthal, C. S. Wang, J. Sloan, G. Scuri, Y. Shi, K. Pezeshki, P. M. Noertoft, J. Vuckovic, and C. P. Anderson, "Proposal for a 3-Wave Mixing Element with Quantum Paraelectric Materials", arXiv (2025) (cit. on p. 6).

[91] O. V. Astafiev, L. B. Ioffe, S. Kafanov, Y. A. Pashkin, K. Y. Arutyunov, D. Shahar, O. Cohen, and J. S. Tsai, "Coherent quantum phase slip", Nature **484**, 355–358 (2012) (cit. on pp. 6, 47).

[92] O. Dupré, A. Benoît, M. Calvo, A. Catalano, J. Goupy, C. Hoarau, T. Klein, K. Le Calvez, B. Sacépé, A. Monfardini, and F. Levy-Bertrand, "Tunable sub-gap radiation detection with superconducting resonators", Supercond. Sci. Technol. **30**, 045007 (2017) (cit. on pp. 6, 47).

[93] S. Mahashabde, E. Otto, D. Montemurro, S. de Graaf, S. Kubatkin, and A. Danilov, "Fast Tunable High-Q-Factor Superconducting Microwave Resonators", Phys. Rev. Appl. **14**, 044040 (2020) (cit. on pp. 6, 47, 60).

[94] N. Zapata, I. Takmakov, S. Günzler, S. Geisert, S. Ihssen, M. Field, A. Nambisan, D. Rieger, T. Reisinger, W. Wernsdorfer, and I. M. Pop, "Granular Aluminum Parametric Amplifier for Low-Noise Measurements in Tesla Fields", Phys. Rev. Lett. **133**, 260604 (2024) (cit. on pp. 6, 49, 50).

[95] J. Sarkar, K. V. Salunkhe, S. Mandal, S. Ghatak, A. H. Marchawala, I. Das, K. Watanabe, T. Taniguchi, R. Vijay, and M. M. Deshmukh, "Quantum-noise-limited microwave amplification using a graphene Josephson junction", Nat. Nanotechnol. **17**, 1147–1152 (2022) (cit. on p. 6).

[96] G. Butseraen, A. Ranadive, N. Aparicio, K. Rafsanjani Amin, A. Juyal, M. Esposito, K. Watanabe, T. Taniguchi, N. Roch, F. Lefloch, and J. Renard, "A gate-tunable graphene Josephson parametric amplifier", Nat. Nanotechnol. **17**, 1153–1158 (2022) (cit. on p. 6).

[97] D. Phan, P. Falthansl-Scheinecker, U. Mishra, W. M. Strickland, D. Langone, J. Shabani, and A. P. Higginbotham, "Gate-Tunable Superconductor-Semiconductor Parametric Amplifier", Phys. Rev. Appl. **19**, 064032 (2023) (cit. on p. 6).

[98] L. J. Splitthoff, J. J. Wesdorp, M. Pita-Vidal, A. Bargerbos, Y. Liu, and C. K. Andersen, "Gate-tunable kinetic inductance parametric amplifier", Phys. Rev. Appl. **21**, 014052 (2024) (cit. on p. 6).

[99] R. Rousset-Zenou, N. Aparicio, S. Messelot, R. D. Schlosser, M. Bjergfelt, J. Renard, M. Hocevar, and J. Nygård, "Gate-tunable Josephson parametric amplifiers based on semiconductor nanowires", arXiv (2025) (cit. on p. 6).

[100] M. Villiers, "Dynamically Enhancing Qubit-Photon Interactions with Anti-Squeezing", PhD thesis (Sorbonne Université, 2023) (cit. on p. 8).

[101] A. Eddins, J. M. Kreikebaum, D. M. Toyli, E. M. Levenson-Falk, A. Dove, W. P. Livingston, B. A. Levitan, L. C. G. Govia, A. A. Clerk, and I. Siddiqi, "High-Efficiency Measurement of an Artificial Atom Embedded in a Parametric Amplifier", Phys. Rev. X **9**, 011004 (2019) (cit. on p. 9).

[102] M. Villiers, W. C. Smith, A. Petrescu, A. Borgognoni, M. Delbecq, A. Sarlette, M. Mirrahimi, P. Campagne-Ibarcq, T. Kontos, and Z. Leghtas, "Dynamically Enhancing Qubit-Photon Interactions with Antisqueezing", PRX Quantum **5**, 020306 (2024) (cit. on pp. 9, 77, 81, 103).

[103] A. Blais, A. L. Grimsmo, S. M. Girvin, and A. Wallraff, "Circuit quantum electrodynamics", Rev. Mod. Phys. **93**, 025005 (2021) (cit. on pp. 9, 13, 19, 21).

[104] B. Abdo, W. Shanks, O. Jinka, J. R. Rozen, and J. Orcutt, "Teleportation and Entanglement Swapping of Continuous Quantum Variables of Microwave Radiation", Phys. Rev. X **15**, 031075 (2025) (cit. on pp. 9, 103).

[105] A. Andrés-Juanes, J. Agustí, R. Sett, E. S. Redchenko, L. Kapoor, S. Hawaldar, P. Rabl, and J. M. Fink, "Entangling remote qubits through a two-mode squeezed reservoir", arXiv (2025) (cit. on pp. 9, 103).

[106] M. Kjaergaard, M. E. Schwartz, J. Braumüller, P. Krantz, J. I.-J. Wang, S. Gustavsson, and W. D. Oliver, "Superconducting Qubits: Current State of Play", Annu. Rev. Condens. Matter Phys., 369–395 (2020) (cit. on p. 9).

[107] *Nobel Prize in Physics 2025*, [Online; accessed 14. Nov. 2025], Nov. 2025 (cit. on p. 10).

[108] J. F. Annett, *Superconductivity, Superfluids and Condensates* (OUP, Oxford, England, UK, Mar. 2004) (cit. on p. 10).

[109] A. J. Leggett, "Macroscopic Quantum Systems and the Quantum Theory of Measurement", Prog. Theor. Phys. **69**, 80–100 (1980) (cit. on p. 10).

[110] M. A. Castellanos-Beltran, K. D. Irwin, G. C. Hilton, L. R. Vale, and K. W. Lehnert, "Amplification and squeezing of quantum noise with a tunable Josephson metamaterial", Nat. Phys. **4**, 929–931 (2008) (cit. on pp. 10, 103).

[111] C. Eichler, D. Bozyigit, C. Lang, M. Baur, L. Steffen, J. M. Fink, S. Filipp, and A. Wallraff, "Observation of Two-Mode Squeezing in the Microwave Frequency Domain", Phys. Rev. Lett. **107**, 113601 (2011) (cit. on pp. 10, 103).

[112] C. Eichler, Y. Salathe, J. Mlynek, S. Schmidt, and A. Wallraff, "Quantum-limited amplification and entanglement in coupled nonlinear resonators", Phys. Rev. Lett. **113**, 110502 (2014) (cit. on pp. 10, 30, 50, 53, 86, 101, 103).

[113] M. Esposito, A. Ranadive, L. Planat, S. Leger, D. Fraudet, V. Jouanny, O. Buisson, W. Guichard, C. Naud, J. Aumentado, F. Lecocq, and N. Roch, "Observation of Two-Mode Squeezing in a Traveling Wave Parametric Amplifier", Phys. Rev. Lett. **128**, 153603 (2022) (cit. on pp. 10, 75, 103).

[114] J. Y. Qiu, A. Grimsmo, K. Peng, B. Kannan, B. Lienhard, Y. Sung, P. Krantz, V. Bolkhovsky, G. Calusine, D. Kim, A. Melville, B. M. Niedzielski, J. Yoder, M. E. Schwartz, T. P. Orlando, I. Siddiqi, S. Gustavsson, K. P. O'Brien, and W. D. Oliver, "Broadband squeezed microwaves and amplification with a Josephson travelling-wave parametric amplifier", Nat. Phys. **19**, 706–713 (2023) (cit. on pp. 10, 75, 103).

[115] A. Alocco, A. Celotto, E. Palumbo, B. Galvano, P. Livreri, L. Fasolo, L. Callegaro, and E. Enrico, "Programmable Microwave Cluster States via Josephson Metamaterials", arXiv, 10.48550/arXiv.2507.22823 (2025) (cit. on p. 10).

[116] U. Vool and M. Devoret, "Introduction to quantum electromagnetic circuits", Int. J. Circuit Theory Appl. **45**, 897–934 (2017) (cit. on p. 10).

[117] T. J. Maldonado, H. E. Türeci, and A. W. Rodriguez, "Mesoscopic theory of the Josephson junction", Phys. Rev. B **111**, L140505 (2025) (cit. on p. 11).

[118] S. Fritz, L. Radtke, R. Schneider, M. Weides, and D. Gerthsen, "Optimization of Al/AlOx/Al-layer systems for Josephson junctions from a microstructure point of view", J. Appl. Phys. **125**, 165301 (2019) (cit. on pp. 12, 42).

[119] A. A. Pishchimova, N. S. Smirnov, D. A. Ezenkova, E. A. Krivko, E. V. Zikiy, D. O. Moskalev, A. I. Ivanov, N. D. Korshakov, and I. A. Rodionov, "Improving Josephson junction reproducibility for superconducting quantum circuits: junction area fluctuation", Sci. Rep. **13**, 6772 (2023) (cit. on pp. 12, 29, 42).

[120] Y. Zheng, S. Li, Z. Ding, K. Xiong, J. Feng, and H. Yang, "Fabrication of Al/AlOx/Al junctions with high uniformity and stability on sapphire substrates", Sci. Rep. **13**, 11874 (2023) (cit. on pp. 12, 29, 42).

[121] J. D. Baran, H. Grönbeck, and A. Hellman, "Mechanism for Limiting Thickness of Thin Oxide Films on Aluminum", Phys. Rev. Lett. **112**, 146103 (2014) (cit. on p. 12).

[122] J. Gorobez, B. Maack, and N. Nilius, "Growth of Self-Passivating Oxide Layers on Aluminum—Pressure and Temperature Dependence", Phys. Status Solidi B **258**, 2000559 (2021) (cit. on p. 12).

[123] M. A. Sillanpää, T. Lehtinen, A. Paila, Y. Makhlin, L. Roschier, and P. J. Hakonen, "Direct Observation of Josephson Capacitance", Phys. Rev. Lett. **95**, 206806 (2005) (cit. on p. 12).

[124] W. Yu-Lin, D. Hui, Y. Hai-Feng, X. Guang-Ming, T. Ye, L. Jie, C. Ying-Fei, Z. Shi-Ping, and Z. Dong-Ning, "Fabrication of Al/AlOx/Al Josephson junctions and superconducting quantum circuits by shadow evaporation and a dynamic oxidation process", Chin. Phys. B **22**, 060309 (2013) (cit. on p. 12).

[125] F. Arute, "Quantum supremacy using a programmable superconducting processor", Nature **574**, 505–510 (2019) (cit. on p. 13).

[126] Y. Zhao, "Realization of an Error-Correcting Surface Code with Superconducting Qubits", Phys. Rev. Lett. **129**, 030501 (2022) (cit. on p. 13).

[127] W. C. Smith, A. Kou, U. Vool, I. M. Pop, L. Frunzio, R. J. Schoelkopf, and M. H. Devoret, "Quantization of inductively shunted superconducting circuits", Phys. Rev. B **94**, 144507 (2016) (cit. on p. 15).

[128] F. Yan, Y. Sung, P. Krantz, A. Kamal, D. K. Kim, J. L. Yoder, T. P. Orlando, S. Gustavsson, and W. D. Oliver, "Engineering Framework for Optimizing Superconducting Qubit Designs", arXiv (2020) (cit. on p. 15).

[129] V. E. Manucharyan, J. Koch, L. I. Glazman, and M. H. Devoret, "Fluxonium: Single Cooper-Pair Circuit Free of Charge Offsets", Science **326**, 113–116 (2009) (cit. on p. 15).

[130] C. Eichler and A. Wallraff, "Controlling the dynamic range of a Josephson parametric amplifier", EPJ Quantum Technol. **1**, 1–19 (2014) (cit. on pp. 16, 23, 44, 50, 53, 105).

[131] C. W. Gardiner and M. J. Collett, "Input and output in damped quantum systems: Quantum stochastic differential equations and the master equation", Phys. Rev. A **31**, 3761–3774 (1985) (cit. on pp. 17, 18).

[132] H. Y. Yuan, W. Yu, and J. Xiao, "Loop theory for input-output problems in cavities", Phys. Rev. A **101**, 043824 (2020) (cit. on pp. 17, 18, 124).

[133] C. Gardiner and P. Zoller, *Quantum Noise: A Handbook of Markovian and Non-Markovian Quantum Stochastic Methods with Applications to Quantum Optics* (Springer Science & Business Media, Aug. 2004) (cit. on p. 17).

[134] D. Rieger, S. Günzler, M. Spiecker, A. Nambisan, W. Wernsdorfer, and I. M. Pop, "Fano Interference in Microwave Resonator Measurements", Phys. Rev. Appl. **20**, 014059 (2023) (cit. on pp. 19, 55, 57–59, 72, 84, 123, 146).

[135] O. Astafiev, A. M. Zagoskin, A. A. Abdumalikov Jr., Y. A. Pashkin, T. Yamamoto, K. Inomata, Y. Nakamura, and J. S. Tsai, "Resonance Fluorescence of a Single Artificial Atom", Science **327**, 840–843 (2010) (cit. on pp. 19, 20).

[136] T. Hönigl-Decrinis, R. Shaikhaidarov, S. E. de Graaf, V. N. Antonov, and O. V. Astafiev, "Two-Level System as a Quantum Sensor for Absolute Calibration of Power", Phys. Rev. Appl. **13**, 024066 (2020) (cit. on p. 19).

[137] M. Spiecker, P. Paluch, N. Gosling, N. Drucker, S. Matityahu, D. Gusenkova, S. Günzler, D. Rieger, I. Takmakov, F. Valenti, P. Winkel, R. Gebauer, O. Sander, G. Catelani, A. Shnirman, A. V. Ustinov, W. Wernsdorfer, Y. Cohen, and I. M. Pop, "Two-level system hyperpolarization using a quantum Szilard engine", Nat. Phys. **19**, 1320–1325 (2023) (cit. on p. 19).

[138] M. Spiecker, A. I. Pavlov, A. Shnirman, and I. M. Pop, "Solomon equations for qubit and two-level systems: Insights into non-Poissonian quantum jumps", Phys. Rev. A **109**, 052218 (2024) (cit. on p. 19).

[139] J. Gambetta, A. Blais, D. I. Schuster, A. Wallraff, L. Frunzio, J. Majer, M. H. Devoret, S. M. Girvin, and R. J. Schoelkopf, "Qubit-photon interactions in a cavity: Measurement-induced dephasing and number splitting", Phys. Rev. A **74**, 042318 (2006) (cit. on pp. 22, 134).

[140] D. Rieger, *Gralmonium – Granular Aluminum Nano-Junction Fluxonium Qubit*, [Online; accessed 21. Nov. 2025], 2024 (cit. on pp. 22, 32).

[141] S. H. Strogatz, *Nonlinear Dynamics and Chaos: With Applications to Physics, Biology, Chemistry, and Engineering* (CRC Press, Boca Raton, FL, USA, May 2018) (cit. on pp. 22, 23, 26).

[142] E. X. DeJesus and C. Kaufman, "Routh-Hurwitz criterion in the examination of eigenvalues of a system of nonlinear ordinary differential equations", Phys. Rev. A **35**, 5288–5290 (1987) (cit. on pp. 26, 110, 117).

[143] *Technical datasheet: Low noise amplifier LNF-LNC0.3-14B. url = https://quantummicrowave.com/product/0-3-14-ghz-cryogenic-low-noise-amplifier*. (Cit. on pp. 27, 69, 131).

[144] *Technical datasheet: Low noise amplifier LNF-LNC0.3-14G. url = https://lownoisefactory.com/product/lnf-lnc4_8g/*. (Cit. on pp. 27, 139, 140).

[145] R. Kaufman, C. Liu, K. Cicak, B. Mesits, M. Xia, C. Zhou, M. Nowicki, J. Aumentado, D. Pekker, and M. Hatridge, "Simple high-saturation-power quantum-limited rf-SQUID-array-based Josephson parametric amplifiers", Phys. Rev. Appl. **24**, 014052 (2025) (cit. on pp. 27, 29, 30, 71).

[146] R. Kaufman, T. White, M. I. Dykman, A. Iorio, G. Stirling, S. Hong, A. Opremcak, A. Bengtsson, L. Faoro, J. C. Bardin, T. Burger, R. Gasca, and O. Naaman, "Josephson parametric amplifier with Chebyshev gain profile and high saturation", arXiv (2023) (cit. on pp. 27, 94).

[147] C. Tannous and J. Langlois, "Classical noise, quantum noise and secure communication", Eur. J. Phys. **37**, 013001 (2015) (cit. on pp. 28, 128).

[148] M. Hatridge, S. Shankar, M. Mirrahimi, F. Schackert, K. Geerlings, T. Brecht, K. M. Sliwa, B. Abdo, L. Frunzio, S. M. Girvin, R. J. Schoelkopf, and M. H. Devoret, "Quantum Back-Action of an Individual Variable-Strength Measurement", Science **339**, 178–181 (2013) (cit. on pp. 28, 136).

[149] M. Malnou, T. F. Q. Larson, J. D. Teufel, F. Lecocq, and J. Aumentado, "Low-noise cryogenic microwave amplifier characterization with a calibrated noise source", Rev. Sci. Instrum. **95**, 034703 (2024) (cit. on pp. 28, 129, 130, 132).

[150] I. Takmakov, P. Winkel, F. Foroughi, L. Planat, D. Gusenkova, M. Spiecker, D. Rieger, L. Grünhaupt, A. V. Ustinov, W. Wernsdorfer, I. M. Pop, and N. Roch, "Minimizing the Discrimination Time for Quantum States of an Artificial Atom", Phys. Rev. Appl. **15**, 064029 (2021) (cit. on pp. 28, 30, 45, 62, 71).

[151] L. Planat, R. Dassonneville, J. P. Martínez, F. Foroughi, O. Buisson, W. Hasch-Guichard, C. Naud, R. Vijay, K. Murch, and N. Roch, "Understanding the Saturation Power of Josephson Parametric Amplifiers Made from SQUID Arrays", Phys. Rev. Appl. **11**, 034014 (2019) (cit. on p. 29).

[152] N. E. Frattini, V. V. Sivak, A. Lingenfelter, S. Shankar, and M. H. Devoret, "Optimizing the Nonlinearity and Dissipation of a SNAIL Parametric Amplifier for Dynamic Range", Phys. Rev. Appl. **10**, 054020 (2018) (cit. on pp. 29, 30, 62, 102).

[153] N. M. Hougland, Z. Li, R. Kaufman, B. Mesits, R. S. K. Mong, M. Hatridge, and D. Pekker, "Pump-efficient Josephson parametric amplifiers with high saturation power", arXiv (2024) (cit. on pp. 29, 31).

[154] J. Heinsoo, C. K. Andersen, A. Remm, S. Krinner, T. Walter, Y. Salathé, S. Gasparinetti, J.-C. Besse, A. Potočnik, A. Wallraff, and C. Eichler, "Rapid High-fidelity Multiplexed Readout of Superconducting Qubits", Phys. Rev. Appl. **10**, 034040 (2018) (cit. on pp. 29, 75).

[155] V. E. Manucharyan, E. Boaknin, M. Metcalfe, R. Vijay, I. Siddiqi, and M. Devoret, "Microwave bifurcation of a Josephson junction: Embedding-circuit requirements", Phys. Rev. B **76**, 014524 (2007) (cit. on p. 29).

[156] J. Y. Mutus, T. C. White, E. Jeffrey, D. Sank, R. Barends, J. Bochmann, Y. Chen, Z. Chen, B. Chiaro, A. Dunsworth, J. Kelly, A. Megrant, C. Neill, P. J. J. O'Malley, P. Roushan, A. Vainsencher, J. Wenner, I. Siddiqi, R. Vijay, A. N. Cleland, and J. M. Martinis, "Design and characterization of a lumped element single-ended superconducting microwave parametric amplifier with on-chip flux bias line", Appl. Phys. Lett. **103** (2013) (cit. on p. 30).

[157] J. Y. Mutus, T. C. White, R. Barends, Y. Chen, Z. Chen, B. Chiaro, A. Dunsworth, E. Jeffrey, J. Kelly, A. Megrant, C. Neill, P. J. J. O'Malley, P. Roushan, D. Sank, A. Vainsencher, J. Wenner, K. M. Sundqvist, A. N. Cleland, and J. M. Martinis, "Strong environmental coupling in a Josephson parametric amplifier", Appl. Phys. Lett. **104** (2014) (cit. on pp. 30, 61, 76, 94).

[158] D. Gusenkova, M. Spiecker, R. Gebauer, M. Willsch, D. Willsch, F. Valenti, N. Karcher, L. Grünhaupt, I. Takmakov, P. Winkel, D. Rieger, A. V. Ustinov, N. Roch, W. Wernsdorfer, K. Michielsen, O. Sander, and I. M. Pop, "Quantum Nondemolition Dispersive Readout of a Superconducting Artificial Atom Using Large Photon Numbers", Phys. Rev. Appl. **15**, 064030 (2021) (cit. on pp. 30, 45).

[159] *Technical datasheet: Bluefors dilution refrigerators. url = https://bluefors.com/products/dilution-refrigerator-measurement-systems/ld-dilution-refrigerator-measurement-system.* (Cit. on p. 31).

[160] W. Dai, G. Liu, V. Joshi, A. Miano, V. Sivak, S. Shankar, and M. H. Devoret, "Optimizing the pump coupling for a three-wave-mixing Josephson parametric amplifier", Phys. Rev. Appl. **23**, 054069 (2025) (cit. on p. 31).

[161] L. Glazman and G. Catelani, "Bogoliubov quasiparticles in superconducting qubits", SciPost Phys. Lect. Notes, 031 (2021) (cit. on p. 32).

[162] G. Stan, S. B. Field, and J. M. Martinis, "Critical Field for Complete Vortex Expulsion from Narrow Superconducting Strips", Phys. Rev. Lett. **92**, 097003 (2004) (cit. on p. 32).

[163] J. L. Chen, "Magnetic response of the superconducting thin film", Physica B **284-288**, 907–908 (2000) (cit. on p. 32).

[164] L. Nulens, N. Lejeune, J. Caeyers, S. Marinković, I. Cools, H. Dausy, S. Basov, B. Raes, M. J. Van Bael, A. Geresdi, A. V. Silhanek, and J. Van de Vondel, "Catastrophic magnetic flux avalanches in NbTiN superconducting resonators", Commun. Phys. **6**, 1–8 (2023) (cit. on pp. 32, 65).

[165] C. Wang, Y. Y. Gao, I. M. Pop, U. Vool, C. Axline, T. Brecht, R. W. Heeres, L. Frunzio, M. H. Devoret, G. Catelani, L. I. Glazman, and R. J. Schoelkopf, "Measurement and control of quasiparticle dynamics in a superconducting qubit", Nat. Commun. **5**, 5836 (2014) (cit. on p. 32).

[166] D. Bothner, T. Gaber, M. Kemmler, D. Koelle, and R. Kleiner, "Improving the performance of superconducting microwave resonators in magnetic fields", Applied Physics Letters **98** (2011) (cit. on pp. 33, 58, 65, 66).

[167] J. Kroll, F. Borsoi, K. van der Enden, W. Uilhoorn, D. de Jong, M. Quintero-Pérez, D. van Woerkom, A. Bruno, S. Plissard, D. Car, E. Bakkers, M. Cassidy, and L. Kouwenhoven, "Magnetic-field-resilient superconducting coplanar-waveguide resonators for hybrid circuit quantum electrodynamics experiments", Phys. Rev. Appl. **11**, 064053 (2019) (cit. on pp. 33, 58, 65, 66).

[168] A. Metelmann, O. Lanes, T.-Z. Chien, A. McDonald, M. Hatridge, and A. A. Clerk, *Quantum-limited amplification without instability*, 2022 (cit. on pp. 33, 34, 76, 77, 81, 88, 92, 102).

[169] N. Roch, E. Flurin, F. Nguyen, P. Morfin, P. Campagne-Ibarcq, M. H. Devoret, and B. Huard, "Widely Tunable, Nondegenerate Three-Wave Mixing Microwave Device Operating near the Quantum Limit", Phys. Rev. Lett. **108**, 147701 (2012) (cit. on p. 35).

[170] O. Lanes, "Harnessing unconventional and multiple parametric couplings for superconducting quantum information", PhD thesis (University of Pittsburgh, 2020) (cit. on pp. 35, 77, 80, 94).

[171] R. W. Cohen and B. Abeles, "Superconductivity in Granular Aluminum Films", Phys. Rev. **168**, 444–450 (1968) (cit. on p. 37).

[172] R. H. Parmenter, "Isospin Formulation of the Theory of a Granular Superconductor", Phys. Rev. **154**, 353–368 (1967) (cit. on p. 37).

[173] F. Friedrich, P. Winkel, K. Borisov, H. Seeger, C. Sürgers, I. M. Pop, and W. Wernsdorfer, "Onset of phase diffusion in high kinetic inductance granular aluminum micro-SQUIDs", Supercond. Sci. Technol. **32**, 125008 (2019) (cit. on pp. 37, 39, 41).

[174] A. Deshpande, J. Pusskeiler, C. Prange, U. Rogge, M. Dressel, and M. Scheffler, "Tuning the superconducting dome in granular aluminum thin films", J. Appl. Phys. **137** (2025) (cit. on pp. 37–39).

[175] F. Yang, T. Gozlinski, T. Storbeck, L. Grünhaupt, I. M. Pop, and W. Wulfhekel, "Microscopic charging and in-gap states in superconducting granular aluminum", Phys. Rev. B **102**, 104502 (2020) (cit. on pp. 38, 40).

[176] U. S. Pracht, N. Bachar, L. Benfatto, G. Deutscher, E. Farber, M. Dressel, and M. Scheffler, "Enhanced Cooper pairing versus suppressed phase coherence shaping the superconducting dome in coupled aluminum nanograins", Phys. Rev. B **93**, 100503 (2016) (cit. on p. 38).

[177] U. S. Pracht, T. Cea, N. Bachar, G. Deutscher, E. Farber, M. Dressel, M. Scheffler, C. Castellani, A. M. García-García, and L. Benfatto, "Optical signatures of the superconducting Goldstone mode in granular aluminum: Experiments and theory", Phys. Rev. B **96**, 094514 (2017) (cit. on p. 38).

[178] K. Steinberg, M. Scheffler, and M. Dressel, "Quasiparticle response of superconducting aluminum to electromagnetic radiation", Phys. Rev. B **77**, 214517 (2008) (cit. on p. 38).

[179] D. Rieger, S. Günzler, M. Spiecker, P. Paluch, P. Winkel, L. Hahn, J. K. Hohmann, A. Bacher, W. Wernsdorfer, and I. M. Pop, "Granular aluminium nanojunction fluxonium qubit", Nature Materials **22**, 194–199 (2023) (cit. on pp. 38, 41, 47, 49, 55, 102, 147).

[180] V. Gupta, P. Winkel, N. Thakur, P. van Vlaanderen, Y. Wang, S. Ganjam, L. Frunzio, and R. J. Schoelkopf, "Low-loss lumped-element inductors made from granular aluminum", Phys. Rev. Appl. **23**, 054067 (2025) (cit. on pp. 38, 42).

[181] Y.-H. Lin, J. Nelson, and A. M. Goldman, "Superconductivity of very thin films: The superconductor–insulator transition", Phys. C **514**, 130–141 (2015) (cit. on p. 38).

[182] A. Glezer Moshe, E. Farber, and G. Deutscher, "Granular superconductors for high kinetic inductance and low loss quantum devices", Applied Physics Letters **117** (2020) (cit. on p. 38).

[183] E. F. C. Driessen, P. C. J. J. Coumou, R. R. Tromp, P. J. de Visser, and T. M. Klapwijk, "Strongly Disordered TiN and NbTiN *s*-Wave Superconductors Probed by Microwave Electrodynamics", Phys. Rev. Lett. **109**, 107003 (2012) (cit. on p. 38).

[184] B. Sacépé, C. Chapelier, T. I. Baturina, V. M. Vinokur, M. R. Baklanov, and M. Sanquer, "Disorder-Induced Inhomogeneities of the Superconducting State Close to the Superconductor-Insulator Transition", Phys. Rev. Lett. **101**, 157006 (2008) (cit. on p. 38).

[185] T. Charpentier, D. Perconte, S. Léger, K. R. Amin, F. Blondelle, F. Gay, O. Buisson, L. Ioffe, A. Khvalyuk, I. Poboiko, M. Feigel'man, N. Roch, and B. Sacépé, "First-order quantum breakdown of superconductivity in an amorphous superconductor", Nat. Phys. **21**, 104–109 (2025) (cit. on p. 38).

[186] S. Bose and P. Ayyub, "A review of finite size effects in quasi-zero dimensional superconductors", Rep. Prog. Phys. **77**, 116503 (2014) (cit. on pp. 38, 39).

[187] N. Bachar, S. Lerer, A. Levy, S. Hacohen-Gourgy, B. Almog, H. Saadaoui, Z. Salman, E. Morenzoni, and G. Deutscher, "Mott transition in granular aluminum", Phys. Rev. B **91**, 041123 (2015) (cit. on p. 38).

[188] D. C. Mattis and J. Bardeen, "Theory of the Anomalous Skin Effect in Normal and Superconducting Metals", Phys. Rev. **111**, 412–417 (1958) (cit. on p. 40).

[189] T. Charpentier, A. Khvalyuk, L. Ioffe, M. Feigel'man, N. Roch, and B. Sacépé, "Universal scaling of microwave dissipation in superconducting circuits", arXiv, 10.48550/arXiv.2507.08953 (2025) (cit. on pp. 40, 42, 49).

[190] T. Weissl, "Quantum phase and charge in Josephson junction chains", PhD thesis (Université de Grenoble, 2014) (cit. on p. 45).

[191] W. Dai, S. Hazra, D. K. Weiss, P. D. Kurilovich, T. Connolly, H. K. Babla, S. Singh, V. R. Joshi, A. Z. Ding, P. D. Parakh, J. Venkatraman, X. Xiao, L. Frunzio, and M. H. Devoret, "Spectroscopy of drive-induced unwanted state transitions in superconducting circuits", arXiv, 10.48550/arXiv.2506.24070 (2025) (cit. on p. 45).

[192] O. Naaman and J. Aumentado, "Synthesis of Parametrically Coupled Networks", PRX Quantum **3**, 020201 (2022) (cit. on pp. 45, 76, 102).

[193] A. J. Annunziata, D. F. Santavicca, L. Frunzio, G. Catelani, M. J. Rooks, A. Frydman, and D. E. Prober, "Tunable superconducting nanoinductors", Nanotechnology **21**, 445202 (2010) (cit. on p. 46).

[194] A. Anthore, H. Pothier, and D. Esteve, "Density of States in a Superconductor Carrying a Supercurrent", Phys. Rev. Lett. **90**, 127001 (2003) (cit. on p. 46).

[195] N. Kirsh, E. Svetitsky, S. Goldstein, G. Pardo, O. Hachmo, and N. Katz, "Linear and Nonlinear Properties of a Compact High-Kinetic-Inductance WSi Multimode Resonator", Phys. Rev. Appl. **16**, 044017 (2021) (cit. on p. 47).

[196] J. Greenfield, C. Bell, F. Faramarzi, C. Kim, R. Basu Thakur, A. Wandui, C. Frez, P. Mauskopf, and D. Cunnane, "Kinetic inductance and non-linearity of MgB2 films at 4K", Appl. Phys. Lett. **126**, 022602 (2025) (cit. on p. 47).

[197] F. Faramarzi, S. Sypkens, R. Stephenson, B. H. Eom, H. Leduc, S. Chaudhuri, and P. Day, "A Near Quantum Limited Sub-GHz TiN Kinetic Inductance Traveling Wave Parametric Amplifier Operating in a Frequency Translating Mode", arXiv, 10.48550/arXiv.2406.00530 (2024) (cit. on p. 47).

[198] S. Zaman, J. Î.-j. Wang, T. Werkmeister, M. Tanaka, T. Dinh, M. Hays, D. Rodan-Legrain, A. Goswami, R. Assouly, A. K. Demir, D. K. Kim, B. M. Niedzielski, K. Serniak, M. E. Schwartz, K. Watanabe, T. Taniguchi, P. Kim, R. Comin, J. A. Grover, T. P. Orlando, P. Jarillo-Herrero, and W. D. Oliver, "Kinetic Inductance of Few-Layer $NbSe_2$ in the Two-Dimensional Limit", arXiv (2025) (cit. on p. 47).

[199] C. G. L. Bøttcher, E. Önder, T. Connolly, J. Zhao, C. Kvande, D. Q. Wang, P. D. Kurilovich, S. Vaitiekėnas, L. I. Glazman, H. X. Tang, and M. H. Devoret, "A transmon qubit realized by exploiting the superconductor-insulator transition", arXiv (2025) (cit. on p. 47).

[200] O. Buisson, P. Xavier, and J. Richard, "Observation of Propagating Plasma Modes in a Thin Superconducting Film", Phys. Rev. Lett. **73**, 3153–3156 (1994) (cit. on p. 47).

[201] M. Zhdanova, I. Pologov, G. Svyatsky, V. Chichkov, and N. Maleeva, "Granular Aluminum kinetic inductance nonlinearity", arXiv (2024) (cit. on p. 47).

[202] M. Khorramshahi, "Pushing the Boundaries of Impedance and Nonlinearity in Superconducting Quantum Circuits Based on Granular Aluminum", PhD thesis (Karlsruher Institut für Technologie (KIT), 2025) (cit. on pp. 47, 102, 103).

[203] H. A. Gersch and G. C. Knollman, "Quantum Cell Model for Bosons", Phys. Rev. **129**, 959–967 (1963) (cit. on p. 50).

[204] A. J. Leggett, "Bose-Einstein condensation in the alkali gases: Some fundamental concepts", Rev. Mod. Phys. **73**, 307–356 (2001) (cit. on p. 50).

[205] M. Ma, B. I. Halperin, and P. A. Lee, "Strongly disordered superfluids: Quantum fluctuations and critical behavior", Phys. Rev. B **34**, 3136–3143 (1986) (cit. on p. 50).

[206] T. Giamarchi and H. J. Schulz, "Anderson localization and interactions in one-dimensional metals", Phys. Rev. B **37**, 325–340 (1988) (cit. on p. 50).

[207] M. P. A. Fisher, P. B. Weichman, G. Grinstein, and D. S. Fisher, "Boson localization and the superfluid-insulator transition", Phys. Rev. B **40**, 546–570 (1989) (cit. on p. 50).

[208] M. Greiner, O. Mandel, T. Esslinger, T. W. Hänsch, and I. Bloch, "Quantum phase transition from a superfluid to a Mott insulator in a gas of ultracold atoms", Nature **415**, 39–44 (2002) (cit. on p. 50).

[209] G. J. Milburn, J. Corney, E. M. Wright, and D. F. Walls, "Quantum dynamics of an atomic Bose-Einstein condensate in a double-well potential", Phys. Rev. A **55**, 4318–4324 (1997) (cit. on p. 50).

[210] O. El Daif, G. Nardin, T. K. Paraïso, A. Baas, M. Richard, J.-P. Brantut, T. Guillet, F. Morier-Genoud, and B. Deveaud-Plédran, "Nonlinear relaxation of zero-dimension-trapped microcavity polaritons", Appl. Phys. Lett. **92**, 081910 (2008) (cit. on p. 50).

[211] S. R. K. Rodriguez, A. Amo, I. Sagnes, L. Le Gratiet, E. Galopin, A. Lemaître, and J. Bloch, "Interaction-induced hopping phase in driven-dissipative coupled photonic microcavities", Nat. Commun. **7**, 1–6 (2016) (cit. on p. 50).

[212] B. Garbin, A. Giraldo, K. J. H. Peters, N. G. R. Broderick, A. Spakman, F. Raineri, A. Levenson, S. R. K. Rodriguez, B. Krauskopf, and A. M. Yacomotti, "Spontaneous Symmetry Breaking in a Coherently Driven Nanophotonic Bose-Hubbard Dimer", Phys. Rev. Lett. **128**, 053901 (2022) (cit. on p. 50).

[213] J. Raftery, D. Sadri, S. Schmidt, H. E. Türeci, and A. A. Houck, "Observation of a Dissipation-Induced Classical to Quantum Transition", Phys. Rev. X **4**, 031043 (2014) (cit. on p. 50).

[214] K. W. Mahmud, H. Perry, and W. P. Reinhardt, "Quantum phase-space picture of Bose-Einstein condensates in a double well", Phys. Rev. A **71**, 023615 (2005) (cit. on p. 50).

[215] W. Casteels and C. Ciuti, "Quantum entanglement in the spatial-symmetry-breaking phase transition of a driven-dissipative Bose-Hubbard dimer", Phys. Rev. A **95**, 013812 (2017) (cit. on p. 50).

[216] T. Zibold, E. Nicklas, C. Gross, and M. K. Oberthaler, "Classical Bifurcation at the Transition from Rabi to Josephson Dynamics", Phys. Rev. Lett. **105**, 204101 (2010) (cit. on p. 50).

[217] A. Giraldo, B. Krauskopf, N. G. R. Broderick, J. A. Levenson, and A. M. Yacomotti, "The driven-dissipative Bose–Hubbard dimer: phase diagram and chaos", New J. Phys. **22**, 043009 (2020) (cit. on p. 50).

[218] D. Sarchi, I. Carusotto, M. Wouters, and V. Savona, "Coherent dynamics and parametric instabilities of microcavity polaritons in double-well systems", Phys. Rev. B **77**, 125324 (2008) (cit. on p. 50).

[219] D. Sarchi, I. Carusotto, M. Wouters, and V. Savona, "Coherent dynamics and parametric instabilities of microcavity polaritons in double-well systems", Phys. Rev. B **77**, 125324 (2008) (cit. on pp. 50, 52).

[220] V. Sivak, N. Frattini, V. Joshi, A. Lingenfelter, S. Shankar, and M. Devoret, "Kerr-free three-wave mixing in superconducting quantum circuits", Phys. Rev. Appl. **11**, 054060 (2019) (cit. on pp. 54, 90–92, 94).

[221] *Technical datasheet: Plassys MEB550S e-beam evaporator. url = https://plassys.com/categories/meb-ebeam/meb550s.* (Cit. on p. 56).

[222] S. Probst, F. B. Song, P. A. Bushev, A. V. Ustinov, and M. Weides, "Efficient and robust analysis of complex scattering data under noise in microwave resonators", Rev. Sci. Instrum. **86** (2015) (cit. on pp. 57, 138).

[223] *Technical datasheet: Cryogenic circulators and isolators. url = https://lownoisefactory.com/product/8-12-ghz-single-junction-isolator-circulator*. (Cit. on pp. 58, 120).

[224] D. Davoudi, A. Mohamed, and S. Barzanjeh, "Hybridized-Mode Parametric Amplifier in Kinetic-Inductance Circuits", arXiv (2025) (cit. on p. 61).

[225] N. E. Frattini, U. Vool, S. Shankar, A. Narla, K. M. Sliwa, and M. H. Devoret, "3-wave mixing Josephson dipole element", Applied Physics Letters **110** (2017) (cit. on p. 62).

[226] A. Bienfait, J. J. Pla, Y. Kubo, M. Stern, X. Zhou, C. C. Lo, C. D. Weis, T. Schenkel, M. L. W. Thewalt, D. Vion, D. Esteve, B. Julsgaard, K. Mølmer, J. J. L. Morton, and P. Bertet, "Reaching the quantum limit of sensitivity in electron spin resonance", Nat. Nanotechnol. **11**, 253–257 (2016) (cit. on p. 65).

[227] W. Vine, M. Savytskyi, A. Vaartjes, A. Kringhøj, D. Parker, J. Slack-Smith, T. Schenkel, K. Mølmer, J. C. McCallum, B. C. Johnson, A. Morello, and J. J. Pla, "In situ amplification of spin echoes within a kinetic inductance parametric amplifier", Sci. Adv. **9** (2023) (cit. on pp. 65, 77, 81, 103).

[228] D. Rieger, "Gralmonium – Granular Aluminum Nano-Junction Fluxonium Qubit", 47.12.01; LK 01, PhD thesis (Karlsruher Institut für Technologie (KIT), 2024), 94 pp. (cit. on p. 66).

[229] M. Féchant, M. F. Dumas, D. Bénâtre, N. Gosling, P. Lenhard, M. Spiecker, S. Geisert, S. Ihssen, W. Wernsdorfer, B. D'Anjou, A. Blais, and I. M. Pop, "Offset Charge Dependence of Measurement-Induced Transitions in Transmons", Phys. Rev. Lett. **135**, 180603 (2025) (cit. on p. 70).

[230] N. Zapata, N. E. Abari, M. Field, P. Winkel, S. Geisert, S. Ihssen, A. Metelmann, and I. M. Pop, "Double-Pumped Kerr Parametric Amplifier Beyond the Gain-Bandwidth Limit", arXiv (2025) (cit. on p. 75).

[231] J. Agustí, Y. Minoguchi, J. M. Fink, and P. Rabl, "Long-distance distribution of qubit-qubit entanglement using Gaussian-correlated photonic beams", Phys. Rev. A **105**, 062454 (2022) (cit. on pp. 75, 103).

[232] Y. Jiang, E. P. Ruddy, K. O. Quinlan, M. Malnou, N. E. Frattini, and K. W. Lehnert, "Accelerated Weak Signal Search Using Mode Entanglement and State Swapping", PRX Quantum **4**, 020302 (2023) (cit. on pp. 75, 78, 98).

[233] M. R. Perelshtein, K. V. Petrovnin, V. Vesterinen, S. Hamedani Raja, I. Lilja, M. Will, A. Savin, S. Simbierowicz, R. N. Jabdaraghi, J. S. Lehtinen, L. Grönberg, J. Hassel, M. P. Prunnila, J. Govenius, G. S. Paraoanu, and P. J. Hakonen, "Broadband Continuous-Variable Entanglement Generation Using a Kerr-Free Josephson Metamaterial", Phys. Rev. Appl. **18**, 024063 (2022) (cit. on p. 76).

[234] N. Klimovich, P. Day, S. Shu, B. H. Eom, H. Leduc, and A. Beyer, "Demonstration of a Quantum Noise Limited Traveling-Wave Parametric Amplifier", arXiv (2023) (cit. on p. 76).

[235] J. Wang, K. Peng, J. M. Knecht, G. D. Cunningham, A. E. Lombo, A. Yen, D. A. Zaidenberg, M. Gingras, B. M. Niedzielski, H. Stickler, K. Sliwa, K. Serniak, M. E. Schwartz, W. D. Oliver, and K. P. O'Brien, "High-Efficiency, Low-Loss Floquet-mode Traveling Wave Parametric Amplifier", arXiv (2025) (cit. on pp. 76, 134).

[236] K. Peng, M. Naghiloo, J. Wang, G. D. Cunningham, Y. Ye, and K. P. O'Brien, "Floquet-Mode Traveling-Wave Parametric Amplifiers", PRX Quantum **3**, 020306 (2022) (cit. on p. 76).

[237] L. Planat, "Resonant and traveling-wave parametric amplification near the quantum limit", PhD thesis (Université Grenoble Alpes, 2020) (cit. on pp. 76, 128).

[238] J. Grebel, A. Bienfait, É. Dumur, H.-S. Chang, M.-H. Chou, C. R. Conner, G. A. Peairs, R. G. Povey, Y. P. Zhong, and A. N. Cleland, "Flux-pumped impedance-engineered broadband Josephson parametric amplifier", Appl. Phys. Lett. **118**, 142601 (2021) (cit. on p. 76).

[239] D. Ezenkova, D. Moskalev, N. Smirnov, A. Ivanov, A. Matanin, V. Polozov, V. Echeistov, E. Malevannaya, A. Samoylov, E. Zikiy, and I. Rodionov, "Broadband SNAIL parametric amplifier with microstrip impedance transformer", Appl. Phys. Lett. **121**, 232601 (2022) (cit. on p. 76).

[240] T. Zhou, W. Xu, Q. Zuo, J. Pan, Z. Li, K. Zhang, T. Guo, Y. Sheng, L. Jing, H. Ma, M. Yu, S. Zhou, B. Li, S. Yang, Y. Yu, J. Zhu, J. Zhang, J. Li, C. Cao, G. Sun, and P. Wu, "Impedance matched Josephson parametric amplifier with a multisection $\lambda/4$ transmission line transformer", Appl. Phys. Lett. **126**, 104002 (2025) (cit. on p. 76).

[241] D. Marković, S. Jezouin, Q. Ficheux, S. Fedortchenko, S. Felicetti, T. Coudreau, P. Milman, Z. Leghtas, and B. Huard, "Demonstration of an Effective Ultrastrong Coupling between Two Oscillators", Phys. Rev. Lett. **121**, 040505 (2018) (cit. on pp. 77, 103).

[242] C. F. Ockeloen-Korppi, E. Damskägg, J.-M. Pirkkalainen, T. T. Heikkilä, F. Massel, and M. A. Sillanpää, "Low-Noise Amplification and Frequency Conversion with a Multiport Microwave Optomechanical Device", Phys. Rev. X **6**, 041024 (2016) (cit. on pp. 77, 80).

[243] L. D. Tóth, N. R. Bernier, A. Nunnenkamp, A. K. Feofanov, and T. J. Kippenberg, "A dissipative quantum reservoir for microwave light using a mechanical oscillator", Nat. Phys. **13**, 787–793 (2017) (cit. on p. 77).

[244] M. Gao, T. Inoue, T. Kurosu, and S. Namiki, "Evolution of the gain extinction ratio in dual-pump phase sensitive amplification", Opt. Lett. **37**, 1439–1441 (2012) (cit. on p. 89).

[245] M. A. Ettabib, F. Parmigiani, A. Kapsalis, A. Bogris, M. Brun, and P. Labeye, "Record phase sensitive extinction ratio in a silicon germanium waveguide", in *2015 Conference on Lasers and Electro-Optics (CLEO)* (IEEE, 2015), pp. 10–15 (cit. on p. 89).

[246] Y. Wu, C. Wang, D. Wang, M. Xu, Y. Zhou, and H. X. Tang, "Broad Spectrum Coherent Frequency Conversion with Kinetic Inductance Superconducting Metastructures", arXiv, 10.48550/arXiv.2503.09054 (2025) (cit. on p. 96).

[247] M. Field, "LoopPA: 3-wave-mixing grAl parametric amplfier using a grAl loop", arXiv (In preparation) (cit. on p. 96).

[248] A. Remm, S. Krinner, N. Lacroix, C. Hellings, F. Swiadek, G. J. Norris, C. Eichler, and A. Wallraff, "Intermodulation Distortion in a Josephson Traveling-Wave Parametric Amplifier", Phys. Rev. Appl. **20**, 034027 (2023) (cit. on p. 102).

[249] C. Zhou, P. Lu, M. Praquin, T.-C. Chien, R. Kaufman, X. Cao, M. Xia, R. S. K. Mong, W. Pfaff, D. Pekker, and M. Hatridge, "Realizing all-to-all couplings among detachable quantum modules using a microwave quantum state router", npj Quantum Inf. **9**, 54 (2023) (cit. on p. 102).

[250] L. Zhong, E. P. Menzel, R. Di Candia, P. Eder, M. Ihmig, A. Baust, M. Haeberlein, E. Hoffmann, K. Inomata, T. Yamamoto, Y. Nakamura, E. Solano, F. Deppe, A. Marx, and R. Gross, "Squeezing with a flux-driven Josephson parametric amplifier", New J. Phys. **15**, 125013 (2013) (cit. on p. 103).

[251] S. Boutin, D. M. Toyli, A. V. Venkatramani, A. W. Eddins, I. Siddiqi, and A. Blais, "Effect of Higher-Order Nonlinearities on Amplification and Squeezing in Josephson Parametric Amplifiers", Phys. Rev. Appl. **8**, 054030 (2017) (cit. on p. 103).

[252] R. Dassonneville, R. Assouly, T. Peronnin, A. A. Clerk, A. Bienfait, and B. Huard, "Dissipative Stabilization of Squeezing Beyond 3 dB in a Microwave Mode", PRX Quantum **2**, 020323 (2021) (cit. on p. 103).

[253] *Technical datasheet: Cryo. direc. coupl. 4-12 GHz. url = https://quantummicrowave.com/cryogenic-components/.* (Cit. on p. 120).

[254] *Technical datasheet: Non-magnetic coaxial cables with SMA connectors SC-219/50-SC. url = http://www.coax.co.jp/en/product/sc/219-50-sc.html.* (Cit. on p. 120).

[255] S.-W. Chang, J. Aumentado, W.-T. Wong, and J. C. Bardin, "Noise measurement of cryogenic low noise amplifiers using a tunnel-junction shot-noise source", in *2016 IEEE MTT-S International Microwave Symposium (IMS)* (IEEE, 2016), pp. 22–27 (cit. on p. 129).

[256] N. Bergeal, F. Schackert, M. Metcalfe, R. Vijay, V. E. Manucharyan, L. Frunzio, D. E. Prober, R. J. Schoelkopf, S. M. Girvin, and M. H. Devoret, "Phase-preserving amplification near the quantum limit with a Josephson ring modulator", Nature **465**, 64–68 (2010) (cit. on p. 129).

[257] J. L. Cano, N. Wadefalk, and J. D. Gallego-Puyol, "Ultra-Wideband Chip Attenuator for Precise Noise Measurements at Cryogenic Temperatures", IEEE Trans. Microwave Theory Tech. **58**, 2504–2510 (2010) (cit. on p. 132).

[258] S. Günzler, P. Winkel, D. Rieger, K. Borisov, M. Spiecker, A. V. Ustinov, I. M. Pop, and W. Wernsdorfer, "Superconducting microwave magnetometer for absolute flux detection", arXiv (2021) (cit. on pp. 138, 140).

[259] O. Astafiev, A. M. Zagoskin, A. A. Abdumalikov Jr., Y. A. Pashkin, T. Yamamoto, K. Inomata, Y. Nakamura, and J. S. Tsai, "Resonance Fluorescence of a Single Artificial Atom", Science **327**, 840–843 (2010) (cit. on p. 138).

[260] L. Grünhaupt, U. von Lüpke, D. Gusenkova, S. T. Skacel, N. Maleeva, S. Schlör, A. Bilmes, H. Rotzinger, A. V. Ustinov, M. Weides, and I. M. Pop, "An argon ion beam milling process for native AlOx layers enabling coherent superconducting contacts", Appl. Phys. Lett. **111** (2017) (cit. on p. 137).

[261] *Technical datasheet: TMM Laminates Rogers Corporation. url = https://www.rogerscorp.com/advanced-electronics-solutions/tmm-laminates/tmm-10i-laminates.* (Cit. on p. 149).